Improving Electrocatalysts through Advanced Nanostructure Characterization

Von der Fakultät für Georessourcen und Materialtechnik der

Rheinisch-Westfälischen Technischen Hochschule Aachen

zur Erlangung des akademischen Grades eines

Doktors der Naturwissenschaften

genehmigte Dissertation

vorgelegt von

Miquel Vega Paredes, M. Sc.

Berichter: **Univ.-Prof. Dr. Christina Scheu**

Univ.-Prof. Dr. Jochen M. Schneider

Tag der mündlichen Prüfung: 21.10.2024

ABSTRACT

Electrocatalysts play a pivotal role in the decarbonization of our world by enhancing the kinetics of electrochemical reactions, thereby boosting the performance of devices such as fuel cells and water electrolyzers. High-performing electrocatalysts are typically based on expensive metals like Pt or Ir, which hinders the widespread commercialization of these devices. It is therefore of great importance to study how to enhance the activity and stability of such expensive materials, which would allow for a lower loading and cost, or to find cheaper, high-performing alternatives.

The stability and activity of a catalyst can be improved by modifying its structure, both on the nanometer scale (e.g., by changing the size or shape of the catalyst) and atomic scale (e.g., by introducing strain, lattice defects, or foreign elements). By studying how the structure of a catalyst affects its performance, it is possible to elucidate structure-properties relationships, which in turn enables the rational design of superior catalysts with optimized structures. Nonetheless, studying the local atomic structure in a representative manner, or its evolution during catalysis presents a formidable challenge. Recent advances in (scanning) transmission electron microscopy have made such studies possible, allowing the determination of degradation or activation mechanisms of electrocatalysts, and the systematic study of the effects of defects on catalysis.

In this thesis, state-of-the-art (scanning) transmission electron microscopy-based techniques are used to develop new insights into how the structure and lattice defects of electrocatalysts influence their performance. Moreover, method development is pursued in cases where the current techniques cannot be successfully applied.

Various electrocatalytic materials with applications in fuel cells and electrolyzers were studied. Firstly, the degradation mechanisms of Rh-core Pt-shell nanoparticles under electrochemical cycling -used to mimic fuel cell operation conditions- were investigated. Using identical location scanning transmission electron microscopy, it was discovered that particle detachment from the carbon support was the main degradation mechanism responsible for the loss of activity during the electrochemical tests, providing valuable insights into which strategies need to be prioritized for developing more stable catalytic systems.

After having seen the potential of the identical location technique on fuel cell investigations, it was investigated how to apply it for gas-evolving reactions, such as those occurring in a water

electrolyzer. It was discovered that the identical location technique could be easily and reproducibly applied to such reactions using the tweezers method, as opposed to the commonly used Teflon cap method.

Next, with the help of this easy-to-implement method, a catalyst for the oxygen evolution reaction, i.e., the anodic reaction in an electrolyzer, was studied. $LaNiO_3$ perovskite nanoparticles were selected for this part due to their low cost and high catalytic activity. The results revealed that Fe traces in the potassium hydroxide electrolyte diffuse into Ruddlesden-Popper planar faults present in the $LaNiO_3$ structure, causing structural changes that enhance the catalytic activity of the perovskites. This work highlighted the importance of defects in the catalytic activity, motivating the study of a different class of defects, namely grain boundaries.

In particular, the aim was to use grain boundaries for increasing the catalytic activity of the expensive noble metal Pt. It was discovered that the catalytic activity of grain boundary-rich Pt nanoparticle assemblies was over 35x higher than single-crystal Pt nanoparticles, thanks to their elevated number of concave grain boundary sites. Moreover, it was seen that the active sites could be stabilized by boron segregation.

Lastly, having showcased the potential of grain boundaries in enhancing the catalytic activity of noble metals, the effect was explored further for Au. Using Au samples with a controlled grain boundary density as a material system, a relationship between grain boundary density, coordination number and catalytic activity was revealed.

This thesis is a demonstration of how material science can contribute to improving the stability and activity of catalysts by tuning their structure and exploiting the potential of defects in catalysis.

ZUSAMMENFASSUNG

Elektrokatalysatoren spielen eine zentrale Rolle bei der Dekarbonisierung unserer Welt, indem sie die Kinetik elektrochemischer Reaktionen verbessern und so die Leistung von Geräten wie Brennstoffzellen und Wasserelektrolyseuren steigern. Leistungsstarke Elektrokatalysatoren basieren jedoch in der Regel auf teuren Metallen wie Pt oder Ir, was die breite Kommerzialisierung dieser Geräte behindert. Daher ist es von entscheidender Bedeutung zu untersuchen, wie die Aktivität und Stabilität dieser teuren Materialien verbessert werden kann, was eine geringere Beladung und niedrigere Kosten ermöglichen würde, oder günstigere, hochleistungsfähige Alternativen zu finden.

Die Stabilität und Aktivität eines Katalysators kann durch Veränderung seiner Struktur erhöht werden, sowohl auf der Nanometerskala (z.B. durch Veränderung der Größe oder Form des Katalysators) als auch auf der atomaren Skala (z.B. durch Einbringen von Spannungen, Gitterdefekten, oder Fremdelementen). Die Untersuchung, wie sich die Struktur eines Katalysators auf seine Leistung auswirkt, ermöglicht es so genannte Struktur-Eigenschafts-Beziehungen aufzustellen, die die Entwicklung besserer Katalysatoren mit optimierten Strukturen ermöglichen. Die Untersuchung der lokalen Atomstruktur in repräsentativer Weise oder ihrer Entwicklung während der Katalyse stellt jedoch eine enorme Herausforderung dar. Die neuesten Fortschritte in der (Raster-)Transmissions-Elektronenmikroskopie haben solche Studien möglich gemacht und erlauben die Bestimmung von Abbau- oder Aktivierungsmechanismen von Elektrokatalysatoren sowie die systematische Untersuchung der Auswirkungen von Defekten auf die Katalyse. In dieser Arbeit kamen modernste elektronenmikroskopische Techniken zum Einsatz, um neue Erkenntnisse darüber zu gewinnen, wie die Struktur und Gitterdefekte von Elektrokatalysatoren deren Leistung beeinflussen. Für die Fälle, in denen die derzeitigen Techniken nicht erfolgreich angewandt werden konnten, wurden Methodenentwicklung betrieben.

Es wurden verschiedene elektrokatalytische Materialien mit Anwendungen in Brennstoffzellen und Elektrolyseuren untersucht. Zunächst wurden die Degradationsmechanismen von Nanopartikeln mit Rh-Kern und Pt-Schale unter elektrochemischen Zyklen untersucht, welche die Betriebsbedingungen von Brennstoffzellen simulieren. Mit Hilfe der Rastertransmissionselektronenmikroskopie an identischen Positionen wurde festgestellt, dass die Ablösung der Partikel vom Kohlenstoffträger der wichtigste Degradationsmechanismus war, der für den Aktivitätsverlust während der elektrochemischen Tests verantwortlich ist.

Dieses Ergebnis lieferte wertvolle Erkenntnisse darüber, welche Strategien für die Entwicklung stabilerer katalytischer Systeme vorrangig zu verfolgen sind.

Nachdem das Potenzial der Methode an identischen Positionen vor und nach elektrochemischen Tests bei Untersuchungen an Brennstoffzellen erkannt worden war, wurde sie für gasentwickelnden Reaktionen, wie sie in einem Wasserelektrolyseur auftreten, weiterentwickelt. Es wurde festgestellt, dass die Technik bei solchen Reaktionen einfach und reproduzierbar mit der Pinzettenmethode angewandt werden kann, im Gegensatz zu der üblicherweise verwendeten Teflonkappenmethode.

Anschließend wurde mit Hilfe dieser einfach zu implementierenden Methode ein Katalysator für die Sauerstoffentwicklungsreaktion, d. h. die anodische Reaktion in einem Elektrolyseur untersucht. $LaNiO_3$-Perowskit-Nanopartikel wurden aufgrund ihrer geringen Kosten und ihrer hohen katalytischen Aktivität für diesen Untersuchungen ausgewählt. Die Ergebnisse zeigten, dass Fe-Spurenelemente im Kaliumhydroxid-Elektrolyten in die Ruddlesden-Popper-Planardefekte in der $LaNiO_3$-Struktur diffundieren und dort strukturelle Veränderungen verursachen, die die katalytische Aktivität der Perowskite erhöhen. Diese Arbeit hat die Bedeutung von Defekten für die katalytische Aktivität hervorgehoben und dazu motiviert, eine andere Art von Defekten, nämlich Korngrenzen, zu untersuchen.

Es wurde festgestellt, dass die katalytische Aktivität von Pt-Nanopartikeln, die reich an Korngrenzen sind, mehr als 35 Mal höher ist als die von einkristallinen Pt-Nanopartikeln, was auf die erhöhte Anzahl konkaver Korngrenzen zurückzuführen ist. Darüber hinaus wurde beobachtet, dass diese Defekte durch Dotierung mit Bor stabilisiert werden können.

Nachdem das Potenzial von Korngrenzen zur Steigerung der katalytischen Aktivität von Edelmetallen aufgezeigt worden war, wurde die Beziehung zwischen Korngrenzen und Katalyse genauer untersucht. Unter Verwendung von Au-Proben mit einer kontrollierten Korngrenzendichte als Materialsystem wurde ein Zusammenhang zwischen Korngrenzendichte, Koordinationszahl und katalytischer Aktivität festgestellt.

Die vorliegende Doktorarbeit zeigt, wie die Materialwissenschaft dazu beitragen kann, die Stabilität und Aktivität von Katalysatoren zu verbessern, indem ihre Struktur optimiert und das Potenzial von Defekten in der Katalyse genutzt wird.

PREFACE

The following publications contributed to this thesis († = Equally contributing):

Paper I

Electrochemical Stability of Rhodium−Platinum Core−Shell Nanoparticles: An Identical Location Scanning Transmission Electron Microscopy Study

Miquel Vega-Paredes, Raquel Aymerich-Armengol, Daniel Arenas Esteban, Sara Martí Sánchez, Sara Bals, Christina Scheu and Alba Garzón Manjón

ACS Nano **2023***, 17,* 16943-16951

Paper II

Expanding the Potential of Identical Location Scanning Transmission Electron Microscopy for Gas Evolving Reactions: Stability of Rhenium Molybdenum Disulfide Nanocatalysts for Hydrogen Evolution Reaction

Miquel Vega-Paredes†, Christina Scheu and Raquel Aymerich-Armengol†

ACS Applied Materials & Interfaces **2023**, 15, 46895-46901

Paper III

Fe-Incorporation in Ruddlesden-Popper Faults for Enhanced Oxygen Evolution in $LaNiO_3$ Perovskites

Miquel Vega-Paredes, Haritha Cheraparambil, Zhenyu Wang, Chanwon Jung, Claudia Weidenthaler, Siyuan Zhang and Christina Scheu

Under preparation

Paper IV

Concave Grain Boundary Stabilized by Boron Segregation for Efficient and Durable Oxygen Reduction

Xin Geng†, Miquel Vega-Paredes†, Xiaolong Lu, ,Poulami Chakraborty, Yue Li, Christina Scheu, Zhenyu Wang and Baptiste Gault

Advanced Materials **2024**, 36, 2404839

Paper V

Grain Boundary Engineering for Efficient and Durable Electrocatalysis

Xin Geng†, Miquel Vega-Paredes†, Zhenyu Wang,Colin Ophus, Pengfei Lu, Yan Ma, Siyuan Zhang, Christina Scheu, Christian H. Liebscher and Baptiste Gault

Nature Communications **2024**, 15, 8534

STATEMENT ON CONTRIBUTIONS TO SCIENTIFIC PUBLICATIONS

Paper I: **M.V-P.** performed the (S)TEM characterization, corresponding data analysis and wrote the manuscript. R.A.A. contributed to performing the electrochemistry measures and the interpretation of the results. **M.V-P.** and D.A.E. performed the electron tomography experiments on the as-synthesized samples. S.M.S. built the 3D atomic models of the Rh@Pt/C NPs. S.B. provided scientific support. C.S. and A.G.M. initiated the study, coordinated the research, provided their scientific support, and contributed to the interpretation of the results. All authors contributed to the manuscript. All authors have approved the final version of the manuscript.

Paper II: **M.V-P.** and R.A-A. contributed equally to this work. **M.V-P.** and R.A.A. performed the electrochemical experiments. **M.V-P.** performed the analysis of the electrochemical data assisted by R.A-A. R.A-A. performed the synthesis and electron microscopy assisted by **M.V-P.** C.S. contributed through scientific discussions. **M.V-P.** and R.A-A. wrote the manuscript, and it was revised and approved by all authors.

Paper III: **M.V-P.** designed the overall experiments with the help of C.S. and S.Z. **M.V-P.** performed the IL-STEM experiments. H.C. performed the synthesis and electrochemistry. Z.W. conducted the DFT calculations. C.J. and C.W. provided scientific support. All authors contributed and have approved the final version of the manuscript.

Paper IV: X.G. and **M.V-P.** contributed equally to this work. X.G. and B.G. designed the overall experiments. X.G. performed the synthesis, APT analysis and electrochemical measurements. **M.V-P.** collected and analyzed the HAADF-STEM and HRTEM images supported by C.S. Z.Y.W. and P.C. conducted the theoretical simulation. X.G., **M.V-P.**, Z.Y.W., C.S. and B.G. collectively wrote the manuscript. All authors contributed and have approved the final version of the manuscript.

Paper V: X.G. and **M.V-P.** contributed equally to this work. X.G. performed the synthesis, electrochemistry and APT measurements. **M.V-P.** performed the HAADF-STEM and HRTEM experiments under the supervision of C.S. **M.V-P.** performed the 4D-STEM experiments with the support of C.O., S.Z., and C.H.L. P.L. and X.G. conducted the theoretical simulation. X.G., **M.V-P.**, P.L., C.S. and B.G. wrote the manuscript. All authors contributed and have approved the final version of the manuscript.

ABBREVIATIONS AND LIST OF SYMBOLS

(μ/m)A	(Micro/milli)amper
(μ/m)L	(Micro/milli)liter
(μ/n/p)m	(Micro/nano/pico)meter
ΔG	Change in Gibbs free energy
4D-STEM	Four-dimensional scanning transmission electron microscopy
Å	Angstrom
ADF	Annular dark field
Ag/AgCl	Silver/silver chloride electrode
APT	Atom probe tomography
AST	Accelerated stress test
Au	Gold
B	Boron
BET	Brunauer-Emmett-Teller
BF	Bright field
BF-Pt NA	Boron-free platinum nanoassembly
CO	Carbon monoxide
CO_2	Carbon dioxide
C_s	Spherical aberration coefficient
CSL	Coincidence site lattice theory
CV	Cyclic voltammetry
DEA	Diethylamine
DFT	Density functional theory
DI	Deionized
E_{oxd}^{anode}	Oxidation potential of anode
$E_{red}^{cathode}$	Reduction potential of cathode
e^-	Electron
e.g.	For example
$E_{binding}$	Binding energy
ECSA	Electrochemically active surface area
EDS	Energy dispersive X-ray spectroscopy
EELS	Electron energy loss spectroscopy
E_{remove}	Energy required to remove a atom

EXAFS	X-ray absorption fine structure
F	Faraday constant
Fcc	Face centered cubic
FFT	Fast Fourier transform
GB	Grain boundary
GB-Pt NA	Grain boundary-rich Pt nanoassembly
GCN	Generalized coordination number
H/M/L Au NA	Gold nanoparticle assembly synthesized with high/medium/low flow rate
H^+	Proton
H_2	Hydrogen (molecular)
H_2O	Water
H_2O_2	Hydrogen peroxide
H_2SO_4	Sulfuric acid
HAADF	High angle annular dark field
HAGB	High angle grain boundary
$HClO_4$	Perchloric acid
HER	Hydrogen evolution reaction
HOR	Hydrogen oxidation reaction
HR	High-resolution
i.e.	That is
ICP-AES	Inductively coupled plasma atomic emission spectroscopy
ICP-OES	Inductively coupled plasma optical emission spectroscopy
IL-(S)TEM	Identical location scanning transmission electron microscopy
Ir	Iridium
KOH	Potassium hydroxide
(k)eV	(Kilo)electronvolt
kV	(Kilo)volt
LAGB	Low angle grain boundary
$LaNiO_3$	Lanthanum nickel oxide
LSV	Linear sweep voltammetry
M	Molar (mols/L)
mg	Milligram
MoS_2	Molybdenum disulfide

NH_3	Ammonia
NP	Nanoparticle
O_2	Oxygen (molecular)
OAm	Oleyamine
OER	Oxygen evolution reaction
ORR	Oxygen reduction reaction
PEM	Proton exchange membrane
Pt	Platinum
Pt(acac)2	Platinum (II) acetylacetonate
RDE	Rotating disk electrode
$Re_xMo_{1-x}S2$	Rhenium-doped molybdenum disulfide
Rh	Rhodium
Rh@Pt/C	Rhodium-core platinum-shell nanoparticles on carbon support
RHE	Reversible hydrogen electrode
RRDE	Rotating ring disk electrode
Ru	Ruthenium
Sigma	∑
(S)TEM	(Scanning) transmission electron microscopy
V_{RHE}	Potential vs the reversible hydrogen electrode
XANES	X-ray absorption near-edge spectroscopy
XAS	X-ray absorption spectroscopy
XPS	X-ray photoelectron spectroscopy
XRD	X-ray diffraction
Z	Atomic number
ZA	Zone axis
α	Convergence angle
$\varepsilon_{xx/yy/xy}$	Component of strain along xx/yy/xy directions
θ	Theta (angle)
λ	Wavelength

ACKNOWLEDGEMENTS

The day after I submitted my thesis to the university, I realized that I had forgotten probably the most important part – the Acknowledgements. I had been so focused on getting everything done before the submission deadline, that I had neglected to include my heartfelt thanks to all the people involved in my journey. They have guided me throughout these years, given me support, and generally, made this an unforgettable experience that I will treasure for years to come. So here we are, several weeks later in Berkeley, writing the acknowledgements filled with gratitude and with a smile on my face from all the fond memories that come to mind when I reflect on my PhD years.

I would like to start my acknowledgements by thanking the two people who made this experience possible: **Christina Scheu** and **Alba Garzón Manjón**. Alba first introduced me to Tina when I was an undergraduate student looking to perform an internship. That internship was my first real research experience, and I was lucky enough to do it in the amazing group that is NG. After my internship, I was convinced that I wanted to pursue a PhD in the same group… and here we are, several years later, extremely happy with that decision. **Tina** is an amazing boss and supervisor who really cares about her students. I am particularly grateful for the scientific freedom she has allowed me. This has enabled me to explore many different directions and be involved in several projects, all of which have allowed me to learn more than if I had been limited to a single, predefined project. I also cannot thank her enough for the confidence she has shown in me by nominating me for scholarships and conferences. Thank you, Tina, I could not have asked for a better supervisor.

One of Tina's decisions that I am most grateful for is the appointment of Alba as my advisor. **Alba** has believed in me from day one and has always pushed me to be the best version of myself. She knew how to handle me and how to keep me going when my motivation was low after unsuccessful experiments. She was the first person I called when I had news about a submitted paper or some new gossip I needed to explain. She has taught me how to use the TEM, how to navigate the bureaucracy and regulations at the institute, and countless useful tricks for academia. I could go on about how Alba shaped this thesis, but suffice it to say that it would have been completely different without her. More than being an advisor, Alba has been a friend of mine. From the beginning, she helped me adapt to a new country and a new work environment. I was really fortunate to have been able to count on her during the long

winter in Germany. Doing beauty nights and eating salmon at her place are memories that will stay with me for years to come.

I would also like to thank **Jochen Schneider** for agreeing to be my official supervisor at the RWTH. I am grateful for his positive feedback on my project and for finding time in his busy schedule to discuss my work and write a letter of recommendation when I needed it.

During my time at MPIE I have had the opportunity to work with really truly brilliant and kind people. I was especially lucky to work with **Xin** and **Spark**. Working with them gave me the opportunity to learn their unique ways of doing science, all of which have made me grow greatly as scientist. There are many other people at MPIE whom I would like to thank. **Christian Liebscher** helped me with the 4D-STEM experiments, **Philipp Watermeyer** introduced me to the Titans, **Volker Kree** was always a phone call away when I needed his help, and I kept bothering **Simon Reckort** about ordering new chemicals and fixing the ultrapure water system. Another person I would like to extend my heartfelt thanks to is **Benjamin Breitbach** for all the effort he put into performing XRD experiments on my unconventional and difficult samples. **Thomas Warkentine** was the first student I supervised, and I want to thank him for his motivation and dedication to the project, continuing the experiments even after I left for the USA.

On a more personal level, there are many people at MPIE who have accompanied me during these years and made them memorable.

First of all, I would like to thank **Raquel**, who has been an amazing office mate and collaborator, and **Ruben**, for his patience in teaching me TEM. I consider them two of my dearest friends, and I am truly fortunate to have had their help and guidance throughout these years. I am really happy to hear that you are coming back to Düsseldorf and I cannot wait to celebrate this good news together.

With them, I also want to thank the rest of the dear friends I have made at MPIE. **Ali**, for always being willing to help me when I had a problem and for the nice workouts together (I know you enjoyed the 100 pull-up challenge despite your complaints!), **Bárbara**, for the trips to the vending machine that were really needed during the low points of the PhD, **Fran**, for always making me laugh, for being a great friend and for the workouts together, and **Marti**, for the sometimes-heated debates that made me rethink things that I took for granted. I look forward to continuing to build fond memories together.

In addition, I have had the chance to meet the really nice and friendly members of the NG group and the SN department. I am happy to have shared moments and become friends with **Ana**, **Chanwon**, **Hendrik**, **Hui**, **Nico**, **Nina** and **Tonya**, and I hope that we will keep in touch after our time at the institute is over.

Outside of the institute, I have also been very fortunate to make great friends who have made my time in Düsseldorf much more enjoyable. I am of course talking about my ex-roommate **Ashwin** (even though the pictures of the two parties we threw have been lost, I will always remember them fondly), **Cris** (thank you for keep coming back to Düsseldorf to visit), **Elsa** (for introducing me to the world of bachata and salsa), **Iván** (for always being ready to play board games or going out), **Laura** (for the hip thrust sessions on Sundays and for motivating me to run a half marathon), and **Mary** (for always being willing to open your house and for preparing delicious food).

Finally, these acknowledgements would be incomplete without mentioning my amazing partner and my loving family. **Irene**, thank you for making me take holidays to get away from the stress of the PhD, for your support, and for your faith in me. I am really happy to have shared this last half of the PhD with you and look forward to our next adventures together. To my **sister**, I would like to say that I enjoyed deeply seeing you again after months of being away. Finally, to my **mom** and **dad**, I have nothing but the deepest love and thanks. Thank you for your support, the regular video calls, for coming to visit me in Düsseldorf, and for spoiling me with delicious food when I visited.

TABLE OF CONTENT

1 Introduction

A catalyst increases the rate of a chemical reaction, enabling it to proceed faster.[1] Despite this simple definition, catalysts are extremely important in our world. For instance, it is estimated that catalytic processes are involved at some step in the production of ~80% of all manufactured goods and that catalysts contribute indirectly to ~30% of the world's gross domestic product.[2] Electrocatalysts are a particular type of catalyst that catalyze electrochemical reactions, that is, reactions that are caused by or that produce an electrical current. As we keep electrifying our world and increasing the share of renewable energy in the electricity mix to reduce our greenhouse gas emissions[3], electrocatalysts will get more and more important. Not only that, electrocatalysts will also contribute directly to reducing our dependency on fossil fuels since they are fundamental for the successful establishment of a hydrogen (H_2)-based economy.[4,5] A schematic representation of the different parts involved in the hydrogen economy is given in **Figure 1-1**.

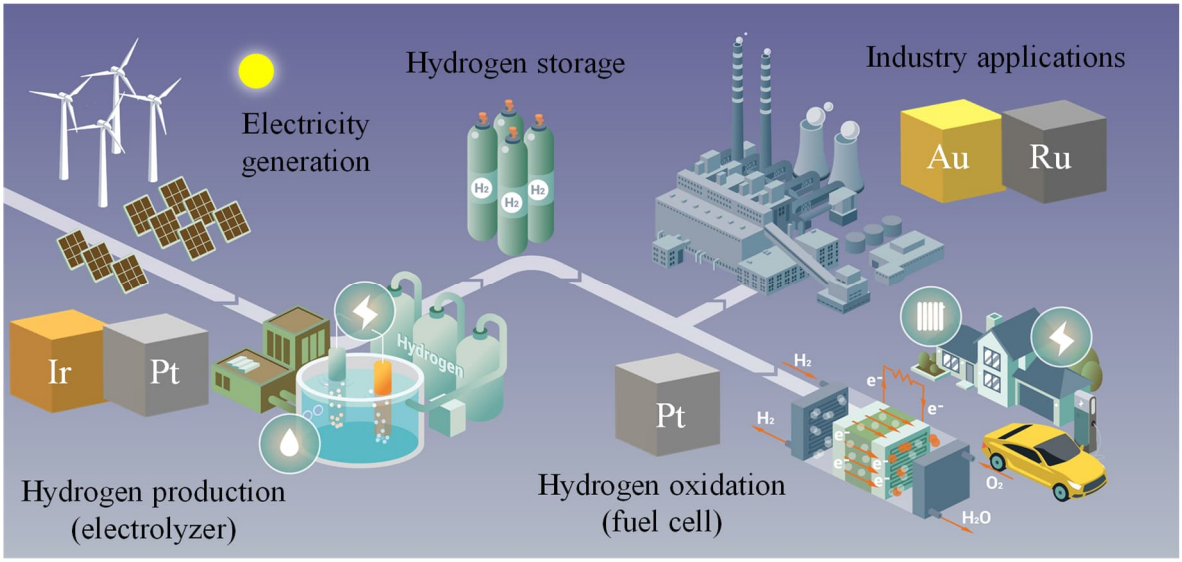

***Figure 1-1**. Schematic representation of a hydrogen-based energy economy. Electrocatalysts are needed in several critical steps. Figure courtesy of Tianyi You (MPIE).*

As a clean energy carrier, H_2 provides a way to store the excess energy produced by renewable energy sources such as the wind or sun. Using the electricity generated by such sources, green H_2 can be produced by splitting water (H_2O) into its elements in an electrolyzer.[6] This H_2 can be stored (although H_2 storage is far from trivial), and during spikes of energy demand, or drops of energy production by renewable sources, oxidized in a fuel cell for generating electricity.[7] Furthermore, H_2 can also be directly used in industry, for instance for producing chemicals like ammonia (NH_3)[6] or hydrogen peroxide (H_2O_2)[8], or metals like green steel[9].

Electrocatalysts are fundamental in order to make this future a reality since they are needed in several critical steps of the process, including hydrogen production[10], storage[11], oxidation[12], and obtention of chemicals in the industry[5,13]. The best-performing catalysts for H_2 production in an electrolyzer are platinum (Pt)[14]- or iridium (Ir)[15]-based, and for H_2 oxidation in a fuel cell are Pt-based[16]. In the industry, a large variety of catalysts can be used depending on the specific reaction, but catalysts based on metals like ruthenium (Ru)[17] or gold (Au)[18] are routinely used. All of these materials have something in common, which is that they are extremely expensive. For instance, the market price of one Kg of Ru is ~13.000 €, for Pt ~ 28.000 €, for Au ~ 65.000 € and Ir is even more expensive at ~145.000 €/Kg (all prices given as of 04.2024).[19] Therefore, to enable a fossil fuel-free, H_2-based economy, we must enhance the performance of existing noble metal-based electrocatalysts to use them more efficiently in lower quantities. Alternatively, we can focus our efforts on developing more affordable alternatives based on earth-abundant elements.

Current noble-metal-based electrocatalysts can perform better by modifying their structure on the nano[20,21] and atomic level[22,23], since these factors affect both the activity and stability of catalysts. Therefore, studying how the structure of catalysts affects their performance is fundamental and one key aspect of this thesis. Building these so-called structure-property relationships enables the rational design of improved catalysts that fulfill the activity and stability requirements for their successful commercial implementation.

Cheaper alternatives to noble-metal-based catalysts are typically composed of abundant elements such as 3d transition metals (e.g., Fe, Cu, Ni) and/or non-metallic elements (N, P, S, O). Nickelates such as lanthanum nickel oxide ($LaNiO_3$)[23] and sulfides like molybdenum disulfide (MoS_2)[24] have emerged as potential replacements for Ir and Pt in electrolyzers as water-splitting catalysts. Nonetheless, non-noble-based catalysts usually perform worse than their noble metal counterparts, especially when considering their stability under operation conditions.[25] For instance, most transition metals are not stable under the acidic environment and the high potentials present at the cathodes of fuel cells,[26] and they suffer important changes in activity and morphology during operation. In order to study such changes as a function of the operation conditions (e.g., applied voltage or time), tools capable of tracking structural modifications on the nanometer or atomic scale under operation conditions are needed. For this reason, an additional key aspect of this thesis was to contribute to the development of these tools.

Despite the importance of studying the effects of the structure on the catalytic performance, it is not straightforward due to the small size of catalysts. Catalysts typically have dimensions of a few nanometers to maximize their fraction of surface atoms, since those atoms interact with the reactant molecules and catalyze the reaction.[27] Additionally, the atomic arrangement also affects the catalytic properties. Local distortions of the lattice parameter[16,28] or defects such as grain boundaries (GBs)[29], stacking faults[22], and vacancies[30,31] have been reported to boost catalytic activity. Nonetheless, the full potential of defects in electrocatalysis remains to be exploited due to the intrinsic difficulty of performing an in-depth study at an angstrom scale that is also representative of the sample. An additional difficulty is exploring how the local atomic structure (e.g., defects) evolves under catalytic conditions, since this requires tracking individual regions of the sample during catalysis, or a thorough characterization from multiple regions to have enough statistical insights.

(Scanning) transmission electron microscopy ((S)TEM) and associated spectroscopy techniques are some of the most powerful tools for studying materials with high spatial resolution. These techniques not only allow for imaging with a sub-Angstrom resolution[32], but also enable elemental and chemical distribution mapping with atomic resolution[33]. Moreover, novel techniques (e.g., four-dimensional (4D)-STEM[34], electron tomography[35,36], identical location[37], *operando*[38]) continue to be developed and improved. Such novel methods provide an unprecedented degree of structural information and possibilities. For instance, using 4D-STEM, the grain boundary type in areas of several μm^2 can be identified[39], potentially with sub-nm resolution[40]. Additionally, the improvement of identical location[37] and *operando*[38] methods enables the study of the local structural changes in individual regions of the sample under operation conditions.

Nonetheless, these novel techniques have been applied to relatively few systems, making the structure-property relationships of many electrocatalysts still unknown and leaving many questions about the role of defects in catalysis unexplored.

1.1 Aim of the thesis

This thesis aims to study how the nano- and atomic structure of electrocatalysts affect their performance, both in terms of activity and stability. In particular, state-of-the-art transmission electron microscopy-based techniques are used for developing insights into the effects of structure and lattice defects in catalysis. This research intends to solve previously unanswered questions due to the difficulties in characterizing the changes in the local structure during

catalysis and the local atomic structure in a representative manner. Additionally, in the cases where the current techniques presented challenges in being applied, method development is pursued in order to enable them.

Several material systems have been explored, all in the context of the H_2 economy. On the electrolyzer side, the earth-abundant MoS_2 and $LaNiO_3$ are investigated as alternatives to the expensive noble metals. On the fuel cell side, efforts are made to study how to improve the activity and stability of Pt-based materials. Lastly, Au is explored as a catalyst for an additional end-use case of H_2, namely the sustainable production of chemicals.

A deep understanding of the structure-properties relationships enables the rational design of more active and more stable electrocatalysts, paving the way for the successful realization of a fossil fuel-free, H_2-based economy and for the green obtention of chemicals.

1.2 Outline

This thesis consists of 9 main chapters. In Chapter 1, the need for developing better electrocatalysts and the importance of studying their structure down to the atomic level are presented. Chapter 2 covers the fundamentals of electrochemistry and catalysis, the reactions investigated during the thesis, the degradation mechanisms suffered by electrocatalysts, and the role of different structure factors on the catalytic performance, with a special focus on grain boundaries. In Chapter 3 the theoretical background of the mostly used characterization techniques is presented. The results achieved during this thesis are presented in Chapters 4 to 8. In Chapter 4, the stability of nanostructured Rh-core Pt-shell particles is studied by means of identical location scanning transmission electron microscopy. Having showcased the potential of this technique in determining the degradation mechanism of electrocatalysts, Chapter 5 deals with how to apply it to catalysts for gas-evolving reactions, for which Re-doped MoS_2 is selected as a material system. The results from Chapter 5 enable the study of the role of planar defects on $LaNiO_3$ perovskites and their changes during the oxygen evolution reaction (Chapter 6). The results of Chapter 6 highlight the critical role that defects can play in affecting the catalytic activity. Therefore, in Chapter 7, the influence of a different type of defect, namely grain boundaries, is explored for Pt nanostructures. Similarly, these investigations reveal that the catalytic properties of Pt are very dependent on the presence of grain boundaries. How to control the density of grain boundaries (and thus the catalytic performance) is explored in Chapter 8 using Au as a model system. Chapter 9 summarizes the

most important results and provides an outlook for future work. In the Appendix, additional data and the Curriculum Vitae are supplied.

2 Fundamentals

2.1 Some basic concepts of electrochemistry

Electrochemistry deals with chemical reactions caused by or that result in charge (e.g., electron) movement. A substance that loses an electron has a higher oxidation state (it is oxidized), while a substance that receives an electron has a lower oxidation state (it is reduced).[41] These oxidation-reduction (or redox) processes are coupled, i.e., for a reduction to take place, an oxidation elsewhere that provides the necessary electrons is required, and vice versa. An electrochemical cell is formed by two electrodes, the anode and the cathode. The reduction reaction takes place at the cathode, while the oxidation occurs at the anode. The reduction potential of a species (E_{red}) is a measure of its tendency to gain electrons (i.e., get reduced), and the oxidation potential (E_{ox}) of its tendency to lose electrons (i.e., get oxidized). Depending on the redox potentials of the cathode and anode species, the reactions in a given electrochemical cell will be thermodynamically favorable or will require some additional energy, as pointed out by the following relationship with the change in Gibbs free energy (ΔG).[41]

$$\Delta G = -zF(E_{red}^{cathode} + E_{oxd}^{anode}) \qquad \textit{Eq. 2-1}$$

Where z is the moles of transferred electrons and F is the Faraday constant.

This gives rise to the two types of electrochemical cells; galvanic and electrolytic.[42,43]

If the magnitude ($E_{red}^{cathode} + E_{oxd}^{anode}$), also referred to as cell potential, is positive, the redox process will be thermodynamically favorable ($\Delta G < 0$), and the electrochemical cell is referred to as "galvanic". Therefore, in galvanic cells, the redox reactions happen spontaneously, and they can convert chemical energy into electrical energy. Fuel cells are one example of galvanic cells, since they produce electricity by oxidizing a fuel, such as hydrogen. Part of the reactions studied in this thesis, such as the hydrogen oxidation reaction (HOR) and the oxygen reduction reaction (ORR), are types of galvanic cell reactions (see section 2.3 for more details).

If the cell potential is negative, the redox process is not thermodynamically favorable ($\Delta G > 0$), and electrical power is needed to drive the reactions. The corresponding electrochemical cell is known as "electrolytic". For instance, water electrolyzers use electricity to split water into oxygen (by oxidizing it) and hydrogen (by reducing it), making the hydrogen evolution reaction (HER) and the oxygen evolution reaction (OER) examples of electrolytic cell reaction.

2.2 Some basic concepts of catalysis

Regardless of whether the reactions are spontaneous or not, electrocatalysts are typically needed to improve their kinetics. Catalysts do not affect the energy of the reactants or products, that is, catalysts do not modify the redox potentials of the anodic and cathodic species. Nonetheless, catalysts lower the energy barrier (known as activation energy) that needs to be overcome for a reaction to take place (**Figure 2-1**). This has the effect of lowering the overpotential of a reaction, which is defined as the potential difference between the thermodynamically expected potential and the potential at which the reaction is experimentally observed.

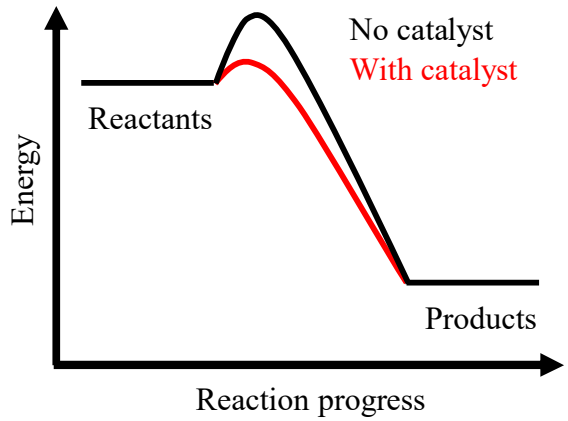

***Figure 2-1**. Role of a catalyst in a chemical reaction. Adapted from Ref [44]*

Overpotentials cause losses of efficiency in an electrochemical cell. For instance, in a galvanic cell, it results in less electrical energy generated than chemical energy consumed. In an electrolytic cell, the existence of overpotential results in a higher energy needed for driving the reactions. Catalysts capable of minimizing significantly the overpotential of a reaction are referred to as being active.

Electrocatalysts lower the activation energy and reduce the overpotential by adsorbing the reactant molecules, weakening some of the reactant molecule's bonds, and facilitating the reaction. There is always an optimal binding energy between the catalyst' surface and the reactants. If the binding energy is too low, the reactant molecule will not bind to the catalyst and no reaction will take place. On the other hand, if the binding energy is too high, the products will not dissociate, and the active site will be blocked.[45] This principle is known as the Sabatier principle, and results in the commonly known volcano plots when plotting catalytic activity versus binding energy (**Figure 2-2**).[45]

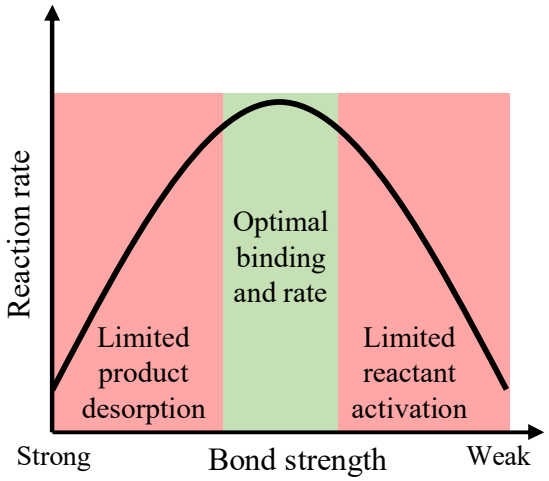

***Figure 2-2**. Schematic representation of the Sabatier principle. Adapted from Ref. [45].*

Good electrocatalysts not only present a high activity towards a given reaction, but they are also able to maintain such high activity for a prolonged period of time, that is, they are both active and stable. That is quite challenging, since electrocatalysts can undergo processes that decrease their activity (see section 2.4). Both the activity and stability can be influenced by the structure. In section 2.5, the different structural factors that affect the performance of electrocatalysts will be addressed. Before that, more information on the reactions of interest will be covered.

2.3 Reactions of interest

For successfully decarbonizing our energy system, it is critical to have active and stable electrocatalysts for all the reactions involved in the electrolyzer side (HER, OER) and the fuel cell side (HOR, ORR). That is why catalysts for all of these reactions have been studied during this thesis. Moreover, electrocatalysts can also be used for the sustainable production of a broad range of fuels and chemicals. Of particular interest is the hydrogen peroxide production reaction, or two-electron ORR, since H_2O_2 is a chemical with numerous applications, such as bleaching agent, detergent production, and disinfectant.[5] Therefore, catalysts for such reactions have also been investigated in this thesis.

2.3.1 Hydrogen evolution reaction

The HER is the cathodic reaction in an electrolyzer, in which hydrogen gas is obtained as a product. The corresponding half-reaction in acidic conditions is:[45]

$$2H^+ + 2e^- \rightarrow H_2 \qquad E^o_{red} = 0\ V \qquad \textit{Eq. 2-2}$$

Where the subscript ° indicates that the reduction potential is measured at a temperature of 298.15 K, pressure of 1 bar, and concentration of 1 mol/L.

In the currently used proton exchange membrane (PEM) electrolyzers, the electrocatalyst of choice for the HER is carbon-supported platinum nanoparticles (NPs)[14], since other materials cannot withstand the corrosive acidic environment at the cathode. Nonetheless, MoS_2-based catalysts have emerged as a low-price Pt alternative, since they are able to maintain their catalytic activity during electrochemical measurements.[46] However, the correlative investigation of the catalyst's structure evolution during the electrochemical testing remains elusive, due to the challenging nature of characterizing the structure of gas-evolving catalysts. One of the objectives of this thesis was to develop the necessary methods for enabling these types of studies (see Chapter 5 for more details).

2.3.2 Oxygen evolution reaction

The OER is the other half reaction in an electrolyzer, that takes place at its anode. In acid media, it can be written as:[45]

$$2H_2O \rightarrow O_2 + 4H^+ + 4e^- \qquad E^o_{ox} = -1.229\,V \qquad \textit{Eq. 2-3}$$

Using Eq. 2-2 and Eq. 2-3, it can be seen that the cell potential of an electrolyzer is negative, meaning that electrical power is needed to drive these chemical reactions. Moreover, the overpotential of the OER is especially high since it involves a complex 4-electron transfer process.[47] Therefore, even more electrical power is required for splitting water in an electrolyzer, which lowers their efficiency and increases the costs. The OER can be effectively catalyzed by noble metal oxides, such as RuO_2 or IrO_2.[15] However, the high cost and low abundance of these materials have fueled ongoing efforts to find suitable, cheaper alternatives. Among the possible alternatives, perovskite transition metal oxides (with chemical formula ABO_3) have emerged as a promising OER catalyst due to their high activity and the possibility of tuning their reactivity by changing the A- and B- site cations.[48] In Chapter 6, the OER catalyst perovskite $LaNiO_3$ is studied.

2.3.3 Hydrogen oxidation reaction

The chemical energy stored in hydrogen gas needs to be converted back on demand to electrical energy, that can be used for powering our vehicles or buildings. The most efficient way of doing that is by electrochemically oxidizing hydrogen in a fuel cell. The HOR is the anodic reaction in a fuel cell. In it, hydrogen gas is oxidized to give protons and electrons. The protons

diffuse across a cationic exchange membrane towards the cathode, while the electrons travel towards the cathode through an external circuit, generating electricity.[49] The HOR half-reaction can be written as:[45]

$$H_2 \rightarrow 2H^+ + 2e^- \qquad E^o_{ox} = 0\ V \qquad \textit{Eq. 2-4}$$

The material of choice for HOR catalysts is also Pt, although its low tolerance for impurities requires that extremely pure hydrogen is used. Combining Pt with other metals such as Ru, either in alloyed[50] or core-shell[51,52] NPs can be a successful strategy for increasing the impurity tolerance of Pt, especially towards carbon monoxide (CO). Nonetheless, Pt-Ru materials suffer from low operating stability, since Ru leaches out during operation, impacting negatively the long-term performance of fuel cells.[50–52] In this thesis, the possibility of replacing Ru with the more stable rhodium (Rh)[53] in HOR catalysts is explored, focusing on studying the stability of this electrocatalyst (see Chapter 4).

2.3.4 Oxygen reduction reaction

In a fuel cell, besides the anodic HOR, the other half-reaction that needs to be considered is the cathodic ORR. Although there are different pathways that the reaction can take, in a PEM fuel cell the four-electron pathway is the most common:[45]

$$4H^+ + 4e^- + O_2 \rightarrow 2H_2O \qquad E^o_{red} = 1.229\ V \qquad \textit{Eq. 2-5}$$

Combining Eq. 2-4 and Eq. 2-5 indicates that the cell potential in a fuel cell is positive, and that is why it can be used for generating electrical power. Nonetheless, the sluggish kinetics and high overpotentials of the ORR limit the performance of fuel cells.[25]

Similar to the previously discussed reactions, Pt or Pt-alloyed NPs are the state-of-the-art catalyst for the ORR. A particular high loading of Pt is needed in the cathode (4-5 times the amount on the anode[52,54]), to compensate for the sluggish kinetics of the reaction. This makes the need for finding ORR electrocatalysts capable of substituting Pt or increasing the intrinsic activity and stability of Pt-based materials particularly pressing. See Chapter 7 for more information on how during this thesis the increase of the activity and stability of Pt nanocatalysts was achieved.

2.3.5 Two-electron oxygen reduction reaction

Besides the common four-electron pathway for the ORR of interest in fuel cells, in which water is obtained as a final product (Eq. (2-5)), there is an alternative, competing reaction, namely,

the two-electron ORR. In it, oxygen is reduced with two electrons to give hydrogen peroxide, according to the following reaction:[5,55]

$$2H^+ + 2e^- + O_2 \rightarrow H_2O_2 \qquad E^o_{red} = 0.695\ V \qquad \textit{Eq. 2-6}$$

This reaction is undesired in a fuel cell, since hydrogen peroxide is a strongly oxidizing agent which can damage the components of the cell. However, it can also be exploited for synthesizing hydrogen peroxide, a product with numerous applications. This direct, electrochemical synthesis of H_2O_2 would enable to decentralize its production which is not possible with the currently used anthraquinone process.[56] Nonetheless, the successful commercialization of electrochemical H_2O_2 production requires a catalyst with high activity, selectivity and stability.[56] The selectivity part is crucial, since the catalyst needs to be active for the electroreduction of oxygen, but in a selective way, i.e., only towards the two-electron pathway. During this thesis, a highly active, selective and stable two-electron ORR catalyst was investigated (Chapter 8).

2.4 Degradation mechanisms of electrocatalysts

Electrocatalysts are typically nanostructured in order to maximize the fraction of surface atoms available for catalyzing a reaction. However, atoms on the surface are inherently less stable than in the bulk, and therefore nanostructured catalysts often suffer from processes that minimize their surface.[57] These processes impact negatively the activity of the catalyst, since they result in fewer surface atoms that can interact with the reactants and catalyze a reaction.[58] Therefore, they are referred to as degradation mechanisms. The most common degradation mechanisms are dissolution, particle detachment, Ostwald ripening, and particle agglomeration.[57] A schematic drawing of some of the most frequent catalyst degradation mechanisms is provided in **Figure 2-3**.

Particle detachment and agglomeration can occur as a consequence of support corrosion. A weakening of the interaction between catalytic particles and the support can result in particle migration and agglomeration on the surface of the support, or detachment of whole particles from the support.[57]

Dissolution of catalytic species affects especially smaller particles due to their higher surface energy.[57] If the dissolved species redeposit on larger particles, making them grow, the phenomenon is known as Ostwald ripening.

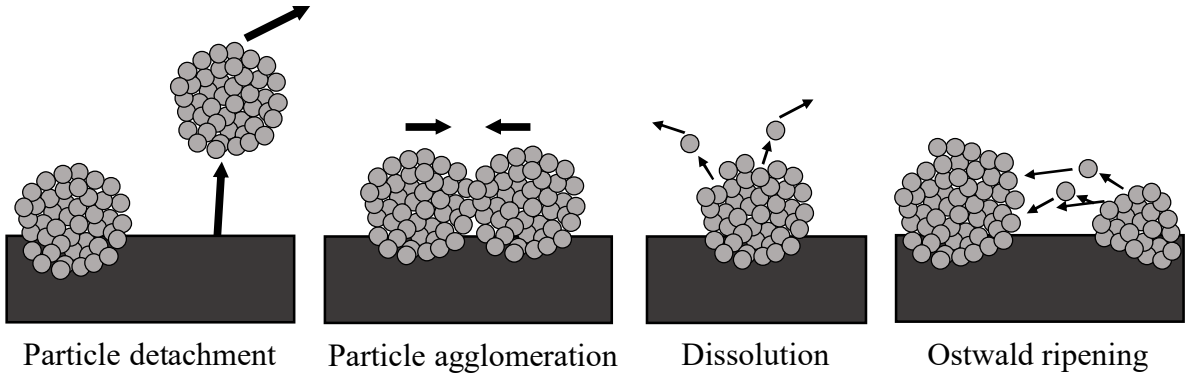

***Figure 2-3**. Schematic drawing showing the different degradation mechanisms of catalytic NPs. Adapted from Ref.* [57]

Additionally, the loss of catalytic activity can also occur if higher-energy lattice defects that are active for a reaction disappear during catalysis. For instance, GBs, which have been identified as active centers for carbon dioxide (CO_2) electroreduction[59,60] and methane oxidation[61], can be modified by heating[62] or under the presence of an applied electrical field[63].

2.5 Structure effects on catalytic performance

The structure of catalysts has a great influence on their performance. In this thesis, a great deal of attention has been placed on studying how different structural features, in particular defects, affect the performance of catalysts. These insights enable the rational tuning of the structure for higher activity and stability. Here and in the following the structure refers to both the type of atoms and their arrangement, i.e., chemical composition and crystal structure.

The effect of the structure on stability can be exemplified in bimetallic NPs (**Figure 2-4**).

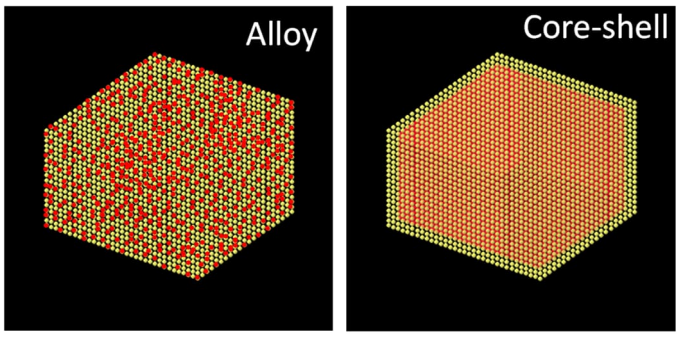

***Figure 2-4**. Model of alloy and core-shell NP with different element distribution and structure. Adapted from own work.*[64]

If these NPs are alloys, with the elements randomly distributed, the surface will contain atoms of both elements. Therefore, the less stable element will be exposed to the electrolyte and can be dissolved. However, if the NPs are nanostructured as core-shell, the less stable element can

be located in the core, and protected from the electrolyte by the shell. This nanostructuration will result in lower dissolution, and therefore higher stability.[65]

Besides the stability, the structure of a catalyst can also affect its activity. Firstly, the structure can affect the fraction of surface atoms,[66] which are the ones that interact with the reactants. Secondly, the structure can affect how these surface atoms interact (bind) with the reactants,[67,68] which influences their intrinsic activity according to the previously discussed Sabatier principle (**Figure 2-2**).

For instance, in the case of the ORR, although Pt is the best-performing element, it still binds oxygen slightly stronger than the optimal value.[69] Therefore, its ORR activity can be increased by reducing the oxygen binding energy, which can be achieved by modifying its structure by assembling the single crystal Pt NPs, forming NP assembly nanostructures (see Chapter 7). In the case of the two-electron ORR, Au binds to weakly a critical reaction intermediate (HOO*)[70]. Therefore, its performance can be enhanced by increasing the Au-(HOO*) binding energy (see Chapter 8).

Next, the particular structural features that affect the catalytic performance will be addressed.

2.5.1 Coordination number

In the bulk of a face-centered cubic (fcc) metal such as Pt, Au or Rh, atoms have a coordination number of 12, i.e., they possess 12 nearest-neighboring atoms.[71] Such an atom is chemically inactive, since it is fully surrounded by others. On the surface, some neighboring atoms are missing. Therefore, surface atoms lack electron density and tend to bond with adsorbates to compensate for it. Different crystallographic surfaces have different coordination numbers,[71] and thus different binding energies for a given adsorbate. For instance, Pt(100) surfaces, with a coordination number of 8, bind more strongly to oxygen species than Pt(111) surfaces (coordination number of 9).[72] As a consequence, Pt(111) surfaces align better with the ORR volcano plot maximum and have higher activity than (100) surfaces.[72] Therefore, one factor that will affect the catalytic activity of NPs is their shape, since it will determine which facets it presents.

Besides the modification of the facets, the coordination number (and thus, the binding energy) can also be tuned by introducing concave or convex sites[73,74] and defects such as stacking faults[22]. These can form active sites at their surface terminations.

2.5.2 Particle size effect

Smaller particles have a higher fraction of surface atoms and therefore possess a higher electrochemically active surface area (ECSA). That is why smaller particles (e.g., nanoparticles) in general perform better than larger particles, and electrocatalysts tend to be nanostructured.[66] However, it also needs to be considered that reducing particle size decreases the fraction of terrace sites, while edges and steps are increased.[75] Since the atoms on the edges and steps have a lower coordination number, they will interact more strongly with the reactants. That is, changing the particle size not only has an impact on the ECSA, but it can also affect the average coordination number of the catalysts, and therefore its interaction with a reactant. This phenomenon can have important implications on the activity-size dependence, for instance, in the ORR activity of Pt NPs. Reducing the size of Pt particles by less than 3 nm is actually counterproductive for the total activity (in terms of activity per gram of Pt). Although the ECSA increases, the fraction of inactive, highly undercoordinated sites with a too-large binding energy with oxygen is higher, and therefore their activity is lower.[68] Other reactions or other materials can follow a different trend, depending on where the material falls in the volcano plot for that specific reaction.

Additionally, the particle size can also affect the stability of catalysts, and Pt particles of less than 3 nm are significantly less stable than bigger ones.[76]

2.5.3 Lattice expansion or contraction

One additional way of modifying the binding energy between the catalyst and the reactant molecules -and thus the catalytic performance- is by expanding or contracting the lattice of the catalyst on its surface. Although there can be different physical reasons for the lattice expansion or contraction (e.g., external load, lattice parameter mismatch with a substrate, dislocations…), this change of lattice parameter on the surface is commonly referred to as surface strain.[77] The effect of lattice parameter change on the binding energy can be rationalized in metals by the d-band model. Changing the lattice parameter of the catalyst modifies the center of the metal d-bands, which has a determinant role in the adsorption energies and activation energy barriers.[78,79] For late transition metals, lattice expansion upshifts the d-band center, resulting in stronger interaction with adsorbates. Lattice compression downshifts the d-band center, weakening the interaction.[77]

The effect of varying the lattice parameter on catalytic activity can be seen by using positive electrode materials such as $LiCoO_2$ as a substrate for Pt NPs.[28] The lattice parameter of such

substrate expands (contracts) in a controlled manner during the charge (discharge) of the battery due to the removal (intercalation) of Li^+. Therefore, the lattice parameter of the Pt NPs deposited on top can be modified in a controlled manner, resulting in enhancement of the ORR activity during compression, and suppression during expansion.[28]

For practical use cases, however, the strategy of using substrates that can shrink or expand is not applicable, so different alternative methods have been developed for changing the lattice parameter of the surface atoms of nanomaterials. One commonly used strategy is to alloy the catalyst with a different element. For instance, alloying Pt with other elements like Ni or Ru downshifts the d-band center of Pt[80], and Pt_3Ni alloyed surfaces have been reported to have some of the highest ORR activities.[81,82] Nonetheless, the presence of the alloyed atoms on the surface difficulties the interpretation of the role of lattice modification, since the electronic structure can also be modified by the neighboring alloyed atom (ligand effect). Another successful strategy for modifying the lattice parameter of the surface atoms consists of having core-shell nanostructures. The lattice mismatch between the core and the shell can introduce strain on the surface atoms, and core-shell electrocatalysts have been shown to be highly active due to an optimization of the binding energy with the reactants.[83,84]

Nonetheless, although these strategies modify the lattice parameter of the surface initially, it also needs to be considered whether it is maintained under electrochemical conditions, especially if the alloyed or core metals suffer from low stability. [51,58,85]

2.6 Grain boundaries

GBs are two-dimensional defects formed in the interface between two crystalline grains (**Figure 2-5a**). They have been extensively studied in this thesis, and therefore the next section is dedicated to describe them and their influence on the catalytic activity with detail.

GBs can be classified according to the misorientation angle between the two grains. If the angle is below 15°, a low-angle grain boundary (LAGB) is formed, which can be considered as an array of dislocations. As the misorientation angle between the two grains increases, more and more dislocations are needed to accommodate the mismatch between the grains. At angles over 15°, the boundary is considered a high-angle grain boundary (HAGB). Randomly oriented HAGBs have a highly distorted, open structure, and therefore they are associated with a higher energy. There are however some special HAGBs. At particular misorientation angles, the two lattices can fit together with a relatively low distortion of the interatomic bonds. This is caused because some lattice positions (i.e., atoms in the case of simple crystals) of the first grain

coincide exactly with some lattice positions of the second grain, thus resulting in lower energy (**Figure 2-5b**). Comparing the number of these coinciding lattice positions, a value (referred to as sigma, ∑) can be assigned to a HAGB. For instance, in a ∑3 GB, for every 3 lattice points, one is common between the two grains.[86–88]

In this thesis, GBs are used in the context of electrocatalysts because GB surface terminations (**Figure 2-5a**) have been shown to act as active centers for some reactions. For instance, it has been proved that GB surface terminations in gold were more active than GB-free surfaces for the electrochemical reduction of CO_2.[29,59] The reason behind the unusually high activity on the GB surface terminations is that these defects effectively combine the two strategies previously discussed for altering the binding energy with the reactant molecules. Firstly, local distortions of the lattice parameter can be found in the vicinity of the surface terminations of the GBs. Secondly, due to the distorted, open structure of the HAGBs, the coordination number of the atoms in the GB surface termination will be different than for other atoms of the surface.[60] These two factors combined make GBs highly interesting defects in electrocatalysis, that need to be studied and exploited for more electrochemical reactions.

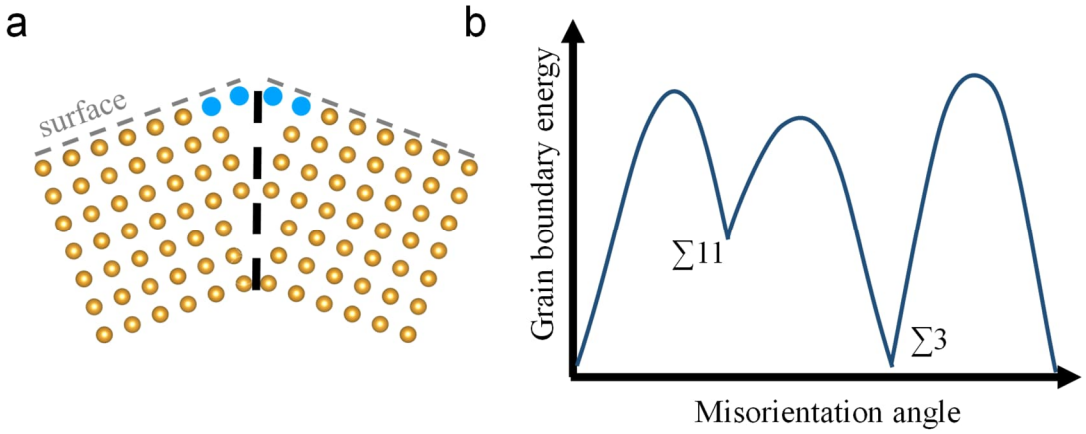

***Figure 2-5**. (a) Schematic drawing of a grain boundary. At its surface termination the atoms can interact with the reactant molecules, helping catalyze a reaction. (b) GB energy as a function of the misorientation angle between grains. At some particular angles, the energy of the GB decreases due to coincidence between lattice points of the two grains, giving rise to HAGBs such as ∑11 or ∑3 GBs. Adapted from Ref.[89]*

3 Characterization techniques

To understand how the structural features of electrocatalysts affect their performance, it is essential to investigate both their structure and electrochemical properties. This chapter will present the most used characterization techniques throughout the thesis and their theoretical foundations. More in-depth information can be found in the textbooks used in the writing of the chapter.[41,90–92]

3.1 (Scanning) transmission electron microscopy

To maximize the surface area available for catalyzing a reaction, electrocatalysts are typically nanoparticles, with sizes ranging from a few nm to hundreds of nm, or present features in the nanoscale regime. Therefore, in order to study their morphology and structure, advanced characterization techniques with a high spatial resolution are required.

Conventional, diffraction-limited light microscopy can resolve objects down to ~200 nm[93], making it unsuitable for the proper characterization of electrocatalysts. In (S)TEM, electrons are used instead of photons as illumination source, and images are formed with the electrons that are transmitted through the sample. In this way, sub-Å resolutions can be achieved.[94] Since the lengths of interatomic bonds are typically larger (e.g., C-C bond ~1.5 Å[55], Pt-Pt bond ~ 2.7 Å), such high resolving power is enough for resolving individual atomic columns, that is, for studying the atomic arrangement.

Moreover, since electrons are charged particles, they interact strongly with matter. This interaction depends on the chemical nature of the sample, and therefore chemical information of the specimen can be accessed, which is the basis of the spectroscopy techniques.

In the following sections, the different operating modes and the information that can be extracted from them will be detailed.

3.1.1 Parallel vs convergent electron beam

There are two principal ways in which the electron beam can illuminate the sample, which gives rise to the two main modes of operation: TEM and STEM (**Figure 3-1**). Despite the numerous differences between these modes, a (S)TEM instrument contains the following parts. 1) The illumination system, which is composed of the electron gun, condenser lenses and apertures, shapes the electron beam interacting with the specimen. 2) The stage, which can be moved with sub-nm precision and is where the sample is placed. 3) The detector/camera, which

is situated after the specimen and is responsible for forming an image with the transmitted electrons.

In TEM mode (**Figure 3-1a**), the lenses of the illumination system are tuned to illuminate the specimen with a parallel beam of electrons, which interacts and propagates across a (relatively) big region of the sample. The image is formed by a lens located after the specimen, known as the objective lens. It takes the electrons transmitted through the sample and forms a magnified image in its image plane. The image can be further magnified by the intermediate and projector lenses and recorded with a screen or camera. Since the objective lens is the imaging-forming lens, aberrations in it will have a great impact on the resolution achievable in TEM. Therefore, aberration-correction methods in TEM mode focus on minimizing the aberrations present in the objective lens, especially its spherical aberration (C_s).

At the back focal plane of the objective lens, a so-called objective aperture can be placed. Such an aperture increases the diffraction contrast of the image, allowing the obtention of a bright field image (if the direct beam is selected while Bragg-scattered electrons are blocked) or a dark field image (if Bragg-scattered electrons are selected while the direct beam is blocked).

In STEM mode (**Figure 3-1b**), the illumination system is tuned for forming a convergent beam of electrons, which scans the sample point by point. The electrons transmitted in a given beam position on the sample can be detected with different detectors (known as bright field (BF), annular dark field (ADF) and high angle annular dark field (HAADF)). The corresponding signal is recorded at an equivalent point (pixel) on the computer screen, forming an image. Therefore, STEM images are built pixel by pixel over several seconds. Since scanning images are not magnified by lenses, their resolution depends on the probe size itself, which is determined by the condenser lens system. Consequently, for enhancing the resolution in STEM mode, spherical aberration correctors of the condenser lenses (also known as probe correctors) can be used.

Most of the microscopy work performed in this thesis was done in STEM mode and will be covered, together with its associated techniques, in the upcoming sections with more detail. Nonetheless, some results presented here involve TEM mode, so it is worth briefly describing it further.

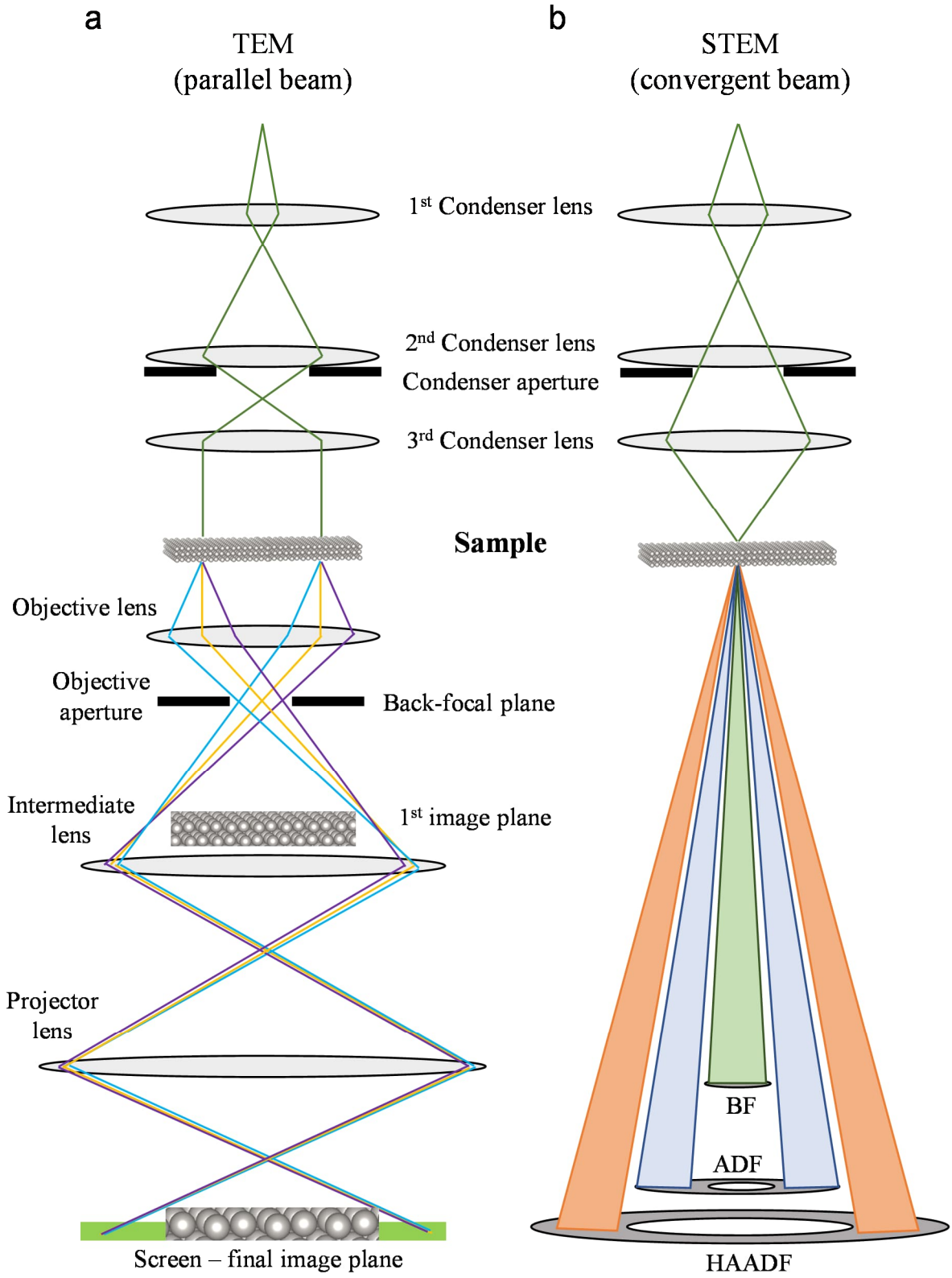

Figure 3-1. *Schematic representation of (a) TEM with parallel beam illumination and (b) STEM, in which a convergent beam scans over the sample. Adapted from Ref* [90].

3.1.2 High-resolution-TEM

When no objective aperture is inserted in the back-focal plane of the objective lens, several electron waves scattered by the specimen propagate through the vacuum and are modified by the lens system before interfering with each other on the screen. The waves have different phases, resulting in interference and subsequent contrast differences in the image formed. Therefore, these images are known as phase contrast images. Their contrast can be difficult to interpret, since it depends on the thickness of the sample, as well as on the focus and aberrations of the objective lens, among other factors. However, their contrast also depends on the atomic structure and orientation of thin specimens, making it possible to obtain high-resolution (HR)-TEM images, in which the atomic distances can be resolved. To facilitate the interpretation of the image contrast, typically a small, negative spherical aberration is introduced to the objective lens by the aberration corrector, which yields high-resolution images with bright-atom contrast on a dark background.[95] In this thesis, HR-TEM images were used to determine the surface facets of NPs.

3.1.3 HAADF-STEM

In STEM, a convergent beam of electrons scans over the specimen. In a given beam position, electrons will be scattered at different angles (**Figure 3-1b**). Using distinct detectors, electrons scattered in different angular ranges can be collected. The BF detector detects electrons scattered at low angles (~0-10 mrads), the ADF at intermediate angles (~15-70 mrads), and the HAADF at high angles (~75-200 mrads).

Due to the high collection angle of the HAADF detector, no Bragg scattered electrons (rich in diffraction information) are detected. Therefore, HAADF images are (almost) free of Bragg effects, and do not present diffraction contrast. On the contrary, at such high angles, Rutherford-scattered electrons are mainly detected. These electrons are incoherent (i.e., without a phase relationship between them), and the images formed by them have mass-thickness (or Z) contrast. This has several important implications. Firstly, it allows for easy-to-interpret, atomic-scale images. Moreover, in HAADF micrographs it is possible to distinguish between elements with different atomic numbers, with higher-Z elements appearing brighter than lower-Z elements. Lastly, since the HAADF signal depends on the thickness of the specimen, it can be used for performing HAADF-STEM tomography, in which a (3D) volume is reconstructed from a series of (2D) HAADF images.

In this thesis, atomic-resolved HAADF images are used, among others, for determining local changes in the lattice parameter, as exemplified in **Figure 3-2**. The positions of the atomic columns are located with accuracy by fitting 2D Gaussians to the local intensity maxima (i.e., the atomic columns). From them, the interatomic distances can be calculated, and the lattice parameter distortion mapped by selecting a reference (undistorted) lattice.[96]

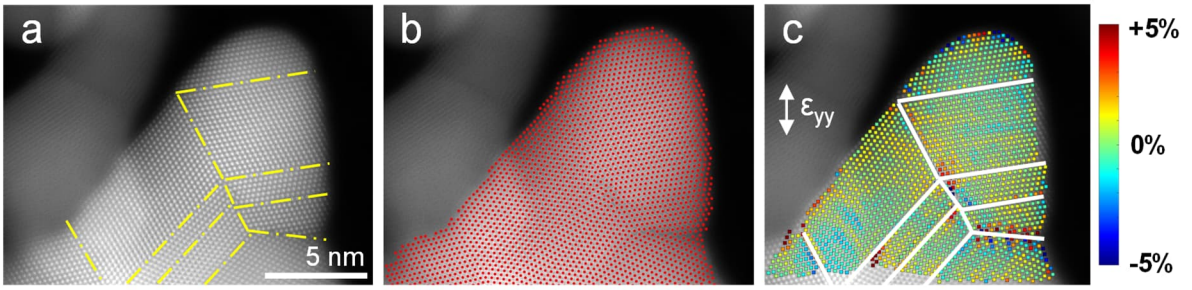

***Figure 3-2**. Real-space strain mapping. From atomic-resolved HAADF images (a), 2D Gaussians are fitted to locate the atomic column positions (b). These can be later used for mapping the relative changes in lattice parameter (c). Adapted from Ref*[97].

3.1.4 HAADF-STEM tomography

One limitation of (S)TEM is that 3D specimens are viewed as 2D projections, which can be misleading and lacking information. As mentioned, HAADF-STEM images have mass-thickness contrast. In particular, as a first approximation for thin samples, the intensity of the HAADF signal increases linearly with the specimen thickness, and can consequently be used for tomographic 3D reconstruction.[91,98]

The workflow in a HAADF-STEM tomography experiment is shown in **Figure 3-3**. HAADF micrographs (normally referred to as projections) are acquired at every few angles, between ±70°. This limited tilting range is a consequence of the stage being located tightly between the upper and lower pole pieces of the objective lens. The projections are then pre-processed and aligned for their posterior feeding into a reconstruction algorithm. Several algorithms are available, with the most common ones being based on iterative methods.[98] In them, an initial guess for the 3D reconstructed volume is used for simulating projection images along the experimental acquisition angles. These simulated images are compared with the experimental ones, and the 3D volume is modified accordingly. The process is repeated iteratively until the optimal volume is found.[91] The reconstructed volume can be later segmented and visualized. In **Figure 3-3**, an example of the utility of tomography in this thesis is presented. With this technique, the reconstructed volume of a core-shell nanoparticle can be segmented to study the

core encapsulation. Open-source Python libraries can be used for all the post-acquisition steps [99–102].

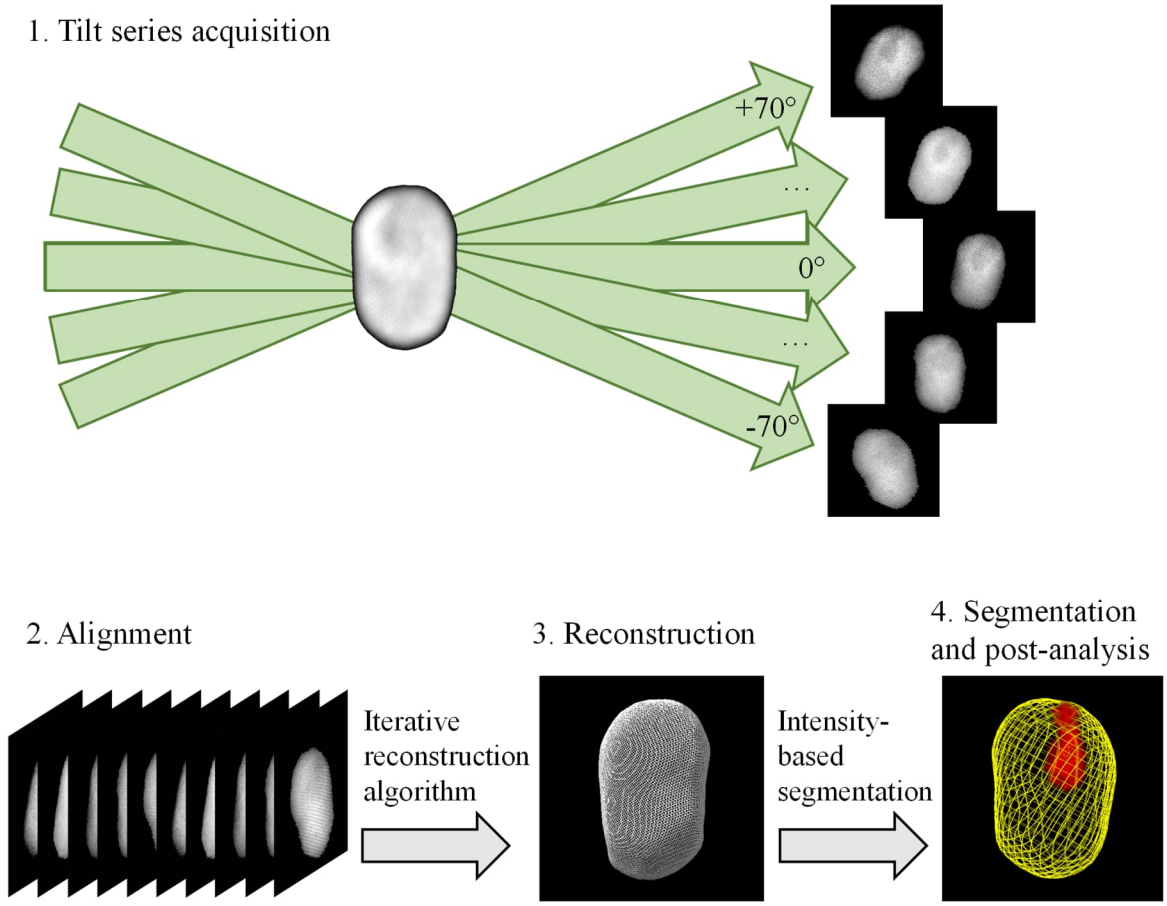

***Figure 3-3**. Scheme depicting the workflow for HAADF-STEM tomography.*

3.1.5 4D-STEM

In HAADF-STEM, a signal is recorded in each beam position, in principle proportional to the number of electrons hitting the HAADF detector. That signal is a number, typically a 16-bit integer. If the beam scans over the sample in a grid of 1024x1024 points, the resulting HAADF image will be a 1024x1024 matrix, whose elements range between 0 and 65535 (2^{16}-1) (**Figure 3-4a**). If the HAADF detector is replaced by a pixelated detector, besides the Rutherford-scattered electrons, the direct electron beam and the Bragg-diffracted electrons can be recorded. Therefore, at each beam position, a 2D diffraction pattern is obtained (**Figure 3-4b**). The corresponding data set is four-dimensional, with 2 real-space and 2 reciprocal-space dimensions, and the technique is known as 4D-STEM[34]. 4D-STEM datasets are quite large in size, easily weighing several gigabytes. They are also very rich in information. For instance, virtual BF or ADF images can be obtained by integrating over the pixels collecting the electrons scattered at low or medium angles, respectively. Additionally, if the crystalline structure of the

sample is known, a library of diffraction patterns for different crystallographic orientations can be simulated, and compared to the experimentally obtained patterns. In this way, the orientation of the sample at each beam position can be extracted, and an orientation map obtained (**Figure 3-4c**).

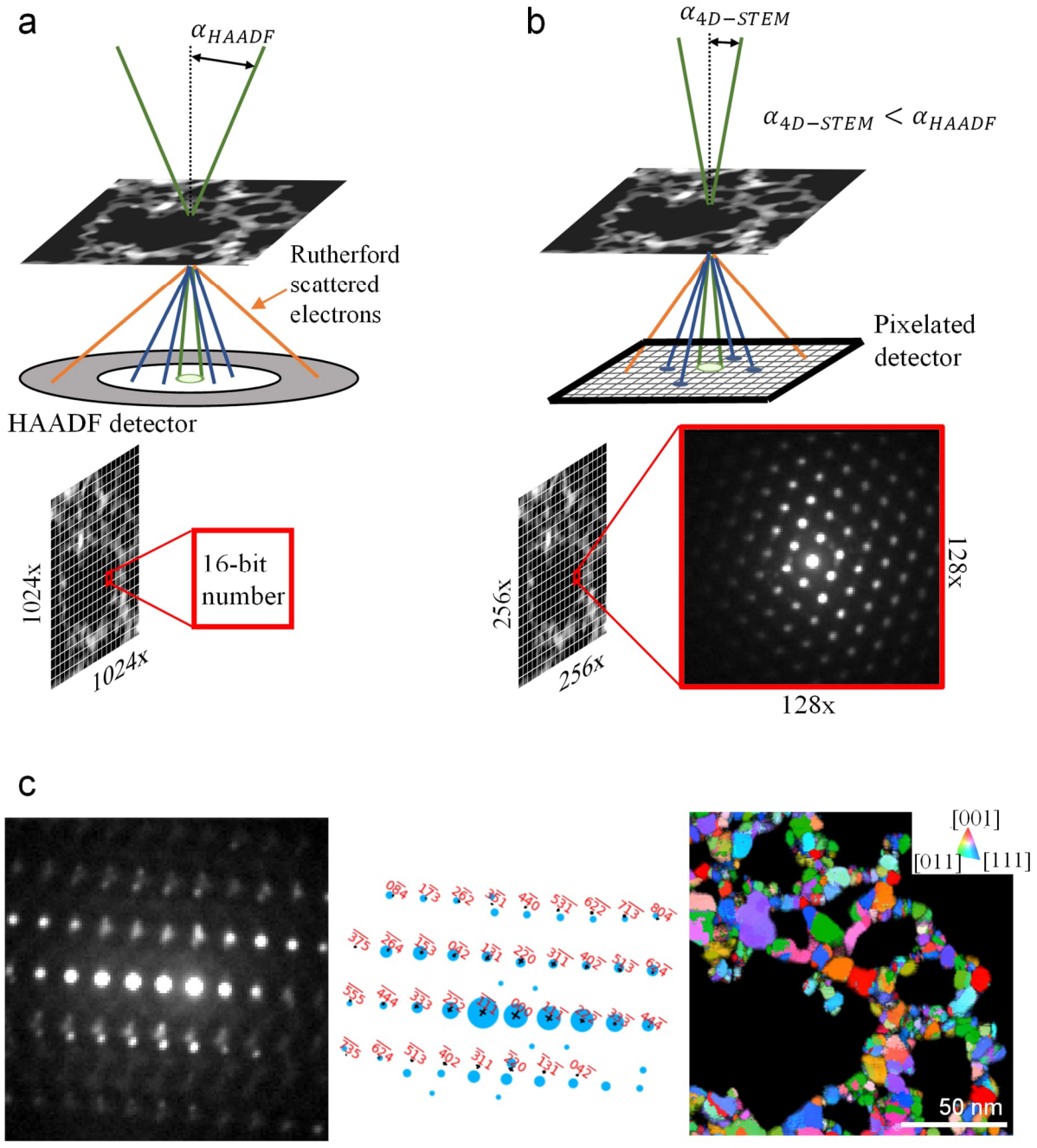

***Figure 3-4**. Data acquisition of HAADF-STEM (a) and 4D-STEM (b) images. In 4D-STEM, a 2D diffraction pattern is recorded at each beam position, giving as a result a four-dimensional data set. Each diffraction pattern can be indexed to determine its orientation by comparing them to simulated patterns, making it possible to obtain orientation maps (c). Figure inspired by Ref [34]. 4D-STEM data taken Ref [97].*

Such orientation maps can be further processed for extracting additional information, i.e., grain size distribution or grain misorientation angle. Moreover, by carefully analyzing distortions in the diffraction patterns, the local lattice distortions of the sample can be mapped.[34]

For performing orientation mapping, the convergence semi-angle (α) in 4D-STEM is smaller than in typical HAADF-STEM. This has the advantage of reducing the diffraction disk size, which would otherwise overlap, hindering their proper identification. Nonetheless, a smaller convergence semi-angle results in a larger electron probe, thus reducing the spatial resolution.

3.1.6 Spectroscopy

Until now the focus has been on using electrons transmitted through the sample for imaging it and obtaining information regarding its crystal structure and orientation. However, electrons are charged particles capable of ionizing matter, i.e., removing the inner-shell electrons from the atom (**Figure 3-5a**). This ionization can be used for extracting chemical and electronic information from the specimen and is the basis of the spectroscopy techniques. In particular, energy dispersive X-ray spectroscopy (EDS) and electron energy loss spectroscopy (EELS) were used in this thesis.

When a high-energy electron interacts with an atom of the specimen, it can transfer part of its energy to the atom, or in other words, it can get inelastically scattered. By measuring the energy lost by the electron beam during its interaction with the specimen, an EELS spectrum can be obtained (**Figure 3-5b**). Therefore, each feature in it (except the zero-loss peak) is related to an inelastic scattering event.

An EELS spectrum has two distinct regions, namely the low loss (0-50 eV) and the high loss (>50 eV) regions. In the low-loss region, the electrons that have not lost energy when going through the sample form the zero-loss peak. In addition, those that lose a small part of their energy to excite collective oscillations of the conduction band electrons constitute the plasmon peak. Band gap transitions (e.g., from valence band to conduction band) are also recorded in this region. In the high-loss region, electrons that have undergone inelastic scattering events with the inner-shell electrons of the specimen's atoms are detected. In such events, a core electron (typically from the K, L, or M shell) is excited to a higher, unoccupied state above the Fermi level. The energy transferred (or lost) by the incoming electron in the ionization process is characteristic of the atom involved, and therefore a source of chemical information. Since there are several possible unoccupied states to which the core electron can get ejected, features in an EELS spectrum are edges instead of sharp peaks. The energy resolution in EELS is

typically below 1 eV, so small energy differences in the ionization process, caused by differences in the valence state or coordination environment of the atom, can be recorded. Consequently, the high-loss edges can be used for extracting the sample composition, but also its oxidation state or its nearest-neighbor atomic structure.

After an atom has been excited, it can relax back to a low energy state by filling the remaining hole in the inner shell with an electron from an outer shell (**Figure 3-5a**), emitting an X-ray or an Auger electron in the process. In both cases, the energy emitted depends on the energy of the two shells involved and is characteristic of an atom, so it can be used for chemical analysis of the sample. By recording the energy of the characteristic X-rays, an EDS spectrum is obtained (**Figure 3-5c**).

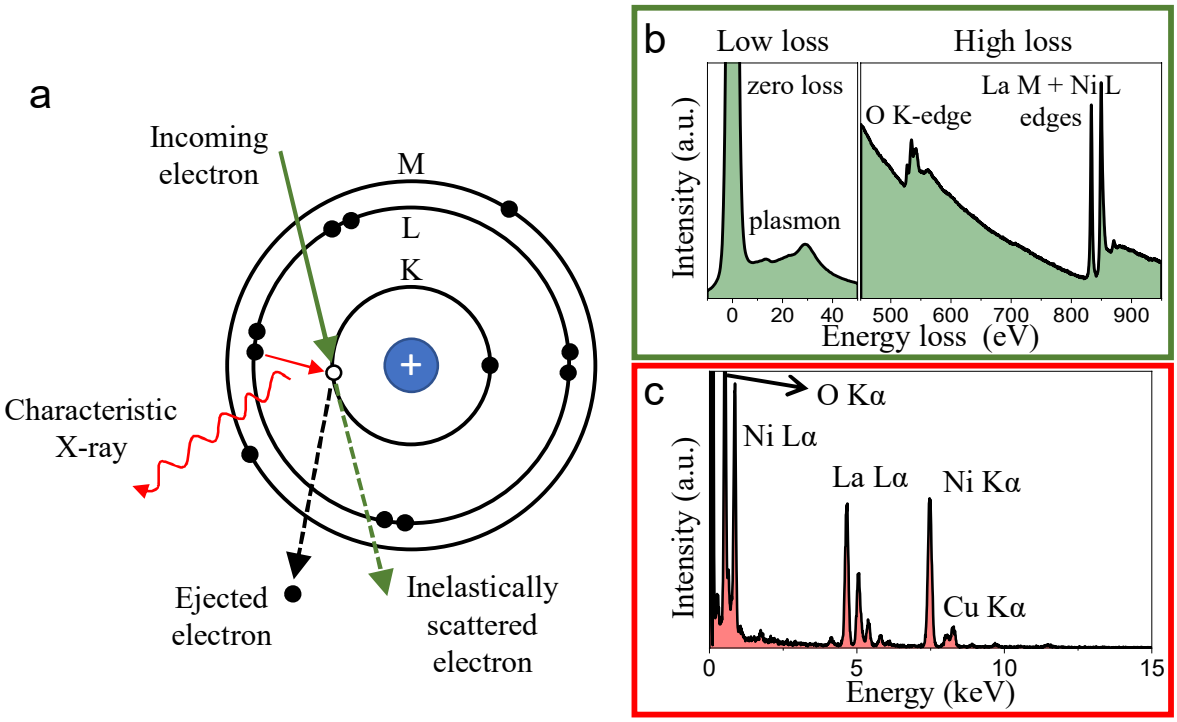

***Figure 3-5**. Inelastically scattering process. (a) An inner-shell electron is excited by an incoming (high-energy) electron from the beam. The remaining hole in the K shell can be filled by an electron from a higher energy shell (L), emitting a characteristic X-ray. By measuring the energy loss of the inelastically scattered electrons, an EELS spectrum (b) can be obtained. The EDS spectrum (c) is obtained by measuring the energy of the emitted X-rays. Figure (a) is inspired by Ref [103]. Data in (b) and (c) are published in Ref [48].*

The signals used in EELS and EDS, i.e., the energy loss of the incident electron beam and the characteristic X-rays, respectively, are two distinct aspects of the same process. These signals are generated whenever a high-energy electron beam interacts with the sample, independently of whether the beam is parallel (TEM) or convergent (STEM). Nonetheless, the EDS and EELS

experiments of this thesis were always performed in STEM mode. In this way, the region of the sample emitting the signal can be pinpointed down to the atomic level, allowing for spectroscopy with a high spatial resolution, which is the main advantage of performing spectroscopy inside an electron microscope.

3.2 Electrochemical techniques

In order to evaluate how good a catalyst is, its performance and stability need to be determined. The most common way for benchmarking an electrocatalyst is to apply a potential to it while simultaneously measuring the resulting current. The techniques that follow this principle are referred to as voltammetric, and they are typically performed in a three-electrode set-up (**Figure 3-6a**). As indicated by its name, it consists of three electrodes, namely the working, the reference and the counter electrode. The working electrode comprises the sample to be characterized, and it is where the reaction of interest takes place. In the counter electrode, the other half reaction takes place, completing the electrical circuit. All the charge needed to balance the electrons at the working electrode passes through the counter electrode. The role of the reference electrode is to measure and control the working electrode potential. Therefore, it needs to have a constant, well-defined potential. Normally a silver/silver chloride (Ag/AgCl) or a reversible hydrogen electrode (RHE) are used as a reference. The set-up is controlled with a potentiostat.

3.2.1 Linear sweep voltammetry and cyclic voltammetry

The two main voltammetric techniques used in this thesis are linear sweep voltammetry (LSV) and cyclic voltammetry (CV). In LSV, the potential is scanned from a lower limit to an upper limit in a linear way (**Figure 3-6b**). Whenever the applied potential is enough for an electrochemical reaction, electrons will flow between the working and counter electrode, and current will be measured. The current measured is proportional to the number of electrons flowing through the circuit and therefore is a measure of the rate of an electrochemical reaction.

CV is similar to LSV. However, in CV experiments the potential is swept back and forth between the lower and upper limits (**Figure 3-6c**)[104]. Therefore, in a single CV scan, the cathodic (towards more reducing, or negative potentials) and anodic (towards more oxidative, or positive potentials) directions are covered. By performing an elevated number of CV scans, it is possible to evaluate how the activity of the sample changes over time. If the current decreases during the CV experiments, it is an indication that the sample is becoming less active over time, and therefore its stability can be determined (**Figure 3-6d**).

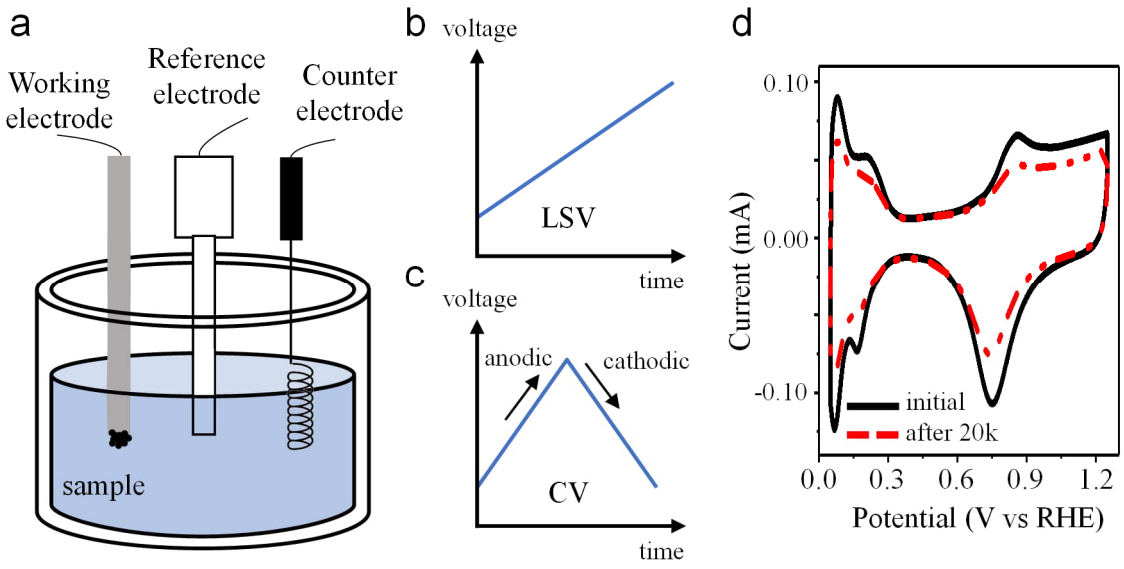

***Figure 3-6**. Testing the electrocatalytic performance of a sample. (a) Scheme of the three-electrode set-up. In LSV, a voltage changing linearly with time is applied in a single direction (b), while in CV the scan is performed in both directions (c). In (d) the CV curves of Pt nanoparticles before and after 20.000 CVs are shown. Notice how the peak current decreases during the cycles, indicative of activity loss during time (i.e., degradation). Figure (a) adapted from Refs [64,105]. Figure (d) adapted from own work [106].*

3.2.2 Rotating (ring) disk electrode

It is convenient for some reactions to use a rotating disk electrode (RDE) as a working electrode, in which the sample can be deposited. An RDE rotates at a controlled rate during the experiments, ensuring that fresh electrolyte is continuously brought to its surface and that reaction products are removed. In this way, mass transport limitations can be avoided, and the intrinsic activity of the catalyst properly evaluated.[107]

An additional ring can be located on the RDE, forming a rotating ring disk electrode. This electrode is particularly useful for studying reactions with two products. The additional ring can be held at a potential that can selectively reduce or oxidize one of the two reaction products, giving information about the selectivity of the reaction towards such a product.[107] In this thesis, an RRDE was used for evaluating the selectivity of gold nanoparticle assemblies towards the two-electron ORR (see Chapter 8 for more details).

3.3 Identical location (S)TEM

Identical location (S)TEM (IL-(S)TEM) combines STEM with electrochemical techniques. Using (S)TEM it is possible to extract information regarding the structure and composition of the sample, including the amount and distribution of elements, their oxidation state, and whether there are defects (and which type) in the crystal lattice of the specimen. Using electrochemical techniques like LSV or CV, the electrochemical performance of the sample can be determined. This includes evaluating how good it is for catalyzing a given reaction (i.e., its activity) and for how long such activity can be maintained (i.e., its stability).

In this thesis, a great deal of attention is placed on studying how the structure of electrocatalysts affects their electrochemical performance. In particular, on studying how changes in the structure modify the activity of a catalyst. This has traditionally been done using *ex-situ* methods. With these methods, the sample is characterized after having undergone electrochemical testing, and compared with the sample before the testing. These methods are well-established and straightforward. Nonetheless, they present some limitations, as only general statistical insights are obtained, which might fail to reflect the exact changes taking place in the system, especially if the changes are subtle.[37] To overcome this challenge, in recent years, *in-situ* electron microscopy methods have been rapidly developing. [38,108] In them, a TEM sample is placed in a special holder that allows for an external stimulus to be applied while inside the microscope. The stimulus can be, among others, heat, potential, a gas, a liquid, or some combination of them. This allows for the direct imaging and correlation of the changes taking place with the applied stimulus. Although very powerful, *in-situ* electron microscopy methods have other limitations. For instance, they require carefully designed control experiments to rule out potential changes in the sample induced by the electron beam. Especially when a liquid is flown through the cell (necessary for electrochemistry), artifactual reactions are common due to beam-induced radiolysis of the liquid[109]. Moreover, the achievable resolution is reduced in the presence of a thick liquid layer down to a few nanometers.[109] Additionally, performing long aging tests is generally not possible, since that would mean blocking the microscope continuously for days and would result in a high total electron dose being applied to the sample (if images are constantly acquired). A third approach that tries to solve the limitations of *ex-situ* and *in-situ* methods is identical location (S)TEM[110]. In it, the pristine sample is first studied thoroughly in the microscope (**Figure 3-7a**) and a series of zoom-out images are taken each time to document the precise regions of interest being characterized. Afterward, that same sample is used as a working electrode in a three-electrode

set-up (**Figure 3-7b**). An electrochemical test or aging experiment is performed (e.g., a certain number of CV curves), and the aged sample is placed back in the microscope. The regions of interest are located again using the zoom-out images, and imaged (**Figure 3-7c**). By comparing the images of the same region before and after the electrochemical test, is possible to determine which changes were induced in individual catalyst NPs during testing, and to correlate them with the changes in the electrochemical properties.

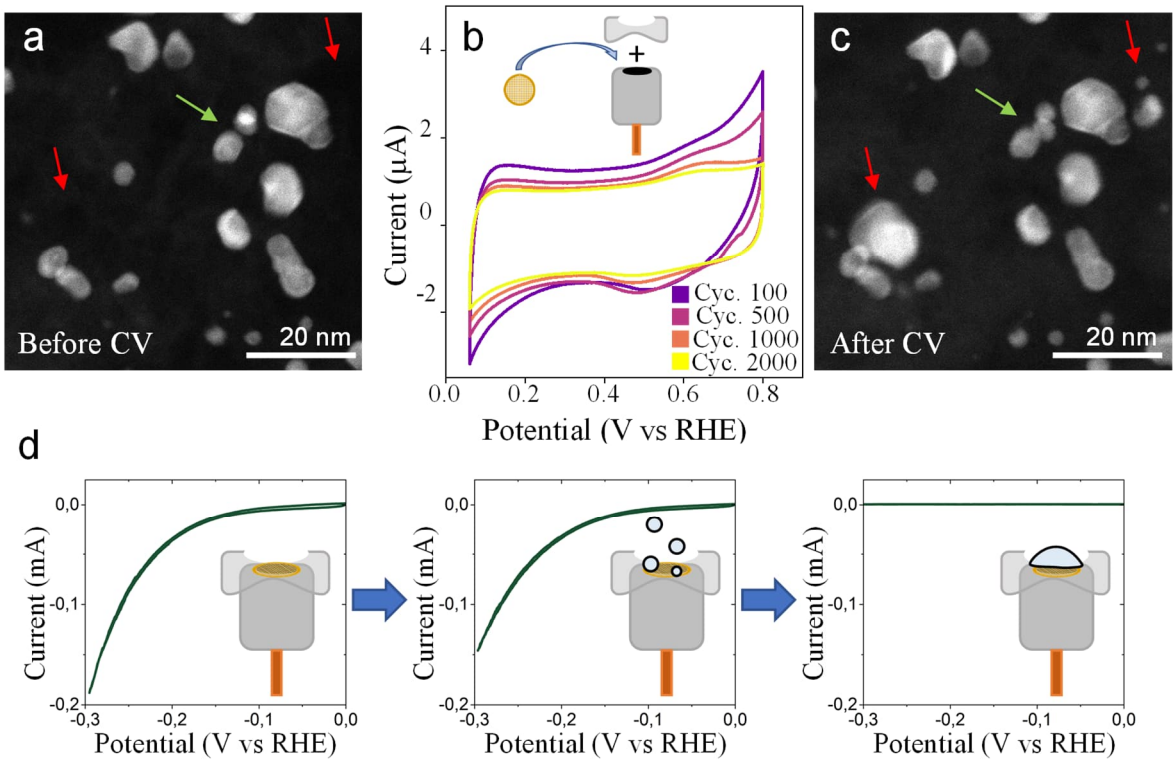

Figure 3-7*. Identical location (S)TEM. Firstly, the fresh sample is placed on a TEM finder grid and characterized in the microscope (a). Then, electrochemistry is performed directly on the same sample-loaded grid (b). Afterward, the regions previously imaged are located again, and the changes with respect to the fresh sample caused by the electrochemical test can be directly seen (c). In (d), the mechanism of loss of electric contact during gas-evolving reactions is depicted. The gas bubbles block the Teflon cap hole, preventing the contact between the electrolyte and the sample. Figures (a-c) adapted from own work* [64]*. Figure (d) adapted from own work* [105]*.*

The studied sample is typically a nanomaterial, which is dispersed on a TEM grid for its characterization on the microscope. In IL-(S)TEM, the grids used are finder-grids, which present some markers that help the posterior identification of the regions of interest.

Generally, the grid loaded with the sample (forming the working electrode) is connected to the potentiostat using a glassy carbon electrode as substrate, since it presents a low activity for most reactions. The grid is held onto the glassy carbon electrode using a Teflon cap (chemically

inert), that has a small hole in the center, allowing electrical contact with the electrolyte (see inset in **Figure 3-7b**). However, gas-evolving reactions cannot be studied using this approach, since the gas bubbles generated during the reaction accumulate in the Teflon cap hole,[111] blocking it and preventing the electrical contact between the sample and electrolyte (**Figure 3-7d**). In this thesis, a systematic study was conducted to validate an easy approach that enables reliable studies of gas-evolving reactions with IL-(S)TEM (see Chapter 5).

4 Rh@Pt Electrochemical Stability of Rhodium−Platinum Core−Shell Nanoparticles: An Identical Location Scanning Transmission Electron Microscopy Study

Note: The following chapter is based on the publication "Rh@Pt Electrochemical Stability of Rhodium−Platinum Core−Shell Nanoparticles: An Identical Location Scanning Transmission Electron Microscopy Study", by M. Vega-Paredes et al. in *ACS Nano* 2023, *17*, 16943-16951. Therefore, the personal pronoun "we" is used throughout this chapter to refer to the group of researchers that were part of this specific study.

In this chapter, the stability of rhodium−platinum core−shell nanoparticles on carbon support (Rh@Pt/C NPs) is assessed and their degradation mechanisms are unraveled using identical location scanning transmission electron microscopy.

Rh@Pt/C NPs are promising candidates as anode catalysts for polymer electrolyte membrane fuel cells. However, their electrochemical stability needs to be further explored for successful application in commercial fuel cells. Here we employ IL-STEM to track the morphological and compositional changes of Rh@Pt/C NPs during potential cycling (10 000 cycles, 0.06−0.8 V_{RHE}, 0.5 M H_2SO_4) down to the atomic level, which are then used for understanding the current evolution occurring during the potential cycles. Our results reveal a high stability of the Rh@Pt/C system and point toward particle detachment from the carbon support as the main degradation mechanism.

4.1 Introduction

Pt−Rh-based materials have attracted a great deal of attention in the last years in a wide range of catalytic applications, including the preferential oxidation of CO in hydrogen,[21,112] the control of NOx and CO emissions from car exhaust,[113] the hydrogen evolution reaction,[114] formic acid oxidation,[115,116] and the hydrogenation of organic compounds,[117,118] among others. Furthermore, Pt−Rh-based materials have been explored as catalysts for proton exchange membrane fuel cells (PEMFCs), both in the cathode[119] and in the anode, where they have been investigated for the oxidation of methanol[120,121] and ethanol[120–122] or as CO-tolerant HOR catalysts.[123,124]

Despite these investigations, the understanding of the electrochemical stability and degradation mechanisms affecting Pt−Rh catalysts and the resulting impact on their catalytic activity

remains limited. This is especially relevant for PEMFCs, since limited catalyst stability is one of the central factors limiting their widespread commercialization.[125] Particle dissolution, agglomeration, Ostwald ripening, and particle detachment have been reported as some of the main phenomena affecting state-of-the-art Pt-based PEMFC catalysts.[126] Moreover, when Pt is alloyed with a less stable transition metal, such as Ni or Co, the preferential dissolution of these metals can take place.[127,128] This process also affects Pt−Ru-based catalysts,[50–52] the materials of choice for CO-tolerant PEMFC anodes due to their superior catalytic activity,[129,130] which impacts greatly their performance toward the HOR. Therefore, it is still necessary to find a durable anode catalyst that can boost the commercial viability of PEMFCs.[129] In this context, Pt−Rh catalysts are promising candidates to replace Pt−Ru-based anodes on PEMFCs if their stability under operating conditions is higher, as hinted by the Pourbaix diagrams of Ru and Rh.[53] However, their electrochemical stability needs to be further explored since not much is known about the degradation mechanisms affecting Pt−Rh catalysts under fuel cell conditions.

In this work, we study the stability of Rh−Pt core−shell nanoparticles on turbostratic carbon support (Rh@Pt/C NPs) during electrochemical cycling (10 000 cycles, 0.06−0.8 V_{RHE}, 0.5 H_2SO_4) by identical location scanning transmission electron microscopy.[110] This particular nanostructure was selected because similar core−shell NPs have been shown to have superior performance than the alloyed counterparts.[21,131,132] IL-(S)TEM is a powerful tool for studying local changes down to the atomic level in nanostructured catalysts, which has been extensively used for gaining insights into the degradation of electrocatalysts[58,133–136] or their support[134,137] under fuel cell conditions. In IL-(S)TEM, the same region of interest can be investigated before and after electrochemical testing, allowing correlation of the changes in the particles with the catalytic activity. This technique solves some of the limitations of *ex-situ* (S)TEM, in which only general statistical insights are possible, which might fail to reflect the exact changes taking place in the system.[37] In addition, it also presents some advantages compared with *in-situ* electrochemical liquid cell (S)TEM, in which the electron beam-induced radiolysis of the electrolyte can produce unwanted artifactual reactions,[109] as well as having its special resolution limited by the presence of a thick liquid layer.[108]

Our results indicate that the investigated Rh@Pt/C NPs are stable systems and point toward particle detachment as the main degradation mechanism taking place during potential cycling.

4.2 Results and Discussion

Characterization of the as-synthesized Rh@Pt NPs.

The as-synthesized Rh@Pt/C NPs were characterized by means of (S)TEM in order to confirm the core–shell structure and study the atomic arrangement (**Figure 4-1**). The higher atomic number of Pt compared to Rh ($Z_{Pt} = 78$, $Z_{Rh} = 45$) results in Pt atoms scattering electrons more strongly and appearing brighter in the HAADF images.[91] Therefore, the bright shell surrounding the dark core in the particle in **Figure 4-1a** is indicative of a Rh-core Pt-shell particle. The fast Fourier transform (FFT; inset **Figure 4-1a**) shows that both the shell and the core are face-centered cubic and oriented along the [011] zone axis (ZA).

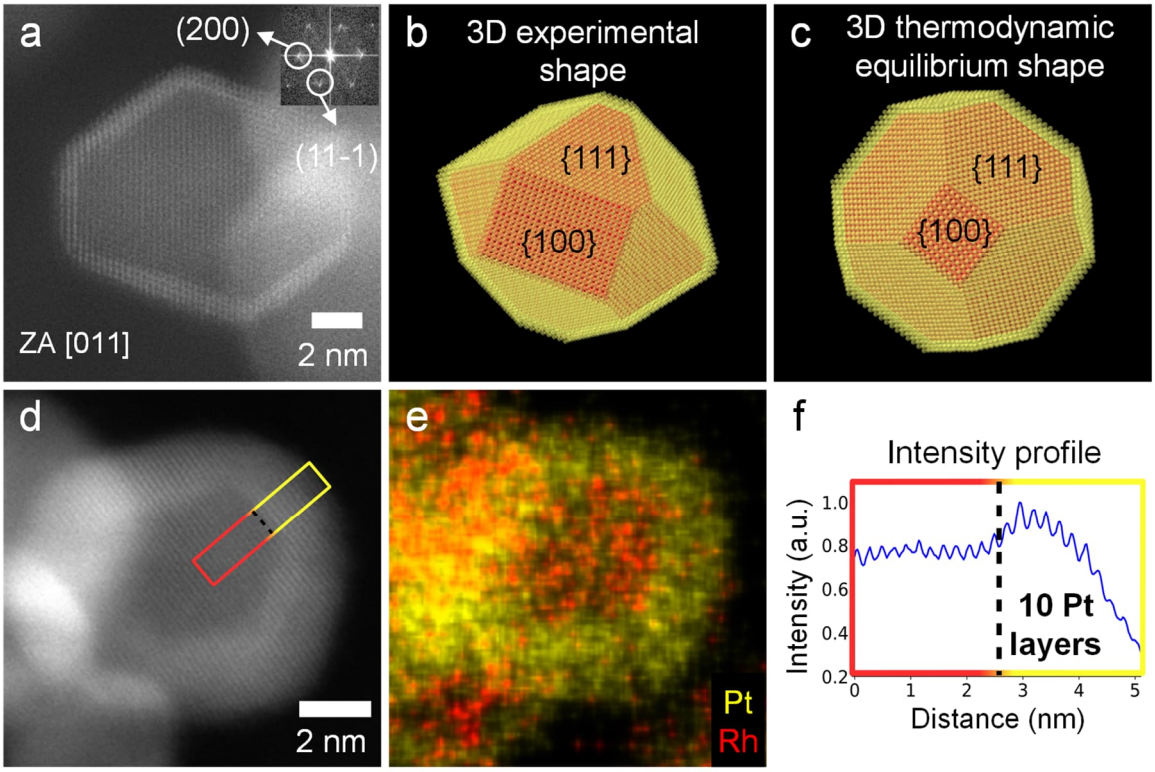

***Figure 4-1**. Structural and compositional characterization of the as-synthesized Rh@Pt/C NPs. (a) HAADF-STEM micrograph of a faceted particle visualized along the [011] ZA. Its FFT is shown as an inset. (b) 3D atomic model of that particle that deviates from the thermodynamic equilibrium shape, shown in (c). (d) HAADF-STEM micrograph, (e) its corresponding EDS composition map, and (f) intensity profile along a NP with a 10-monolayer-thick Pt shell.*

The NPs have been further analyzed by HR-TEM and subsequent FFT analysis. The results show that the Rh@Pt/C NPs investigated in this work are highly faceted and present the lowest energy {111} and {100} facets (**Figure 4-2**).[138] However, their shape deviates from that of the thermodynamic equilibrium (**Figure 4-1b,c**), as they present asymmetric facets that distort the

3D structure from the expected cuboctahedron. The shell thickness is measured to be between three (**Figure 4-1a**) and 10 (**Figure 4-1d-f**) Pt monolayers. Nonetheless, even in the particles with a shell of only three Pt monolayers, the Rh core appears to be fully encapsulated, which is desirable since an incomplete core coverage would result in the less stable Rh being exposed to the electrolyte during cycling/operation, and therefore in a lower stability.[51]

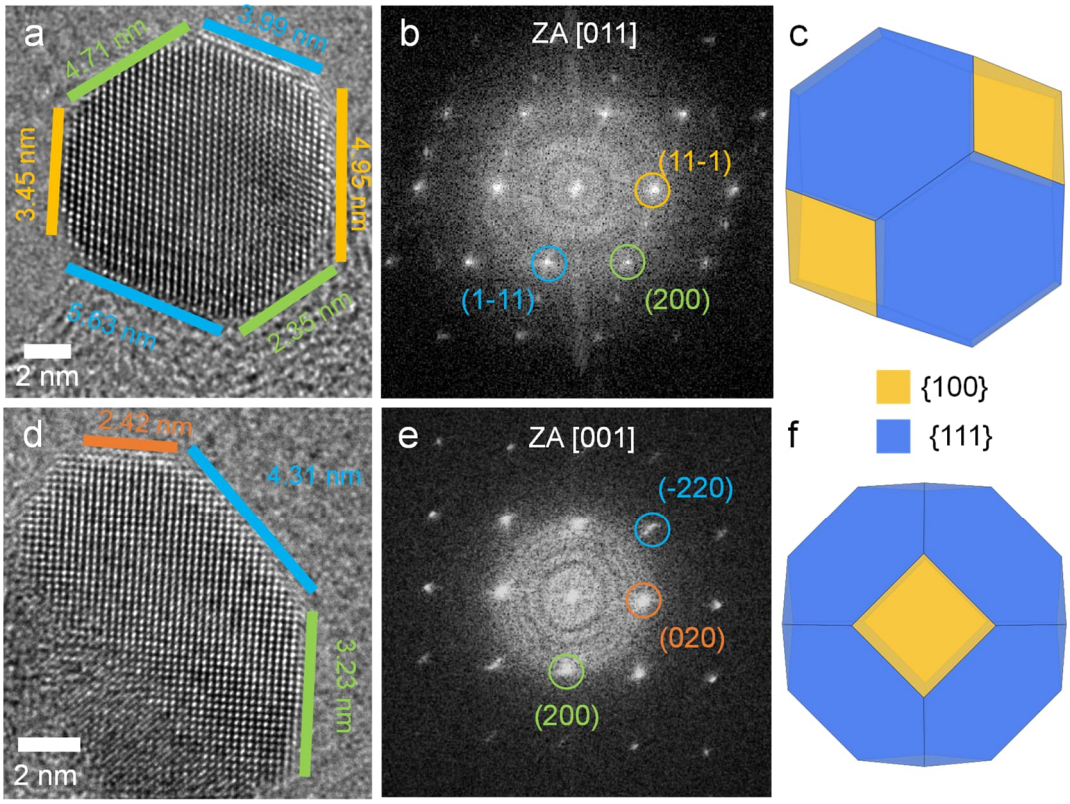

***Figure 4-2**. HR-TEM micrographs (a,d) and respective FFTs (b,e) of two Rh@Pt/C NPs oriented along the [011] and [001] ZA. In (c,f) the Wulff constructions of Rh along the corresponding zone axis are provided. Notice how the experimental shape of the NPs deviates from that expected on the thermodynamic equilibrium.*

Since the encapsulation of the core is a 3D phenomenon, the NPs were further investigated by high-resolution electron tomography (**Figure 4-3**). In **Figure 4-3a**, the intensity-based segmentation of a reconstructed Rh@Pt/C NP at atomic resolution is shown. The low-intensity voxels are assigned to Rh, whereas those with high intensity correspond to Pt (**Figure 4-3b**). An animated version of the reconstruction and ortho-slices through the 3D data set can be found in the web version of the article.[64] These results confirm that the Rh core is fully surrounded by the Pt shell, and therefore a high electrochemical stability can be expected.

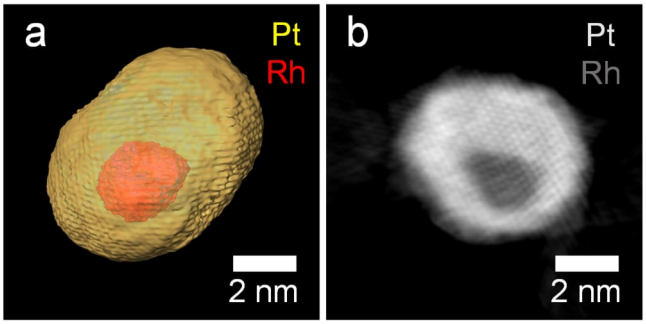

***Figure 4-3**. High-resolution tomography of as-synthesized Rh@Pt/C NPs. (a) Segmented 3D volume and (b) ortho-slice of the reconstruction.*

Electrochemical accelerated stress tests.

After the initial characterization of the Rh@Pt NPs, accelerated stress tests (ASTs) were carried out, as described in the Experimental methods. The upper potential limit of 0.8 V_{RHE} differs from ASTs found in the literature, in which higher upper potential limits are used for studying the degradation associated with start-up or shut-down events.[58,139] However, the development of system strategies mitigates the degradation during these events,[140,141] making a lower upper potential limit more suitable for studying anode catalyst degradation studies.[52]

Figure 4-4 shows the changes in the Rh@Pt/C-TEM grid voltammograms that occurred during the potential cycles.

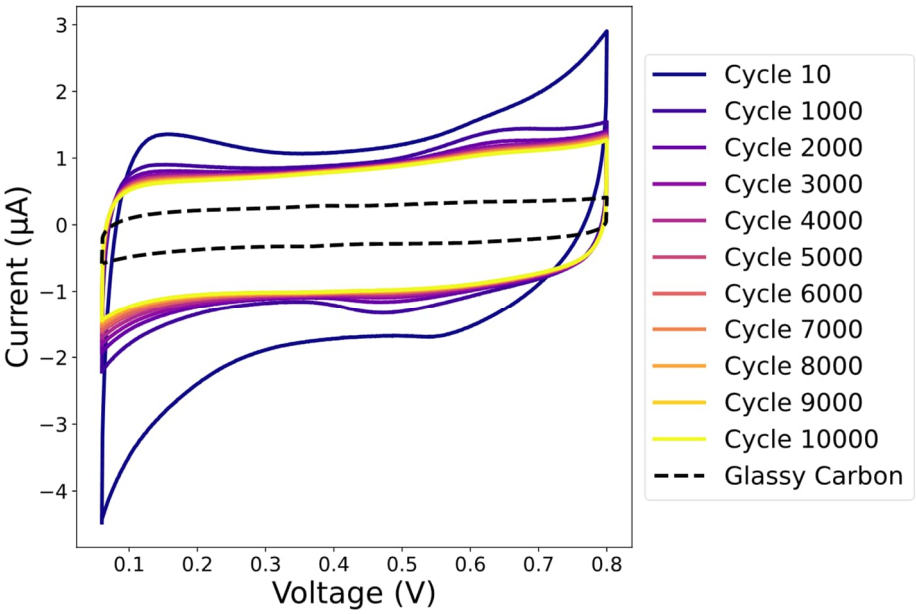

***Figure 4-4**. Voltammograms showing the changes in the Rh@Pt/C NPs' activity during the potential cycles.*

A cyclic voltammetry recorded with the bare glassy carbon electrode is also provided as a blank current. The comparatively higher current obtained after adding the TEM grid confirms the correct electrical connection of the grid to the electrode.

In the initial cycles oxidation and reduction peaks are present at 0.65 V_{RHE} and 0.55 V_{RHE}, respectively, which can be attributed to Pt.[142] Additionally, a peak in the hydrogen underpotential deposition region is also seen. During the potential cycles, the cyclic voltammetry curves flatten progressively, and after 10 000 cycles only capacitive current can be observed, which can be attributed to the carbon support.[143] This is indicative of a loss of active catalyst during the potential cycles, which could be caused by the common degradation mechanisms of fuel cell catalysts (particle dissolution, agglomeration, Ostwald ripening, and particle detachment from the carbon support). Moreover, since the cycles are performed on a TEM grid loaded with Rh@Pt/C NPs without any binder, large groups of Rh@Pt/C NPs not properly attached to the TEM grid can also get removed (**Figure 4-5**), which partially explains the loss of current observed in **Figure 4-4**.

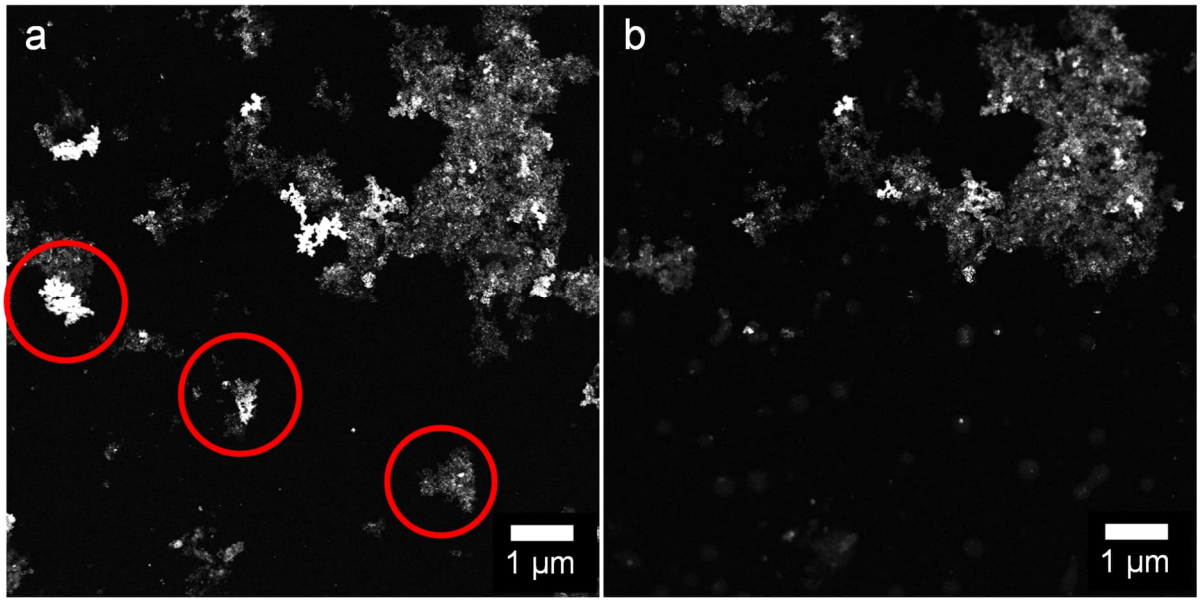

***Figure 4-5**. Detachment of big groups of Rh@Pt/C NPs during the ASTs from the TEM grid due to the absence of a binder (Nafion).*

Nonetheless, loss of current is still observed for the voltammograms performed on Rh@Pt/Cglassy carbon (**Figure 4-6a**) to a smaller extent. Since that electrode contained Nafion as a binder, the removal of large groups of Rh@Pt/C NPs cannot solely explain the loss of activity of Rh@Pt/C NPs, and other degradation mechanisms need to be considered.

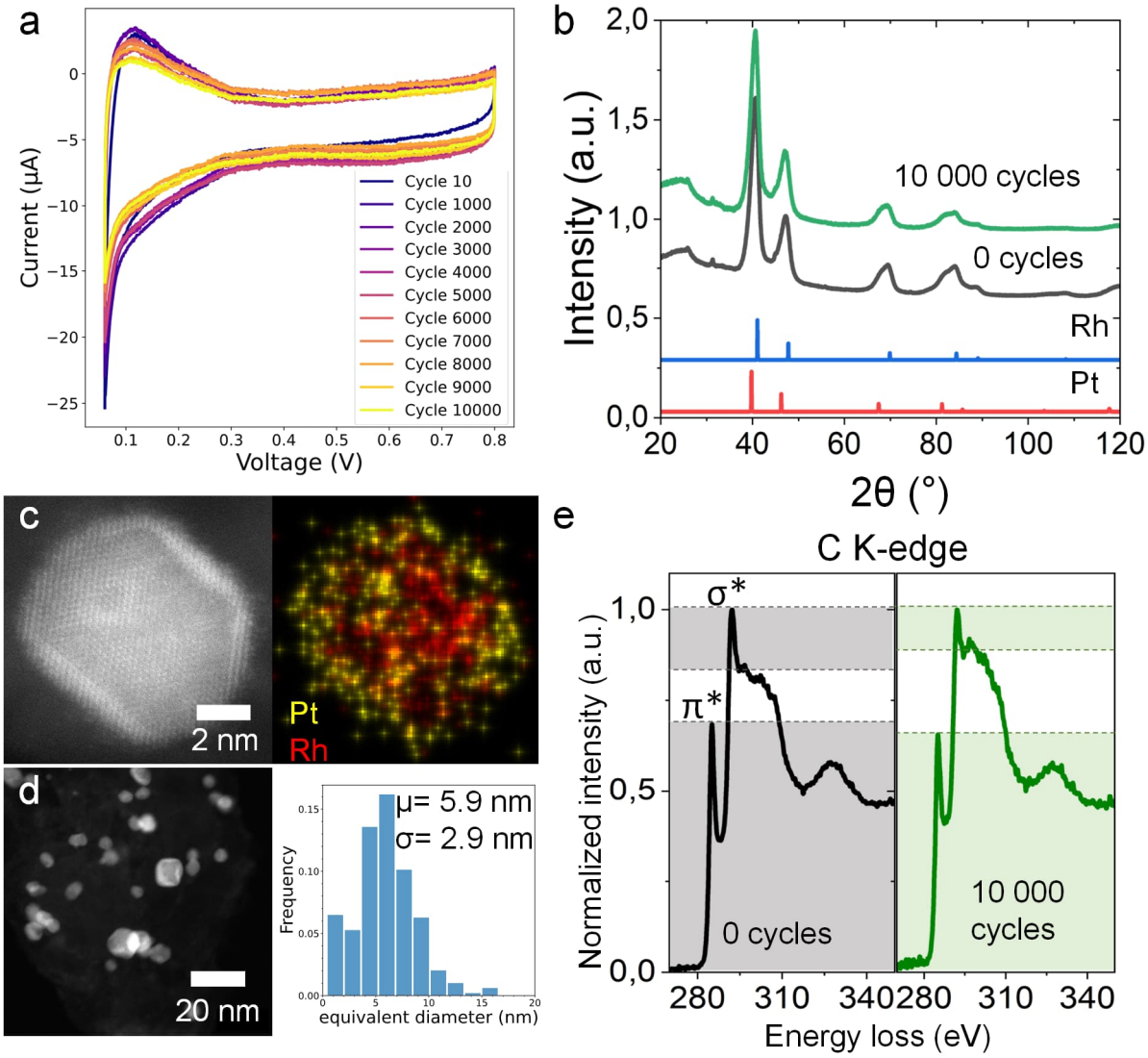

***Figure 4-6**. Ex-situ characterization. (a) Voltammograms performed on a Rh@Pt/C NPs ink deposited on a glassy carbon electrode. (b) XRD diffractograms of the Rh@Pt/C NPs at 0 (in gray) and 10 000 (in green) cycles. The diffractograms of Pt (ICSD-76951) and Rh (ICSD-76952) are also provided for comparison. The additional reflection at 31.5° is most likely stemming from CaS impuritutes of the carbon support. HR-STEM image, corresponding EDS composition map (c), lower resolution STEM micrograph with particle size distribution histogram (d) and EELS spectra (e) of the Rh@Pt NPs ink after 10 000 cycles.*

Identical location STEM

In order to understand the causes behind the current degradation observed in **Figure 4-4**, IL-STEM experiments were performed. **Figure 4-7** shows how a representative region of the sample changed during the potential cycles.

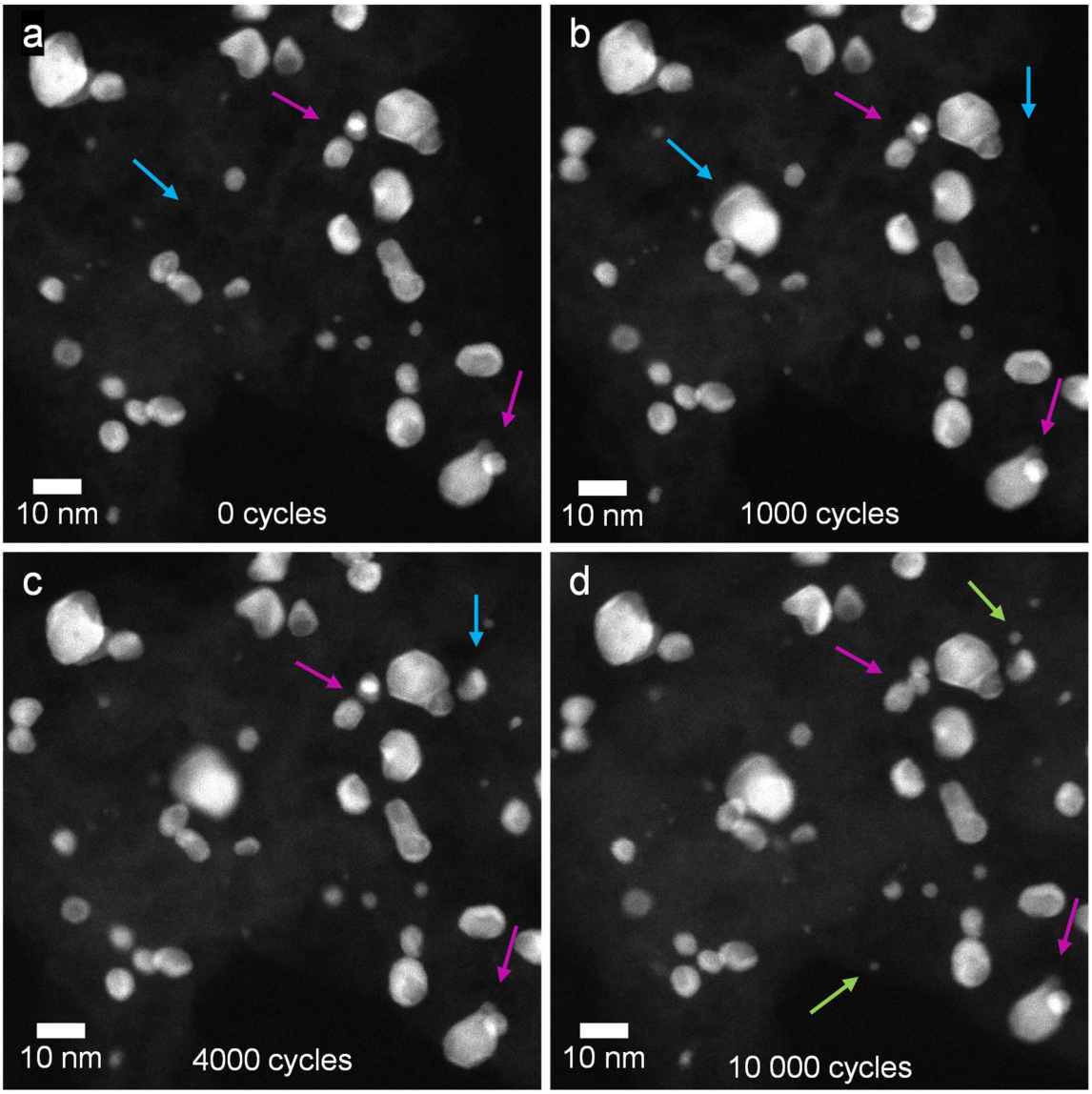

***Figure 4-7**. HAADF-STEM micrographs showing a region of the sample at (a) 0, (b) 1000, (c) 4000, and (d) 10 000 AST cycles. The different colored arrows indicate particle movement (purple), particle reattachment from another region (blue), and particle reprecipitation from dissolved species (green).*

The evolution of an additional region is provided in **Figure 4-8** to demonstrate the reproducibility of the results. In both IL-STEM datasets particle movement and particle reprecipitation from dissolved species are observed.

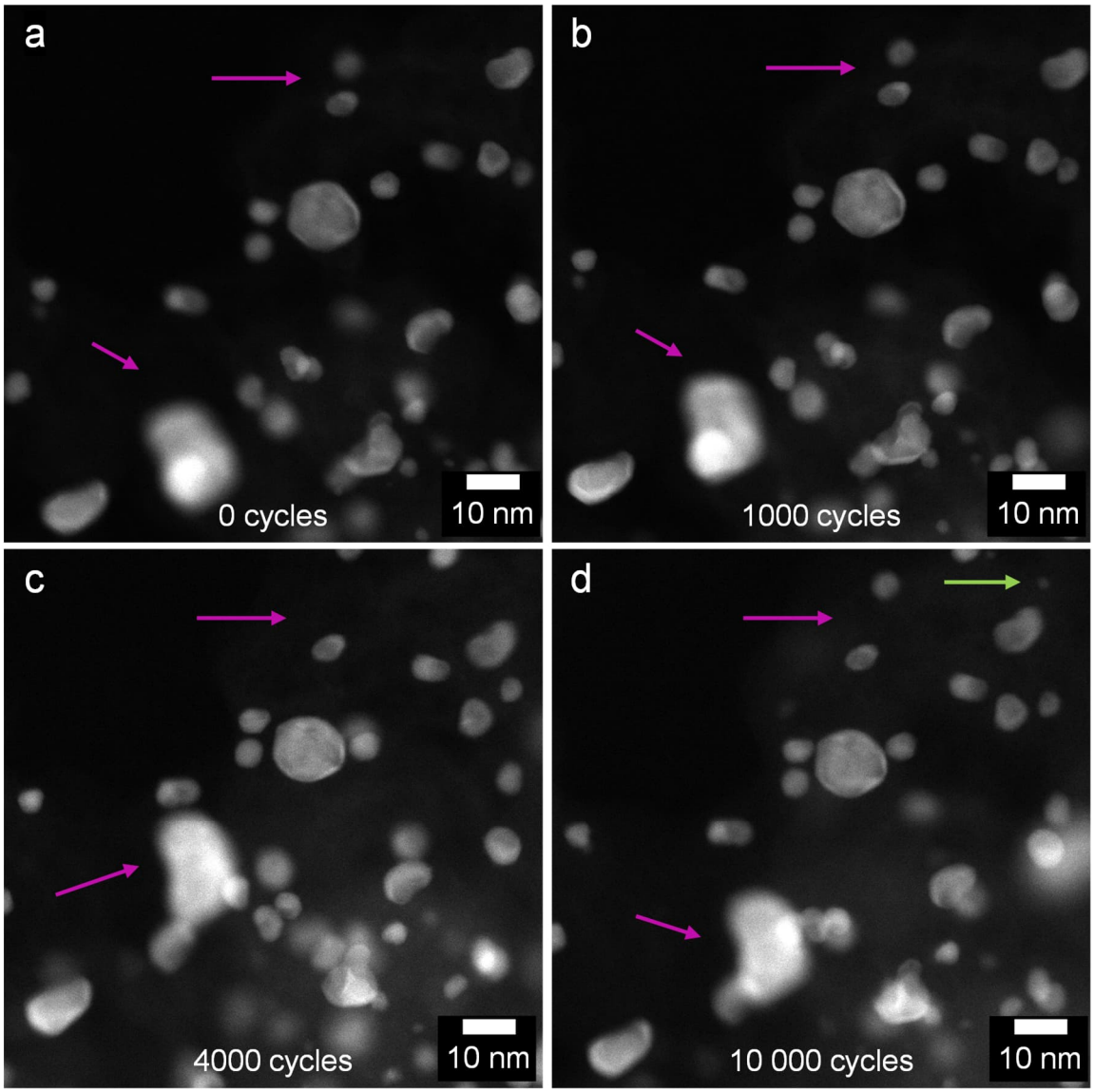

Figure 4-8. *IL-STEM dataset of a different region of the sample. The HAADF-STEM images were taken after (a) 0, (b) 1000, (c) 4000 and (d) 10 000 AST cycles. The arrows indicate particle movement (purple) and particle reprecipitation from dissolved species (green).*

No clear particle growth or agglomeration can be seen, and a constant mean particle size (represented by the equivalent diameter) of ~5.9 nm is found during the cycles (**Figure 4-9**). For the analysis, several hundreds of NPs have been evaluated to get statistical significant information.

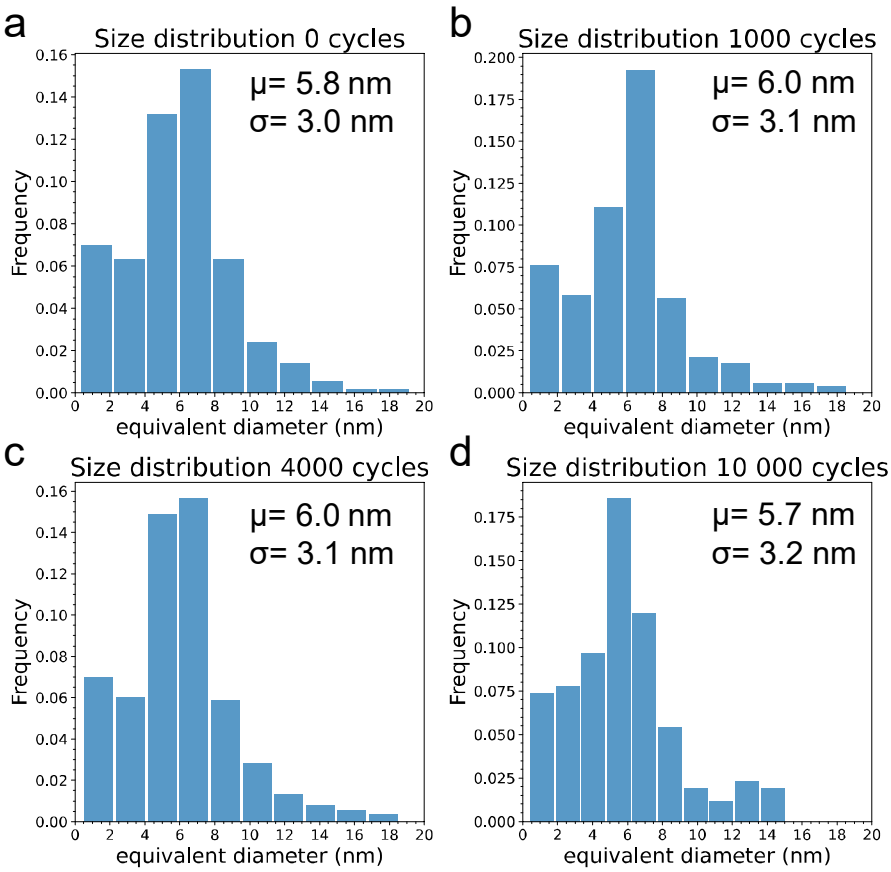

Figure 4-9. *Particle size distribution histograms at 0 (a), 1000 (b), 4000 (c) and 10 000 (d) potential cycles. The mean diameter (μ) and standard deviation (σ) are provided in each histogram.*

A similar particle size distribution was found for the particles cycled directly after drop casting on the glassy carbon electrode (**Figure 4-6d**). The fact that the mean particle size does not increase during ASTs is indicative of the stability of the particles under cycling conditions. Thus, the observed loss of current of the catalytic material cannot be attributed to a decrease in the ECSA of the catalysts derived from NP growth. Nonetheless, small-particle nucleation is observed after 10 000 cycles (**Figure 4-7** and **Figure 4-8**, green arrows). Although it is possible that part of the small particles could be originating from redeposition of Pt ionic species dissolved from the Pt-wire counter electrode, small-particle nucleation was also observed when a glassy carbon counter electrode was used (**Figure 4-10**). The presence of small Pt particles was also reported in previous IL-STEM studies on Pt–Ni NPs and was attributed to the dissolution and reprecipitation of catalytic species.[144] Although the authors claimed that these dissolved species could migrate on the carbon support and redeposit onto other particles, resulting in Ostwald ripening, this is not observed in the mean particle size of the Rh@Pt/C NPs, which indicates that this Ostwald ripening is not significant in our system for the chosen

conditions. Besides the constant mean particle size, X-ray diffraction experiments on the Rh@Pt/C NPs (**Figure 4-6b**) also reveal that the crystalline structure of the NPs did not change during the potential cycles.

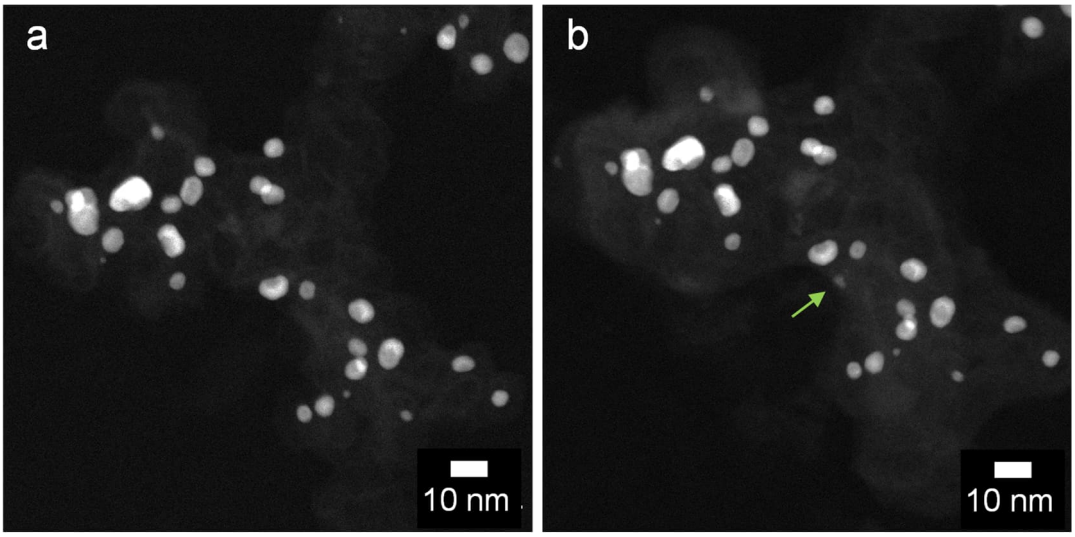

***Figure 4-10**. Small particle nucleation also takes place when using a glassy carbon counter electrode as revealed by the HAADF-STEM micrographs (a,b).*

During all of the AST cycles, particle movement (**Figure 4-7** and **Figure 4-8**, purple arrows) can be observed. This is a well-documented phenomenon occurring in PEMFCs,[145–148] which is caused by changes in the underlaying carbon support (i.e., the turbostratic carbon). Carbon corrosion is thermodynamically possible at voltages E > 0.207 V_{RHE}, and although it is kinetically slow at typical PEMFC potentials, it is known to be catalyzed by the Pt present in the catalyst NPs.[148] This particle movement can result in particle aggregation and coalescence, which decrease the ECSA of the catalyst and can be one of the main degradation mechanisms behind the loss of performance in PEMFCs. However, the particle movement observed for the Rh@Pt/C NPs during the potential cycles is subtle. Since the movement can take place both in and out of plane, from the 2D projections, it cannot be properly quantified. To assess if the Rh@Pt/C NPs have a tendency of decreasing their distance and would eventually get aggregated if more cycles are performed, low-magnification HAADF-STEM tomography experiments at different points of the potential cycles (0, 1000, 4000, 10 000) were carried out. For the animated movies of the segmented reconstructed volumes, the reader is referred to the web version of the article.[64] Similarly to the HAADF micrographs, the low-magnification 3D reconstructions also show particle movement during the potential cycles, which results in small fluctuations in the average nearest neighbor distance (**Figure 4-11**). However, no clear trend can be discerned, meaning that the Rh@Pt/C NPs are not significantly aggregated during the

ASTs. Therefore, particle aggregation/agglomeration can be excluded as the main degradation mechanisms of these particles.

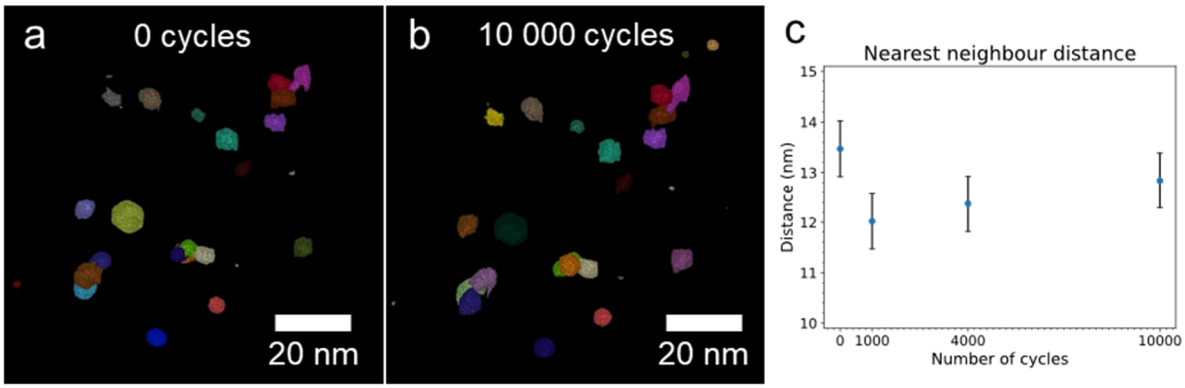

***Figure 4-11**. Segmented tomograms at 0 (a) and 10 000 (b) cycles. (c) Changes in the nearest neighbour distance during the ASTs, indicating that despite the particle movement, there is no tendency towards particle aggregation/agglomeration.*

Besides particle movement, another consequence of the turbostratic carbon support corrosion is particle detachment, which results in the loss of catalyst material with the corresponding drop in ECSA and PEMFC performance. During IL-STEM experiments, the detached particles can (i) reattach in another region containing Rh@Pt/NPs, (ii) reattach on the TEM grid, and (iii) be washed out by the electrolyte. Examples of particle reattachment from a different region can be seen in Figure 4 (blue arrows), where particles that are not present at 0 cycles appear after 1000 or 4000 cycles. Lower magnification images were also checked to discard the possibility of particle migration from a neighboring region. Particle reattachment on the TEM grid can also be observed frequently, since after potential cycling Rh@Pt particles without a turbostratic carbon support can be found on the TEM grid (**Figure 4-12a−c**). Considering that all of the particles were found deposited on the carbon support before the cycles, this is a clear indication of particle detachment from the carbon support and reattachment on the TEM grid.

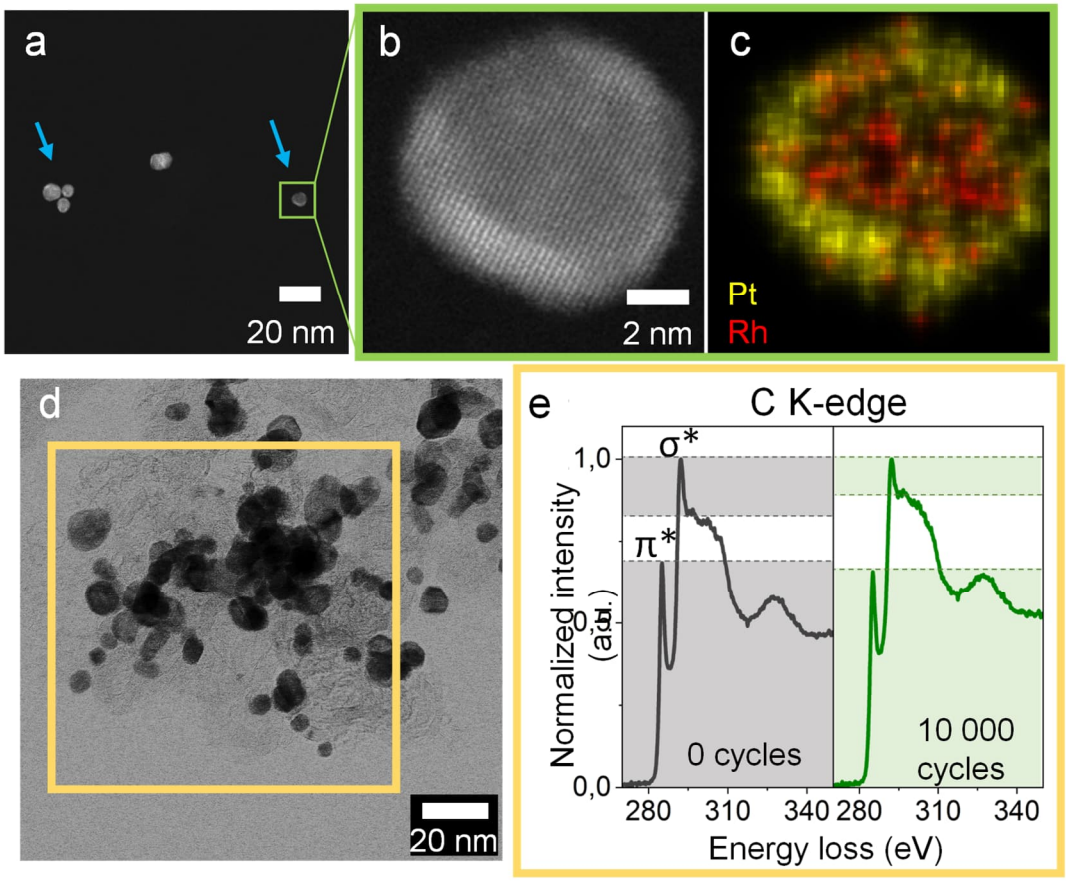

***Figure 4-12**. Particle detachment due to C support corrosion. (a) Rh@Pt particles found after 1000 ASTs without a carbon support (blue arrows) that have reattached from other regions of the sample. HAADF micrograph (b) and EDS map (c) of one particle. (d) Bright-field STEM micrograph, showing the region where the EELS spectra (e) were taken at 0 and 10 000 cycles.*

To see better the lack of turbostratic carbon support, intensity saturated micrographs of the area depicted in **Figure 4-12** are provided in **Figure 4-13**, together with carbon-supported Rh@Pt/C NPs for comparison. When the carbon support is present, it can be clearly distinguished from the amorphous carbon from the TEM due to the presence of graphitic (0001) planes.

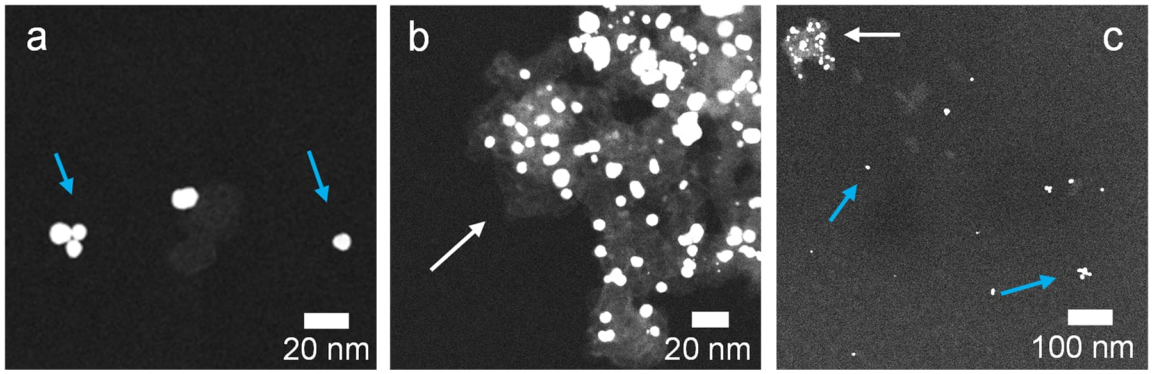

***Figure 4-13**. Saturated HAADF-STEM micrograph of Rh@Pt/C NPs showing the difference between the turbostratic carbon supported NPs (indicated with white arrows) vs particles without carbon support (blue arrows).*

Moreover, particles being directly detached from the turbostatic carbon support were also observed. HAADF-STEM images demonstrating this in different regions are presented in **Figure 4-14**.

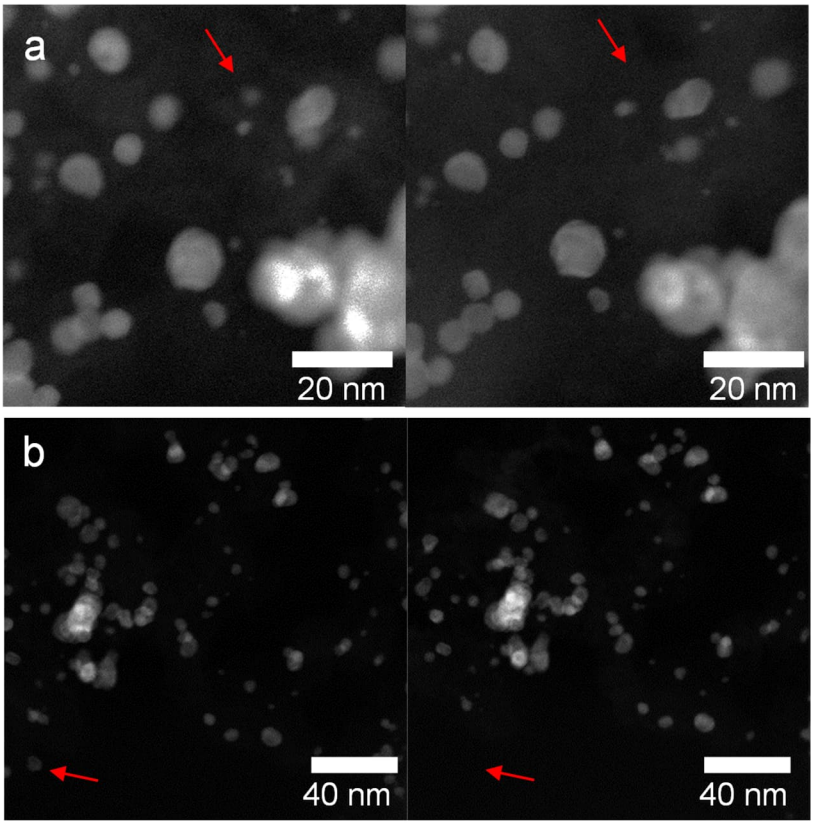

***Figure 4-14**. Particle detachment observed during the IL-STEM experiments in two different regions (a,b).*

These results indicate that particle detachment from the carbon support (as a consequence of support degradation) is a relatively frequent phenomenon in Rh@Pt/C NPs. The degradation of the carbon support was further confirmed by EELS (**Figure 4-12d,e**). The EELS spectrum of the carbon K-edge before cycling is typical for graphitic carbon materials, with peaks corresponding to transitions to antibonding π^* states (~285 eV) and antibonding σ^* states (~292 eV).[149] After 10 000 cycles, the intensity of these peaks decreased, demonstrating an amorphization of the carbon support.[150] Nonetheless, pronounced π^* and σ^* peaks are still observed, indicating that the amorphization is partial and explains the moderate particle movement and detachment observed in the IL-STEM experiments. A similar partial amorphization was seen in a region not previously exposed to the electron beam (**Figure 4-15**, red line), ruling out possible electron beam effects, and for the carbon support on the Rh@Pt/C NPs cycled directly after drop casting on the glassy carbon electrode (**Figure 4-6e**).

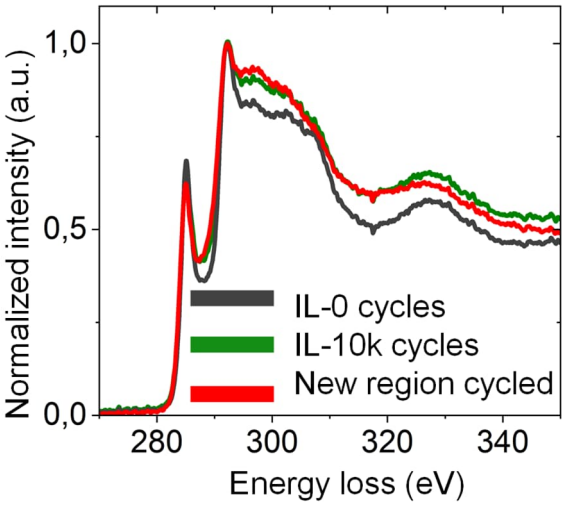

***Figure 4-15**. EELS spectra after 10 000 cycles (red) of a region not previously explored with the electron beam. A similar partial amorphization is seen as in the identical location region (black before cycle, green after).*

As previously discussed, no particle aggregation/agglomeration, significant catalyst dissolution, or Ostwald ripening (**Figure 4-7**, **Figure 4-9**) is observed in the IL-STEM experiments. Therefore, the lower current observed in **Figure 4-4** and **Figure 4-6a** upon electrochemical cycles is assigned to be predominantly caused by particle detachment from the turbostratic carbon support. Efforts for increasing the stability of Rh@Pt/C particles should focus on enhancing the support− NP interaction, which could be achieved by functionalizing the support[151], replacing it with another material, such as oxide-[152] or graphene[153]-based supports, or assembling the NPs into nanoassemblies that can have multiple anchoring points with the substrate.[16]

Besides the previously mentioned degradation mechanisms, in bimetallic systems, other phenomena can occur. For instance, in bimetallic Pt−Ru particles, preferential dissolution of Ru can take place.[50] Even in core−shell NPs, Ru-core dissolution can take place if the Pt-shell is not fully covering the core[51] or by thermally induced shape fluctuations of the shell,[154] both of which result in the less stable core metal being exposed to the electrolyte, with its consequent dissolution. EDS spectral images were acquired during the ASTs to study the changes in the elemental composition and distribution of the Rh@Pt/C NPs. In **Figure 4-16**, the elemental distribution maps of a Rh@Pt/C NP are shown.

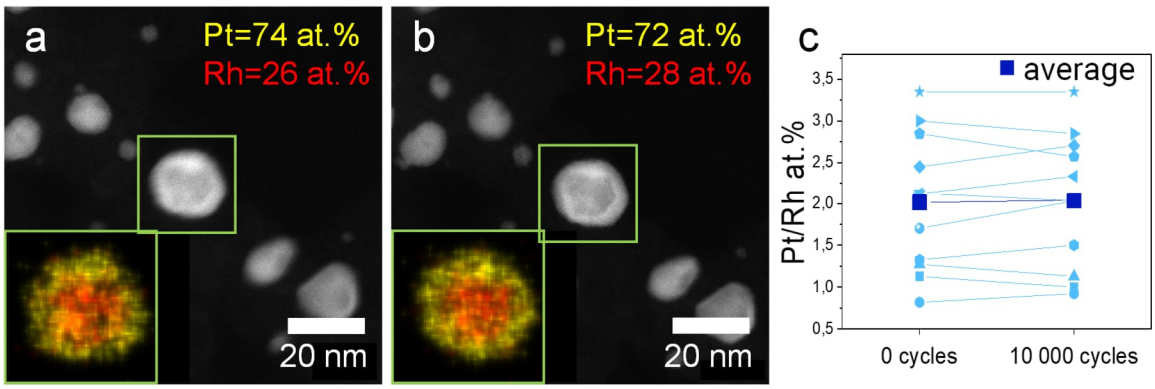

***Figure 4-16**. Composition changes in Rh@Pt/C NPs during ASTs. HAADF-STEM micrographs of the same region are shown at 0 (a) and 10 000 (b) potential cycles. As insets, the EDS composition maps of the central NP are provided. (c) Evolution of the Pt/Rh at. % ratio quantified from the EDS composition maps for 11 different particles.*

EDS maps of other particles are provided in **Figure 4-17**. These results reveal an identical core–shell structure before and after the ASTs, indicating the compositional stability of the NP system.

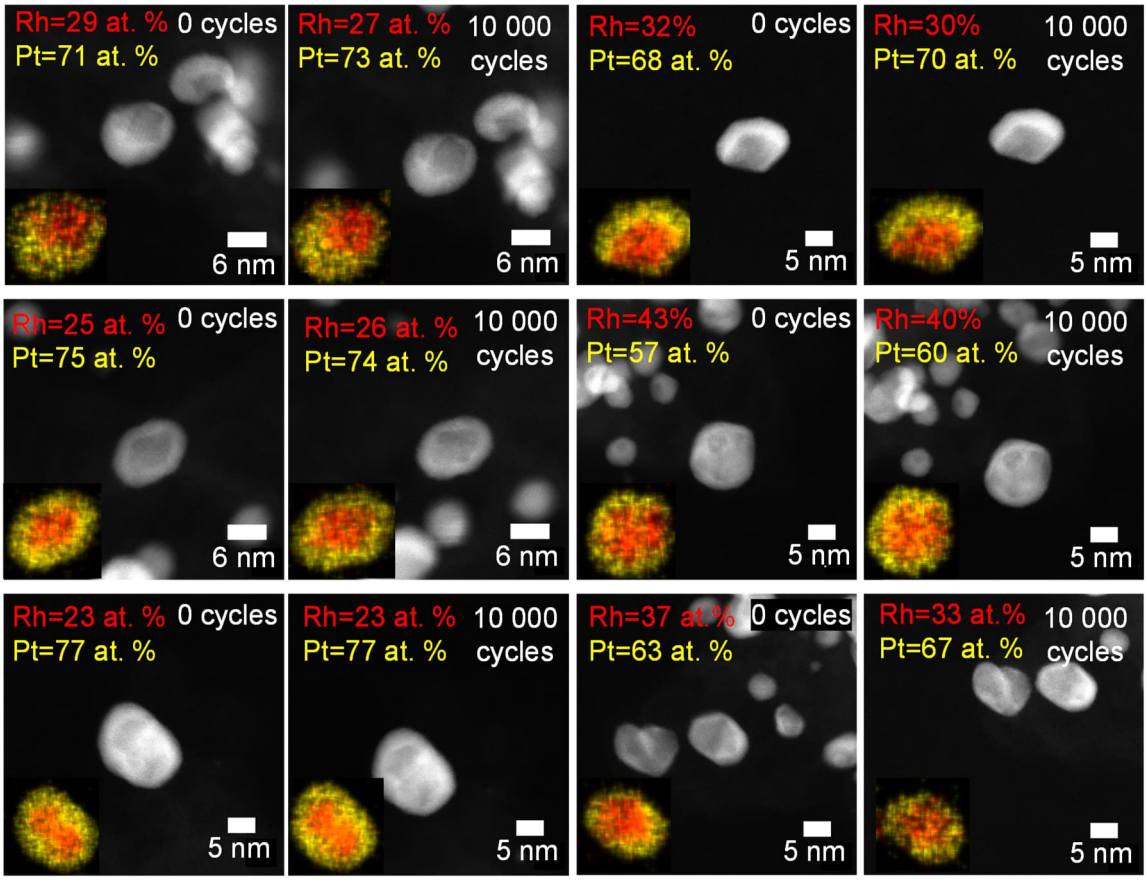

***Figure 4-17**. Selected HAADF-STEM micrographs and EDS maps showing the composition and elemental distribution changes in Rh@Pt/C NPs during the ASTs.*

Moreover, no Rh preferential dissolution is detected, since the composition of the particles remains unaltered during potential cycling, with only small variations of up to 3 at. % (near the sensitivity of the technique) that do not follow a clear trend (**Figure 4-16c**). This is in good agreement with the HR-STEM observations and EDS composition maps performed on particles cycled directly after drop casting on the glassy carbon electrode (**Figure 4-6c**), which further prove the preservation of the core–shell structure.

This was further confirmed in lower magnification EDS experiments in order to increase the statistics in the measures (**Figure 4-18**). **Figure 4-18** corroborates that there are no significant changes in the elemental composition during the ASTs. This is most likely caused by the full Rh core encapsulation (**Figure 4-1**, **Figure 4-3**) and by the higher electrochemical stability of Rh than Ru.[53]

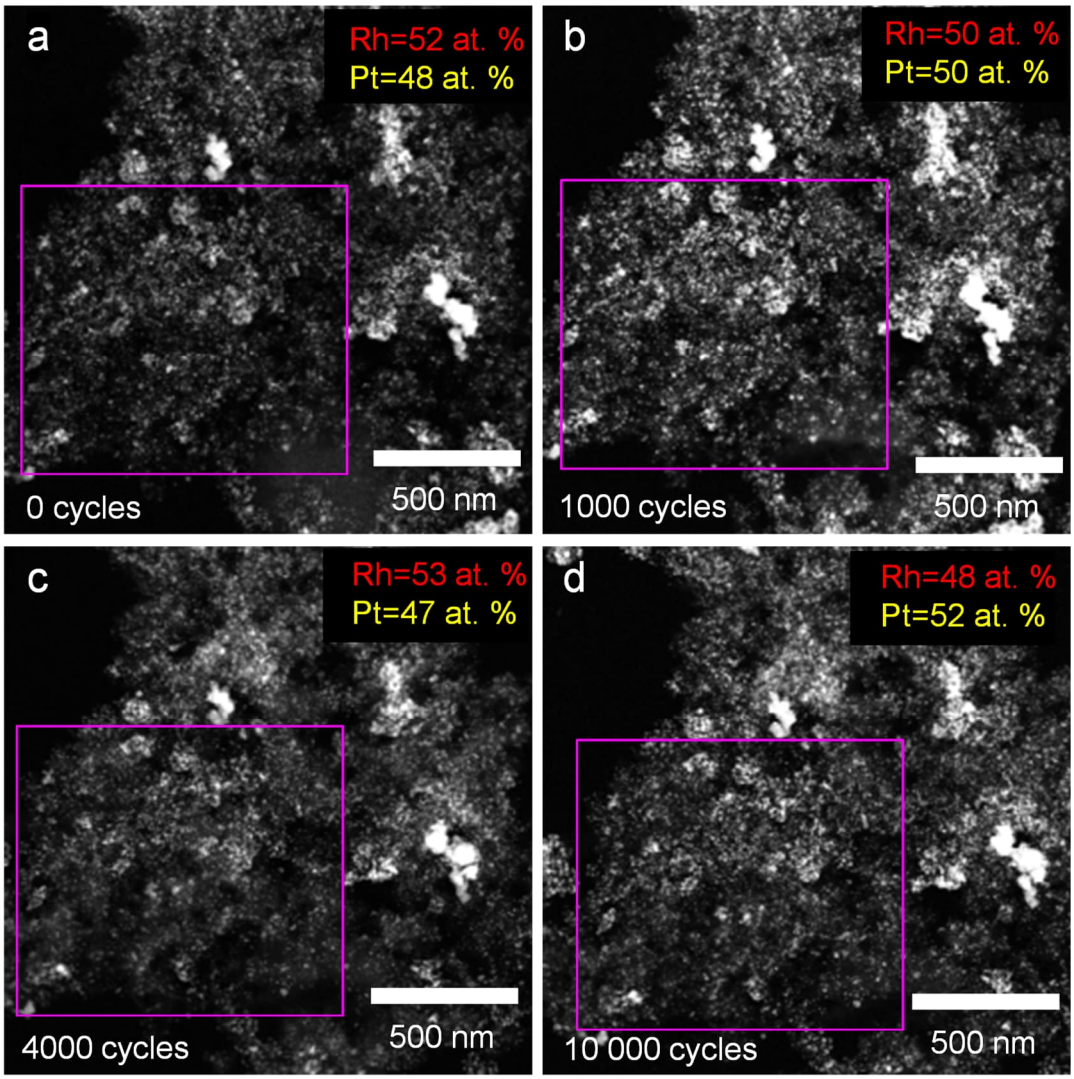

***Figure 4-18**. Composition at 0 (a), 1000 (b), 4000 (c) and 10 000 (d) potential cycles. The Pt and Rh atomic ratio from the region delimited by a purple square is provided.*

Even though the size and composition of Rh@Pt/C NPs remained practically constant during potential cycles, a careful analysis of high-resolution STEM micrographs shows that changes at the atomic level took place (**Figure 4-19**).

Both dissolution (i.e., atoms present at 0 cycles that are not present after 10 000 cycles) and redeposition (i.e., atoms not present in the as-synthesized particle, that appear after the ASTs) of atomic columns can be observed. These two phenomena occur in the surface steps involving atoms with unsaturated bonds. A similar behavior was reported by Rasouli et al.[144] for Pt−Ni NPs in more oxidative conditions (0.6−1.1 V_{RHE}), in which the atoms on high-energy sites (steps and kinks) dissolved during potential cycling. Our results indicate that in the case of Rh@Pt/C NPs atomic column dissolution can take place, even under the milder conditions used for our ASTs. Beyond dissolving in the electrolyte, these species can either redeposit on previously existing particles or nucleate forming small particles, as seen in **Figure 4-7** (green arrows), explaining their origin.

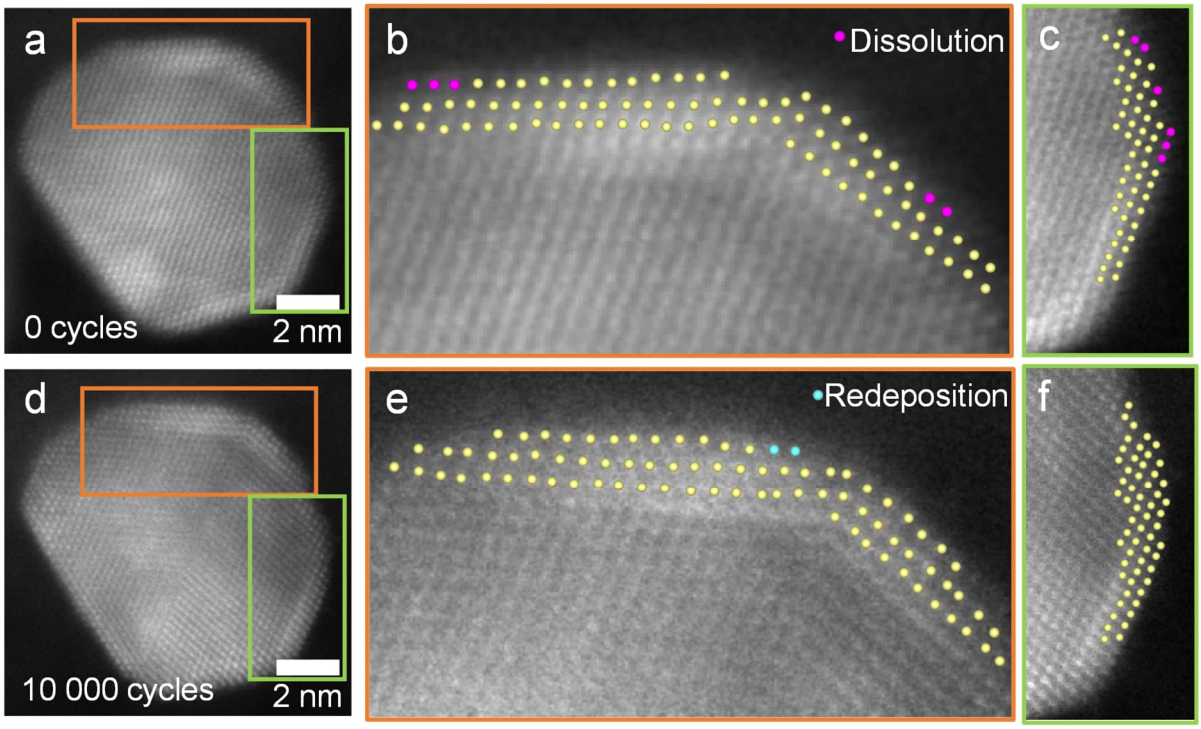

***Figure 4-19**. Atomic scale changes in Rh@Pt/C NPs after 10 000 cycles. The same particle at 0 (a, b,c) and 10 000 (d,e,f) cycles is shown. The atomic column positions of the outermost three atomic layers are indicated by yellow dots. The pink dots indicate those atomic columns that dissolved during the ASTs, while the blue dots indicate those that got redeposited.*

To sum up, our results indicate that Rh@Pt/C NPs are very stable systems under the studied conditions, as opposed to comparable Ru@Pt/C NPs.[51,52] Moreover, they also point out that

particle detachment from the turbostratic carbon support is the main phenomenon causing the loss of active catalyst material in Rh@Pt/C NPs during ASTs. Therefore, efforts for increasing the stability should focus on enhancing the carbon support−particle interaction or on finding different support materials.

4.3 Conclusions

In the present work, the stability of Rh@Pt/C NPs obtained via a two-step polyol synthesis was explored. After initial characterization of the particles showing a complete Rh-core encapsulation, accelerated stress tests in the form of potential cycles (0.06−0.8 V_{RHE}, 10 000 cycles) were performed on a bulk electrode and a TEM grid. The loss of activity seen in the voltammograms during the potential cycles was correlated to the morphological and compositional changes observed on the TEM grid in IL-STEM experiments.

The main degradation mechanism affecting the Rh@Pt/C NPs was found to be particle detachment from the carbon support. Although atomic column dissolution and redeposition were observed, no significant changes in the particle size or composition were detected.

Our results indicate that Rh@Pt/C particles are very stable under the tested electrochemical conditions and point out that efforts to improve even further the stability should focus on enhancing the support−particle interaction.

4.4 Experimental methods

Rh@Pt/C NPs synthesis

Carbon-supported Rh@Pt/C NPs were prepared via a two-step polyol synthesis. The detailed synthesis protocol has been previously described elsewhere.[52] A nominal catalyst loading of 21.1 wt % Rh and 20.0 wt % Pt was used. The carbon support was Cabot FCX 400.

Electrochemical cycling

To study the degradation of the Rh@Pt/C NPs, these were subjected to ASTs by cyclic voltammetry acquired in a three-electrode setup. As counter and reference electrodes, a Pt wire (Redoxme) and a RHE (Gaskatel) were respectively used. The system was controlled by a Gamry 600 reference potentiostat. Before the ASTs, a 0.5 M sulfuric acid electrolyte (H_2SO_4, Suprapur, Sigma-Aldrich) was purged for 30 min with argon. The potential window was chosen between 0.06 V_{RHE} and 0.8 V_{RHE}, and a total of 10 000 cycles were carried out, conditions previously used for studying the degradation of an anode catalyst in PEMFCs.[51,52]

4. Stability of Rh@Pt nanoparticles

The Rh@Pt/C-glassy carbon working electrode was obtained by drop casting 10 µL of ink (1 mg of Rh@Pt/C + 30 µL of Nafion + 2 mL of isopropanol) in a polished glassy carbon electrode. After the cycles, the electrode was scratched to detach some of the cycled Rh@ Pt/C NPs, which were later characterized using X-ray diffraction (XRD) and STEM.

Additionally, to study how individual Rh@Pt/C NPs changed during potential cycles in identical location conditions, 10 µL of a 0.28 mg/mL dispersion of Rh@Pt/C on deionized (DI)-water (0.055 µS/cm) was drop cast onto a holey carbon-coated Au TEM finder grid and left drying overnight. After the initial characterization of the Rh@Pt/C NPs, this TEM grid was fixed on a glassy carbon electrode with a holey Teflon cap and used as a working electrode on the same three-electrode setup. This allowed for tracking changes in specific regions (and particles within those regions) between 0, 1000, 4000, and 10 000 potential cycles.

(S)TEM characterization

HR-TEM micrographs of the as-synthesized Rh@Pt/C NPs were obtained in an image-corrected Titan Themis microscope (Thermo Fisher Scientific) operated at 300 kV. The corrector was set to introduce negative spherical aberration on the objective lens, which together with an overfocus results in bright atom contrast.[95] The TEM images were recorded on a CMOS 4k × 4k camera.

The Rh@Pt/C NPs were characterized as synthesized and after 1000, 4000, and 10 000 potential cycles by means of STEM. STEM micrographs were acquired in a probe-corrected Titan Themis microscope (Thermo Fisher Scientific) operated at 300 kV by using a HAADF detector. A convergence angle of 23.8 mrad was used, resulting in a probe of around 0.1 nm. 3D atomic models were constructed from the STEM micrographs using the Rhodius software.[155,156] The equilibrium thermodynamic shape was built taking as a reference the Wulff construction for Rh.[157] EDS spectral images were acquired to study the chemical composition and elemental distribution of Rh@Pt/C NPs. To minimize the electron-beam-induced damage on the particles, the acquisition time of the EDS spectral images was limited to 5 min and they were only taken on the as-synthesized NPs and at the end of the AST (after 10 000 cycles). Moreover, HAADF micrographs before and after the acquisition were taken and compared to rule out electron-beam-induced morphological changes. Quantification from the EDS spectral images was performed with the Cliff-Lorimer method.[158] EELS data were acquired in STEM mode with a dispersion of 0.100 eV per channel and a pixel acquisition time of 1 s using the Quantum Gatan imaging filter. All of the spectra were acquired on NPs lying on holes of the

TEM grid, to avoid the contribution from the carbon of the grid. For the high-resolution STEM-HAADF tomography, a "cubed" aberration-corrected Thermo Fisher Titan X-Ant-EM operating at 300 kV was utilized to acquire the HAADF-STEM projections. In addition, to study the nearest neighbor distance variation during potential cycles, low-magnification tomography was performed.

The acquisition of the high-resolution tomography of the as-synthesized NPs was performed following a specific methodology to minimize the beam damage. Projections were acquired using a Fischione model 2020 single tilt holder over a tilt range of ±72° with angular increments of 3°. At each tilt, 5 frames were acquired with a 1.5 μs dwell time, while the image resolution was set to 2048x2048 pixels. Next, we used these images as input for a non-rigid registration method in combination with a convolutional neural network (CNN) [159]. The obtained series were aligned using cross-correlation and 3D reconstructions were obtained using the Simultaneous Iterative Reconstruction Technique (SIRT) algorithm, as implemented in Astra Toolbox[101]. This volume was then segmented based on the voxel intensity, to differentiate between the Rh core and the Pt shell. On the other hand, to study the changes of the Rh@Pt/C NPs in 3D at lower magnification, tilt-series between -65° and +65° with angular increments of 5° were acquired with a single tilt holder (Fischione Instruments, Model 2020) using the FEI Tomography software, aligned[102,160] and reconstructed using open source Python libraries. The reconstruction was performed using 100 iterations of SIRT, as implemented in TomoPy[99,161]. The reconstructed volumes were then segmented using the watershed algorithm[160] and visualized with Napari[100]. The nearest neighbor distance was calculated from the location of the central voxel (3D-pixel) in each of the segmented NPs. The relatively big angular increments of 5° during the tilt-series acquisition of the low magnification tomography were chosen as a compromise between the number of projections (resolution of the reconstruction) and electron dose received by the NPs, especially considering that several tilt series of the same region at different potential cycles were acquired.

X-ray diffraction experiments

The XRD experiments were performed on a Rikaku Smartlab 9kw diffractometer, using a micro area optics setup and Cu Kα radiation as an X-ray source. The cycled particles for the XRD experiments were obtained by scratching the cycled Rh@Pt/C-glassy carbon working electrode.

5 Expanding the Potential of Identical Location Scanning Transmission Electron Microscopy for Gas Evolving Reactions

Note: The following chapter is based on the publication "Rh@Pt Electrochemical Stability of Rhodium−Platinum Core−Shell Nanoparticles: An Identical Location Scanning Transmission Electron Microscopy Study", by M. Vega-Paredes, C. Scheu and R. Aymerich Armengol in *ACS Applied Materials and Interfaces* 2023, *15*, 46895-46901. Therefore, the personal pronoun "we" is used throughout this chapter to refer to the group of researchers that were part of this specific study.

After having seen the potential of identical location STEM in determining the degradation mechanisms of fuel cell catalysts in Chapter 4, here we explore how to apply it to gas-evolving reactions like those involved in the production of green H_2.

In general, IL-STEM provides valuable insights into the mechanisms of activity and degradation of nanocatalysts during electrochemical reactions. However, the technique suffers from limitations that hinder its widespread use for nanocatalysts of gas-evolving reactions *e.g.* the hydrogen evolution reaction. The main issue is the production of bubbles that cause the loss of electric contact in the identical location measurements, which is critical for the correct cycling of the nanocatalysts and interpretation of the electron microscopy results. Herein, we systematically evaluate different set-ups, materials and tools to allow the facile and reliable study of the stability of HER nanocatalysts. The optimized conditions are applied for the study of layered rhenium molybdenum disulfide ($Re_{0.2}Mo_{0.8}S_2$) nanocatalysts, a relevant alternative to Pt catalysts for the HER. With our approach, we demonstrate that although the morphology of the $Re_{0.2}Mo_{0.8}S_2$ catalyst is maintained during HER, chemical composition changes could be correlated to the electrochemical reaction. This study unlocks the potential of the IL(S)TEM technique for the construction of structure-property relationships of nanocatalysts of gas-evolving reactions.

5.1 Introduction

IL-(S)TEM is a powerful technique to study the stability of nanocatalysts during electrochemical reactions[162,163]. In IL-(S)TEM, the same region of a TEM specimen is analyzed before and after electrochemical testing. This methodology allows for the direct correlation of the morphological and compositional changes of nanocatalysts to the electrochemical conditions they were subjected to, thus providing insights into the corrosion mechanisms[58,64]

or the nature of the active species[164] down to the atomic scale. When compared to in-situ liquid cell (S)TEM[108], IL-(S)TEM possesses the advantages of higher spatial resolution, longer-term studies of up to several thousands of potential cycles, and reduced electron beam-induced effects, which can produce undesirable side reactions. [37,165]

First introduced by Mayrhofer et al. [110,166], IL-(S)TEM was originally developed for the study of the degradation of fuel cell nanocatalysts, with several studies focusing on the effects of oxygen reduction reaction[167,168] and ramping up/down conditions[58,169] on the nanocatalysts. When applied to such fuel cell nanomaterials, processes like Ostwald ripening, particle detachment, movement, agglomeration and dissolution were identified as corrosion mechanisms[170–172].

However, beyond fuel cell technology, the IL-(S)TEM method has only mildly expanded to other electrochemical application fields, such as batteries[173,174] and water-splitting catalysis. Water-splitting converts water to oxygen and hydrogen gases through the oxygen evolution and the hydrogen evolution reaction, respectively[175–178]. These reactions have recently attracted a lot of interest as a method of obtaining green hydrogen fuel, key for the successful decarbonization of the economy[179,180]. Nevertheless, to date, only a few degradation studies on materials such as Ir-based[181–183], perovskite[164] or Ni/Fe-based[184] OER catalysts have been conducted with IL-(S)TEM. When it comes to HER, even fewer investigations on Pt-based nanoparticles have been reported[111,185].

The reduced number of IL-(S)TEM research on gas evolving reactions can be related to their intrinsic difficulty[37,111]: the bubbles formed on the TEM grids do not easily release, thus blocking their surface and preventing electrical contact with the electrolyte. When the electrical contact is lost, the nanomaterial can no longer catalyze the reaction, and therefore no corrosion mechanisms nor active species can be identified. This problem is especially severe for HER, and existing studies for gas evolving reactions had to resort to the use of expensive modified rotating disk electrodes[185], specialized equipment such as the modified floating electrode[186,187], or keeping an unrealistically low overpotential of 100 mV to avoid energic bubbling[111]. Besides limiting the potential applications of IL-(S)TEM, such pitfalls also jeopardize the correct interpretation of the results of IL-(S)TEM conducted in catalysts with high electrochemical stability, e.g. noble metals or materials such as MoS_2-based nanocatalysts[24], where the absence of structural corrosion could be attributed both to loss of contact due to bubbles and to the

inherent stability of the material. Therefore, it is still necessary to develop a reliable and widely accessible methodology for performing IL-(S)TEM on HER catalysts.

Herein, we explore different IL-(S)TEM methods to enable the study of HER nanocatalysts. From different electrical connections of the TEM grid to the working electrode and materials used for the set-up to the electrochemical conditions, we determine an easy approach for conducting reliable IL-(S)TEM investigation for HER which can be widely implemented due to its simplicity. Moreover, we applied the optimized procedure to investigate the morphological and chemical stability of $Re_{0.2}Mo_{0.8}S_2$ nanocatalyst across electrochemical testing through 4000 cyclic voltammetries conducted in the range from 0 to -0.25 V_{RHE}. We selected $Re_xMo_{1-x}S_2$ nanocatalysts as an ideal case study due to their high activity and stability under HER conditions[188,189], making the correct interpretation of the IL-(S)TEM results especially critical. We found that connecting the grid to the working electrode using tweezers of an inert metal (as opposed to the typically used glassy carbon electrode) is a reliable, reproducible and easy-to-implement method that can be widely adapted by the community, unlocking the huge potential of IL-STEM to the water splitting field, were the stability of the catalysts is yet the bottleneck for the practical application of acid electrolyzers.

5.2 Results and Discussion

Technique development

To enable electrochemistry on a TEM finder grid it has to be connected as the working electrode. The electrical contact is usually ensured by fixing the grid on a glassy carbon rod electrode with a Teflon cap with a hole to ensure electrolyte-grid contact[58] (**Figure 5-1a**). Alternatively, the TEM grid can also be connected with through a wire[133] or tweezers[136] of an inert material in the conditions of study (**Figure 5-1b,c**).

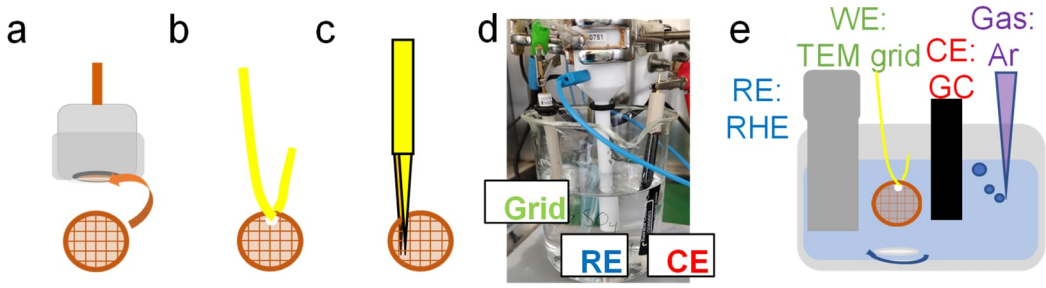

***Figure 5-1**. Scheme of the methods for connecting a TEM finder grid as a working electrode. (a) glassy carbon rod and a Teflon cap, (b) a conducting wire and (c) tweezers. Experimental (d) and schematic (e) set-up used for the IL experiments. RE is the reference electrode, CE is the counter electrode and WE is the working electrode.*

To systematically compare the performance of these methods for the study of HER, 20 cyclic voltammetries were performed with Au/C grids containing $Re_{0.2}Mo_{0.8}S_2$ nanocatalysts at 10 mV/s of scan rate from 0 to -0.3 V_{RHE} (**Figure 5-2**). To prevent current loss derived from particle detachment, the grid was loaded with an ink of the active $Re_{0.2}Mo_{0.8}S_2$ nanomaterial and Nafion. As blank measurements, CVs with an unloaded Au grid and without a grid were also acquired for each method.

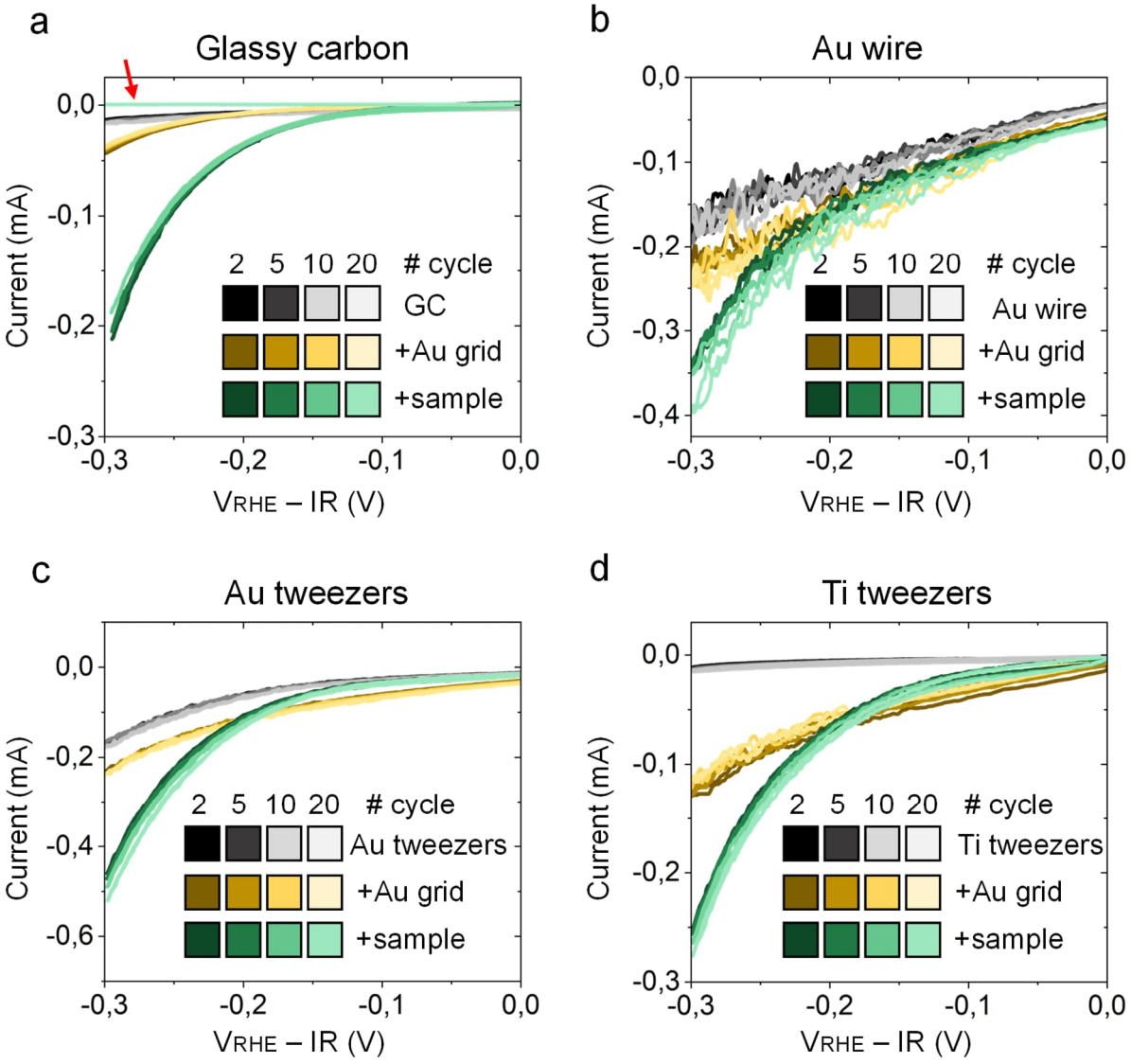

***Figure 5-2**. Comparison of the different methods of electrical contact of the TEM grids for IL-(S)TEM, (a) glassy carbon, (b) Au wire, (c) Au tweezers and (d) Ti tweezers. The potential was cycled from 0 to -0.3 V_{RHE} at a scan rate of 10 mV/s.*

The electrochemical results when using the glassy carbon rod electrode in **Figure 5-2a** show that the bare glassy carbon rod has a low current intensity in the potential range analyzed, which is increased when attaching an Au TEM grid confirming the electrical contact. Loading the

TEM grid with $Re_{0.2}Mo_{0.8}S_2$ nanocatalyst resulted in a larger HER current. However, the electrical contact is reduced until being completely lost during HER, as evidenced by the current drop even below the GC baseline in the 20th CV (**Figure 5-2a**, red arrow). Specifically, the drop of current occurred at the 16th CV (**Figure 5-3**).

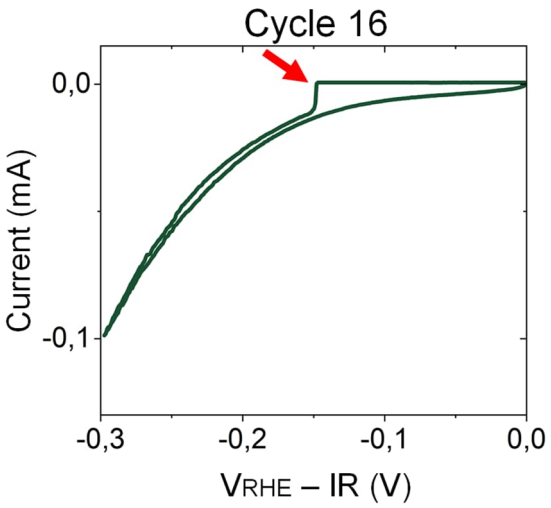

***Figure 5-3**. Loss of electrical contact in the 16th CV when cycling the sample using a glassy carbon rod electrode and Teflon cap for electrical contact and cycling from 0 to -0.3 V_{RHE} at 10 mV/s.*

The loss of contact is explained by the evolution of hydrogen gas from the $Re_{0.2}Mo_{0.8}S_2$ nanocatalyst on the TEM grid. Unable to completely detach from the interface between the grid and the Teflon cap, the hydrogen bubbles grow, eventually covering completely the hole of the Teflon cap that provides contact of the electrolyte with the glassy carbon and TEM grid (see schematic in **Figure 5-4**).

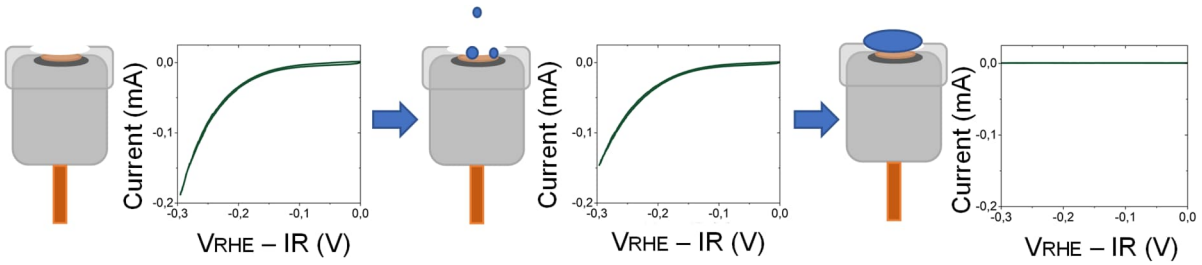

***Figure 5-4**. Mechanism of loss of electric contact due to gas evolution occurring when using the glassy carbon rod electrode and a Teflon cap.*

The experiment was also performed with a higher scan rate of 100 mV/s to account for milder gas evolution conditions, yet the contact was also lost by the 40th CV (**Figure 5-5**). Thus, the

typical IL-(S)TEM approach using glassy carbon rod electrodes proved unsuitable for the study of HER catalysts.

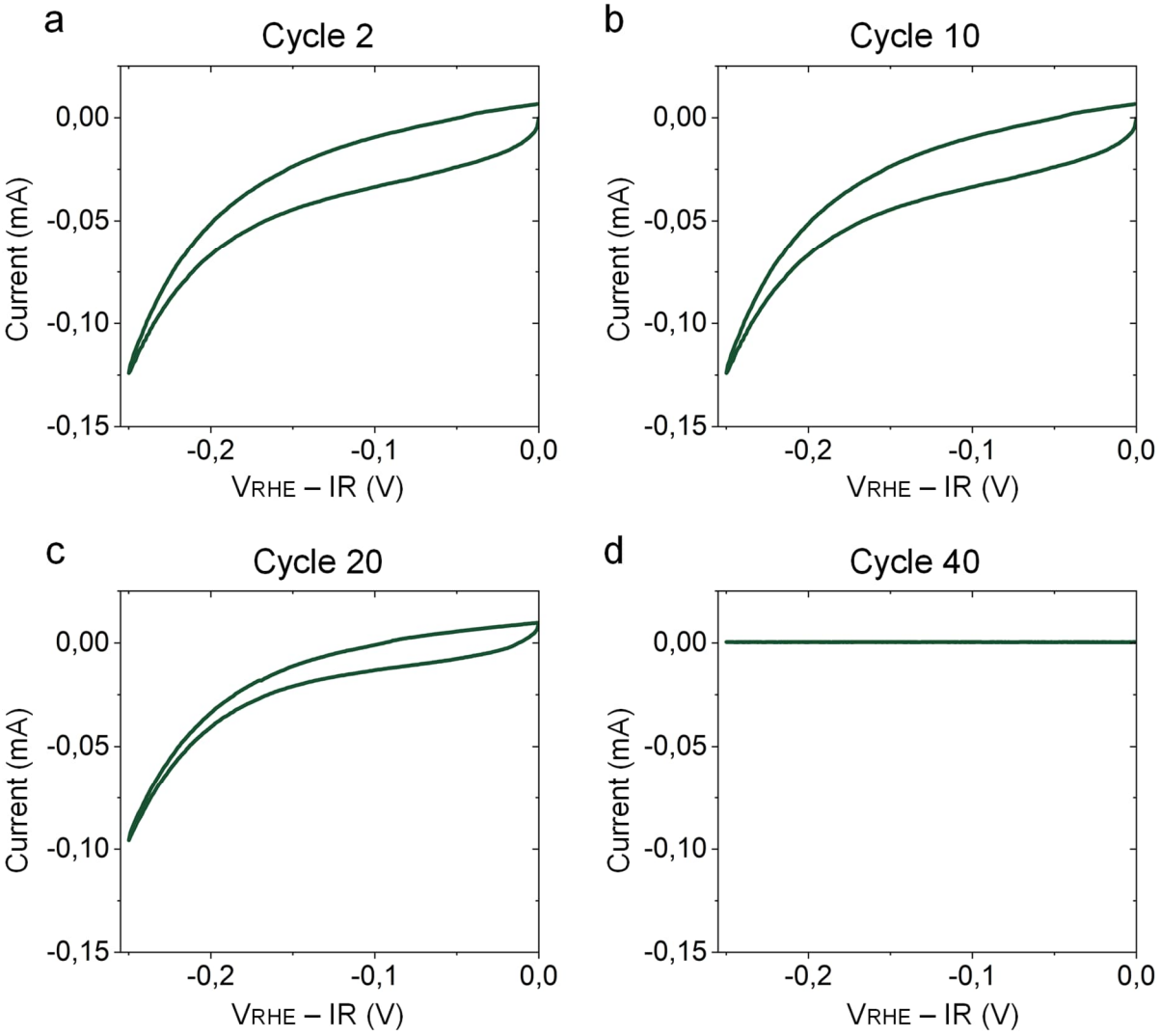

***Figure 5-5**. (a-d) Progressive loss of electrical contact when cycling the sample using the glassy carbon rod electrode with Teflon cap cycling from 0 to -0.25 V_{RHE} at 100 mV/s. At the 40th cycle, there is no more measurable current due to the loss of electric contact derived from bubbles.*

The use of a metallic wire as a method of electric contact (**Figure 5-1b**), in which the grid is pierced with the wire to mount it, was tested next using an Au wire. Despite minimizing the area of gold exposed from the wire by covering part of the surface with Teflon tape, the baseline current derived from the Au wire had higher intensity (**Figure 5-2b**). This is detrimental for the IL-(S)TEM measurements, as the current passing through the sample becomes very sensitive to the area of exposed Au from the wire, affecting both the stability of the nanocatalysts and the reproducibility of the measurement (**Figure 5-6**).

5. Identical location for gas evolving reactions

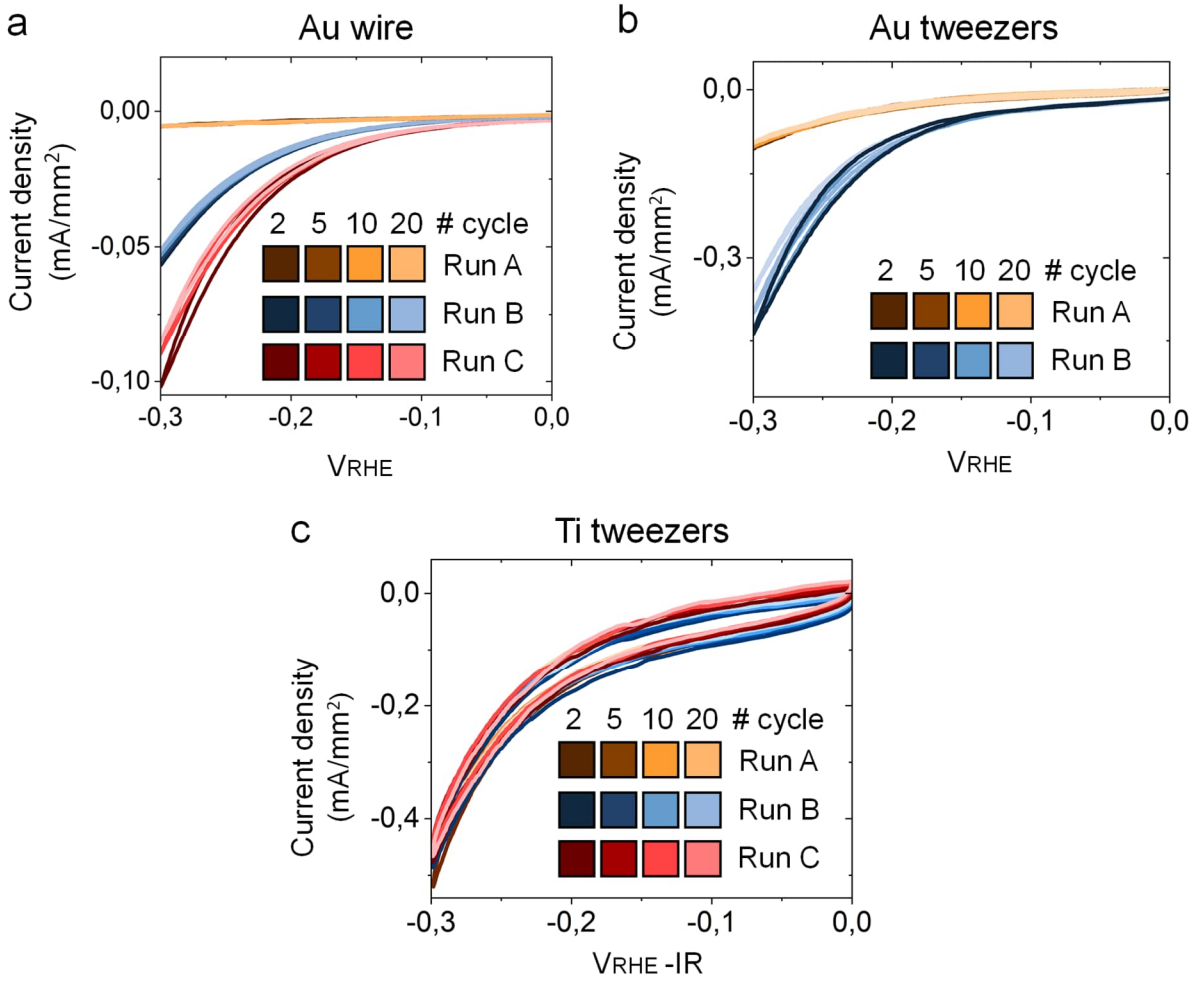

***Figure 5-6**. Different replicate runs of CVs were performed on $Re_{0.2}Mo_{0.8}S_2$ nanocatalysts loaded on the Au TEM grid using (a) the Au wire, (b) the Au tweezers and (c) the Ti tweezers method. The electrochemical measurements were performed at a scan rate of 100 mV/s.*

Nevertheless, with this method, the contact with the TEM grid with and without $Re_{0.2}Mo_{0.8}S_2$ nanocatalyst was still confirmed in the form of a current increase. During the 20 CVs of the test, no loss of electric contact was observed, which can be attributed to the comparatively larger area of the TEM grid exposed to the electrolyte, promoting bubbles release to the electrolyte. However, this method of electrical contact produced noisy electrochemical data due to the movement of the gold wire and the grid itself in the stirred electrolyte, as well as the stronger bubbling of hydrogen from the gold wire surface. Such bubbles were observed along the wire and distributed all across the grid surface, but especially on the interface of the Au wire and TEM grid (see schematic in **Figure 5-7**).

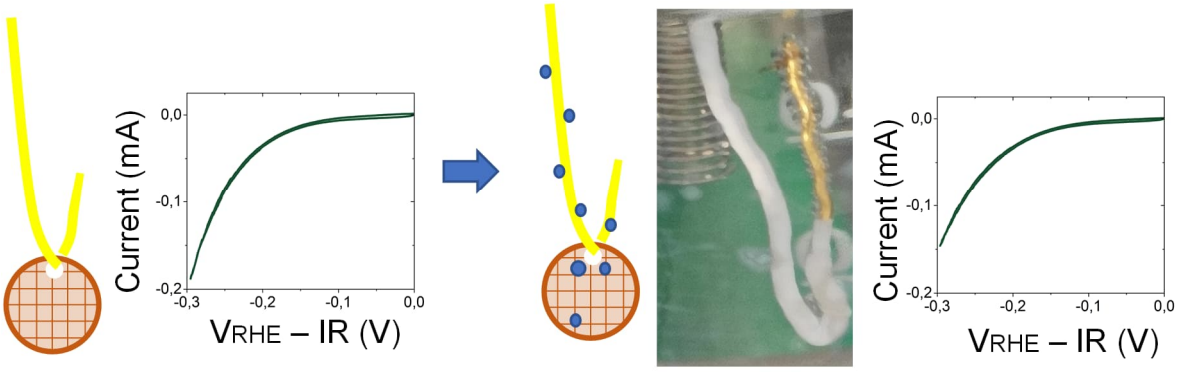

***Figure 5-7**. Schematic showing loss of current mechanism by the growth of bubbles on the TEM grid and Au wire.*

The uncontrolled build-up of bubbles across the TEM specimen surface prevents the correct interpretation of the IL-(S)TEM data, since there is no guarantee of electrical contact with the electrolyte in the areas of analysis during the electrochemical experiment. Similar results in terms of bubble build-up and data noisiness were obtained despite the attempt to lower the background current with a wire material with a lower current such as W (**Figure 5-8a**). Using a Ti wire also produced data noisiness (**Figure 5-8b**). Due to these issues and to the fact that the wire method of contact also compromises the structural integrity of the TEM grid as a hole needs to be made on it, an alternative method was pursued.

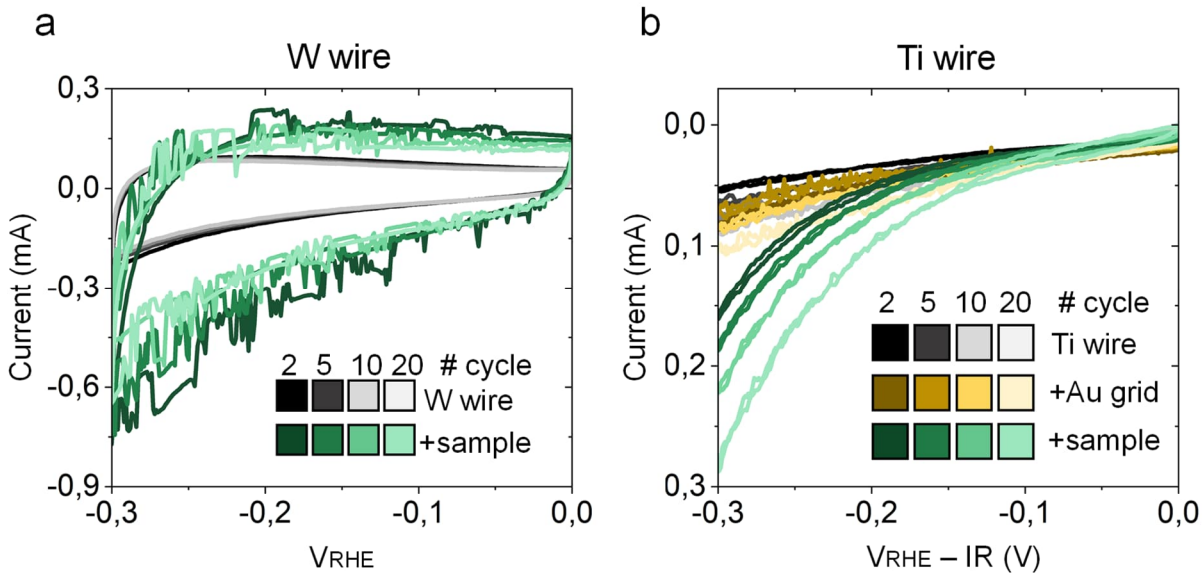

***Figure 5-8**. CV from 0 to -0.3V at 100 mV/s using a (a) W wire and (b) Ti wire. Notice that the Ti wire suffers from a clear surface activation process.*

Finally, metallic tweezers were used as electric contact for the TEM specimen. **Figure 5-2c** and **Figure 5-2d** show the CV results using Au and Ti tweezers, respectively. Compared to the metallic wire method, the electrochemical data acquired with tweezers is less noisy, which can

be attributed to the improved fixation of the grid from one side by the tweezers. Furthermore, the bubbles are also easily detached from the surface of the grid due to the mild movement that the fixation still allows, and only a few of them are stuck exclusively at the interface between the tweezers and the grid (**Figure 5-9**).

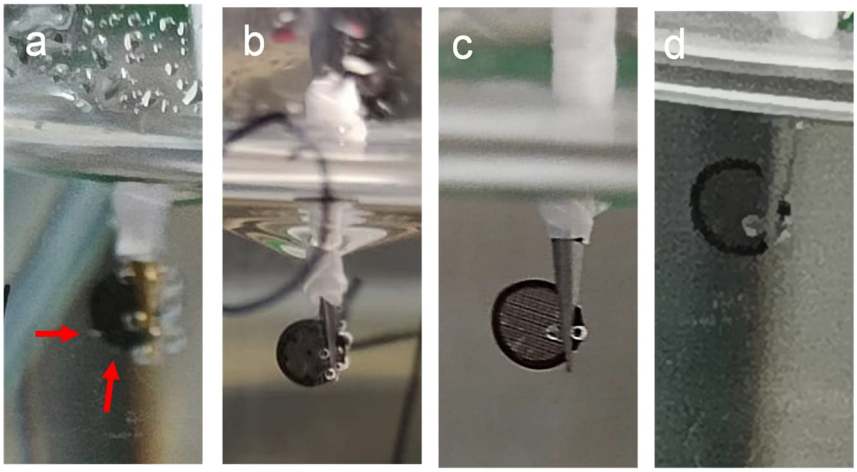

Figure 5-9. *Gas evolution on the TEM grid when cycling from 0 to -0.3 V vs. RHE using (a) Au tweezers, 1 mV/s of scan rate, cycle 20 (b) Ti tweezers, 1 mV/s of scan rate, cycle 20. Gas evolution on the TEM grid when cycling from 0 to -0.25 V vs. RHE using (c) Ti tweezers, 100 mV/s of scan rate, cycle 1000 (d) Ti tweezers, 100 mV/s of scan rate, cycle 4000. The TEM grid diameter is 3 mm. Notice that bubbling in the Au tweezers set-up is stronger and the bubbles are distributed all over the grid surface, while in the Ti tweezers approach, only a few bubbles stay exclusively at the tweezer-grid interface.*

Thus, the (S)TEM can be conducted and interpreted as long as the areas of analysis are taken on the opposite side of the grid.

Since the Au tweezers showed less reproducibility on the current response among replicates than Ti tweezers (**Figure 5-6b, c**), the latter was the method of choice for reliable IL-(S)TEM for HER. The lower reproducibility of the Au tweezers was attributed to the higher HER activity of Au compared to Ti. Since Au has higher HER activity, small changes in the area of tweezers submerged will have a noticeable impact on the overall HER current

Similar results were found when increasing the scan rate to 100 mV/s (**Figure 5-10**), evidencing the versatility of the tweezers method.

5. Identical location for gas evolving reactions

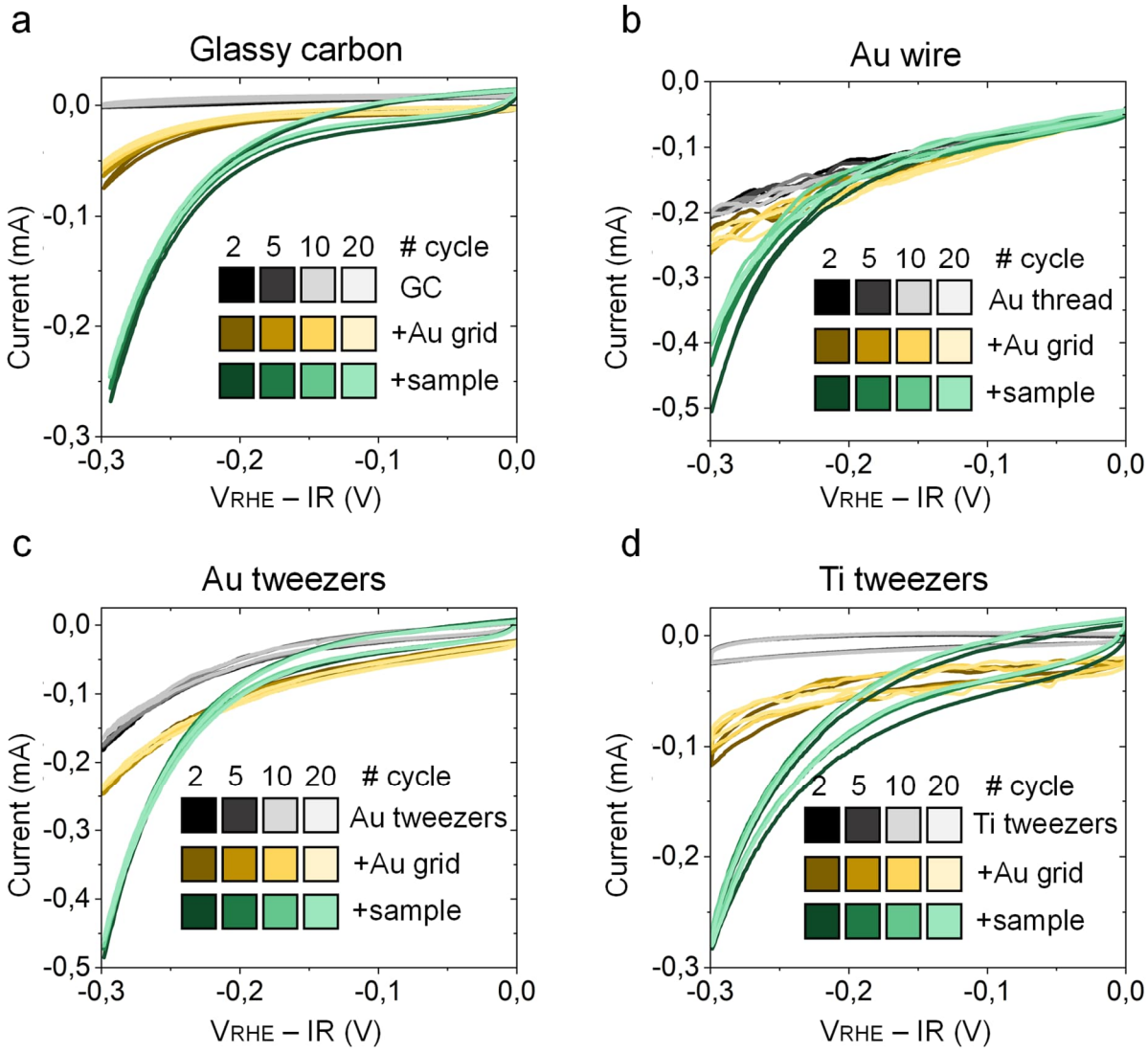

***Figure 5-10**. Comparison of the different methods of electrical connection of the TEM grids for IL-(S)TEM at 100 mV/s, (a) Glassy carbon rod electrode, (b) Au wire, (c) Au tweezers and (d) Ti tweezers. The potential was cycled from 0 to -0.3 V vs. RHE for 20 cycles.*

IL-STEM on $Re_{0.2}Mo_{0.8}S_2$ nanocatalysts

Before conducting IL-STEM measurements, 4000 CVs were conducted from 0 to -0.25 V_{RHE} on a $Re_{0.2}Mo_{0.8}S_2$ electrode grown on a carbon paper substrate ($Re_{0.2}Mo_{0.8}S_2$/CP). Scanning electron microscopy (SEM) images of the electrode are given in **Figure 5-11**, showing a homogeneous coating of the CP substrate by the $Re_{0.2}Mo_{0.8}S_2$ nanostructures.

The results of the CV measurements on this electrode are provided in **Figure 5-12a**. The results demonstrate that the reaction overpotential did not suffer any detectable changes, which showcases the high electrochemical stability retained by this material.

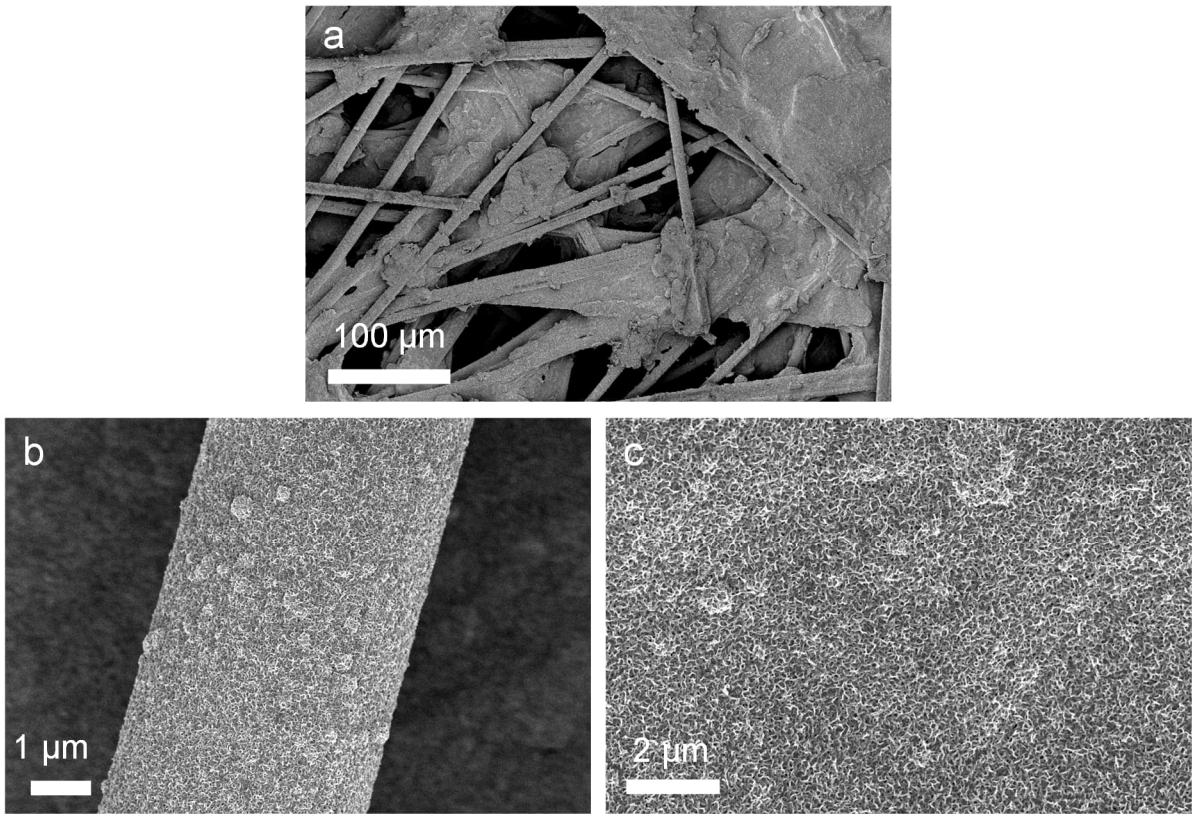

Figure 5-11. *SEM micrographs showing the surface of $Re_{0.2}Mo_{0.8}S_2$/CP electrode. (a) Overview showing fibers and flat area. (b) Detail of a CP fiber covered with the $Re_{0.2}Mo_{0.8}S_2$ nanoflowers layer. (c) Detail of a CP flat area covered with the $Re_{0.2}Mo_{0.8}S_2$ nanoflowers.*

To understand whether the morphology was equally maintained stable or whether some changes and/or degradation occurred, the 4000 CVs were subsequently performed in an IL-STEM set-up using the Ti tweezers to establish the electric contact (**Figure 5-12b**).

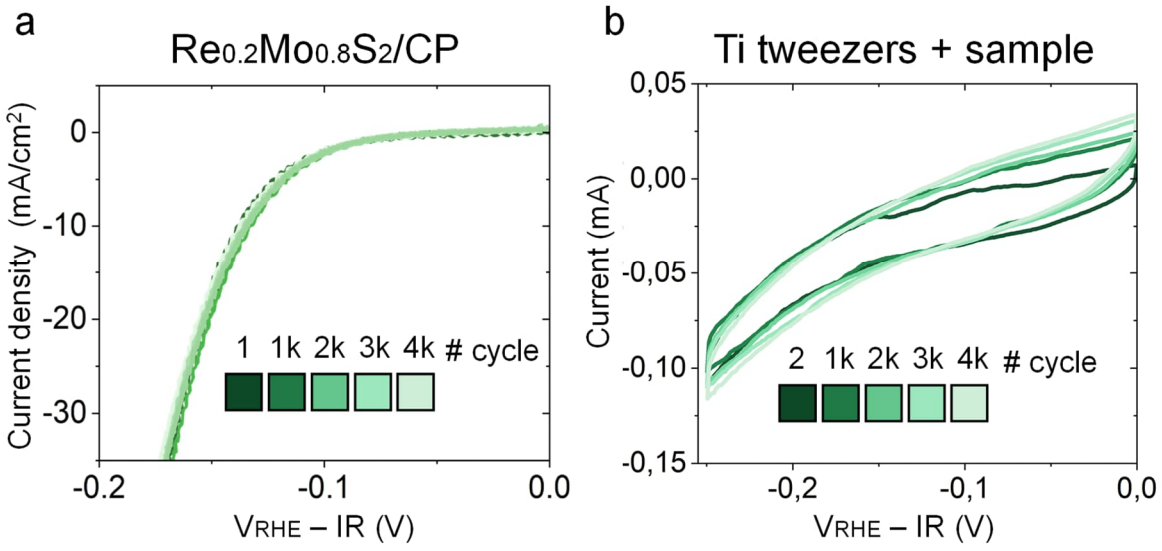

Figure 5-12. *4000 CVs of $Re_{0.2}Mo_{0.8}S_2$ acquired from 0 to −0.25 V_{RHE} (a) $Re_{0.2}Mo_{0.8}S_2$/CP electrode. (b) $Re_{0.2}Mo_{0.8}S_2$/Au/C TEM grid, acquired with Ti tweezers.*

The current was maintained fairly stable across the 4000 CVs measured, with a small increase possibly derived from the activation of the Ti tweezers. An increase of the same order of magnitude is observed in the current of the 4000 CV for the Ti tweezers without any sample, confirming its origin in the tweezers themselves (**Figure 5-12**, **Figure 5-13**). This increase may be related to an activation of the Ti metal surface, which is passivated at air conditions. Despite the Ti being stable against corrosion at diluted sulfuric acid conditions, we hypothesize that such acid conditions summed to the reducing potential conditions of the HER regime may affect such passivation layer, leading to an increase of current.

The only bubbles observed after the 4000 CVs on the IL-STEM grid were exclusively localized on the grid-tweezer interface, far from the areas where the STEM analyses were conducted (**Figure 5-9**), which is key for a reliable interpretation of the results.

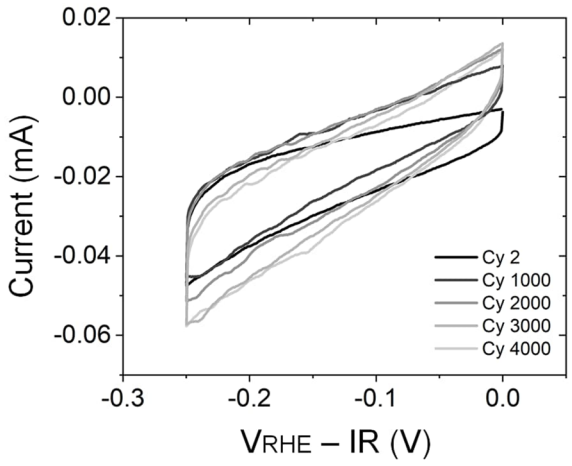

***Figure 5-13**. 4000 CV performed on the Ti tweezers from 0 to -0.25 V_{RHE} at a scan rate of 100 mV/s. Notice that there is an increase of current that stabilizes after 3000 CV of value ~0.01 mA.*

Figure 5-14 shows the morphological evolution of the $Re_{0.2}Mo_{0.8}S_2$ nanomaterials during electrocatalysis. These catalysts possess a nanoflower structure made up of few-layered nanosheets assembled in a porous 3D structure. Such morphology is maintained down to the nanometric scale without visible changes after the 4000 CVs. These results are consistent with the high stability observed in the electrochemical measurements (**Figure 5-12**). However, in a few areas at the edges of the nanoflowers, some redistributed material was observed (**Figure 5-14d**) as a result of the electrochemical cycling.

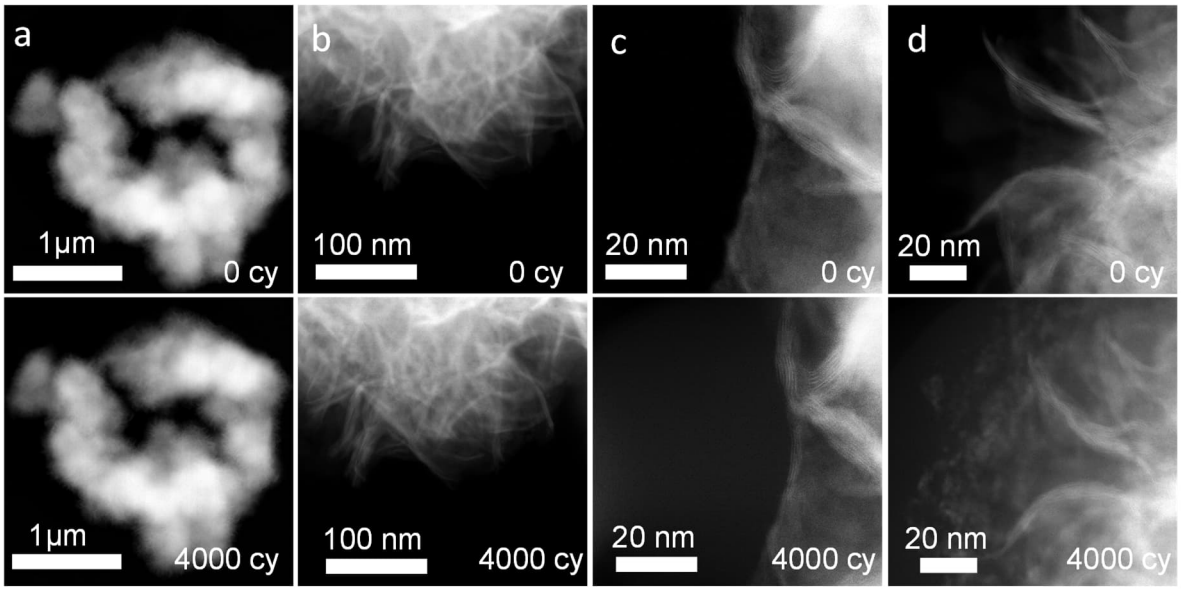

***Figure 5-14**. (a-d) Different areas imaged in identical location conditions before and after 4000 CVs showing the morphology evolution of $Re_{0.2}Mo_{0.8}S_2$ nanocatalyst.*

EDS measurements were performed in such areas to understand the composition of the appeared layer of material. The measurements (**Figure 5-15**) revealed that the redistributed material on the edges of $Re_{0.2}Mo_{0.8}S_2$ nanoflowers is exclusively composed of carbon, oxygen, and fluorine, matching the composition of the Nafion binder used for the $Re_{0.2}Mo_{0.8}S_2$ ink drop cast on the TEM specimen. This partial redistribution of the Nafion did not hinder the morphology comparison among cycles and further confirmed the successful electrochemical cycling conducted on the grid. A similar Nafion degradation after cycling was observed in an area not previously imaged, ruling out a possible electron beam-induced effect.

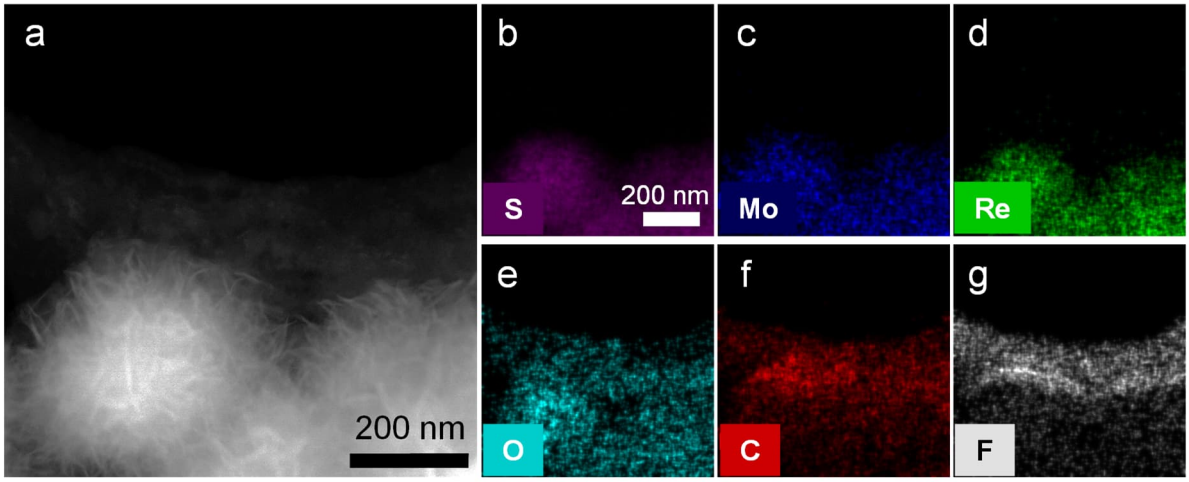

***Figure 5-15**. (a) HAADF-STEM image and corresponding EDS elemental maps (b-g) of an area with Nafion attached to the edge of the $Re_{0.2}Mo_{0.8}S_2$ nanocatalyst.*

5. Identical location for gas evolving reactions

In addition to the morphology analyses, EDS studies were also conducted in IL-STEM to track changes in the chemical composition of the nanocatalyst (**Figure 5-16**). **Figure 5-16d** shows the evolution of the oxygen content normalized by the sulfur in several IL-STEM areas (Normalized O at.% = 100(at. % O/(at.%O + at.%S)). To avoid the contribution of the oxygen content of the carbon layer of the TEM grid, the quantifications were performed in nanoflowers exposed to the vacuum of a hole in the TEM grid. The results show that the oxygen content dropped in most of the nanoflowers analyzed, with an average decrease of 6 at. %. This is also observed when in the EDS maps, which show a lower oxygen content with respect to sulfur despite maintaining the morphology of the nanoflower assembly (**Figure 5-16a, b**). The initial oxygen content on the fresh material is related to the molybdenum precursor and the temperature used during the hydrothermal synthesis. Previous reports demonstrated that below 220°C, this synthesis yields MoS_2 with a percentage of Mo-O bonds stemming from unreacted molybdenum precursor[190,191]. Such oxygen leads to an enhanced HER performance due to improved conductivity derived from a narrower band gap[190]. Our IL-STEM investigation indicates that the reduction conditions at which the $Re_{0.2}Mo_{0.8}S_2$ nanoflowers were subjected to evolve hydrogen lead to the reduction of this oxygen content.

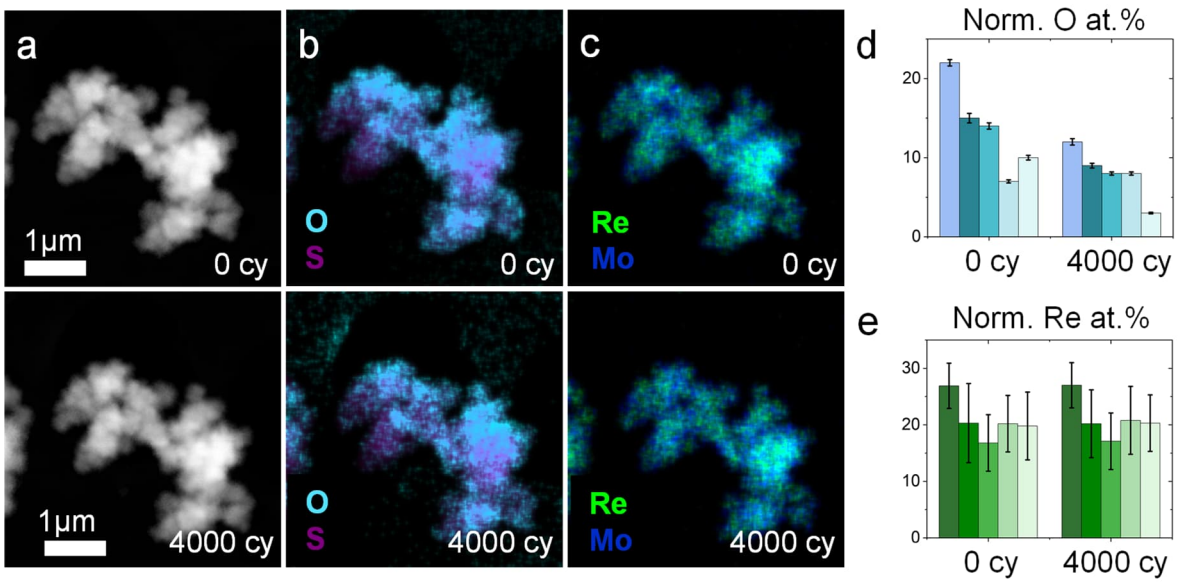

***Figure 5-16**. Composition changes during IL-STEM analyzed by EDS. (a) HAADF-STEM image and corresponding composition maps showing the distribution of (b) oxygen and sulfur and (c) rhenium and molybdenum before and after 4000 CVs. Evolution of the normalized oxygen (d) and rhenium (e) content during 4000 CV in different IL-STEM areas.*

However, in the span of 4000 cycles, this decrease did not affect the HER activity of the $Re_{0.2}Mo_{0.8}S_2$ nanocatalyst, which is mainly boosted by the rhenium content. As such, the stability of the Re is crucial for the long-term maintenance of the catalytical performance[46,188]. Thus, the normalized Re at.% (normalized Re at.% = 100(Re at.%/(Re at.% + Mo at.%)) was also compared in IL-STEM by EDS. Contrary to the oxygen content, the Re content was maintained stable in all areas of analysis (**Figure 5-16c, e**) with an average of 21 at.% Re at cycles 0 and 4000, which explains the excellent stability of the $Re_{0.2}Mo_{0.8}S_2$ activity for HER shown in **Figure 5-12**.

Overall, the IL-STEM results of the $Re_{0.2}Mo_{0.8}S_2$ indicate high electrochemical stability and confirm that the tweezers method of electrical connection of the TEM grid in IL-STEM set-up is suitable for the analysis of HER nanocatalysts, opening the door for a simple to implement, reliable and reproducible method for unlocking the potential of IL-(S)TEM on gas evolving systems, which can contribute on the development of the next generation of electrocatalysts for such reactions.

5.3 Conclusions

Different IL-(S)TEM set-ups, namely the use of glassy carbon rod and Teflon cap, metallic wires and metallic tweezers, were tested and compared for the study of HER nanocatalysts. The use of metallic tweezers proved to be the only easy and reliable approach to perform IL-(S)TEM measurements for gas-evolving reactions. With this approach, the stability of $Re_{0.2}Mo_{0.8}S_2$ nanocatalysts was successfully analyzed by means of 4000 potential cycles until -0.25 V_{RHE}, which are realistic and common conditions for the study of the stability of HER catalysts. The IL-(S)TEM microscopy results confirmed excellent retention of the layered nanoflower morphology of the nanocatalyst and the Re and Mo stoichiometric ratio was maintained stable. Nevertheless, the presence of oxygen stemming from the synthesis precursors, which has been related to enhanced performance on MoS_2-based nanocatalysts, was observed to decrease as a result of the electrochemical test. The approach to achieve reliable electrical contact can be directly applied to stability studies of other nanocatalysts and gas-evolving reactions, unlocking the potential of the IL-(S)TEM to other areas of research where the stability of the catalysts is still the bottleneck.

5. Identical location for gas evolving reactions

5.4 Experimental section

Materials

Sulfuric acid (H_2SO_4, Suprapur, Sigma-Aldrich) and deionized water (0.055 S/cm^2) were used as electrolyte for electrochemical measurements. Ammonium heptamolybdate tetrahydrate, ($(NH_4)_6Mo_7O_{24}\cdot 4H_2O$, 99.98%, ammonium perrhenate (NH_4ReO_4, >99%, Merck), Sigma-Aldrich), thiourea ($SC(NH_2)_2$, >99.0%, Sigma-Aldrich) and ethanol (EtOH, >99.8, Carl Roth) were used for the synthesis of $Re_{0.2}Mo_{0.8}S_2$ nanoflowers. Nafion (5 wt.% in a mixture of alcohols and water, Sigma-Aldrich) and isopropanol (iProp, 99.9%, Schmitz) were used to prepare an ink to drop cast on the TEM grids. Hydrophilic carbon paper (CP, HCP030N, Hesen) substrates were used to synthesize $Re_{0.2}Mo_{0.8}S_2$/CP electrodes.

Synthesis

$Re_{0.2}Mo_{0.8}S_2$ nanoflowers were synthesized with a hydrothermal approach[192]. 10 ml of a solution containing 0.99 g of $(NH_4)_6Mo_7O_{24}\cdot 4H_2O$, 2.28 g of $SC(NH_2)_2$ and 0.38 g of NH_4ReO_4 was heated for 20 h at 200 °C inside an autoclave. After cooling down to room temperature, the black product was cleaned by centrifugation-redispersion cycles in water and ethanol. Finally, the suspension was dried at 110°C and the powder was ground in an agate mortar.

To prepare $Re_{0.2}Mo_{0.8}S_2$/CP electrodes the hydrothermal synthesis was modified diluting 2700 times the concentration of the precursor solution and two carbon paper substrates of a size of 2 cm x 1 cm were included in the autoclave for heat treatment, with an area of 1 cm^2 covered with Teflon tape. No nanoflowers grew on such a covered corner of the electrode, which was later used for making the electric connection with the potentiostat.

Electrochemical measurements

The IL(S)TEM electrochemical measurements were performed in a three-electrode set-up with a Gamry Reference600 potentiostat using a RHE (Gaskatel) as a reference and a glassy carbon rod (6/60 mm, Redoxme) as the counter electrode. Holey carbon gold TEM finder grids (Plano) were used as the working electrode. The working electrode connection was secured either with a glassy carbon electrode (3 mm electrode size, BioLogic), an Au wire (0.6 mm diameter, >99.99%, Redoxme), a Ti wire (0.5 mm, 99.99%, Thermofisher), reverted Au tweezers (Plano) or reverted Ti tweezers (Plano). The active surface area in contact with the electrolyte was limited using Teflon tape to wrap the Au wire and Au/Ti tweezers in order to control the background current and effectively estimate the surface of the working electrode for

normalization of the current. All measurements were performed in 0.5 M H_2SO_4 degassed with Ar while stirring. Ohmic drop correction was applied to all measurements before plotting.

The electrochemical measurements on the $Re_{0.2}Mo_{0.8}S_2$/CP electrode were conducted on an H-cell separated with a Nafion membrane. The reference electrode was an RHE and a GC rod was used as counter, while the electrolyte (0.5 M H_2SO_4) was degassed with Ar and continuously stirred. 4000 CVs were conducted at a scan rate of 100 mV/s from 0 to -0.25 V vs. RHE, and every 1000 cycles a slow CV at a scan rate of 1 mV/s was acquired. The potentiostat used was a Metrohm PGSTAT-204. Ohmic drop correction was applied to all measurements before plotting to ensure a fair comparison of the different electric contact methodologies.

Electron microscopy measurements

To prepare the TEM grids, an ink containing 5 mg of $Re_{0.2}Mo_{0.8}S_2$ catalyst powder and 10 µL of a Nafion solution in 2 mL of isopropanol was prepared from which 30 µL were drop cast.

The STEM measurements were conducted at 300 kV acceleration voltage in a Titan Themis 60-300 from Thermofisher equipped with a probe aberration corrector. The EDS was performed using the Bruker Super X-EDS detector of the instrument. The SEM measurements were conducted in a ZEISS Gemini microscope with an in-lens secondary electron detector.

6 Fe-Incorporation in Ruddlesden-Popper Faults for Enhanced Oxygen Evolution in $LaNiO_3$ Perovskites

Note: The following Chapter is based on the publication "Fe-incorporation in Ruddlesden-Popper faults for enhanced oxygen evolution in $LaNiO_3$ perovskites", by M. Vega-Paredes et al., currently under preparation. Therefore, the personal pronoun "we" is used throughout this chapter to refer to the group of researchers that were part of this specific study.

Having found that the tweezers method enables the performance of IL-STEM experiments on gas-evolving reactions, we apply it to the study of perovskite oxide catalysts for the oxygen evolution reaction, which are key for the production of green hydrogen.

Perovskite oxides are an important class of catalysts for alkaline oxygen evolution. Strategies for enhancing their catalytic activity include adding Fe traces to the electrolyte and modifying the atomic structure locally by introducing defects such as Ruddlesden-Popper (RP) planar faults. However, how trace amounts of Fe in the electrolyte affect the structure of the active RP faults remains unexplored. Here, we study the local structural changes of RP-rich $LaNiO_3$ perovskites during oxygen evolution when Fe traces are intentionally added to the electrolyte. We demonstrate that Fe incorporates into the RP faults, causing them to expand. As a consequence, compressive strain gets induced into neighboring $LaNiO_3$ layers, which has been shown to boost the catalytic activity of $LaNiO_3$. Our results provide new mechanistic insights into how to increase the oxygen evolution activity of perovskite oxide materials.

6.1 Introduction

The oxygen evolution reaction is a key electrochemical process that limits the performance of water electrolyzers and metal-air batteries due to the sluggish kinetics of the four-electron transfer process.[193,194] In acidic media, iridium and ruthenium-based oxides have been shown to possess the best OER performance, both in terms of activity and stability.[195,196] Nonetheless, the high cost and scarcity of noble metals Ir and Ru have driven the search for alternative, non-precious metal-based OER catalysts, among which transition metal oxides have emerged as promising candidates due to their relatively high activity and stability under alkaline conditions.[5,197]

In particular, perovskite oxide materials, of the general form ABO_3, have garnered much attention.[198–200] The A-site is typically occupied by rare-earth or alkaline metals, while a transition metal fills the B-site[201,202] Complete or partial substitution of A or B-site cations

offers perovskite oxides a high composition tunability, which allows for the optimization of their geometric and electronic structures, and therefore their OER activity.[198–200]

Nonetheless, the elevated number of possible perovskite oxides has highlighted the importance of developing mechanistic insights that drive the rational design of better-performing OER catalysts.[200] Mechanistic structural insights are especially relevant when considering that doping the oxide lattice by adding "impurities" to the electrolyte has emerged as a promising strategy for enhancing their OER activity,[203–205] further increasing the number of potential perovskite structures. One work that nicely showcased the value of deciphering the structural origin of the OER activity in perovskite oxides was performed by Lopes et al.[164] They proved that the catalytic activity of $La_{1-x}Sr_xCoO_3$ perovskites was enhanced by traces amount of Fe impurities present in the potassium hydroxide (KOH) electrolyte due to the formation of a Fe-rich, Co hydr(oxy)oxide surface layer which contains dynamically stable active sites.[164] These insights could be later extended to other perovskite material systems such as $LaNiO_3$[48], $PrNiO_3$[23], $NdNiO_3$[23], $LaNi_xFe_{1-x}O_3$[206], or $La_{0.6}Ca_{0.4}Fe_{0.7}Ni_{0.3}O_3$[207] that showed similar OER activity enhancement in the presence of elemental traces in the electrolyte.

Besides Fe impurity doping, the OER activity of perovskite oxides can be alternatively enhanced by modifying their local atomic arrangement. Generating strain[208], oxygen octahedra distortions[209] or point defects such as oxygen[30] or cation[31] vacancies have been reported to be effective strategies for boosting water oxidation. Similarly, the OER activity of perovskite oxides can be increased by introducing Ruddlesden-Popper planar faults into the crystal structure.[210,211] These two-dimensional defects comprise [AO] monolayers intergrown in the perovskite ABO_3 lattice.[212] In perovskites such as $LaNiO_3$, the [LaO] layer has a net +1 charge (since La is formally +3), resulting in local distortions of the oxygen octahedra for screening the charge and higher OER activity in RP-rich $LaNiO_3$ samples.[210,212]

Despite the success of the existing strategies for boosting the OER activity of perovskite oxides, several key questions remain unanswered. In particular, it is unknown how trace amounts of Fe in the electrolyte affect the structure of the active RP faults. That is especially critical to answer since the Fe-induced OER enhancement is highly influenced by the atomic arrangement [23] and Fe traces are commonly found in commercial alkaline solutions.[204,213,214]

Here, we report on the effects of trace amounts of Fe added to the alkaline electrolyte on RP faults present in $LaNiO_3$ perovskite nanoparticles. We found that Fe atoms diffuse into the RP faults during catalysis, increasing the interplanar distances within the RP fault layers. As a

consequence, neighboring $LaNiO_3$ layers contract, reducing their interlayer distance and locally inducing compressive strain on the $LaNiO_3$ lattice. Such distortion of the lattice has been shown to modify the density of states on the surface of $LaNiO_3$, boosting its catalytic activity. Our results reveal a new OER activity enhancement mechanism that can be exploited for the rational design of more active perovskite oxides.

6.2 Results and discussion

Initial characterization of $LaNiO_3$ nanoparticles

$LaNiO_3$ nanoparticles were synthesized by a solution combustion method followed by a calcination step.[48,215] Bright field-scanning transmission electron microscopy micrographs (**Figure 6-1a**) show the presence of numerous planar defects in the $LaNiO_3$ perovskite structure. These 2D defects propagate across the particle to its surface, where they form a line defect that can interact with the reactant molecules.

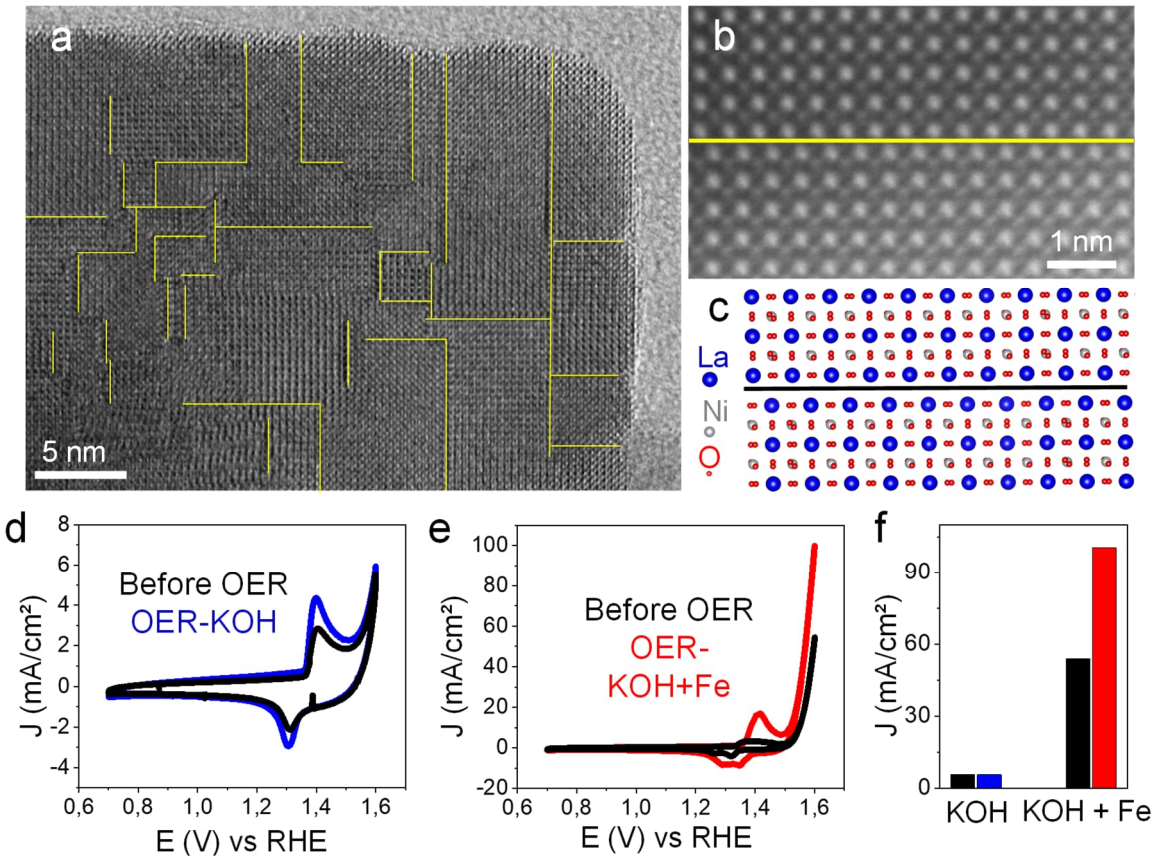

***Figure 6-1**. Structural and electrochemical characterization of $LaNiO_3$ nanoparticles. (a) BF-STEM micrograph of a $LaNiO_3$ nanoparticle. Defects found in the structure are marked with yellow lines. (b) High-resolution HAADF-STEM image of an RP fault. (c) Atomic arrangement of La (blue), Ni (gray), and O (red) atoms in the fault region. The RP fault is formed by the intercalation of [LaO] layers in the perovskite structure. (d) CVs in Fe-free KOH. (e) CVs in KOH with added Fe traces. (f) Comparison of current densities at 1.6 V_{RHE}.*

High-resolution STEM images of the defects (**Figure 6-1b, Figure 6-2**) reveal that they are RP faults, formed by [LaO] layers intergrown in the perovskite $LaNiO_3$ structure (**Figure 6-1c**).[216,217]

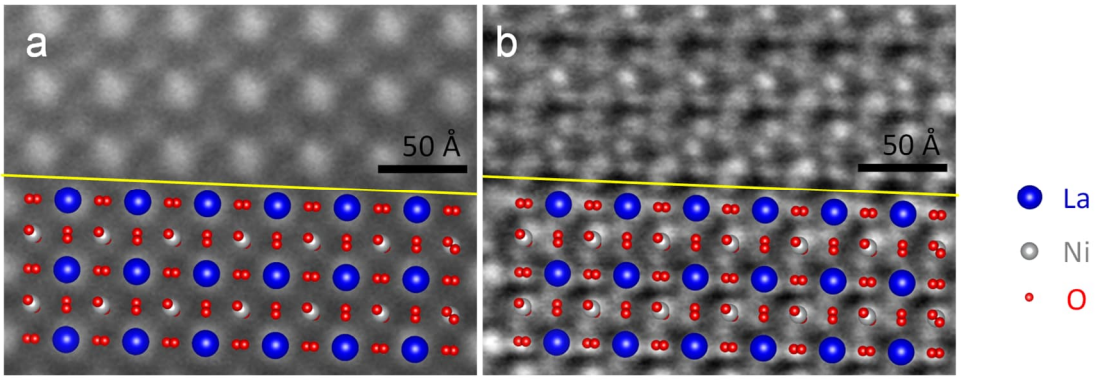

***Figure 6-2**. High-resolution HAADF (a) and BF (b) micrographs of an RP fault, with the corresponding atomic arrangement overlapped.*

The Fe-dependent OER activity was studied by performing cyclic voltammetry experiments in purified KOH (**Figure 6-1d**) and in KOH with added Fe traces (**Figure 6-1e**) (see the Experimental Section for more details). In the presence of Fe, the OER activity is enhanced during the CV runs, doubling the current density at 1.6 V_{RHE} (**Figure 6-1f**). In Fe-free KOH, such enhancement is not observed (**Figure 6-1d,f**). Linear sweep voltammetry experiments show a similar Fe-dependent OER activity (**Figure 6-3**).

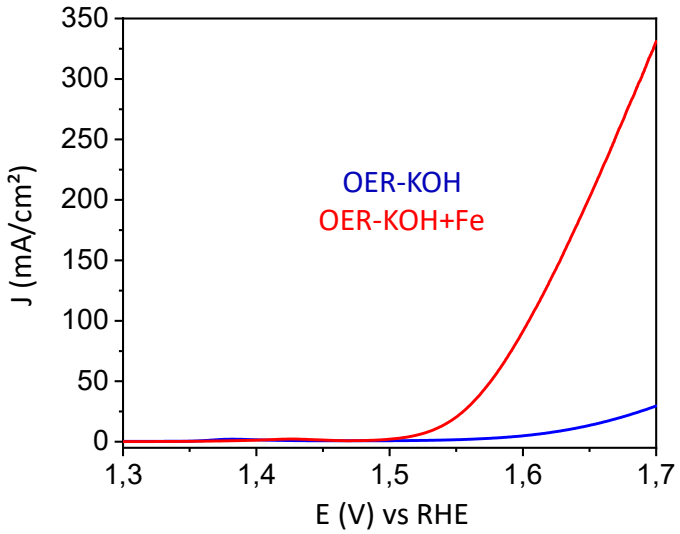

***Figure 6-3**. Linear sweep voltammetry after 50 CVs in Fe-free KOH (blue) and KOH+Fe traces (red).*

6. Fe traces on electrolyte interaction with Ruddlesden Popper faults

Structural evolution of RP faults during OER

Having confirmed the presence of numerous RP faults and the Fe-dependent OER activity of the $LaNiO_3$ particles, we investigated the structural effects of having Fe traces in the electrolyte on the RP using IL-STEM.[64,110] With this technique, the same nanoparticle (**Figure 6-4a**) can be studied before (**Figure 6-4b**) and after (**Figure 6-4c**) catalysis, allowing the correlation of the changes in electrochemical performance (**Figure 6-5**) with the changes in the structure.

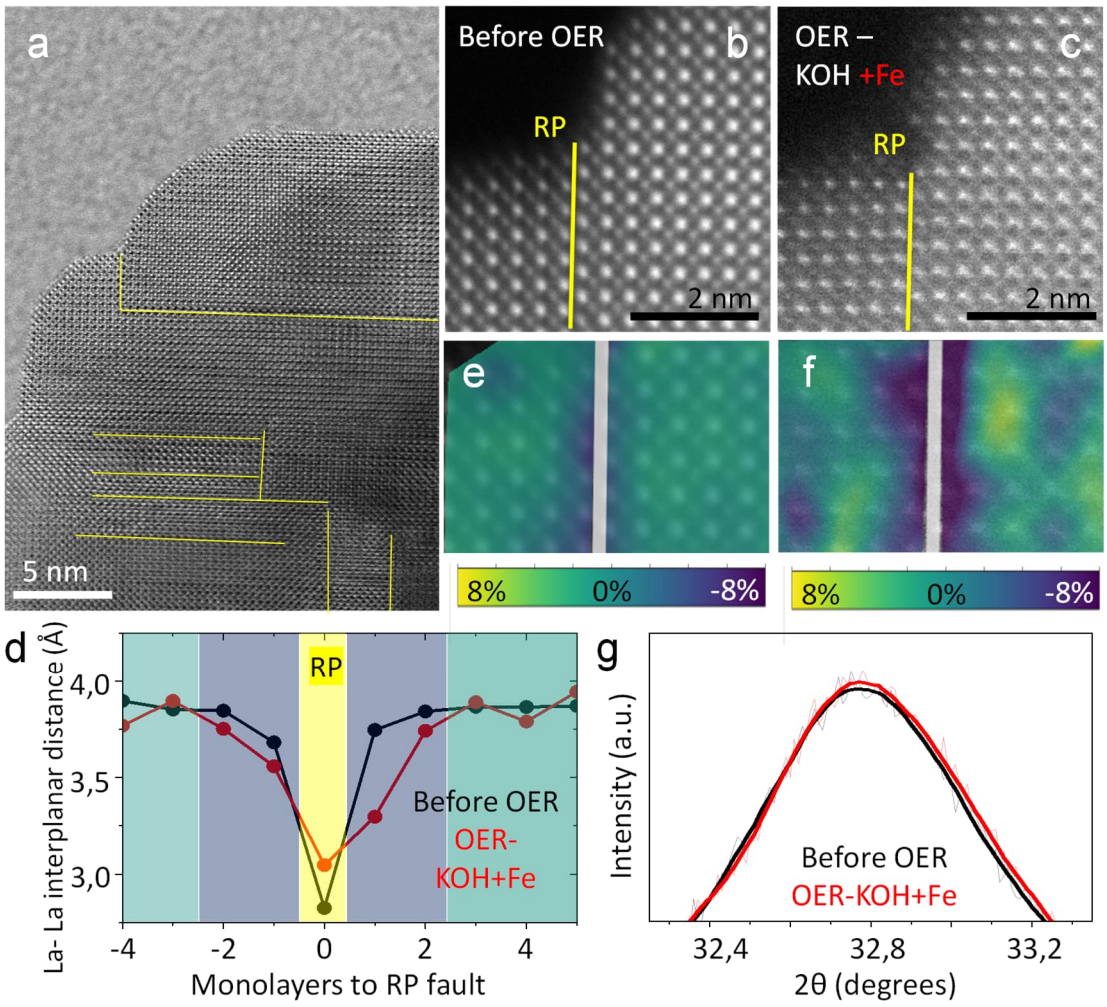

***Figure 6-4**. Changes in RP faults during OER in the presence of Fe impurities in the electrolyte. (a) BF-STEM image of $LaNiO_3$ particle before OER. (b) RP fault before catalysis. (c) Same RP fault as in (b) after OER in KOH with added Fe traces. (d) Changes in the interplanar distances around the RP fault. Notice how during OER the RP fault expands, causing the adjacent layers of $LaNiO_3$ to contract. Strain maps before (e) and after (f) OER (see Experimental Section for more details). (g) High-resolution XRD pattern before and after OER.*

IL-STEM results show that the interatomic distance of the RP fault planes increases during OER catalysis, from 2.83 Å to 3.05 Å (**Figure 6-4d**). As a consequence of such expansion, neighboring $LaNiO_3$ layers get contracted (**Figure 6-4d**), introducing compressive strain into

them (**Figure 6-4e,f**). This effect is very local, affecting only 2 adjacent [LaO]-[NiO_2] units on each side of the RP fault. The 1st neighboring [LaO]-[NiO_2] unit contracts by ~7.7% and the second by ~2.5%. Further away from the fault, the interplanar distance between consecutive [LaO] layers remains unchanged at ~3.84 Å, in good agreement with the reported $LaNiO_3$ structure.[218]

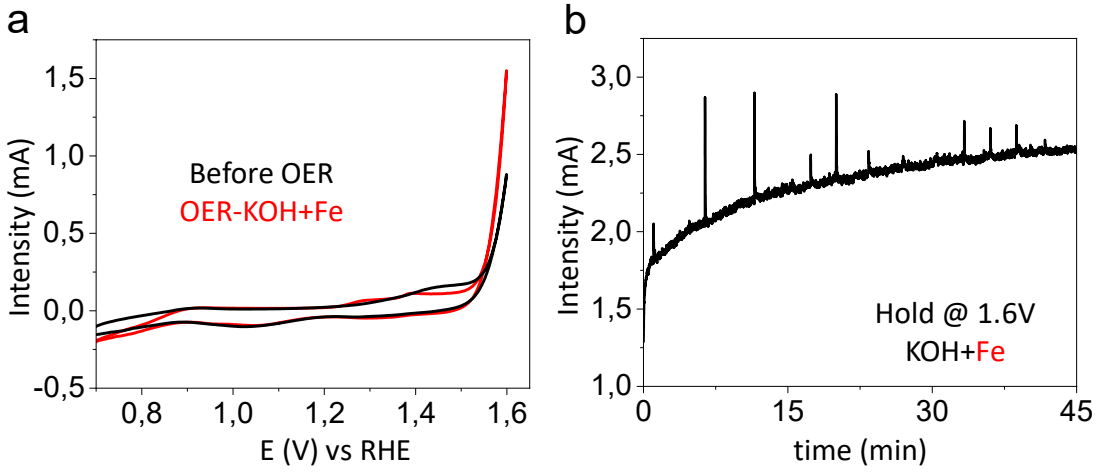

***Figure 6-5**. Electrochemical curves of the IL-STEM experiments shown in **Figure 6-4**. (a) CV before and after OER. (b) The sample was held at 1.6 V_{RHE} (OER potential) for 45 minutes to trigger the morphological changes that are later observed in the microscope. Note how the current increases during the potential hold due to the presence of Fe traces in the electrolyte.*

Despite the local nature of this lattice contraction, the elevated number of faults results in a noticeable effect on the overall $LaNiO_3$ structure. Indeed, XRD measurements indicate an asymmetric broadening towards higher 2θ angles during catalysis (**Figure 6-4g, Figure 6-6**), consistent with a small proportion of the $LaNiO_3$ layers getting compressed during OER.

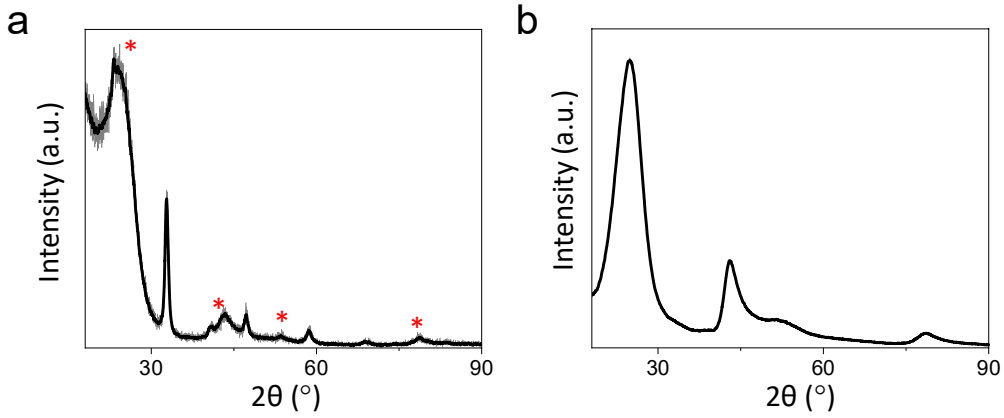

***Figure 6-6**. (a) Overview of XRD pattern before OER. The peaks of the substrate (glassy carbon) are marked with red asterisks. These were identified by micro-area XRD measurements on a sample-free glassy carbon area (b). The reflection at 2θ=32.8° is selected for the higher resolution XRD measurements due to its low substrate contribution, especially towards higher 2θ angles.*

When performing equivalent experiments in Fe-free KOH, no RP fault expansion or adjacent $LaNiO_3$ layers contraction were observed (**Figure 6-7**), suggesting the importance of Fe in triggering this phenomenon.

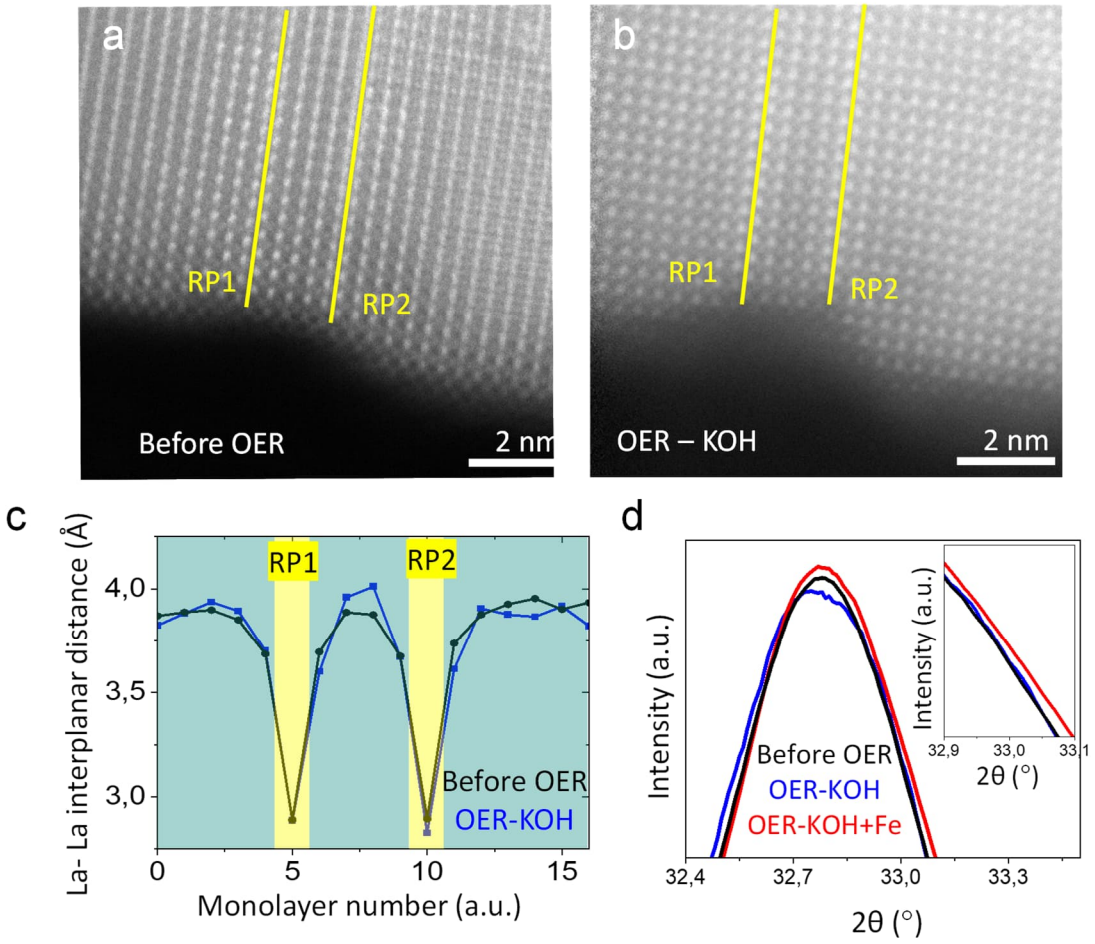

***Figure 6-7**. Fe-free KOH. (a) HAADF-STEM before catalysis of a particle with two RP faults. (b) The same particle after OER in Fe-free KOH. (c) Changes in interplanar distance. No RP fault expansion is observed in the absence of Fe. (d) Comparison of XRD pattern before OER (black), after OER in Fe-free KOH (blue), and in KOH+Fe (red). Notice how only in the presence of Fe traces on the electrolyte, an asymmetric broadening towards higher 2θ° is observed, indicating that the $LaNiO_3$ lattice only contracts partially when Fe is added to the electrolyte. The differences in the left part of the peak stem from different substrate (glassy carbon) contributions (see **Figure 6-6**).*

Fe incorporation on RP faults during OER

The key role of Fe on the observed RP fault expansion with consequent $LaNiO_3$ layers contraction is further evidenced by studying the distribution of Fe after OER (**Figure 6-8a,b**), especially considering that no Fe is detected in the pristine $LaNiO_3$ particles (**Figure 6-9**).

6. Fe traces on electrolyte interaction with Ruddlesden Popper faults

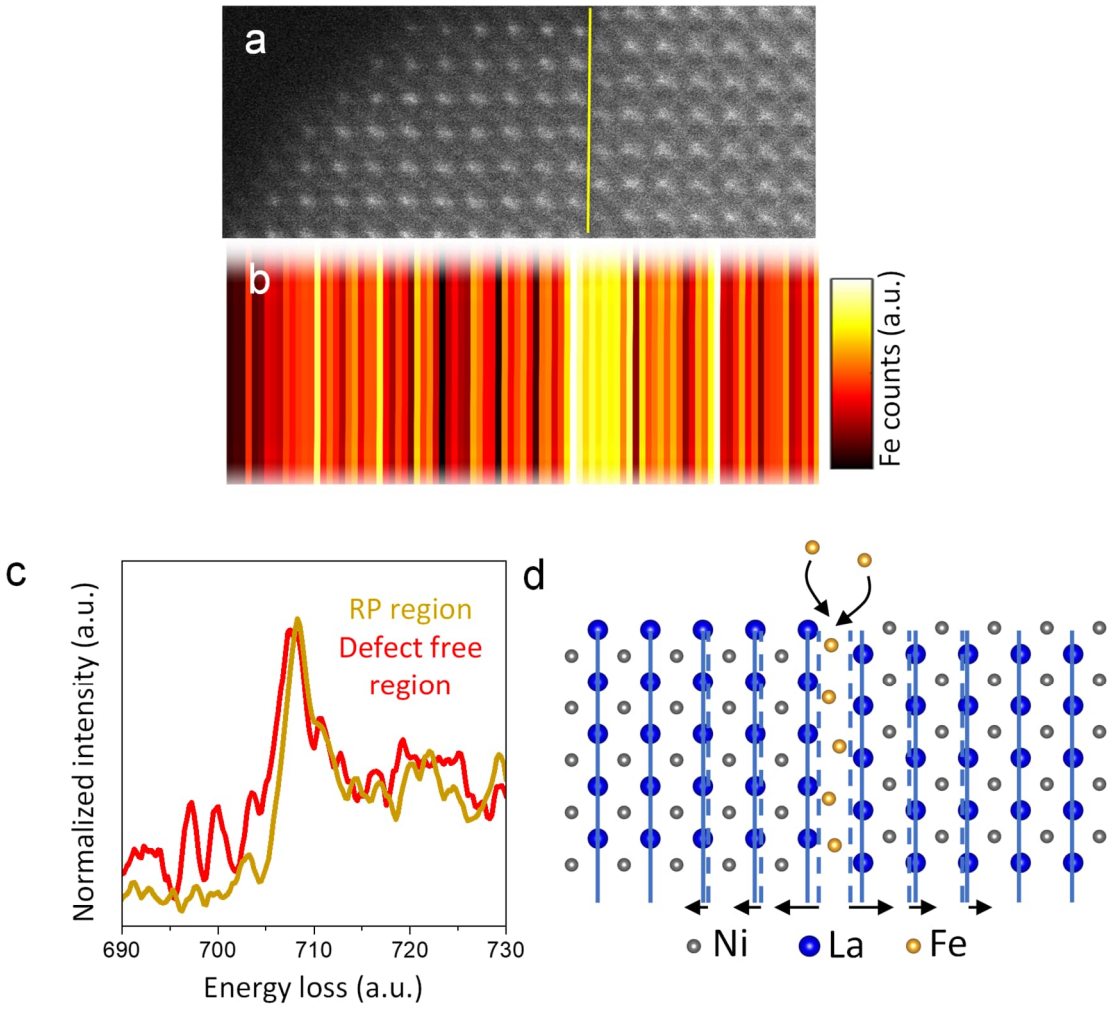

***Figure 6-8**. Fe incorporation on RP fault during OER. (a) HAADF-STEM image of AN RP fault after OER and (b) corresponding Fe distribution extracted from the EELS data. Notice how on the RP fault region more Fe is detected. (c) Comparison of Fe L_3 edge at the RP fault region and in defect free area (d) Schematic drawing with the proposed mechanism for the changes in d-spacing on the $LaNiO_3$ layers experimentally observed.*

After OER, Fe is detected all over the particle due to the formation of a Fe-rich hydr(oxide) surface layer during catalysis, in good agreement with previous reports.[48,219] Nonetheless, a higher Fe concentration is measured in the RP fault region by electron energy loss spectroscopy (**Figure 6-8a,b**), suggesting that Fe traces in the electrolyte diffuse into the RP fault during OER. This hypothesis is further supported by analyzing the Fe L_3-edge (**Figure 6-8c**), since the shift towards higher energy losses measured at the RP fault region is indicative of Fe being in a different chemical environment than in the rest of the particle (surface).

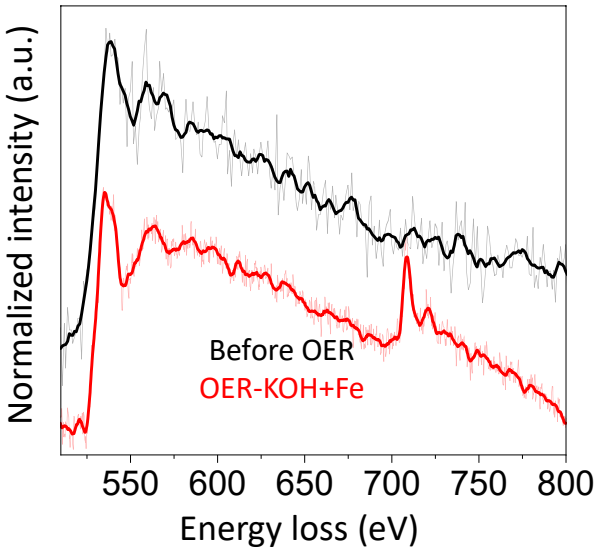

Figure 6-9. *EELS spectra before and after OER with Fe traces added to the electrolyte. Fe signal (Fe $L_{2,3}$-edge starting at 708 eV) is only detected after OER catalysis.*

Our results indicate that Fe traces in the electrolyte incorporate in the RP fault during OER catalysis, causing the expansion observed in the IL-STEM experiments. Such an expansion pushes the neighboring $LaNiO_3$ layers together, inducing their compression (**Figure 6-8d**). A similar behavior is observed in other RP faults (**Figure 6-10**).

Currently, density functional theory (DFT) calculations are being performed to further prove this hypothesis, and to elucidate the nature of the Fe incorporation (i.e., interstitial or substitutional). DFT calculations can also provide information on how the observed local compression of the $LaNiO_3$ lattice affects the electronic structure and catalytic activity. Nonetheless, experiments performed on epitaxially strained $LaNiO_3$ perovskites indicate that compressive strain boosts their OER activity due to a tuning of the electronic structure[208], so we would expect a similar behavior for our system.

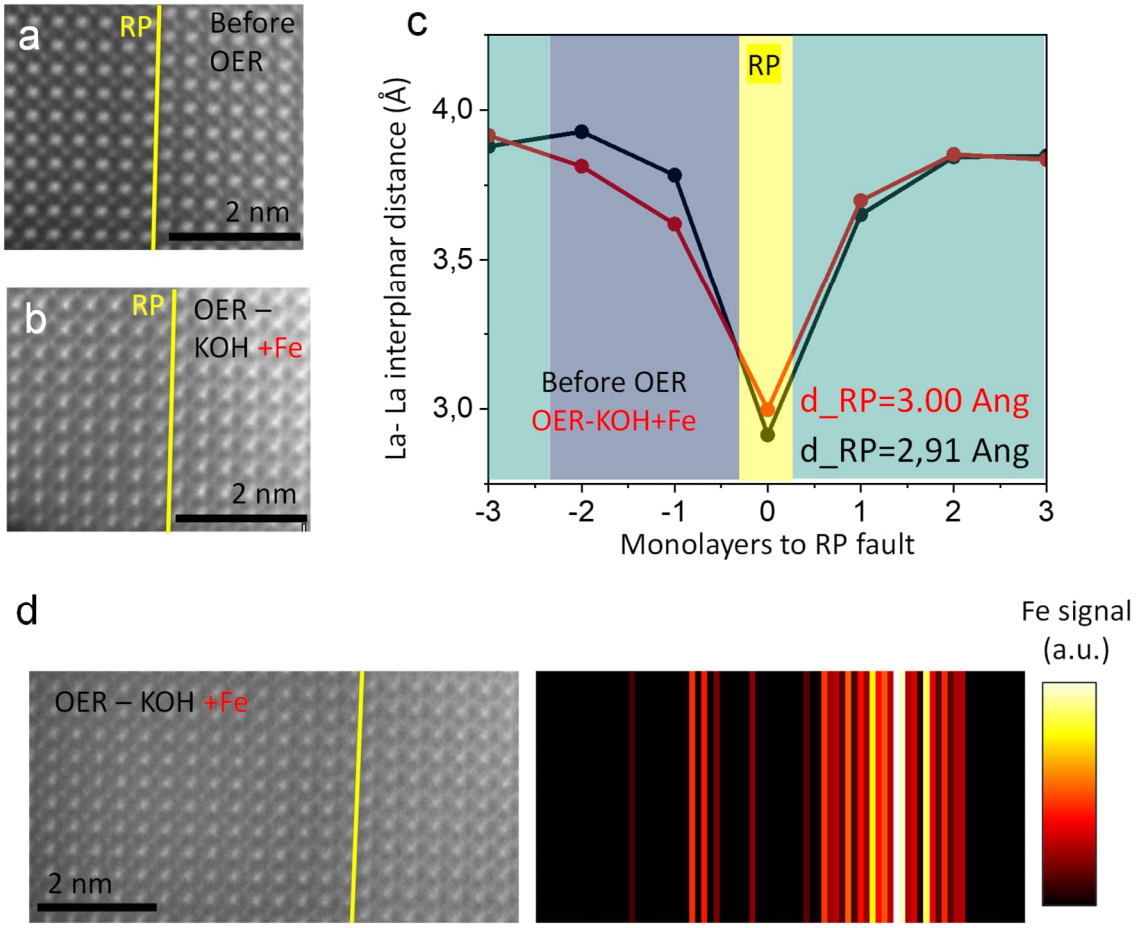

***Figure 6-10**. Structural and compositional changes on another RP fault during OER. (a) HAADF-STEM image before OER. (b) Same fault after OER. (c) Changes in interplanar distances, where an expansion of the RP fault layer is observed. In the right region of the RP fault the lower quality of the STEM micrograph might influence the d-spacing measurements. (d) A higher Fe signal is detected in the RP fault region by EELS.*

6.3 Conclusions

To summarize, we have explored the effects of adding trace amounts of Fe to the electrolyte on Ruddlesden-Popper (RP) planar faults present in $LaNiO_3$ perovskite oxides. Both Fe traces in the electrolyte and RP faults are known to enhance the OER activity of perovskite oxides.

We found that Fe incorporates into the RP fault during OER catalysis, causing it to expand. Consequently, the $LaNiO_3$ lattice gets locally compressed, resulting in local structural changes of the perovskite structure. We expect this local lattice compression to be favorable for the OER catalytic activity of $LaNiO_3$, and DFT calculations are currently being performed to shed light on this issue. Our results reveal a new mechanism for enhancing the OER activity of perovskite oxides, and highlight the importance of studying the local structural changes occurring during catalysis.

6.4 Experimental section

Synthesis of $LaNiO_3$ nanoparticles

The $LaNiO_3$ perovskites were synthesized by a solution combustion method followed by a calcination treatment. More details can be found in Ref. [48] The presence of numerous RP faults probably stems from local unstoichiometric concentrations of the La and Ni precursors. In the regions where the La concentration is higher, the formation of RP faults is favoured.[210]

Scanning transmission electron microscopy

STEM experiments were performed on a Cs-probe corrected Thermo Fisher Titan microscope operated at an accelerating voltage of 300 kV. A semi-converge angle of 23.8 mrad and a camera length of 100 mm were used for image acquisition, yielding a collection angle for the HAADF detector of 78-200 mrad and for the BF of 0-10 mrad.

The d-spacing measurements between La-La were performed on high-resolution HAADF-STEM micrographs. A series of frames with a fast acquisition time (dwell time 2.0 µs) were acquired and stacked using cross-correlation. This was done to minimize sample drift during the acquisition of a frame, which would distort the d-spacing measurements. Using open-source Python packages, the atomic column positions were located using two-dimensional Gaussian fitting, and the corresponding planar distances calculated.[102,220] The interplanar distance distortion maps (referred to as strain maps in the text, see Figure 6-4e,f) were calculated by comparing the experimentally found La-La interplanar distance (equivalent to d(012) in the [-22-1] zone axis) with the bulk equilibrium La-La interplanar distance (d(012)=3.83 Å, ICSD 93919)[218].

EELS data was acquired in STEM mode using the Quantum ERS spectrometer (Gatan) with a dispersion of 0.25 eV per channel and a pixel time acquisition of 1 s (with sub-pixel scan activated to minimize beam damage effects). The EELS data was analyzed using the DigitalMicrograph Software (Gatan, version 3.51) and non-negative Matrix Factorization, as implemented in the published Matlab codes from Ref [221].

6. Fe traces on electrolyte interaction with Ruddlesden Popper faults

Electrochemical characterization

The electrochemical measurements were performed in a three-electrode set up, equipped with a RDE (PINE Research Instrumentation). As a reference and counter, a reversible hydrogen electrode (HydroFlex, Gaskatel) and Pt wire were used, respectively. 1 M KOH was purified using a previously described method to remove all Fe and cations.[222] When necessary, Fe traces (7.5 ppm) were added to the electrolyte using $FeNO_3$ as a source. The Fe concentration on the electrolyte was confirmed by inductively coupled plasma-optical emission spectrometry (ICP-OES) measurements.

Identical location scanning transmission electron microscopy

For performing the identical location STEM experiments, a 10 µL droplet of a solution containing $LaNiO_3$ (0.3 mg/mL) was drop cast on a holey carbon gold TEM finder grid (Plano). The sample was left to dry overnight. After the initial characterization in the TEM, the sample was connected to the potentiostat (Gamry Reference600) using reverted Au tweezers (Plano). This connection method was chosen as opposed to the typical glassy carbon substrate + Teflon cup to allow for the release of gas bubbles generated during the OER.[105] The sample underwent electrochemical testing in the form of 5 CVs (0.6-1.7 V_{RHE}) + potential hold (45 mins at 1.6 V_{RHE}) + 5 CVs (0.6-1.7 V_{RHE}), either in Fe-free KOH (1 M) or in KOH (1 M) containing 7.5 ppm of Fe ($FeNO_3$ from Sigma-Aldrich was used as the iron source). After completion of the electrochemical testing, the grids were rinsed with DI-water and characterized again in the TEM. Individual nanoparticles were tracked after electrochemistry using marks in the TEM finder grids and a series of zoom-out images, allowing us to see how they changed during electrochemical testing.

X-ray diffraction

For the XRD measurements, a $LaNiO_3$ ink (1.5 mg $LaNiO_3$ nanoparticles, 15 µL Nafion, 0.2 mL isopropanol, 0.2 mL µL DI-water) was drop cast onto a glassy carbon electrode and left drying overnight. After initial XRD characterization, the sample underwent electrochemical testing in KOH (1 M) + 7.5 ppm Fe, following the protocol used in the IL-STEM experiments (5 CVs (0.6-1.7 V_{RHE}) + potential hold (45 mins at 1.6 V_{RHE}) + 5 CVs (0.6-1.7 V_{RHE})). The same sample was later investigated again by XRD, to ensure a reliable interpretation. A new sample was prepared following the same procedure and cycled in Fe-free KOH 1 M for its posterior XRD characterization.

The XRD measurements were performed on a Rikaku Smartlab 9KW using Cu Kα radiation as the source for X-rays (λ=1.54059 Å). Due to the geometry of the sample and to minimize the contributions from the glassy carbon substrate, a grazing incidence geometry was chosen. Overview pattern were acquired first (10-120°), followed by slower scans (referred to as "high-resolution" in the text) of the reflections of interest (30-36°) for a higher signal-to-noise ratio.

7 Concave Grain Boundary Stabilized by Boron Segregation for Efficient and Durable Oxygen Reduction

Note: The following chapter is based on the publication "Concave Grain Boundary Stabilized by Boron Segregation for Efficient and Durable Oxygen Reduction", by X. Geng, M. Vega-Paredes et al., in *Advanced Materials* 2024, 36, 2404839. Therefore, the personal pronoun "we" is used throughout this chapter to refer to the group of researchers that were part of this specific study.

Chapter 6 highlighted the importance of defects in catalysis. This chapter aims to use a different defect, namely grain boundaries, for increasing the catalytic activity of Pt towards the oxygen reduction reaction.

The oxygen reduction reaction is a key electrochemical process that limits fuel cell and metal-air battery efficiency due to its sluggish kinetics, even when catalyzed by expensive metal Pt. Enhancing the mass activity of Pt catalysts is imperative to minimize Pt usage, for which both the specific activity and electrochemically active surface area need to be optimized. Here, we propose ultrafine, grain boundary-rich Pt nanoparticle assemblies as efficient ORR catalysts. Their nanowire morphology inherently offers a large ECSA, and their high density of concave GB sites provides elevated specific activity. The atoms located at the concave GB sites exhibit higher coordination numbers and lattice distortion compared to isolated NP, resulting in a moderate reduction in oxygen binding energy and their consequent activation towards ORR. Furthermore, we prove that the GBs can be stabilized by boron segregation, preserving the active sites during catalysis. The boron-stabilized, concave GB sites-rich Pt nanoassemblies demonstrate remarkable ORR specific and mass activities of 9.18 mA/cm2 and 6.40 A/mg_{Pt} (at 0.9 V vs. the reversible hydrogen electrode), respectively, surpassing commercial Pt/C catalysts by over 35-fold, while exhibiting negligible decay in ORR activity following 60,000 potential-scanning cycles. The versatility of our approach can be applied to a wide range of catalytically active NPs.

7.1 Introduction

The oxygen reduction reaction plays a crucial role in energy conversion for metal-air batteries and fuel cells[5,223,224]. Pt and its alloys are currently state-of-the-art catalysts for ORR[16,82,225]. Nonetheless, the high costs and limited durability of Pt catalysts hinders the commercial viability of fuel cells[226–228]. Therefore, it is imperative to boost the mass activity of Pt catalysts

(defined as the catalytic activity per unit mass), which would allow for the preservation of the activity while reducing the Pt loading. In addition, their structural stability has to be increased, so that the activity is maintained for an elevated period of time. The mass activity is determined by both specific activity (normalized to surface area) and ECSA (normalized to mass). An optimal mass activity can be achieved by increasing specific activity and ECSA.

The most effective approach to enhance ECSA is by reducing the size of nanoparticles, since ECSA increases when lowering particle size[68]. However, reducing particle size leads to a significant increase in the proportion of undercoordinated corner, edge, or step sites, which exhibit stronger binding to oxygenated intermediates compared to terrace sites, and thus lower specific activity for ORR[68]. Consequently, the specific activity of ultra-small NPs (less than 3 nm) is significantly lower than that of larger NPs. Additionally, ultra-small NPs suffer from poor stability, since they are prone to aggregation during electrochemical cycling and Oswald ripening[229,230]. Achieving the large ECSA of ultra-small NPs without compromising their specific activity and stability would greatly enhance the mass activity and commercial viability of fuel cells. However, achieving such a goal is highly challenging and new catalyst design strategies are required.

To date, the highest specific activities have been obtained on $Pt_3Ni(111)$ single crystals[81], owing to their nearly optimal oxygen binding energy[231] derived from synergistic contributions between strain[80], ligand[232] and ensemble effects[233]. However, under the oxygen-rich and highly acidic conditions at the cathode of fuel cells, such alloy catalysts are prone to transition metal leaching[234,235] and NP agglomeration[229,230], resulting in low stability. Hence, besides alloying Pt with transition metals, alternative strategies are required to optimize the ORR activity and durability of Pt catalysts.

One further strategy for enhancing the specific activity involves increasing the coordination number of Pt catalysts (e.g., by constructing octahedral shapes[81] or local concave geometries[236–238]). The increase in coordination number results in a moderate weakening of Pt-O binding, optimizing it[73,225]. Nonetheless, despite the high initial ORR activity of octahedral Pt NPs, prolonged electrochemical cycling induces shape alterations, thereby deteriorating their durability[234]. The strategy of local concave geometry has also been shown to boost specific activity[236]. However, the stability of Pt atoms at the concave sites and how to further enhance their stability to prevent electrochemical dissolution remain unexplored. Moreover, synthesizing Pt catalysts with high-density of concave sites in a controlled manner poses

significant challenges. Another approach for achieving high specific activity is by increasing the surface distortion of Pt catalysts[239]. Surface distortion can be introduced through inhomogeneous alloying, (electro)chemical surface destruction, or the formation of grain boundaries[239]. However, prolonged electrochemical cycling induces structural changes in lattice-distorted Pt catalysts, resulting in lower lattice distortion and a notable decrease in catalytic activity[28,240–242]. Hence, enhancing the stability of Pt catalysts with high surface distortion has been scarcely studied. The inadequacy of the previously exposed methods to optimize simultaneously the ECSA and specific activity, results in catalysts with insufficient mass activity, that additionally suffer from low stability. Therefore, new strategies need to be developed for ORR catalysts.

Here, we propose ultrafine Pt nanoparticle assemblies with a large number of concave GBs (GB-Pt NAs) as efficient and durable ORR catalysts. Spherical Pt NPs with an average size of 2 nm are interconnected via GBs, forming ultrafine nanowire-shaped Pt nanoassemblies. The abundance of concave sites near the surface terminations of GBs at GB-Pt NAs elevates locally the coordination number of atoms. Moreover, notable lattice distortion in the vicinity of the GB is observed as a consequence of the assembly process. The higher coordination number and lattice distortion in GB-Pt NAs collectively yield a moderate reduction in oxygen binding energy, optimizing it and thereby significantly enhancing its specific activity relative to Pt NPs. Moreover, the ultrafine nanowire geometry of GB-Pt NAs provides a large ECSA. As a result, GB-Pt NAs demonstrate specific and mass activity exceeding those of commercial Pt/C catalysts by factors of around 40. The stabilization of concave GB sites is achieved by boron (B) segregation at the GBs. The activity of Pt NAs with ~10 at.% of B kinetically trapped at GBs exhibits minimal decay, with negligible changes observed in both nanostructure and chemical composition after a 60,000-cycle electrochemical accelerated durability test (0.6–1.1 V vs RHE). Our findings highlight the effectiveness of building concave GB sites through NP coalescence as a highly efficient approach for tuning coordination number and lattice distortion in nanocatalysts. When stabilized by trapping heteroatoms on high-energy GBs, this strategy yields exceptionally active and durable electrocatalysts.

7.2 Results and Discussion

Grain boundary-rich Pt NPs assemblies

Ultrafine nanowire-shaped GB-Pt NAs (**Figure 7-1a,b, Figure 7-2a**), with an average crystallite size of 2.1±0.4 nm (**Figure 7-2b**), were prepared by continuously bubbling H_2 gas

into a solution containing well-dispersed and uniformly sized (2.0±0.1 nm) citrate-capped Pt NPs (**Figure 7-1c**, **Figure 7-2b**). GB-Pt NAs exhibit a large specific surface area and a highly porous structure, as demonstrated by Brunauer-Emmett-Teller (BET) measurement (see Appendix, **Figure A7-1, Table A7-1**).

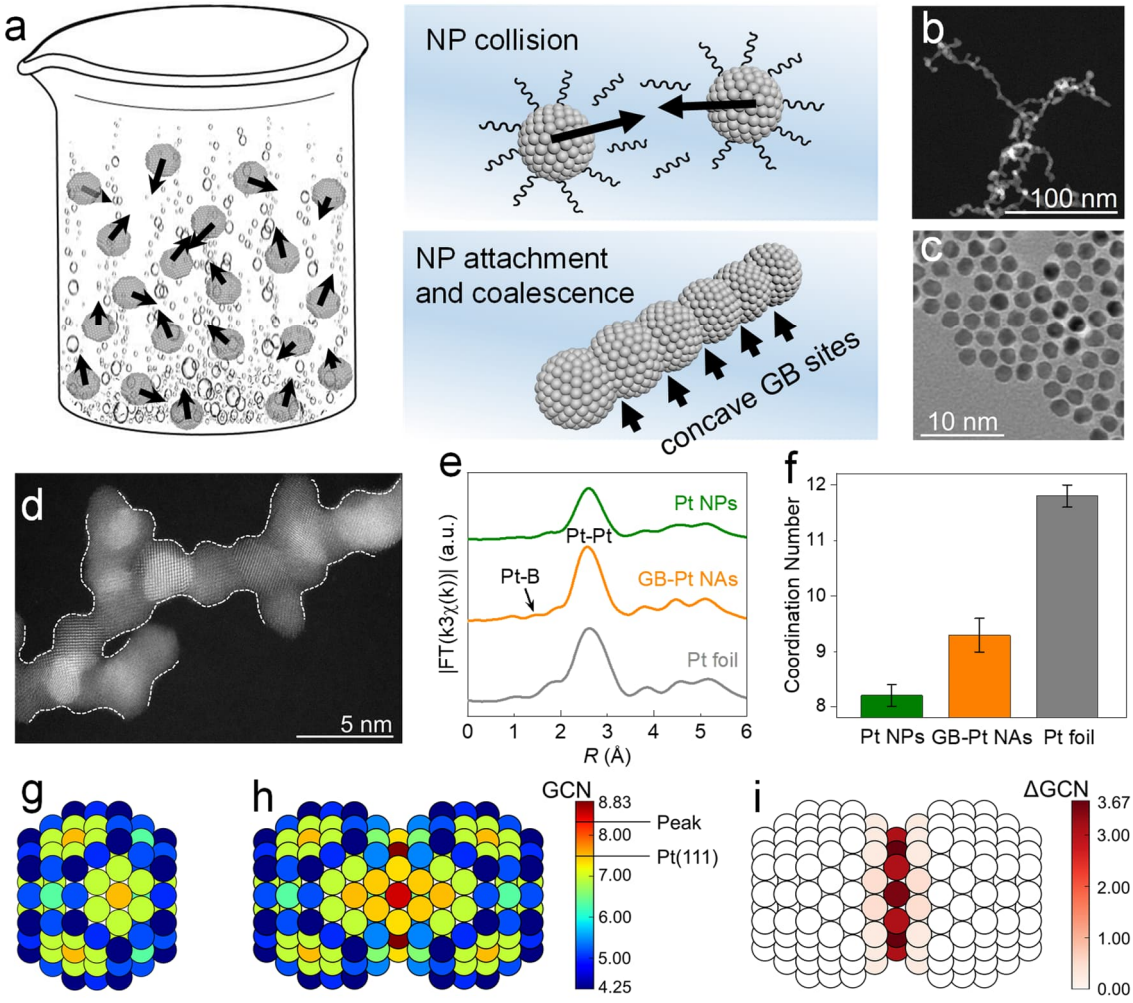

Figure 7-1. *Preparation and structural characterization of Pt NAs with a high density of concave sites. (a) Coalescence and assembly are driven by H_2 gas bubbling of Pt NPs into Pt NAs rich with concave GB sites at the surface. (b) HAADF-STEM image of GB-Pt NAs. (c) TEM image of Pt NPs before assembly process. (d) HAADF-STEM image of GB-Pt, highlighting concave surfaces. (e) EXAFS spectra for Pt L3-edge for Pt NPs, GB-Pt NAs and Pt foil. (f) Coordination number calculated from the Fourier-transformed EXAFS spectra. GCNs of the (g) Pt_{201} NP and (h) Pt_{383} Σ3 (111) twin GB model, with the subscripts denoting the total number of Pt atoms in each model. (i) Difference in GCN (ΔGCN) between g and h.*

The diameter of GB-Pt NAs corresponds to the size of the NP building blocks, allowing for control over the Pt NAs' diameter by adjusting the NP size (**Figure A7-2**). H_2 plays a dual role in the assembly process[243]. First, atomic H, originating from H_2 dissociation on the Pt surface, gradually replaces citrate ligands until their complete removal, as confirmed by infrared

spectroscopy (**Figure A7-3)**. H_2-bubbling hence progressively destabilizes the Pt NPs leading to a decrease of the ζ potential of the solution over time (**Figure A7-4**). Second, convection from continuous H_2 bubbling drives collisions between NPs, leading to the gradual assembly of isolated NPs, resulting in their attachment and coalescence to form GBs. The diffusion-limited cluster aggregation process (**Figure A7-5**) promotes the assembly of isolated NPs into clusters, chains, and eventually a porous ultrafine nanowire-shaped network (**Figure 7-2d**).

During the growth process, the spherical NPs collide, attach and coalesce with each other, being ultimately connected through GBs. As a result, the atoms in the vicinity of the GBs are in a concave environment (**Figure 7-1d, Figure 7-2c**). Given that the surface energy of a one-dimensional nanowire with a concave surface is thermodynamically more stable than that with a flat surface (**Figure A7-6**), the highly porous nanowire-shaped GB-Pt NAs have high stability without experiencing significant aggregation.

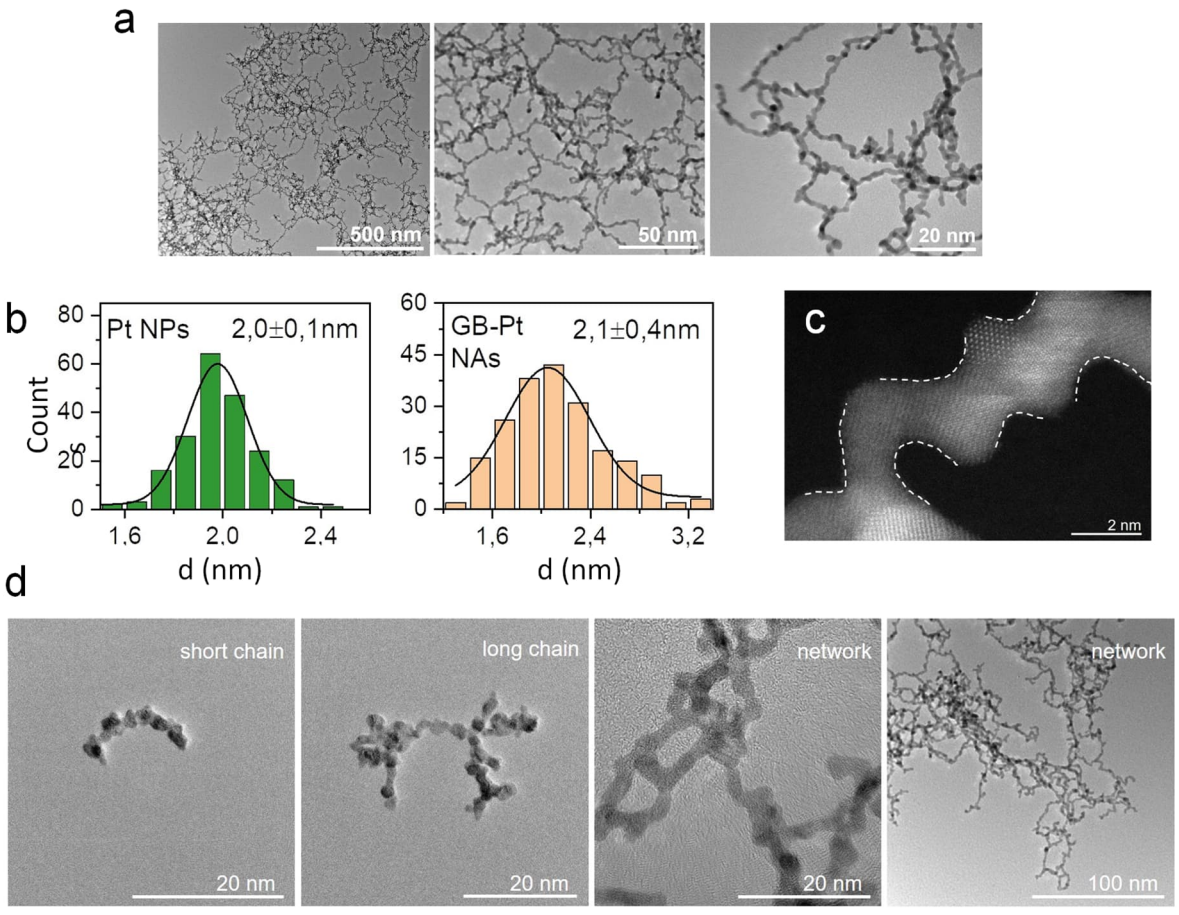

Figure 7-2*. (a) TEM images of GB-Pt NAs at different magnifications. A defocus was introduced to enhance the contrast. (b) Size distribution obtained by analyzing 200 NPs or crystallites in Pt NPs and GB-Pt NAs derived from TEM images. (c) High-resolution HAADF-STEM image of GB-Pt NAs in which concave surface are outlined in white. (d) TEM images of the samples taken out during the assembly process of Pt NPs.*

The substantial density of concavities adjacent to GBs contributes to a higher coordination number for GB-Pt NAs (~9.3) in contrast to that of Pt NPs (~8.2), as measured by extended X-ray absorption fine structure (EXAFS) (**Figure 7-1e,f** and **Table A7-2**).

To unravel the underlying factors contributing to the rise in coordination number, we conducted density functional theory calculations. Computations were performed on a representative truncated-octahedral NP model composed of 201 Pt atoms (**Figure 7-1g**), along with a Σ3 twin boundary model established between two NPs (**Figure 7-1h**) with size resembling those observed experimentally (detailed computational procedures are outlined in the Experimental methods). Analysis of the NP model revealed that the generalized coordination number (GCN) of atoms at the corners and edges, a descriptor for ORR activity[73], ranged from 4 to 7 (**Figure 7-1g**). Upon the coalescence of two NPs to form a GB, the corner and edge atoms constitute the concave sites near the GBs (**Figure 7-1h**). Interestingly, the GCN of the layers of atoms adjacent to the GBs ranges from 7.5 to 9.1 (**Figure 7-1h**), increasing by up to ~3.7 compared to the single NPs (**Figure 7-1i**). It has been reported that GCN within this range is expected to display optimal ORR activity[73], suggesting that GB-Pt NAs may serve as promising ORR catalysts. The variation in conventional coordination number exhibits a similar trend to the change in GCN (**Figure A7-7**).

To study with more detail the presence of GBs, HAADF-STEM experiments were performed. Among a randomly selected set of twenty GBs, we identified three Σ41 GBs, two Σ33 GBs, and fifteen Σ3 GBs (**Figure 7-3a**, **Figure 7-4**, **Figure A7-8**) based on the CSL[244].

Some initially spherical NPs have changed their morphology as a result of the assembly process, e.g., crystallites NP2, NP3 and NP4 in **Figure 7-3a**, potentially inducing local displacement of the atoms from their relaxed equilibrium positions. The relative displacements in atomic positions were analyzed by measuring the local deviations of atomic positions relative to a reference lattice (center of the grain)[96]. The atomic positions were found by fitting two-dimensional Gaussians in the local intensity maxima (i.e., the atomic column positions), allowing us to locate them with great accuracy.[96] More details are given in the Experimental methods.

Higher levels of atomic deviations are observed in the vicinity of the GBs (**Figure 7-3b,c**), indicating an increased lattice distortion near the surface terminations of the GBs.

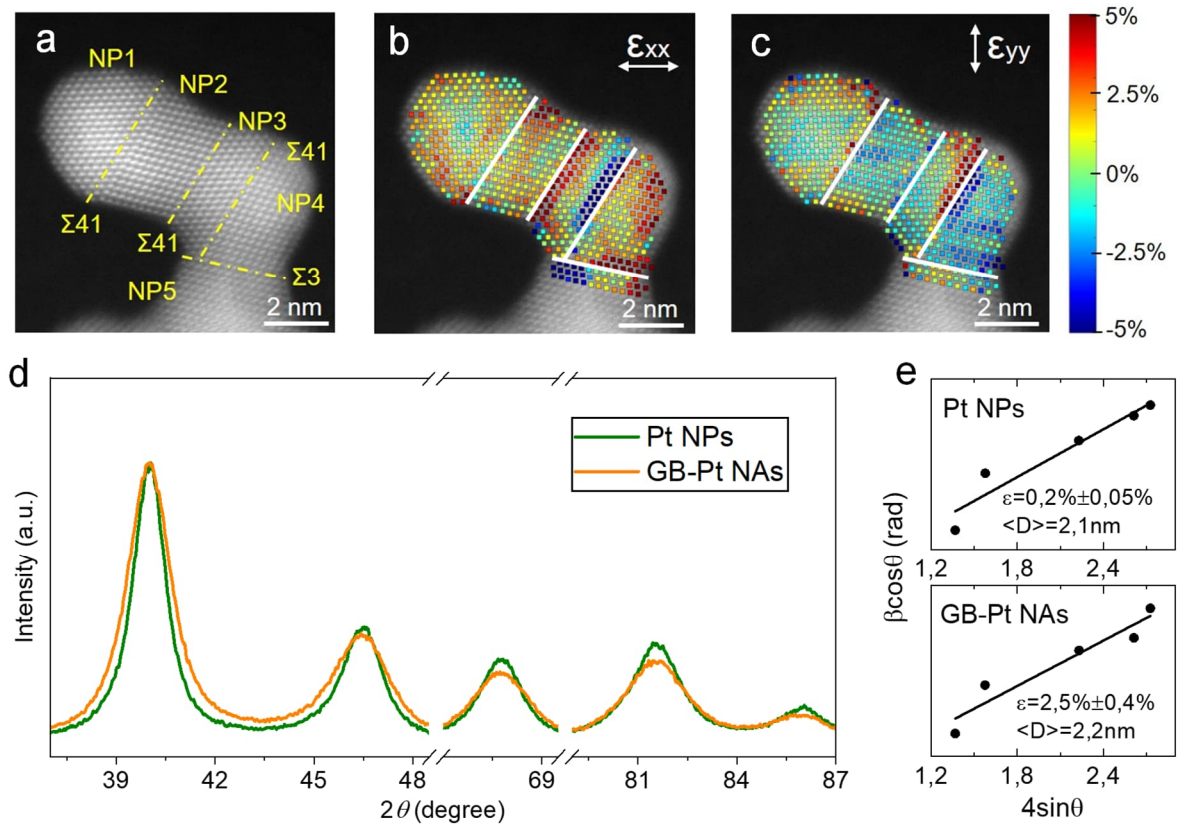

***Figure 7-3**. (a) HAADF-STEM image of the GBs between the Pt NP building blocks within GB-Pt NAs. (b,c) Real space relative displacement maps along the x (ε_{xx}) and y (ε_{yy}) directions. (d) High-resolution XRD patterns of Pt NPs and GB-Pt NAs showing (111), (200), (220), (311), and (222) diffraction peaks. (e) Williamson–Hall plots derived from the XRD patterns.*

This heightened lattice distortion is further statistically proven by the broader high-resolution X-ray diffraction peaks observed in GB-Pt NAs compared to those of Pt NPs (**Figure 7-3d**). Notably, despite the identical size of these two samples, Williamson-Hall fitting revealed an average lattice distortion of 2.5% in GB-Pt NAs, which is significantly higher than the 0.2% observed in Pt NPs (**Figure 7-3e**). Although some high-index facets were observed after the assembly process (**Figure A7-9**), they constitute a minor fraction of the facets in GB-Pt NAs. This conclusion is supported by the EXAFS results, which show an increase in the coordination number after assembly. Such an increase would not be possible if a significant number of high-index facets had been formed.

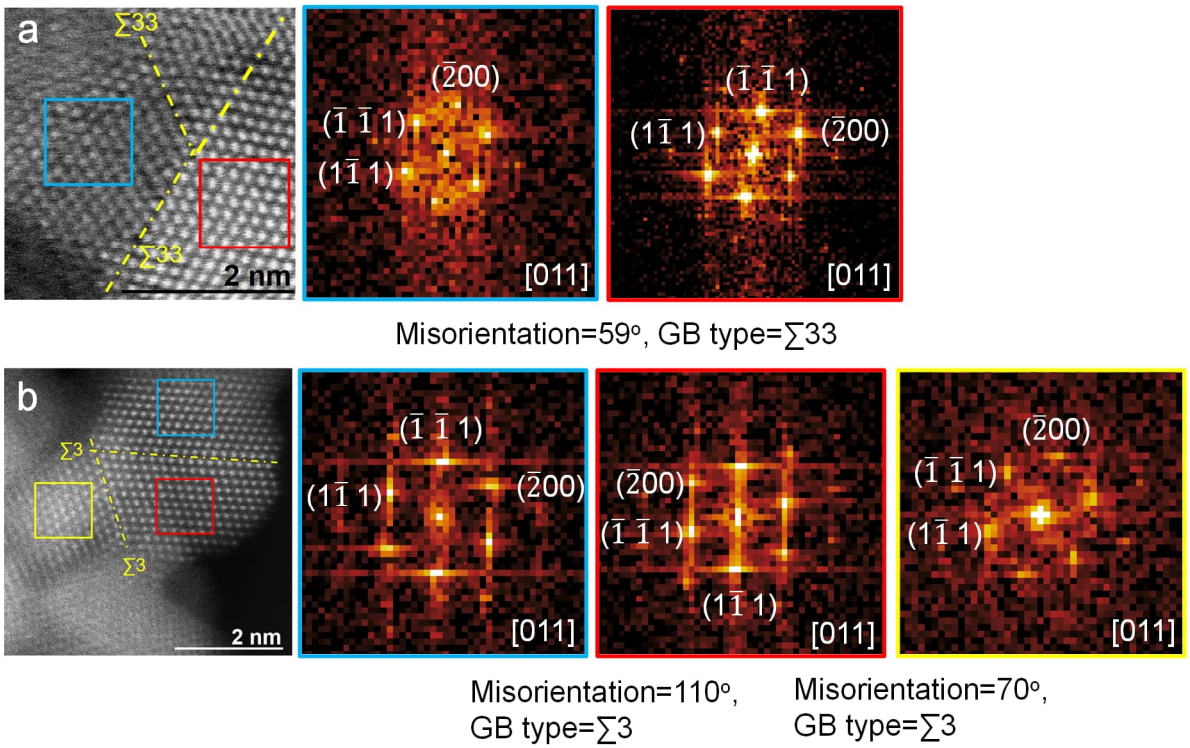

***Figure 7-4**. (a) HAADF-STEM image and FFT diffractograms of Σ33 GBs identified based on the coincidence site lattice theory. (b) HAADF-STEM image and FFT diffractograms of Σ3 GBs.*

Boron doping for stabilizing GBs

Due to the misorientation between adjacent grains, the arrangement of atoms at GBs often exhibits disorder, leading to significantly reduced stability[245]. Under external stimuli such as heating or applying an electric field, atoms at GBs are prone to migration, resulting in poor stability of GBs[63,246,247]. For instance, GBs in polycrystals begin to destabilize and migrate when heated to temperatures below half of their melting point, ultimately leading to their annihilation[246,247]. Furthermore, the application of an electric field can induce changes in the arrangement of atoms at GBs, even triggering transitions from disorder to order[63]. Consequently, stabilizing GBs in nanocrystals poses significant challenges. In order to lower the energy of the GBs and increase the stability of the assemblies, we doped GB-Pt NAs with boron (B) (**Figure A7-10**). This was achieved by adding boric acid during the synthesis of the NP building blocks, prior to the assembly process. To both quantify and map the spatial distribution of B across the Pt NPs and NAs, we used atom probe tomography (APT) of Pt samples embedded into a Ni matrix (see Experimental methods, **Figure A7-11**). The B species are originally located at the surface of Pt NPs at a concentration of ~8 at.% (**Figure 7-5a,b**). In contrast, no B is found at the surface of GB-Pt NAs, as evidenced by the 1D composition profile

calculated as a function of the distance to the isosurface (known as proximity histogram) that delineates the Ni matrix/GB-Pt NAs interface (**Figure 7-5c,d**). Distinctive concavities in a 2 nm thin-slice through the APT 3D atom map of GB-Pt NAs (**Figure A7-12**) in **Figure 7-5e**, allows for the identification of GBs formed through the collision of NPs. **Figure 7-5f** highlights that B mostly distributes near GBs, reaching approx. 10 at.% B as quantified by the 1D compositional profile in **Figure 7-5g**.

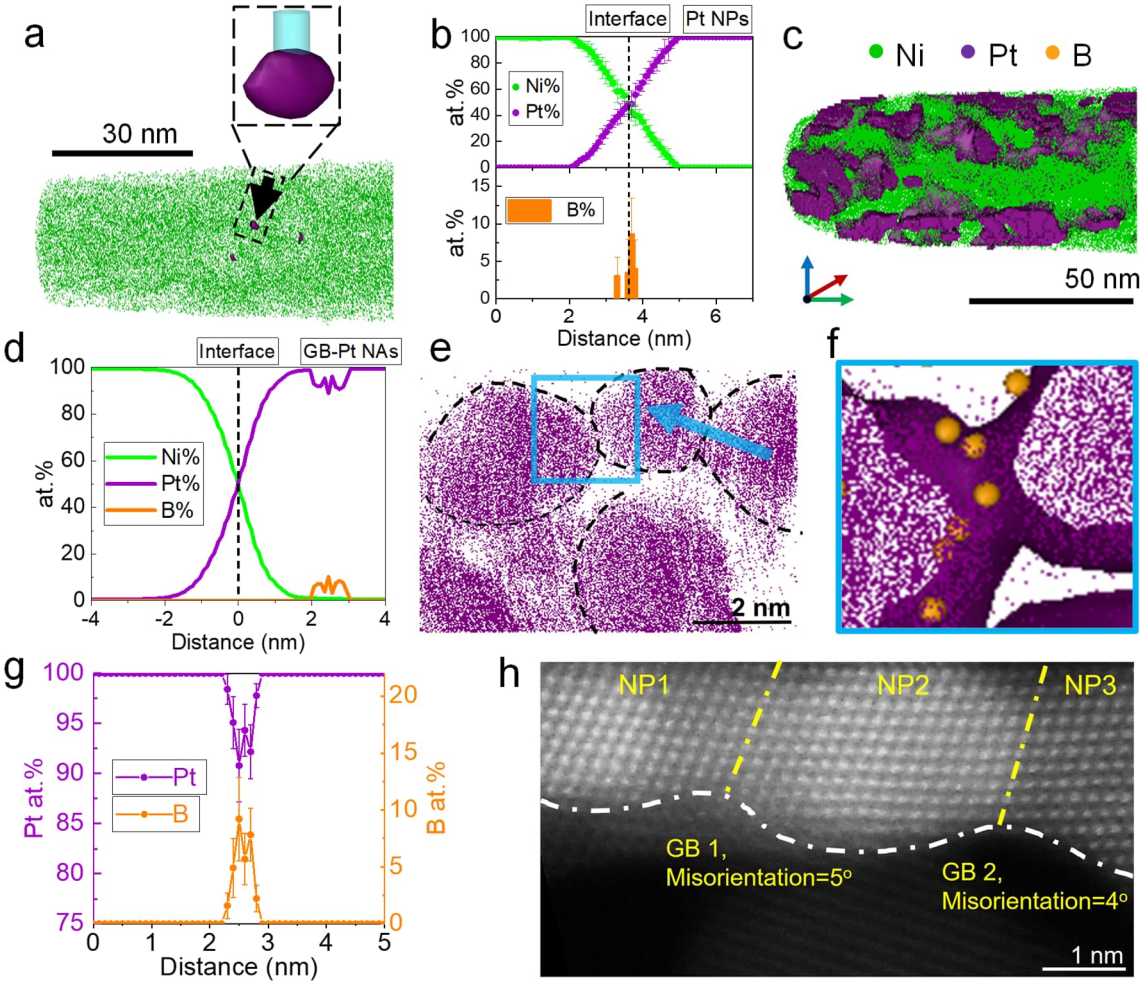

***Figure 7-5**. Segregation of boron at GBs and its impact on the structure of Pt NAs. (a) 3D atom map of Pt NPs embedded in a Ni matrix to allow APT measurements. The inset shows a Pt NP. (b) 1D compositional profiles of Ni, Pt, and B elements within Pt NPs (c) 3D atom maps of GB-Pt NAs embedded in Ni. (d) Proximity histogram of Ni, Pt, and B across the Ni matrix/GB-Pt NAs interface. (e) A 2 nm thin-sliced tomogram from a 3D atom map (**Figure A7-12**) of GB-Pt NAs. The particles are delimited by black lines (f) Extracted tomogram of GB region (B atoms=orange spheres). (g) 1D profiles of Pt and B along the arrow in **Figure 7-5e**. (h) HAADF-STEM image of the low-angle GBs between Pt NPs building blocks within BF-Pt NAs.*

The rapid attachment of Pt NPs by collisions is too fast for surface-bound B species to detach, leading to their kinetic trapping within the GBs. Nearest-neighbor analysis reveals that the Pt-

B distance is ~0.2 nm (**Figure A7-13**), closely matching the value observed in EXAFS (**Figure 7-1e**) and significantly shorter than when B is merely adsorbed on the Pt surface. This shorter distance suggests strong covalent bonding between B and Pt in GB-Pt NAs. Additionally, the Pt-Pt bonds in GB-Pt NAs are shorter than those in Pt NPs, indicating that the segregation of B species in the GBs leads to stronger Pt-B and Pt-Pt bonding.

To investigate the role of B in the assembly of Pt NPs, the source of B was intentionally excluded during synthesis to produce B-free Pt nanoassemblies (referred to as BF-Pt NAs, **Figure A7-14**). BET measurement indicates that BF-Pt NAs also possess a large specific surface area and a highly porous structure, similar to GB-Pt NAs (**Figure A7-15**, **Table A7-1**). HAADF-STEM image of BF-Pt NAs (**Figure 7-5h**) shows crystallites interconnected through low-angle GBs (**Figure A7-16**), despite exhibiting otherwise similar microstructural characteristics to GB-Pt NAs (**Figure 7-6**). The lattices of adjacent Pt NPs are aligned, i.e. there is almost no misalignment to accommodate the transition from one building block to another. Moreover, the coordination number (~8.8, **Figure A7- 17**, **Table A7-2**) and lattice distortion (0.9%, **Figure A7- 18**) of BF-Pt NAs fall between those of Pt NPs and GB-Pt NAs, indicating a critical role of B in achieving the formation of concave GB sites with high coordination number and lattice distortion.

The structural disparities between GB-Pt NAs and BF-Pt NAs can be rationalized by considering the effects of B atoms in high-energy GBs. The relaxation of lattice distortion in metals primarily takes place through mechanisms such as GB sliding, diffusion, or dislocation sliding.[60,248–251] Furthermore, random high-angle GBs are inherently thermodynamically metastable and can progressively disappear by lattice rotation to facilitate site matching,[250] or by GB migration and annihilation at one of the many available free surfaces, thereby removing lattice distortion and partially eliminating the concavities. We postulate that the trapping of B greatly stabilizes the GBs in GB-Pt NAs, limiting atomic rearrangement and effectively suppressing the release of lattice distortion. We performed targeted DFT calculations of the segregation energy of a single B atom at a Σ3 (111) GB (see Experimental methods), which is the most abundant GB we observed experimentally. Adding a B atom to the GB plane, or the immediately adjacent layers, lowers the free energy by -0.363eV, or -0.467eV, respectively (**Figure A7-19**). B-segregation to GBs in Pt-based materials had also previously been reported to be energetically favorable[252], and B at GBs may lower the free energy of high-energy GBs and hence the driving force for migration and annihilation[253,254]. This accounts for the notable

abundance of high-angle GBs in GB-Pt NAs, including higher-energy GBs such as Σ41 and Σ33, accompanied by increased lattice distortion.

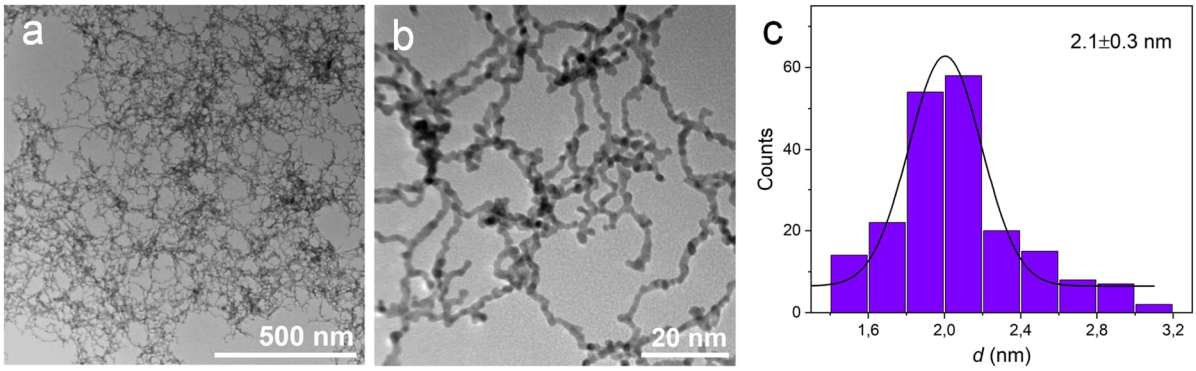

***Figure 7-6**. (a-b) TEM images of BF-Pt NAs with lower and higher resolutions. (c) The size distribution was obtained by analyzing 200 crystallites of BF-Pt NAs derived from TEM images.*

ORR activity

Having successfully synthesized ultrafine Pt NAs with a high density of GB concave sites and lattice distortion, we tested their ORR catalytic performance. Before electrochemical property testing, the synthesized Pt NPs, BF-Pt NAs, and GB-Pt NAs were each dispersed onto a commercial carbon support, making electrodes denoted as Pt NPs/C, BF-Pt NAs/C, and GB-Pt NAs/C respectively, which are benchmarked against commercial Pt/C (see Experimental methods). CVs for these four electrodes are plotted in the insets of **Figure 7-7a-d**, and their respective ECSAs are 95.8, 63.5, 69.7, and 74.1 $m^2\ g_{Pt}^{-1}$.

Despite the loss of surface area due to the assembly process in BF-Pt NAs and GB-Pt NAs, their ECSA remains comparable to commercial Pt/C, which can be attributed to their ultrafine nanowire network geometry with a high porosity[16]. ORR polarization curves are measured in a 0.1 M $HClO_4$ solution saturated with O_2, with iR drop correction applied, and are plotted in **Figure 7-7a-d**, for Pt NPs/C, BF-Pt NAs/C, GB-Pt NAs/C and commercial Pt/C.

The GB-Pt NAs/C shows a remarkable specific activity of 9.18 mA/cm^2 and an impressive mass activity of 6.40 A/mg_{Pt} at 0.9 V versus RHE, i.e. nearly 40 times higher compared to commercial Pt/C (**Figure 7-7e**) and 14.5 times higher than the 2020 U.S. Department of Energy target (0.44 mA/cm2). Compared to state-of-the-art Pt-based ORR nanocatalysts, including pure Pt (grey dots, **Figure 7-7b**) and Pt-based alloys (cyan diamonds, **Figure 7-7f**) from recent publications, the GB-Pt NAs/C (orange star, **Figure 7-7f**) is one of the most efficient ORR catalysts reported to date (see **Table A7-3** for references).

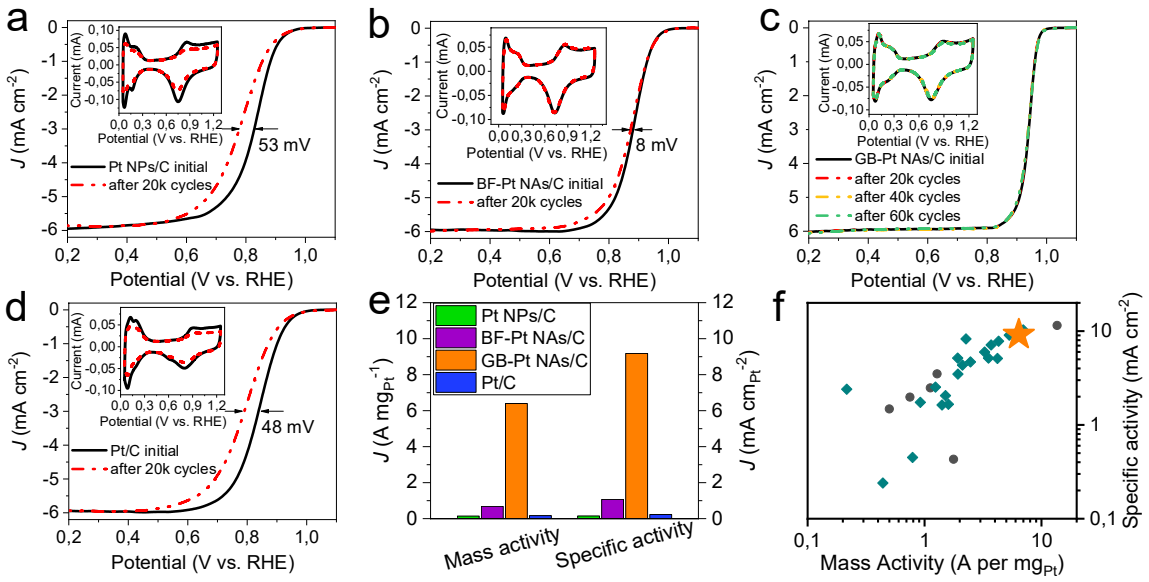

Figure 7-7*. Electrochemical characterization of ORR activity. (a-d) ORR polarization curves of Pt NPs/C, BF-Pt NAs/C, GB-Pt NAs/C and commercial Pt/C pre- and post-durability test. The insets show the CV variations. The solid black line represents the initial test results of the catalyst, while the dashed-dot curves in red, yellow, and green depict the outcomes after the 20000, 40000, and 60000 potential-scanning cycles, respectively. (e) Specific and mass activities at 0.9V versus RHE. (f) The comparison of specific activity and mass activity at 0.9V versus RHE of GB-Pt NAs/C and the state-of-the-art ORR catalysts from the literature (see* ***Table A7-3*** *for references*).

To elucidate the underlying mechanisms driving higher activity of GB-Pt NAs, we performed DFT calculations utilizing both the NP and Σ3 twin boundary models. According to the Sabatier volcano principle governing ORR catalysts, optimal activity occurs when the oxygen binding energy ($E_{binding}$) is ~0.2 eV lower than that on the flat Pt (111) surface[69,80]. In single Pt NPs, the Pt-O bond energies at the corner and edge sites are too high (**Figure 7-8a**) and therefore not active towards ORR. Considering that ~50% of surface atoms on Pt NPs with a size of 2 nm are positioned at corners and edges[255,256], half of the surface sites are not active for ORR. However, when a concave GB site is formed at the surface, the Pt-O binding energies are altered significantly (**Figure 7-8b**). Within the vicinity of GBs, the Pt-O bond undergoes significant weakening (**Figure 7-8c**), nearly reaching the optimal $E_{binding}$. It enables the transformation of initially inactive sites into highly active catalytic sites for ORR (**Figure 7-8d**). The formation of concave GBs at the surface leads to a decrease in $E_{binding}$, which enables the transformation of initially inactive edges and corner sites into highly active catalytic sites for ORR along the nanoassembly structure (**Figure 7-8d**).

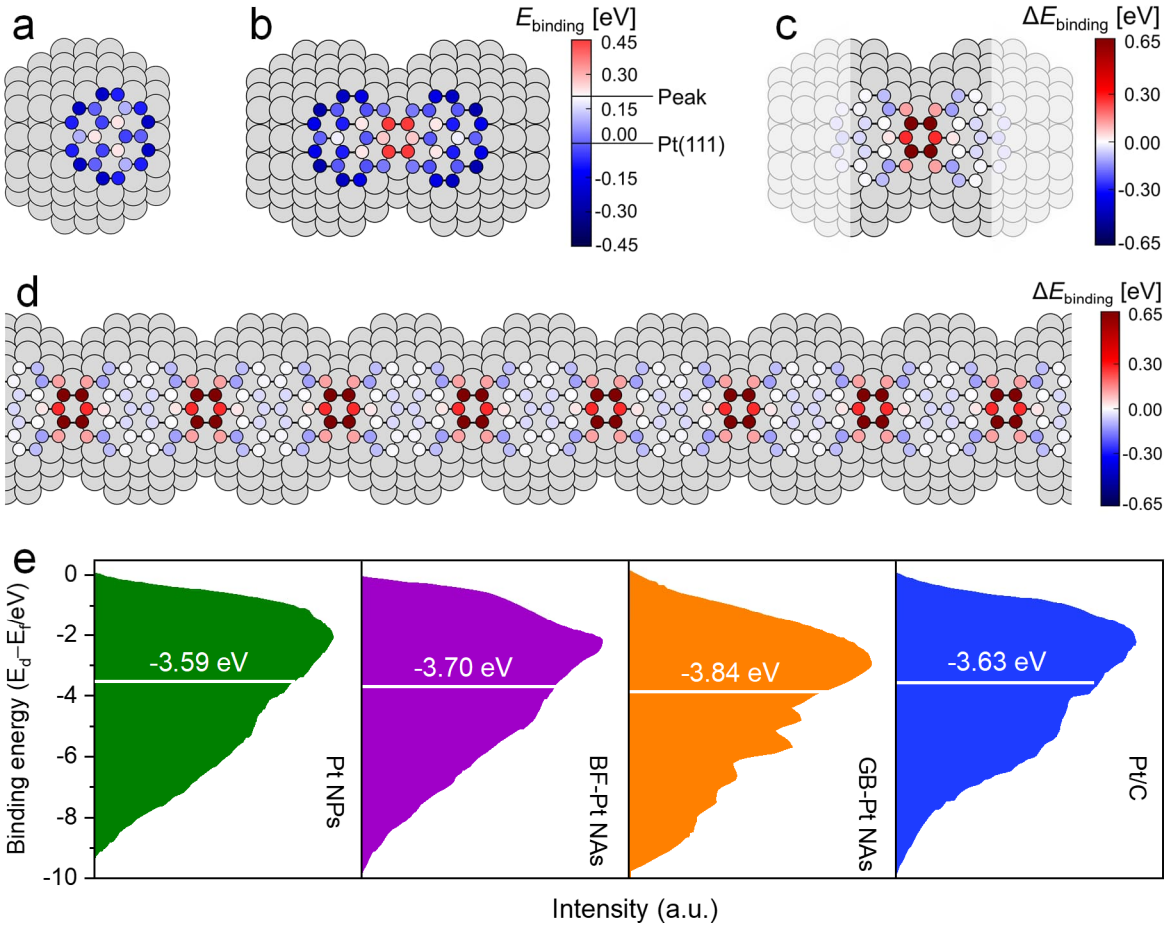

***Figure 7-8**. Mechanisms underlying the enhancement of ORR activity. Calculated binding energies ($E_{binding}$) for O on fcc and hcp sites on the (111) facet of (a) Pt_{201} NP and (b) Pt_{383} Σ3 (111) twin GB model. The values for Pt (111) surface and the peak of the Sabatier volcano are provided as references[257]. Gray spheres represent Pt, and colored small dots represent oxygen adsorption sites. (c) Difference in binding energy ($\Delta E_{binding}$) of O on the building block of Pt_{383} Σ3 (111) twin GB and the Pt_{201} NP. (d) Array of packed Pt_{383} Σ3 (111) twin GB blocks model. (e) Surface valence band photoemission spectra of Pt NPs, Pt/C, BF-Pt NAs and GB-Pt NAs.*

DFT calculations conducted using the slab model reveal that the oxygen binding energy at the concave site of Σ3 GB closely approaches the optimal value observed near the peak of the volcano plot (**Figure A7-20**), indicating its superior activity towards ORR. In contrast, the oxygen binding energy at the concave site lacking GBs is significantly weaker compared to that on the flat (111) surface (**Figure A7-20**), highlighting the essential role played by both concave geometry and GBs in enhancing ORR activity. This suggests that the synergistic effects of concave geometry and GBs are indispensable for optimizing catalytic performance in ORR.

The reduction in $E_{binding}$ is further experimentally corroborated by a gradual reduction in the d-band center observed in surface valence band photoemission spectra[225], with the trend as follows: Pt NPs (-3.59 eV) > Pt/C (-3.63 eV) > BF-Pt NAs (-3.70 eV) > GB-Pt NAs (-3.84 eV) (**Figure 7-8e**). The optimization of $E_{binding}$ of Pt NAs with a high number of concave GB sites at the surface can be attributed to both the increased coordination number and lattice distortion, induced by the GBs[236–239].

Stability during catalysis

The electrochemical durability of the four electrodes is assessed by subjecting them to 20000 cycles in a 0.1 M $HClO_4$ solution in the range 0.6–1.1 V vs. RHE (**Figure 7-7a-d**). The results are presented in **Figure 7-9a**.

Following cycling, both Pt NPs/C and commercial Pt/C exhibited notable negative shifts in their ORR polarization curves, accompanied by a 20–30% decline in specific activity and 50% mass activity. In contrast, for BF-Pt NAs/C, the specific activity and mass activity only shift by 13.1% and 14.7%, respectively. Encouragingly, upon reaching 20000 cycles, the shift in ORR polarization curves of GB-Pt NAs/C is negligible. The specific activity only experiences a modest loss of 2.2%, while the mass activity decreases by merely 2.9%, highlighting their outstanding durability (**Figure 7-9a**). Even after 60000 cycles, the specific and mass activity of GB-Pt NAs/C demonstrate almost negligible activity decay (5.1% loss of specific activity, 7.5% loss of mass activity).

To the best of our knowledge, the excellent initial activity of GB-Pt NAs, paired with its exceptional durability makes it the highest-performing ORR catalyst after 60000 accelerated durability tests reported to date.

The superior stability of the nanoassemblies (both GB-Pt NAs and BF-Pt NAs) compared to the NPs can be attributed to their different geometry. While the small Pt NPs migrate and aggregate during electrochemical testing (**Figure 7-10a,b**), resulting in a significant decrease in ECSA[16], the nanowire geometry of Pt NAs with multiple anchoring points on the carbon support makes them less mobile during the accelerated tests (**Figure 7-10c,d**)[16]. Therefore, the Pt NAs maintain their ECSA during testing.

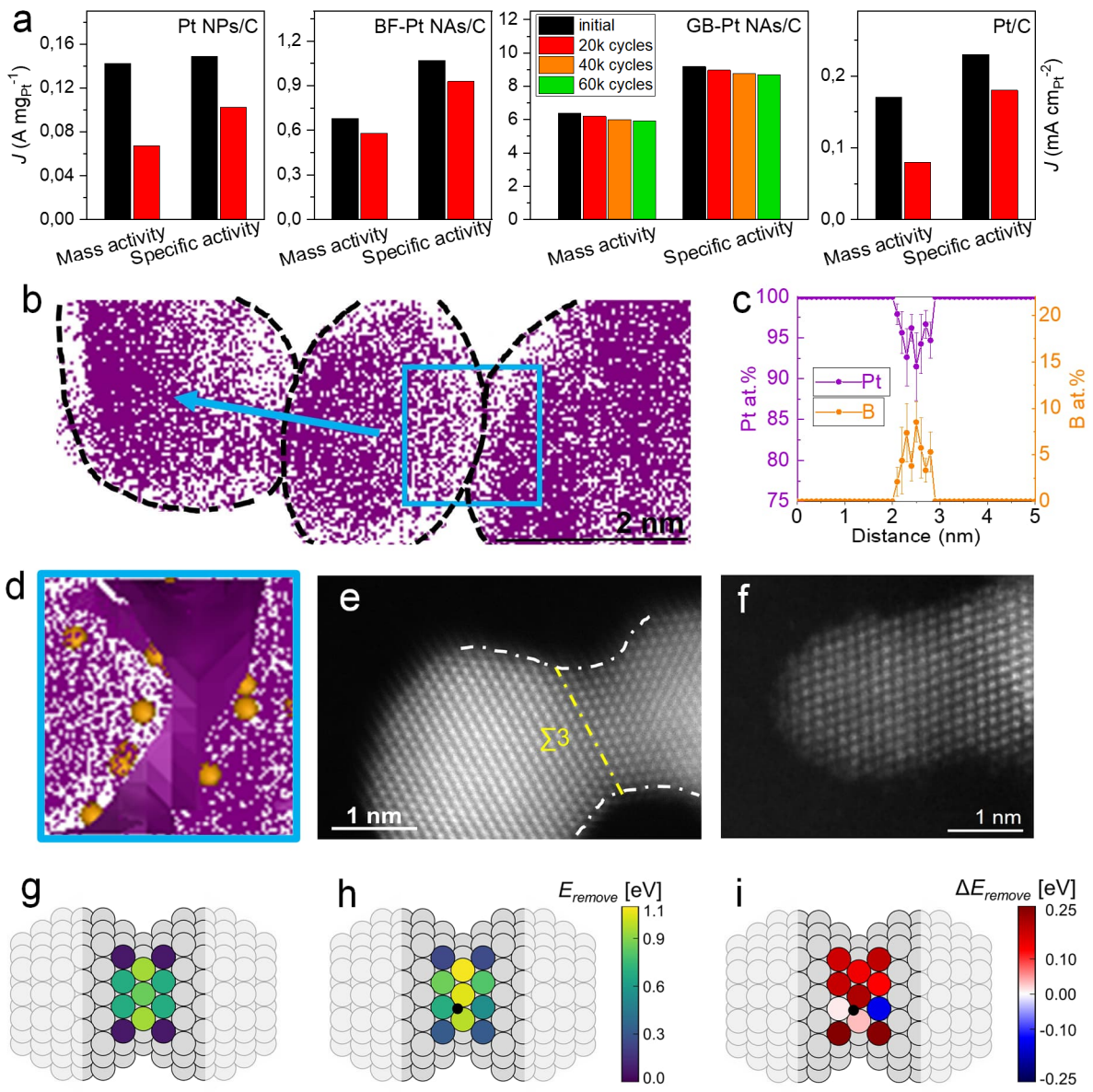

Figure 7-9. *Study of the mechanisms contributing to durability enhancement. (a) Mass and specific activities before and after durability test. (b) Tomogram from an APT 3D atom map (**Figure A7-21**, **Figure A7-22**) of GB-Pt NAs after 60k durability test. (c) 1D composition profiles of Pt and B along the blue arrow in **Figure 7-9b**. (d) Tomograms of the region delineated by the blue box in **Figure 7-9b**(orange spheres are B atoms). HAADF-STEM image of (e) GB-Pt NAs after 60k durability test and (f) BF-Pt NAs after 20k durability test. E_{remove} from the GB region without B (g) and with a B atom intercalated on the sublayer of the GB (h). (i) Change in E_{remove} upon addition of a B atom. The B atom is represented with a black circle.*

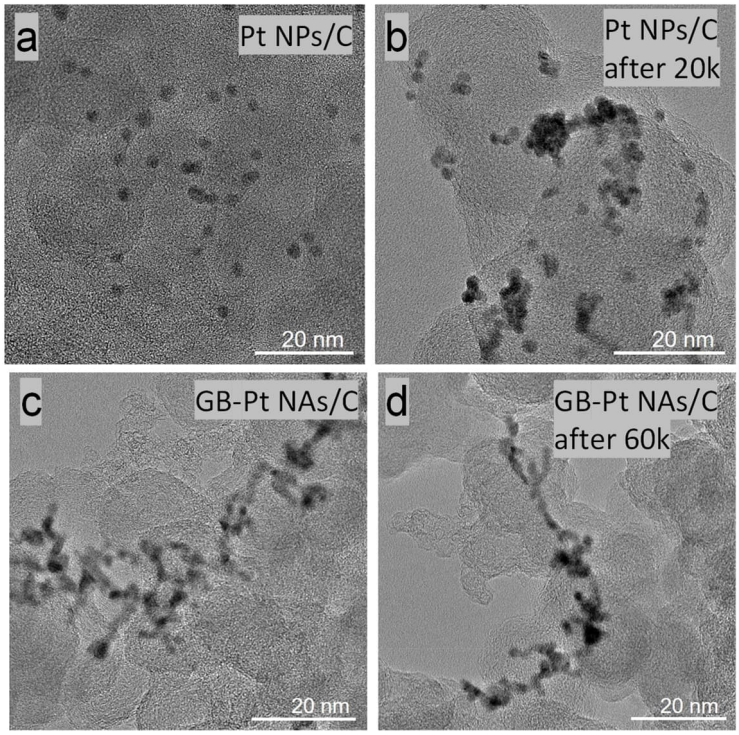

***Figure 7-10**. (a-b) TEM images of Pt NPs/C before (a) and after (b) 20.000 durability test. (c-d) TEM images of GB-Pt NAs/C before (c) and after (d) 60.000 durability test. A defocus was purposely introduced to visualize better the carbon support.*

Following durability testing, no significant changes were observed in the structure and chemical composition of GB-Pt NAs (**Figure 7-9b–e**, **Figure 7-11**), with the B concentration on the GBs maintained at ~10 at.%. In the overall catalyst, the B concentration remained unchanged at ~1 at.%. The concave GBs that connect NP building blocks in GB-Pt NAs is preserved after testing (**Figure 7-9e**, **Figure 7-11**). In addition to Σ3 GBs, even higher-energy GBs such as Σ11 and Σ33 are observed post-testing. This demonstrates the exceptional structural stability of GB-Pt NAs. In BF-Pt NAs, both the number of low-angle GBs and concave sites get reduced during the durability testing (**Figure 7-9f**), which explains their larger loss in specific and mass activity compared to GB-Pt NAs/C.

To validate the ORR performance observed at the RDE level, H_2-air proton exchange membrane fuel cells (PEMFC) tests were conducted using fuel cells with either GB-Pt NAs/C or BF-Pt NAs/C as cathode catalyst, each with a Pt loading of 0.1 mg/cm^2. The H_2-air fuel cell with GB-Pt NAs/C exhibited a current density of 1.52 A/cm^2 at 0.6 V and achieved a peak power density of 0.935 W/cm^2, surpassing the performance of the BF-Pt NAs/C-based system, which reached 1.09 A/cm^2 at 0.6 V and peak power density of 0.814 W/cm^2 (**Figure A7-23**). Moreover, the H_2-air PEMFC with GB-Pt NAs/C operated stably at a constant voltage of 0.6

V for over 100 h, displaying negligible current density decay (~2.1%). In contrast, the BF-Pt NAs/C-based fuel cell showed a significant degradation of ~22.7% under the same conditions.

The superior durability of GB-Pt NAs compared to BF-NAs points towards B segregation at GBs as an effective strategy for stabilizing these high-energy, metastable defects. B segregation plays a dual role in enhancing the structural stability of GB-Pt NAs in two ways. First, it increases the GB strength (**Figure A7-24**). B segregation leads to the formation of strong covalent B-Pt bonds, which enhance cohesion at the GBs and reduce their susceptibility to migration and annihilation. Second, it stabilizes the surface Pt atoms near GBs (**Figure 7-9g-i**). B segregation at the GBs increases the energy required to remove surface Pt atoms near the GBs. EXAFS analysis indicates that B segregation results in shorter Pt-Pt bonds within GB-Pt NAs (**Table A7-2**), thereby strengthening surface Pt-Pt interactions. This stabilization effectively inhibits the dissolution of surface Pt atoms and maintains the concave geometry near the GBs. The combined effect of B segregation—reinforcing the GBs and stabilizing surface Pt atoms—significantly enhances the structural stability of GB-Pt NAs. Consequently, the durability tests did not result in significant structural changes or notable degradation in the ORR performance of GB-Pt NAs.

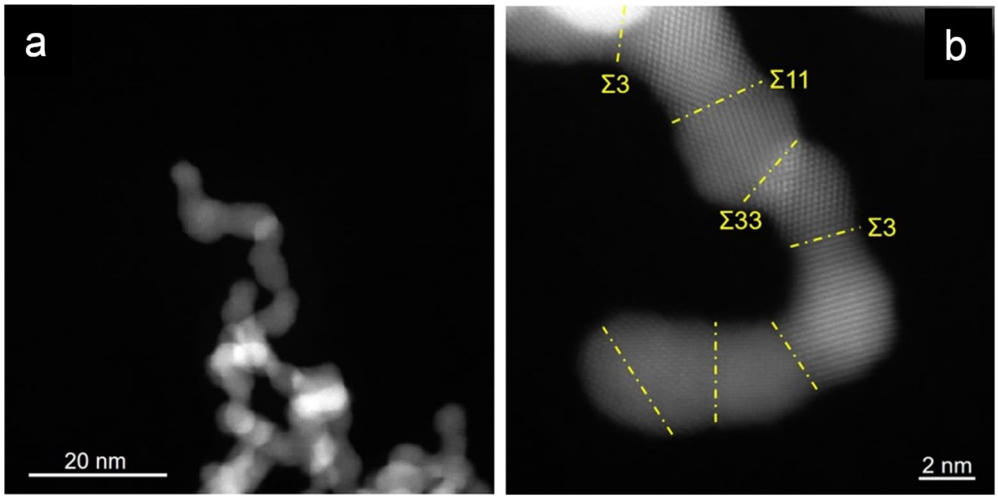

***Figure 7-11**. Low (a) and high-magnification (b) HAADF-STEM images of GB-Pt NAs after durability testing, with the GBs between the Pt NP building blocks within the GB-Pt NAs indicated by yellow dashed lines.*

7.3 Conclusions

To summarize, we propose a design strategy for ORR catalysts to enhance their mass activity and durability. The mass activity is optimized by simultaneously maintaining the inherently high ECSA of ultra-small (~2 nm) Pt NPs, while substantially enhancing their specific activity.

This is achieved by assembling the Pt NPs into ultrafine, GB-rich nanowire-shaped Pt nanoassemblies (GB-Pt NAs). The assembly process results in the formation of multiple concave GB sites at their surface terminations, which increase the local coordination number. Additionally, it induces lattice distortions in the vicinity of the GBs. These two factors combined lower the oxygen binding energy, thus activating previously inactive ORR sites. As a consequence, GB-Pt NAs (rich in concave GB sites) exhibit outstanding ORR activity, with specific activity and mass activity reaching 9.18 mA/cm2 and 6.40 A/mg_{Pt} at 0.9 V vs. RHE, respectively, representing enhancements of 40-fold and 38-fold compared to commercial Pt/C catalysts. Additionally, B-segregation at the GBs is proven to lower their energy and to help maintain excellent ORR activity for 60,000 potential-scanning cycles (0.6 to 1.1 V vs. RHE). Future research evaluating the performance of GB-Pt NAs/C in practical fuel cell tests could provide a more comprehensive understanding of the ORR performance of these catalysts under real fuel cell conditions, and explore the B stabilization effects in a practical device.

Our findings present an effective strategy for enhancing the activity and durability of ORR catalysts, which can be applied across a range of catalytically active NP systems.

7.4 Experimental methods

Chemicals and materials

Platinum (II) acetylacetonate ($Pt(acac)_2$, 97%, Sigma Aldrich), oleylamine (OAm, 70%, Sigma Aldrich), diethylamine (DEA, Sigma Aldrich), sodium citrate dihydrate ($C_6H_9Na_3O_9$, Sigma Aldrich), citric acid ($C_6H_8O_7$, Sigma Aldrich), boric acid (H_3BO_3, Sigma Aldrich), cyclohexane (C_6H_{12}, Sigma Aldrich), ethanol (Sigma Aldrich), isopropanol (Sigma Aldrich), perchloric acid ($HClO_4$, 70%-72%, Sigma Aldrich), commercial carbon support (XC-72R), Nafion (5%, Sigma Aldrich), commercial Pt/C catalyst (20 wt%, Johnson Matthey (JM) Inc), dialysis tubing (Thermo Scientific SnakeSkin, 3.5K MWCO), and dialysis tubing closures (Thermo Scientific) were used as received.

Synthesis of Pt NPs

Initially, 9 mL of OAm (27.4 mmol) underwent degassing by argon at 80°C for 20 minutes, followed by the addition of 0.051 mmol of Pt(acac)2 (20 mg) in a 25 mL round-bottomed flask. After vigorous magnetic stirring for 30 minutes, homogeneous complexation of Pt(acac)2 with OAm was achieved. The flask was then transferred to an oil bath preheated to 210°C and allowed to equilibrate for 10 minutes until reaching the desired temperature. Subsequently, 100

sccm of carbon monoxide was introduced and bubbled through the mixture for 1 minute. The flask was then removed from the oil bath and allowed to cool naturally. The OAm-capped Pt NPs were precipitated with ethanol by centrifugation, followed by re-dispersion in cyclohexane. This precipitation/re-dispersion process was repeated three times. The resulting OAm-capped Pt NPs were dispersed in 5 mL of cyclohexane for ligand exchange to citrate. Subsequently, citrate (Sigma Aldrich) was used to replace OAm on the surface of the Pt NPs. Ligand exchange from OAm to citrate was conducted in two steps. (1) 5 mL OAm-capped Pt NPs were mixed with 5 mL DEA and stirred for 24 h. The solution was centrifuged, washed with ethanol, and redispersed in 10 mL of DEA. The DEA-capped Pt NPs were subjected to stirring for 24 h, leading to the complete replacement of OAm with DEA, as demonstrated in **Figure A7-3**. The Pt NPs were then washed with ethanol and re-dispersed in 5 mL DI H2O. (2) 1 mL 10 mg/mL sodium citrate and 1 mL 10 mg/mL boric acid were added in 5 mL aqueous DEA-capped Pt NPs, followed by sonicating for 1 h and magnetic stirring for 24 h. The complete ligand exchange from DEA to citrate was confirmed through Fourier-transform infrared spectroscopy, as depicted in **Figure A7-3**. For BF-Pt NAs, 1 mL 10 mg/mL citric acid rather than boric acid was adopted in this step. The citrate-capped Pt NPs were washed and re-dispersed in DI H_2O.

Preparation of Pt NAs

Initially, to remove impurity ions from the citrate-capped Pt NP solution, a dialysis method was employed. The Pt NP solution was introduced into dialysis tubing, which was then suspended in a 1 L beaker containing DI water. Magnetic stirring was applied to the DI water to facilitate the diffusion of impurity ions from within the dialysis tubing. The DI water was refreshed twice daily, and the dialysis process was carried out for three days. Subsequently, a flow of high-purity H2 gas, with a flow rate of 200 sccm, was continuously injected and bubbled through a 10 mL solution of ~3.6 μM citrate-capped Pt NPs for 5 hours. During this process, a noticeable color change from grayish-brown to clear occurred, indicating the formation of GB-Pt NAs. After cessation of the H2 gas purging, the solution was allowed to settle for 2 hours, enabling the GB-Pt NAs to settle at the bottom of the beaker. The supernatant was then carefully removed using a pipette, and the GB-Pt NAs underwent thorough washing with DI water. The synthesis of GB-Pt NAs followed the same procedure employed for BF-Pt NAs, with the exception of omitting boron in the Pt NP solution.

Electron microscopy

High-angle annular dark-field scanning transmission electron microscopy imaging was conducted using a Thermo Fisher Titan Themis 80-300 microscope equipped with probe Cs correction, operating at an accelerating voltage of 300 kV. Additionally, high-resolution transmission electron microscopy (HR-TEM) was performed utilizing a Cs image aberration-corrected Thermo Fischer Titan Themis 60-300 microscope, also operating at 300 kV. The estimation of particle size distribution was carried out employing Nano Measurer 1.2 software. The acquired HAADF-STEM images were subjected to analysis and processing using Gatan Microscopy Suite 3.0 (GMS 3.0) Software. The identification of crystallographic planes and zone axis was achieved by evaluating the interplanar spacing (d-spacing) and angles derived from FFT images. The identification of GB types was accomplished by examining the misorientations between two neighboring grains possessing the same zone axis.

The crystal lattice parameters, atomic column positions, and local lattice deformation observed in HAADF-STEM images were investigated employing the MATLAB program known as STATSTEM[96]. STATSTEM is a software tool designed to extract atomic positions in real space from high-resolution STEM images. In contrast to the Fourier space-based strain calculation approach employed by the geometric phase analysis algorithm, STATSTEM offers a method for identifying and refining atomic column positions in the real space through the fitting of two-dimensional Gaussians in the local maxima of intensity (*i.e.*, the atomic columns). Utilizing real space methods, as provided by STATSTEM, offers the advantage of circumventing artifacts that may arise from the Fourier transform.

X-ray characterization

The high-resolution XRD patterns were obtained utilizing a Bruker Powder X-ray diffractometer equipped with a Cu Kα radiation source. For the analysis of crystallite size and non-uniform strain, the Williamson-Hall equation $\beta\cos\theta=K\lambda/\langle D\rangle+4\varepsilon\sin\theta$ was employed. Here, β represents the full width at half maximum (FWHM) of the diffraction peaks, K is the Scherrer constant, λ is the wavelength, $\langle D\rangle$ corresponds to the average crystallite size, and ε denotes the strain.

X-ray photoelectron spectroscopy (XPS) data were collected using an Al Kα X-ray Photoelectron Spectrometer (Thermo Scientific) and calibrated based on the C1s peak at 284.8 eV. The XPS data were subjected to analysis and fitting using a composite function (30% Lorentzian+70% Gaussian) with the aid of the Avantage software.

The determination of the valence band spectra's center of gravity (ε_d) involves calculating the integral $\varepsilon_d = \frac{\int N(\varepsilon)\varepsilon d\varepsilon}{\int N(\varepsilon) d\varepsilon}$ within the energy ranging -10 eV to -1 eV, with N(ε) denoting the density of states.

X-ray absorption spectroscopy (XAS) measurements were carried out at the BL14W1 beamline of the Shanghai Synchrotron Radiation Facility, where the synchrotron storage ring operated at an energy of 3.5 GeV and the linear electron accelerator operated at 150 MeV.

Atom probe tomography

The Pt NPs or GB-Pt NAs were incorporated into a Ni matrix through the utilization of a co-electrodeposition technique[258]. The experimental setup involved employing a Cu foil (0.2 cm^2) as the working electrode, which was etched using 0.5 M H_2SO_4, and a Pt mesh (2 cm^2) serving as the counter electrode. The electrolyte consisted of a well-mixed aqueous nickel solution (5 mL) containing 1.5 g $NiSO_4 \cdot 6H_2O$ and 0.225 g citric acid, along with 10 mg of Pt NPs or GB-Pt NAs, which underwent ultrasonication for 1 hour. The working electrode was subjected to a constant current of -19 mA for 500 s, ensuring the co-encapsulation of Pt NPs or GB-Pt NAs within the Ni film on the Cu foil.

To prepare a needle-shaped APT specimen, a Ga-plasma focused ion beam (FEI 600 DualBeam) was utilized following the standard APT sample fabrication procedure[253,254]. The embedded Pt nanoassemblies or nanoparticle within the Ni film caused protrusions on its surface. These regions were carefully sectioned and transferred onto Si coupons as lamellas. The lamella was then sharpened to achieve a needle-shaped APT specimen.

The needle-shaped specimens were introduced into a LEAP 5076 XS instrument (Cameca) for analysis. All APT experiments were conducted in pulsed laser mode, employing specific parameters such as a temperature of 50 K, a detection rate of 0.8%, a laser energy of 60 pJ, and a laser pulse frequency of 125 kHz. The obtained data underwent analysis and reconstruction utilizing the standard voltage reconstruction protocol, facilitated by the commercially available IVAS 3.8.4 software (Cameca).

Other characterization methods

The zeta potential of the Pt nanoparticle solution loaded into quartz cuvettes was determined using a Zetasizer Nano-ZS instrument (Malvern Instruments, UK) in high-resolution mode. Fourier-transform infrared spectroscopy (FTIR) spectra were acquired using a Bruker Tensor 27 FTIR spectrophotometer. Furthermore, the Pt concentration in the ink was quantified via

inductively coupled plasma atomic emission spectroscopy (ICP-AES) using a 710-ES instrument from Varian.

Electrochemical characterization

The electrochemical measurements were carried out using a CHI660E electrochemical workstation (CHI Instrument) with a rotating disk electrode (PINE Instrument) at room temperature. The glassy carbon electrodes (diameter=5mm, geometric area=0.196cm^2), Pt wire and Ag/AgCl electrode (3.0 M KCl) were used as working electrode, counter electrode, and reference electrode, respectively. All the potentials were converted to RHE. The RHE calibration of 3.0 M KCl Ag/AgCl reference electrode was performed in a high purity H_2 saturated 0.1 M $HClO_4$ aqueous solution where polished Pt wires were used as the working and counter electrodes. The linear scanning voltammetry was run at a scan rate of 1 mV/s, and the potential of zero current was taken as the reaction potential of the hydrogen electrode. The potential measured with the 3.0 M KCl Ag/AgCl electrode were calculated as following: E(RHE) = E(Ag/AgCl) + 0.269V. The GB-Pt NAs were dispersed in DI water by sonicating for 1 h, followed by adding commercial Vulcan carbon (XC-72) with a mass four times than Pt (wt% of Pt=20%) and sonicating for another 1 h to make Pt /C samples. Then, the GB-Pt NAs/C were dispersed in the mixture of isopropanol and Nafion (5%) (v:v=1:0.005) to form a homogeneous ink by sonicating for 1 h. Prior to the electrochemical test, the Pt particles were uniformly dispersed onto the commercial Vulcan support via the sufficient ultrasonic dispersion (named as Pt NPs/C, BF-Pt NAs/C and GB-Pt NAs/C). The concentration of Pt was controlled to be 0.25 mg_{Pt}/mL measured by ICP-AES. The uniform catalyst layer was prepared by pipetted 5 μL of the ink onto the glassy carbon electrode followed by drying at ambient conditions. The loading amount of Pt was controlled at 6.4 μg/cm^2.

The cyclic voltammetry tests were conducted in N_2-saturated 0.1 M $HClO_4$ aqueous solution with a scan rate of 50 mV/s. The ECSA was calculated by integrating hydrogen adsorption charge on CV curves by assuming a value of 210 μC/cm^2 for the adsorption of a hydrogen monolayer. The ORR tests were performed in O_2-saturated 0.1 M $HClO_4$ electrolyte with a scan rate of 10 mV/s with a rotating rate of 1600 rpm. The current densities of the ORR polarization curves were normalized to the geometric area of the glassy carbon electrode (0.196 cm^2). The specific and mass activities were calculated by normalizing the kinetic current to the ECSA and mass of the loading Pt, respectively. The accelerated durability tests were carried out by applying the cyclic potential sweeps in the range of 0.6 V–1.1 V vs. RHE at a sweep

rate of 100 mV/s for 60000 cycles in O_2-saturated 0.1 M $HClO_4$ electrolyte at room temperature.

DFT calculations

All density functional theory calculations were carried out using the Vienna ab initio simulation package (VASP)[259], employing the projected-augmented wave (PAW) method to describe core electrons[260]. A basis set cutoff of 400 eV was utilized, consistent with previous studies[243]. The generalized gradient approximation (GGA) with the Perdew-Burke-Ernzerhof (PBE) functional was employed to evaluate the exchange-correlation energy for the Σ3 (111) [110] twin GB model. Its revised version from Hammer et al. (RPBE) was utilized for Pt (111) slab models, Pt_{201} NP models and Pt_{383} Σ3 [110] (111) GB models[261].

The Pt (111) surface was constructed as a four-layer ($2\sqrt{3}\times2\sqrt{3}$) slab. The bottom two layers of Pt (111) surface were kept frozen, while the other layers and adsorbed molecules were allowed to be relaxed. A vacuum thickness of 14 Å was added to surface slab models to prevent appreciable interaction between periodic images. The Monkhorst-Pack scheme was employed to sample the Brillouin zone using a Γ–centred 3×3×1 k-point grid for atomic structure optimization[262]. For Pt_{201} NP and Pt_{383} Σ3 [110] (111) GB models, a vacuum space of >14 Å was included to eliminate interactions between periodic images. During structural optimization, only the Γ point was sampled for the Brillouin zone, with energy and force convergence thresholds set at 10^{-6} eV and 0.01 eVÅ^{-1}, respectively.

The oxygen binding energy, denoted as E_{binding}, was calculated using the equation:

$$E_{binding} = E^{Y}_{Pt+O} - E^{Y}_{Pt} - \mu_O \qquad \textit{Eq. 7-1}$$

where *Y* stands for slab, NP or GB. E^{Slab}_{Pt+O}, E^{NP}_{Pt+O} and E^{GB}_{Pt+O} represent the total energies of the Pt (111) surface slab models, Pt_{201} NP models and Pt_{383} Σ3 [110] (111) GB models with the adsorbed O species, respectively.

Similarly, E^{Slab}_{Pt}, E^{NP}_{Pt} and E^{GB}_{Pt} stand for the total energies of the Pt (111) surface slab models, Pt_{201} NP models and Pt_{383} Σ3 [110] (111) GB models without the adsorbed O species, respectively. μ_O corresponds to the chemical potential of O, derived as half of the total energy of an isolated O_2 molecule. The calculated binding energy of O on the FCC hollow site of Pt(111) is -1.56 eV, consistent with the value reported by Nørskov et al. (-1.57 eV)[69].

The energy required for the removal of one Pt atom from Pt383 Σ3 [110] (111) GB models, with or without a B atom, is denoted as E_{remove}. This energy is calculated using the following equations:

For removal without a B atom:

$$E_{remove} = E_{Pt}^{GB} - E_{Pt}^{GB+Vac} - \mu_{Pt} \qquad \textit{Eq. 7-2}$$

For removal with a B atom:

$$E_{remove} = E_{Pt+B}^{GB} - E_{Pt+B}^{GB+Vac} - \mu_{Pt} \qquad \textit{Eq. 7-3}$$

where E_{Pt}^{GB} and E_{Pt}^{GB+Vac} represent the total energies of Pt_{383} Σ3 [110] (111) GB models without and with a Pt vacancy, respectively. Similarly, E_{Pt+B}^{GB} and E_{Pt+B}^{GB+Vac} represent the total energies of Pt_{383} Σ3 [110] (111) GB models without and with a Pt vacancy in the presence of a B atom. μ_{Pt} corresponds to the chemical potential of Pt, which is derived from the total energy of the Pt FCC bulk phase per atom.

The Σ3 (111) [110] twin GB is selected as a representative high-angle GB. The supercell shown in **Figure A7-19** contains 12 atomic layers (6 atoms per layer, 72 atoms per cell) and represents a cell doubled along the $[1\bar{2}1]$ and tripled along [111] directions. The GB supercell includes one GB where a B solute atom was placed at the GB layer such that possible interactions between them are avoided. The single B atom replaces one of six equivalent host atoms in the GB plane as shown in **Figure A7-19**. The dimension of all the models was fixed during structural optimizations allowing relaxations only along the direction perpendicular to the GB plane. A 2x8x16 Monkhorst-pack k-point mesh was used in all calculations of GB structures. The force convergence criterion for atomic relaxation was set to 0.02 eVÅ^{-1}.

The ability of a heteroatom *X* to segregate to the GB can be characterized by the segregation energy given by:

$$E_{seg} = (E_{Pt+B}^{GB} - E_{Pt}^{GB}) - \left(E_{Pt+B}^{bulk} - E_{Pt}^{bulk}\right) \qquad \textit{Eq. 7-4}$$

Here, $E_{Pt}^{GB}, E_{Pt+B}^{GB}$, E_{Pt}^{bulk} and E_{Pt+B}^{bulk} are the total energy of the pure Pt GB, GB in presence of the B atom, pure bulk Pt and bulk Pt with heteroatom *B* respectively. A negative segregation

energy indicates that the heteroatoms prefer to segregate towards GB from the bulk environment.

The conventional coordination number describes the number of atoms, ions, or molecules surrounding a central atom or ion as its first-nearest neighbors within a complex, coordination compound, or crystal. In contrast, the generalized coordination number expands upon this concept by incorporating a weighted average of both first-nearest and potentially second-nearest neighbors[263]:

$$GCN_i = \sum_{j=1}^{n} \frac{CN_j}{\{CN_j\}_{max}} \qquad \textit{Eq. 7-5}$$

Here, GCN_i represents the generalized coordination number of atom i, with n denoting the total number of first-nearest neighbors. CN_j denotes the conventional coordination number of these first-nearest neighbors, while $\{CN_j\}_{max}$ indicates its maximum value.

8 Grain Boundary Engineering for Efficient and Durable Electrocatalysis

Note: The following Chapter is based on the publication “Grain Boundary Engineering for Efficient and Durable Electrocatalysis”, by X. Geng, M. Vega-Paredes et al., in *Nature Communications* 2024, 15, 8534. Therefore, the personal pronoun ”we” is used throughout this chapter to refer to the group of researchers that were part of this specific study.

Having seen the potential of defects and grain boundaries to enhance the catalytic activities of nanomaterials, Chapter 8 deals with how to control the grain boundary density and which structural changes induced by grain boundaries are responsible for the enhanced catalytic activity.

Grain boundaries in noble metal catalysts have been identified as critical sites for enhancing catalytic activity in electrochemical reactions such as the oxygen reduction reaction. However, conventional methods to modify grain boundary density often alter particle size, shape, and morphology, obscuring the specific role of grain boundaries in catalytic performance. This study addresses these challenges by employing gold nanoparticle assemblies to control grain boundary density through the manipulation of nanoparticle collision frequency during synthesis. We demonstrate a direct correlation between increased grain boundary density and enhanced two-electron oxygen reduction reaction activity, achieving a significant improvement in both specific and mass activity. Additionally, the gold nanoparticle assemblies with high grain boundary density exhibit remarkable electrochemical stability, attributed to boron segregation at the grain boundaries, which prevents structural degradation. This work provides a promising strategy for optimizing the activity, selectivity, and stability of noble metal catalysts through precise grain boundary engineering.

8.1 Introduction

In heterogeneous catalysis, the catalysts’ activity and stability are critical factors for practical applications[264]. Integration of strain, through incorporating microstructural defects or doping, is an effective strategy for synthesizing highly active nanocatalysts [22,59–61,254,265–269]. Lattice strain modulates the surface electronic structures, i.e. d-band center and width, which can be used for optimizing the binding energy of reaction intermediates and hence reducing the overall energy barrier for specific reactions[78,270]. In addition, microstructural defects offer distinctive coordination environments and surface configurations, which also tune the electronic structures

and reaction pathways[22,59–61]. Grain boundaries are two-dimensional structural defects that can effectively synergize these strategies: they can induce local lattice strain[59,60], atomic step ridges[60], and offer unique active sites for reactions like the four-electron oxygen reduction reaction.[239,271–274] For instance, Maillard et al. demonstrated that Pt–Ni nanocrystals with increased surface distortion exhibit superior four-electron ORR activities compared to their less defective counterparts.[239,273,274] However, due to the challenge of introducing GBs in nanocatalysts in a controlled manner, the understanding of how GBs modulate catalytic activity and their potential to catalyze other reactions remains limited. Existing strategies for tuning GB density modify also the size, shape and morphology of nanocatalysts, hampering the interpretation of the relationship between GBs and catalytic activity.[271] Our understanding is also limited by incomplete characterization of GB type distribution, their atomic arrangement and local composition. This lack of understanding leads to a negligence of the potential of GBs to regulate not only the catalytic activity but also selectivity towards certain pathways. For instance, having an active catalyst for oxygen reduction,[271,272] that is also selective towards its two-electron pathway would enable the electrochemical production of hydrogen peroxide (H_2O_2), a chemical widely used in various industries.[5,56,275]

In addition, the stability of GBs during electrocatalysis is also debated. Some studies suggest that Pt GBs are stable during four-electron ORR,[271,276] while others report poor stability of GBs in polycrystalline PtCo nanowires compared to single-crystal counterparts. Atoms at GBs are thermodynamically unstable due to their high energy, which can lead to structural degradations and catalyst deactivation.[272] Inconsistent stability reports may be due to local compositional variations and trace impurities at GBs,[253] which are challenging to detect with conventional techniques but have been reported to effectively stabilize these defects. For instance, boron (B) is reported to stabilize the GBs of bulk polycrystals by lowering their energy,[277,278] enhancing overall structural integrity. However, its effect on GB stabilization in nanocatalysts remains unexplored. Advanced atomic-scale characterization methods, such as atom probe tomography (APT),[253] HAADF-STEM,[279] and 4D-STEM,[280] are essential for investigating the local composition and structure near GBs, thus advancing our understanding of their catalytic roles.

Here, we have achieved the formation of GB-rich nanoparticles assemblies through the collision, attachment, and coalescence of Au NPs' surfaces devoid of capping agents (**Figure 8-1a**). The NP collisions are driven by the continuous bubbling of H_2 gas into the solution, and the GB density can be controlled by the gas flow rate that modifies the collision frequency. The introduction of GBs leads to pronounced lattice distortions, resulting in local strain near

the GB regions, stacking faults, dislocations and atomic step ridges. Furthermore, an expansion of the crystal lattice parameter and a simultaneous reduction in coordination number is observed with the formation of an increased number of GBs. The Au nanoassemblies exhibit an outstanding performance towards the two-electron ORR, a more than two orders of magnitude increase in mass and specific activity with respect to GB-poor Au NPs, showcasing the pivotal role of GBs in promoting high reactivity and selectivity. Moreover, the stability of Au nanoassemblies has been found to depend on the concentration of boron species (stemming from boric acid used during the synthesis) that segregate to the GBs to lower their free energy, inhibiting diffusion and annihilation of GBs. Heteroatom engineering at the GBs demonstrates the capacity to stabilize exceptionally active GBs and helps maintain the outstanding two-electron ORR properties, with minimal degradation over a period extending beyond 100 hours.

8.2 Results and Discussion

Grain boundary-rich nanoparticle assemblies

The introduction of H_2 gas at a high flow rate (300 standard cubic centimeters per minute, sccm) into a solution containing citrate-capped Au NPs (**Figure 8-1b, Figure 8-2**) initiates the attachment of Au NPs into porous, nanoscale assemblies (denoted as H-Au NAs, **Figure 8-1c**), in which the NPs act as building blocks that maintain their initial size (see Appendix, **Figure A8-2**).The assembly of Au NPs comprises three distinct stages. Firstly, under mildly alkaline conditions (pH=10), the initially capped citrate ligands undergo gradual detachment from the NP surface (**Figure A8-3**) due to their instability (**Figure A8-4**),[281] and as a consequence, OH^- ions can adsorb onto the NP surface. During this stage, the steric repulsion between Au NPs originating from the citrate ligands is alleviated, although electrostatic repulsion persists due to the adsorption of OH^- ions (**Figure A8-5a-c**).[282] Secondly, the continuous bubbling of an excess amount of hydrogen gas into the Au NP solution facilitates competitive adsorption between OH^- ions and H atoms. This results in the gradual replacement of surface-bound OH^- ions by H atoms, thereby transforming the negatively charged NP surface into a nearly neutral state and eliminating electrostatic repulsion between Au NPs (**Figure A8-5c**). Thirdly, the introduction of H_2 gas into the NP solution induces turbulence and convection currents, thereby increasing the frequency of NP collisions. Upon approaching each other, two NPs can undergo spatial rotation, followed by attachment and coalescence at regions devoid of ligands to form a GB.

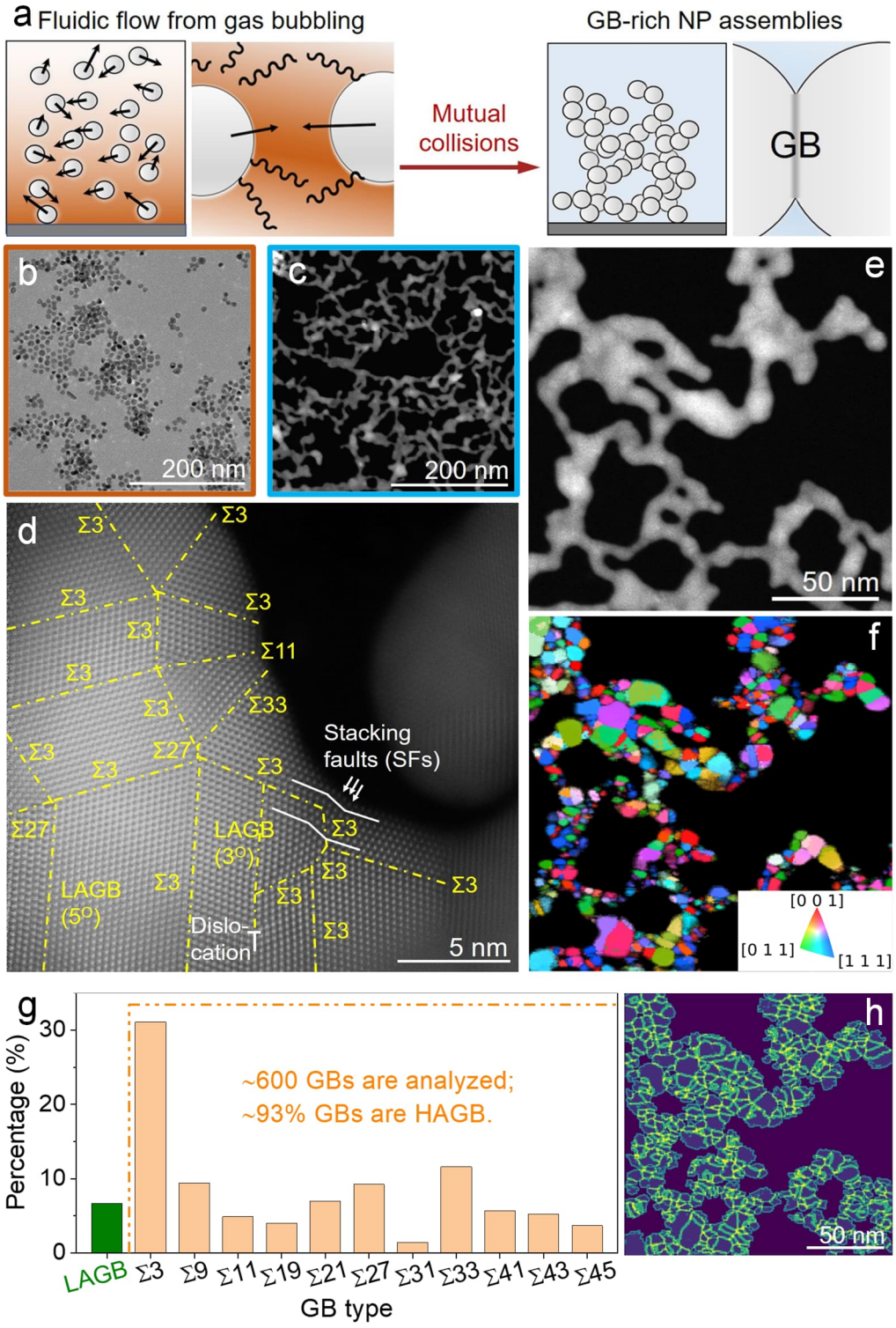

Figure 8-1. *Synthesis of GB-rich nanoassemblies. (a) Illustration depicting the formation of GB-rich Au NAs through the collision, attachment, and coalescence of NPs. (b) TEM image of Au NPs. (c) HAADF-STEM image of H-Au NAs. (d) High-resolution HAADF-STEM micrograph of the GBs between the Au NP building blocks within H-Au NAs. (e) HAADF-STEM image and (f) grain orientation maps from the corresponding 4D-STEM dataset for H-Au NAs. The inset shows the color code for the out-of-plane coordinates. (g) Histogram plots of the GB types derived from ~600 GBs in the 4D-STEM data. (h) 4D-STEM map highlighting the boundaries between grains.*

The primary driving force for this spontaneous attachment is the elimination of bare regions lacking ligand protection, possessing high surface energies, thereby reducing the total energy of the system.[283] Other structural defects such as step sites, stacking faults, and dislocations may arise due to imperfect orientation during the attachment process. Furthermore, NP attachment typically results in anisotropic growth, giving rise to nanowire morphology.[284] If other gases (e.g., Ar, N_2) are used instead of H_2, the NP attachment does not occur (**Figure A8-5d-i**) due to the electrostatic repulsions between OH^- capped NPs' surfaces. Each H-Au NAs consists of individual Au crystals, which can be regarded as their NP building blocks, connected by GBs (**Figure 8-1d**). Among a randomly selected set of 22 GBs (**Figure 8-1d**, **Figure A8-6**), we have identified 16 Σ3 GBs, 1 Σ11 GB, 2 Σ27 GBs, 1 Σ33 GB based on CSL theory[244], and 2 low-angle GBs. We also observed five-fold twin boundaries in Au NAs (**Figure 8-1d**). A small number of them could be present in the Au NPs before assembly, while the rest could be formed through high-energy GB decomposition and partial dislocation slipping during NP attachment.[250]

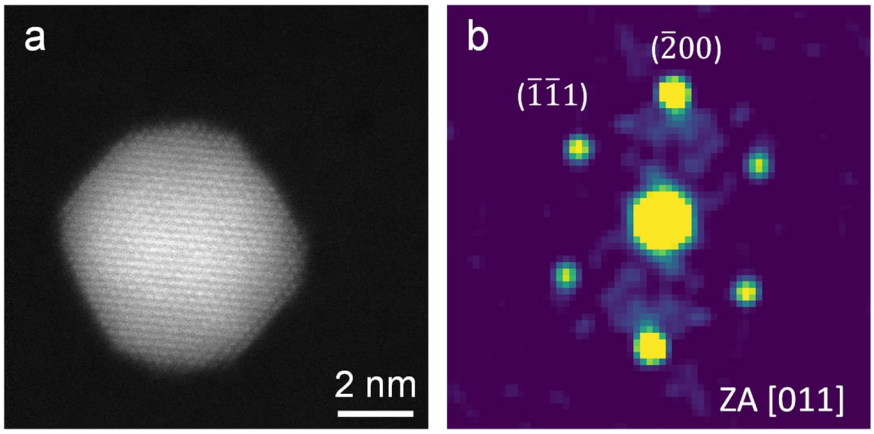

***Figure 8-2**. High-resolution HAADF-STEM image of an Au NP oriented along the [011] zone axis (a) and corresponding FFT (b).*

Remarkably, the shapes of individual NP building blocks within H-Au NAs have changed significantly when compared to the isolated Au NPs. Spherical NPs have formed nanoassemblies with nearly polygonal grains, implying that collisions among NPs or their posterior reorientation have induced important deformations in the structure of these building blocks (**Figure 8-3a**).

To obtain a statistical analysis of the GBs present in H-Au NAs, we have employed 4D-STEM (**Figure 8-1e-h**, **Figure A8-7**, **Figure A8-8**, **Figure A8-9**)[34,285]. Among ~600 GBs, H-Au NAs contain ~7% LAGBs and ~93% HAGBs, including 31% Σ3 GBs along with other CSL GBs

(**Figure 8-1g**). Although a trace number of Au NPs possess low-energy Σ3 GBs (**Figure A8-10**), the vast majority of them are found to be free of GBs (**Figure A8-11**), implying that most of the GB defects are formed during the assembly process. Therefore, the GB density of Au NPs is set to 0 μm^{-1}. in the follow up discussion. During the collision event between two NPs initially randomly oriented, they can reorient to lower energy orientations,[250] explaining why lower energy GBs (i.e., Σ3) are more frequently observed. As the assemblies grow there are lower degrees of freedom left, and higher energy HAGBs form as well. Beyond GBs, H-Au NAs contain stacking faults and dislocations (**Figure 8-1d**), which can be remnants of the rotation process of multiple NPs merging.[250]

The surface of the H-Au NAs exhibits a high number of atomic step ridges (**Figure 8-3a-c, Figure A8-12**), which are likely a result of surface reconstruction taking place during the assembly process. Relative to terrace sites, step sites possess lower coordination numbers, thus exhibiting higher catalytic activity.[59,286–288] Moreover, the GB terminations at the surface form line defects with a distinct coordination environment (**Figure 8-3d**), which can also enhance the catalytic activity.[7] Numerous triple junctions (i.e., a line defect where three GBs converge) are also observed on H-Au NAs (**Figure 8-3a**, **Figure 8-4**). These line defects propagate to the surface of the NAs, creating a point defect that can act as a catalytically active site. Additionally, deviations of the relaxed atomic positions are observed in the nanoassemblies, as seen by the distortions on the GBs structural units in the vicinity of the triple junctions (**Figure 8-3d,e**) and by the presence of lattice strain.

High levels of strain are found next to the higher energy GBs (i.e., ∑9, ∑27) and triple junctions (**Figure 8-3f-h**). This results in strain-rich surface regions next to the defects' surface terminations, which can optimize the binding energy of reaction intermediates. Strain maps from the 4D-STEM data in a larger area (hundreds of square nanometers) reveal a similar uneven distribution of the strain, with higher strain levels located in the regions between the NP building blocks (**Figure 8-3i-k**, **Figure A8-7**, **Figure A8-8**, **Figure A8-9**).

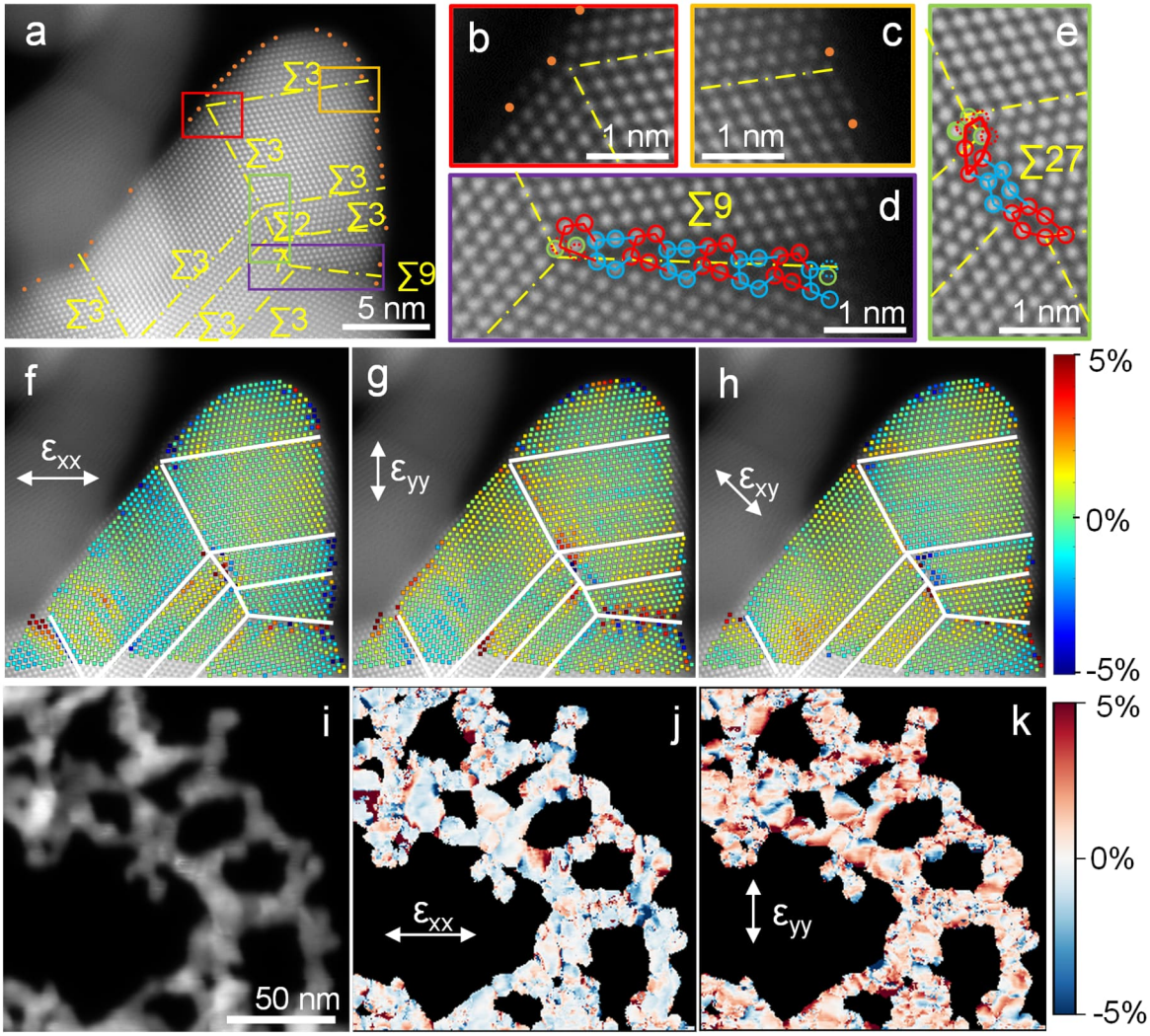

Figure 8-3. *Defects and strain characterization for H-Au NAs. (a) HAADF-STEM image of GBs and undercoordinated surface atoms (orange dots) in H-Au NAs. Enlarged regions showing the (b, c) surface terminations and structure of (d) Σ9(221) and (e) Σ27(552) GB. (f-h) Real space strain maps along the x (ε_{xx}), y (ε_{yy}) and xy (ε_{xy}) directions. (i) Virtual annular dark field image from the 4D-STEM data. (j, k) Corresponding relative strain maps (ε_{xx}, ε_{yy}).*

Tuning the grain boundary density

We now demonstrate how the H_2 gas bubbling can modulate the GB density in the NAs, by using both a low flow rate of 30 sccm (L-Au NAs) and a medium flow rate of 100 sccm (M-Au NAs). With increasing flow rate, the NAs transitioned in morphology from a loosely connected network to a network with more ramifications, still containing GBs (**Figure 8-5a-e**, **Figure A8-13**, **Figure A8-14**). This can be attributed to an increase in the frequency of collisions among NPs induced by the increasing fluid flow (**Figure A8-15**), since it leads to a homogenization of growth probabilities across various sites, thereby contributing to the augmented number of ramifications.

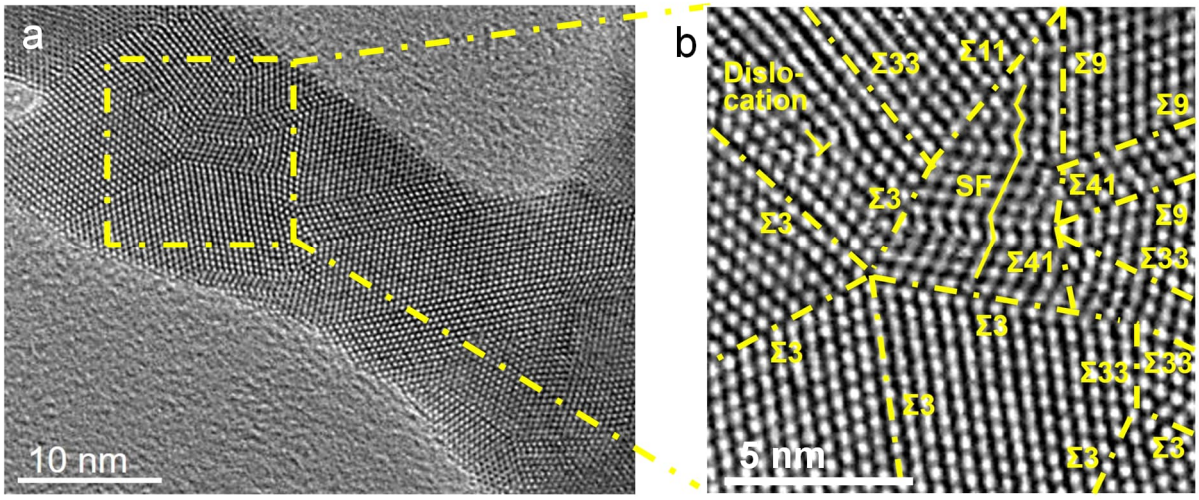

Figure 8-4. *(a) Low- and (b) high-magnification HR-TEM images of H-Au NAs. The different defects present in the crystal lattice are indicated.*

The GB surface density is defined as the ratio of the total GB surface length to the exposed surface area. For calculating it, we relied on the surface area reduction during the assembly process assuming that each NP attachment leads to the creation of a GB (see Experimental section)[243] and that crystallite size does not change significantly during the assembly process, as confirmed by the size distribution histograms calculated from the STEM images (**Figure A8-16**). The surface area is quantified by monitoring the reduction of gold oxides using cyclic voltammetry under equivalent catalyst load (**Figure 8-5f**). With this method, we estimate that the GB surface density within the Au NAs progressively increases with the gas flow rate from 98 μm^{-1} at 30 sccm (L-Au), 160 μm^{-1} at 100 sccm (M-Au), to 235 μm^{-1} at 300 sccm (H-Au) (**Figure 8-5g**, see Experimental section for more details). This trend aligns with the morphology evolution evaluated by STEM (**Figure 8-5a-e**), which indicates a higher degree of NP interconnectivity at elevated flow rates, and therefore a higher GB density (**Figure 8-5g**).

Brunauer-Emmett-Teller (BET) measurements indicate that L-Au NAs, M-Au NAs, and H-Au NAs possess large specific surface areas and high porosity (**Figure A8-17**). Among these, L-Au NAs exhibits the largest specific surface area, pore diameter, and pore volume, while H-Au NAs has the smallest. The specific surface area and porosity of M-Au NAs are intermediate between those of L-Au NAs and H-Au NAs. The trends in BET-measured specific surface areas of Au NAs are consistent with electrochemical measurements. 4D-STEM measurements indicate that both L-Au NAs and M-Au NAs have a similar GB type distribution to H-Au NAs, comprising approximately 10% LAGBs and 90% HAGBs, including about 30% Σ3 GBs

alongside other CSL GBs (**Figure A8-18**). The rate of hydrogen gas bubbles did not affect the GB type distribution.

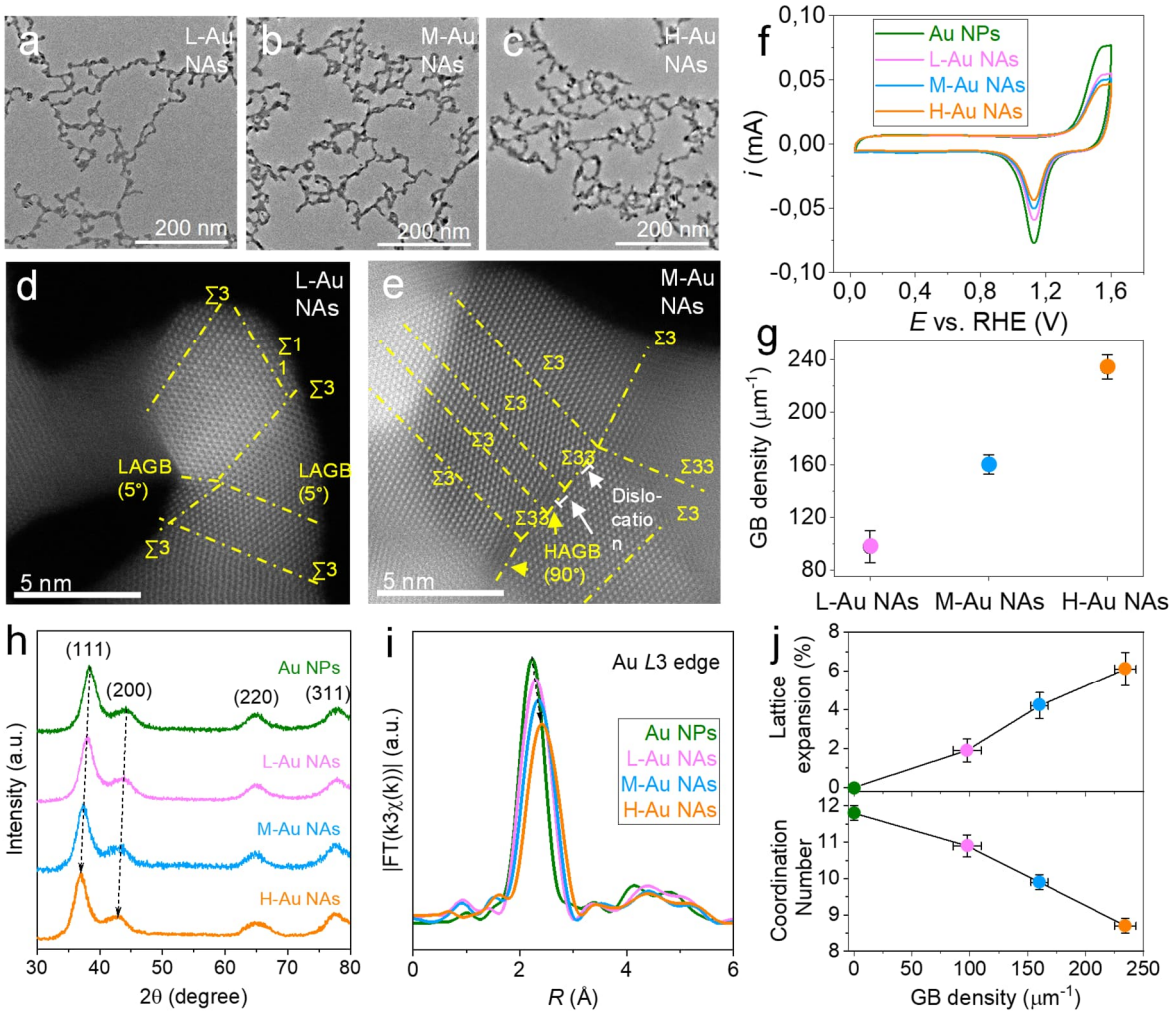

***Figure 8-5**. Tuning the GB density by varying H_2 flow rate. TEM images of Au NAs prepared from (a) a low-flow-rate (L-Au NAs), (b) a medium-flow-rate (M-Au NAs) and (c) a high-flow-rate (H-Au NAs). HAADF-STEM image of the GBs in (d) L-Au NAs and (e) M-Au NAs. (f) Cyclic voltammograms. (g) Relationship between gas flow rates and GB surface density. (h) XRD patterns of L-Au NAs, M-Au NAs and H-Au NAs. (i) Fourier-transformed EXAFS spectra for Au L3-edge for Au NPs, L-Au NAs, M-Au NAs, and H-Au NAs. (j) Correlation between GB surface density and lattice expansion/coordination number.*

The XRD peak positions of (111) and (200) crystallographic planes of Au NAs exhibit a monotonous shift towards lower angles (**Figure 8-5h**) indicating a gradual expansion of the lattice with increasing gas flow rate (used in the assembly process). This is further confirmed by analyzing the Fourier-transformed EXAFS spectra in the frequency domain, which reveal an increase in the bond length of the NAs with an increasing flow rate (**Figure 8-5i**). The lattice expansion derived from EXAFS analysis of L-Au NAs, M-Au NAs, and H-Au NAs are approximately 2%, 4%, and 6%, respectively. Interestingly, we found a linear relationship

between GB density and the degree of lattice expansion. Additionally, the EXAFS spectra indicate that there is a sequential reduction in coordination number (**Figure 8-5I,j**,), transitioning in the order of Au NPs (~12), L-Au NAs (~10.9), M-Au NAs (~9.9), and H-Au NAs (~8.7) (**Table A8-1**). The decline in coordination numbers can be ascribed to the increased density of defects[22,73], including atomic step ridges, dislocations and stacking faults, likely stemming from an elevated collision rate. This reduction in coordination number may result in an enhancement of the reactivity of atoms within Au NAs[225].

Two-electron oxygen reduction reaction activity

Having demonstrated that we can tune the GB surface density, lattice parameter and coordination number of Au NAs via the H_2 flow rate control, we test their catalytic activity towards two-electron ORR to study the influence of GBs in their catalytic performance. Developing an efficient, selective and durable catalyst in acidic media for this reaction has represented a challenge[289], yet it is critical to secure an environmentally friendly way to synthesize H_2O_2[5,56], a product with extensive industrial applications[56]. The electrocatalytic performance towards the two-electron ORR is assessed for both Au NPs and Au NAs employing a rotating ring-disk electrode with a calibrated collection efficiency of 36% in an oxygen-saturated 0.1 M $HClO_4$ electrolyte (**Figure 8-6a**, **Figure A8-19**). In comparison to Au NPs, Au NAs exhibit a significant enhancement in the onset potential (i.e., lower overpotential) required to achieve a current density of 0.1 mA cm^{-2} (**Figure 8-6a**), accompanied by a notable increase in H_2O_2 selectivity (**Figure 8-6b**). As the applied potential varies, the selectivity for two-electron ORR in Au NPs diminishes, while Au NAs maintain consistent selectivity (**Figure 8-6**). This reduction in selectivity for Au NPs is due to the aggregation of under-coordinated surface atoms, which are more prone to aggregation than more-coordinated atoms,[229,230] leading to fewer under-coordinated atoms with higher two-electron ORR selectivity remaining exposed. In contrast, the coordination number of Au NAs remains unchanged after the two-electron ORR test, likely because the network geometry of Au NAs and their multiple contact points with the carbon support reduce motion and aggregation tendencies.

The lower overpotential and H_2O_2 selectivity presented by H-Au NAs make them outstanding two-electron ORR catalysts, outperforming all existing H_2O_2 catalysts in acidic media (**Figure 8-6c**, **Table A8-2**). Moreover, we found that there exists a linear relationship between the onset potential/selectivity of two-electron ORR and GB surface density (**Figure 8-6d**). When

contrasted with Au NPs, H-Au NAs exhibit an enhancement exceeding two orders of magnitude in both specific and mass activity with respect to the two-electron ORR (**Figure 8-6d**). It suggests that the exceptional performance for H-Au NAs may be attributed to the highest GB surface density, largest lattice expansion, and lowest coordination number as a consequence of NP collisions.

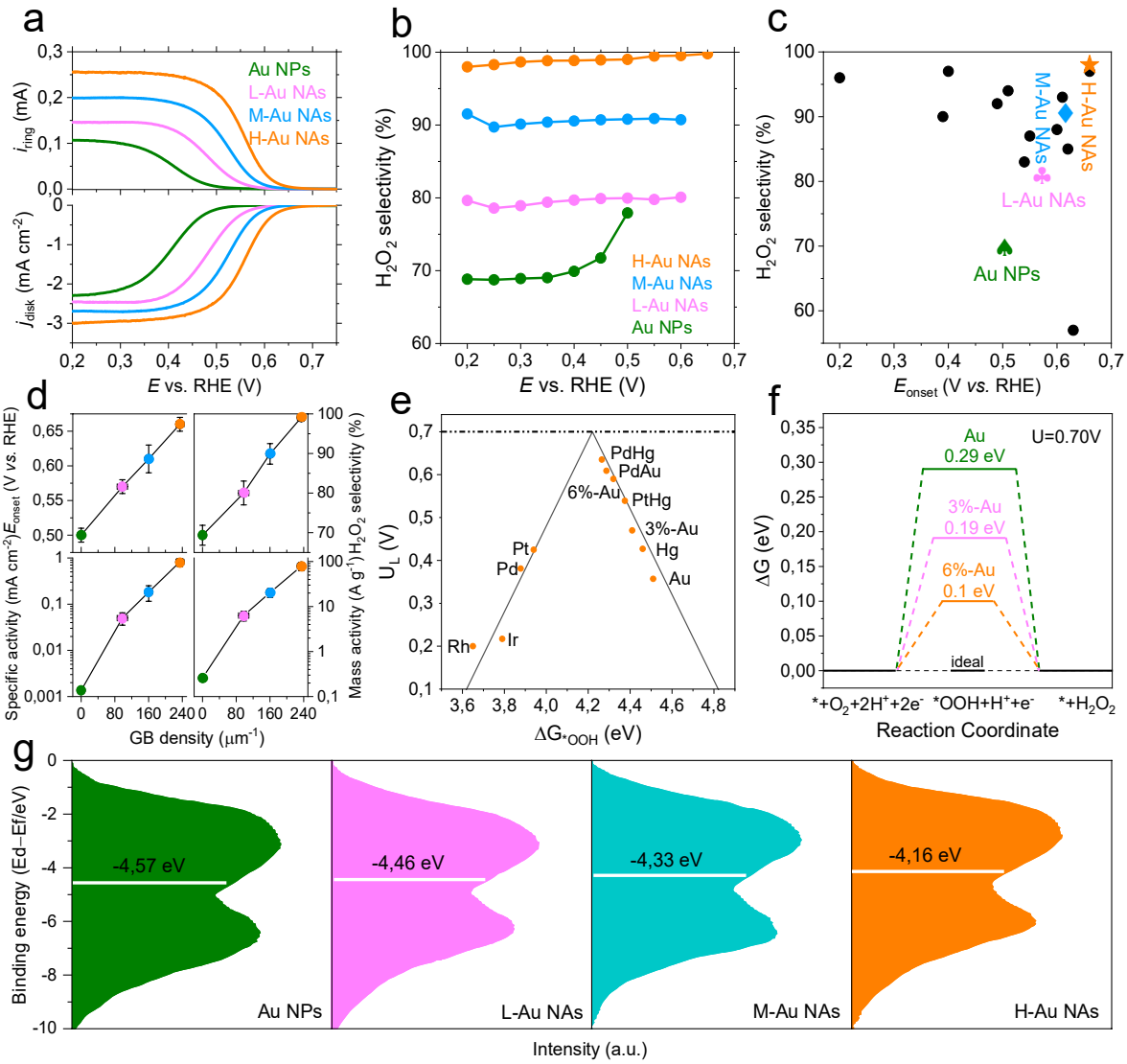

***Figure 8-6**. Two electron ORR activity. (a) LSV of Au NPs, L-Au NAs, M-Au NAs and H-Au NAs, and detected H_2O_2 currents on the ring electrode (upper panel). (b) H_2O_2 selectivity during the potential sweep. (c) Comparison of the onset potential and H_2O_2 selectivity with state-of-the-art H_2O_2 catalysts (see **Table A8-2** for references). (d) Relation between GB density and the two-electron ORR activity. (e) Calculated two electron ORR volcano plot. (f) Calculated reaction coordinate diagrams for Au and lattice-expanded Au. (g) Experimental surface valence band photoemission spectra of L-Au NAs, M-Au NAs and H-Au NAs.*

To rationalize the two-electron ORR high activity of the Au NAs, we calculated the volcano plot using the limiting potential (U_L) as a performance indicator (**Figure 8-6e**). This potential

is defined as the maximum potential at which both the one-electron reduction of O_2 to *OOH and the subsequent one-electron reduction of *OOH to H_2O_2 is energetically favorable. Metals with a strong binding energy to the *OOH intermediate specie such as Pd or Pt have an excellent ORR activity but tend to directly reduce O_2 to H_2O via the four-electron pathway, resulting in a poor selectivity towards the two-electron ORR[290]. On the contrary, metals like Au or Hg that interact weakly with *OOH can selectively produce H_2O_2, but tend to have a low catalytic activity[8]. However, by expanding the lattice, it is possible to optimize the binding energy between Au and *OOH. The Au positions located on the right leg of the volcano plot indicates a low affinity for *OOH adsorption (**Figure 8-6e**), consequently preventing the correct adsorption of O_2 molecules. The lattice expansion significantly enhances the adsorption strength of *OOH on the Au surface, progressively shifting it towards the maximum of the volcano plot (**Figure 8-6e**). Remarkably, the Au with a 6% lattice expansion (same mean lattice expansion found for the H-Au NAs) exhibits a free energy deviation of merely 0.1 eV from the ideal state, a value significantly lower than that of the unstrained Au (0.29 eV) (**Figure 8-6f**). Moreover, in the surface regions next to the GBs, particularly high levels of strain are found (**Figure 8-3**), which can further increase the *OOH adsorption energy, resulting in even a better alignment with the volcano plot maximum. Additionally, the lower coordination number[291] and higher defect density[271,292–294] in H-Au NAs can also strengthen the *OOH adsorption, further aligning it with the volcano plot maximum. Analysis of surface valence band photoemission spectra reveal a progressive increase in the d-band center energy, following the order: Au NPs (-4.57 eV) < L-Au NAs (-4.46 eV) < L-Au NAs (-4.33 eV) < L-Au NAs (-4.16 eV) (**Figure 8-6g**). Both the increased lattice expansion and the reduced coordination number jointly contribute to an upward shift in the d-band center[225], which correlates with an elevation in the adsorption energy of *OOH on Au surfaces. Experimental measurements of the d-band center, in conjunction with theoretical computations, consistently prove that lattice expansion serves to increase the adsorption strength of *OOH on the surface of Au. This increment, together with the high density of GBs and other structural defects, results in H-Au NAs being an outstanding catalyst for the two-electron ORR.

Durability under electrochemical conditions

To assess the durability, Au NPs and NAs are subjected to a continuous 100-h operation in the RRDE setup with a fixed disk potential of 0.35V (**Figure 8-7a**).

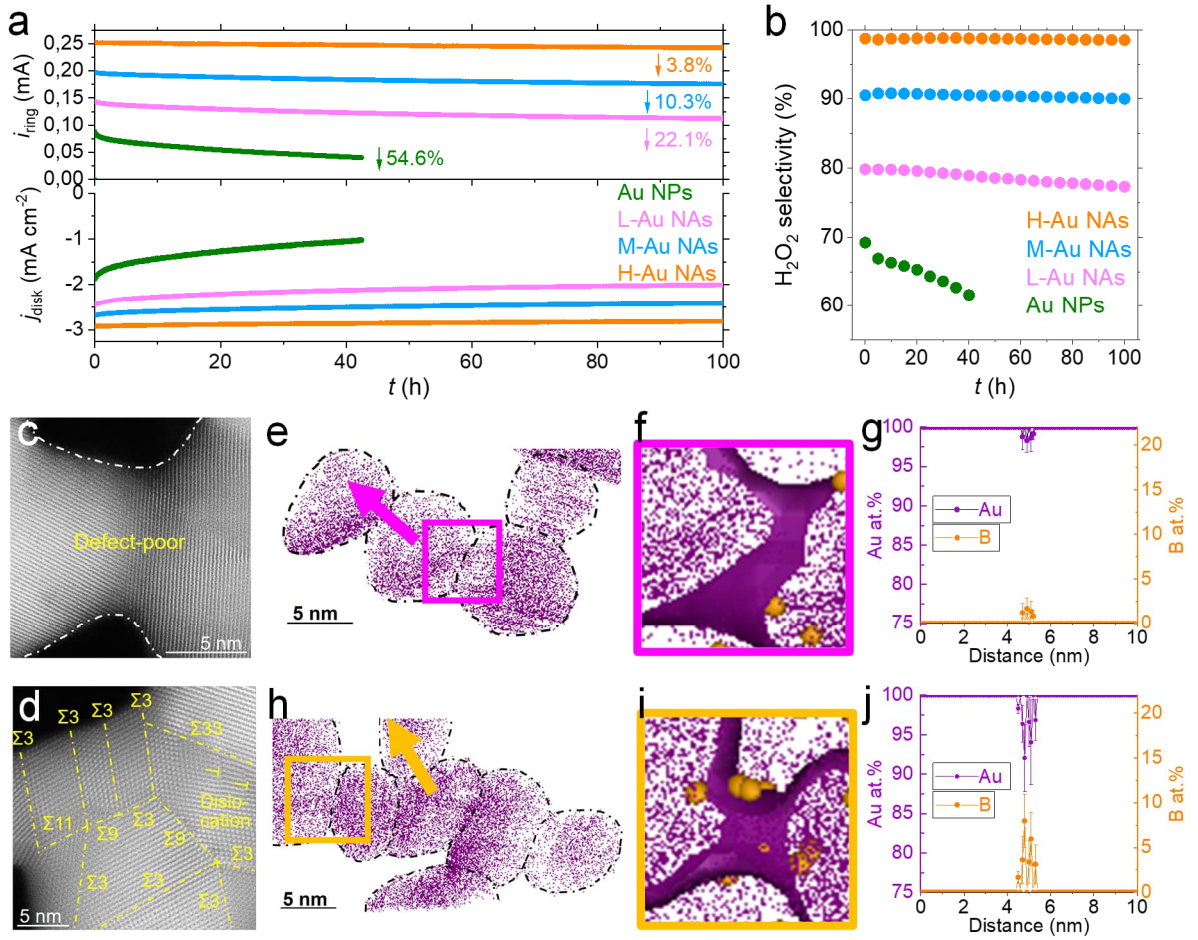

Figure 8-7*. Electrochemical and structural stability. (a) Durability measurements of Au NPs, L-Au NAs, M-Au NAs and H-Au NAs. (b) H_2O_2 selectivity during durability tests. HAADF-STEM images of (c) L-Au NAs and (d) H-Au NAs after tests. 2 nm thin-sliced tomogram (**Figure A8-24**, **Figure A8-27**) of (e) L-Au NAs and (h) H-Au NAs. Tomogram of (f) L-Au NAs and (i) H-Au NAs of the region delineated by the box (B atoms=orange spheres). Composition profiles of Au and B on (g) L-Au NAs and (j) H-Au NAs (direction indicated by arrow).*

Notably, Au NPs exhibit a rapid decay in both disk and ring currents, with ~55% activity loss within the initial 40-h of operation at an applied potential of 0.35 V vs. RHE. In contrast, Au NAs demonstrate significantly improved durability, with a considerably smaller decline in activity relative to Au NPs, and their H_2O_2 selectivity remains largely unaffected (**Figure 8-7b**). The diminished durability of Au NPs relative to Au NAs can be attributed to their susceptibility to motion, aggregation, and Ostwald ripening process during electrochemical reactions (**Figure 8-8**)[229,230].

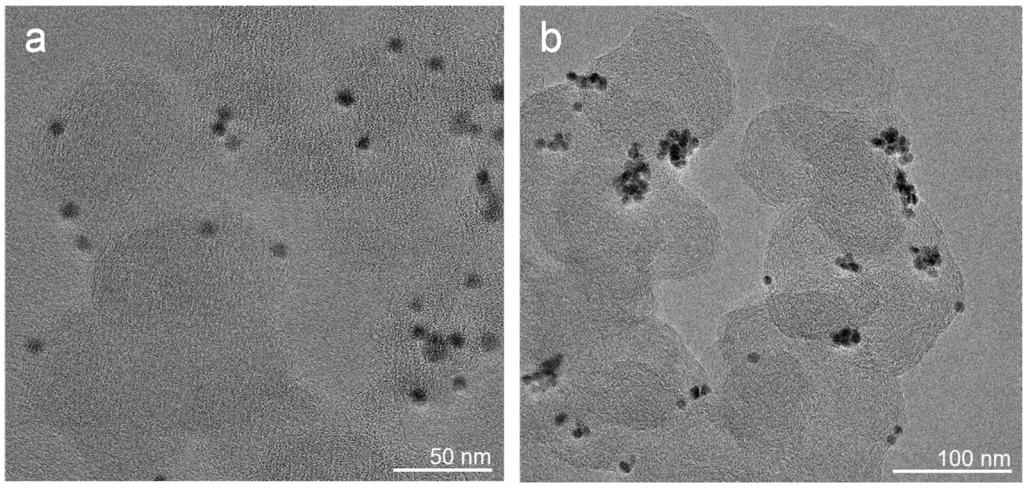

***Figure 8-8**. TEM images of Au NPs/C before (a) and after (b) durability test. The images are intentionally defocused to show the carbon support.*

The network geometry of Au NAs, coupled with multiple contact points with the carbon support, likely reduces such motion and aggregation tendencies[16]. Additionally, it may hinder Ostwald ripening typically observed in spherical NPs, thereby contributing to their excellent durability. The overall morphology and the dimensions of Au NAs supported on carbon exhibit minimal alteration during the durability tests (**Figure 8-9**).

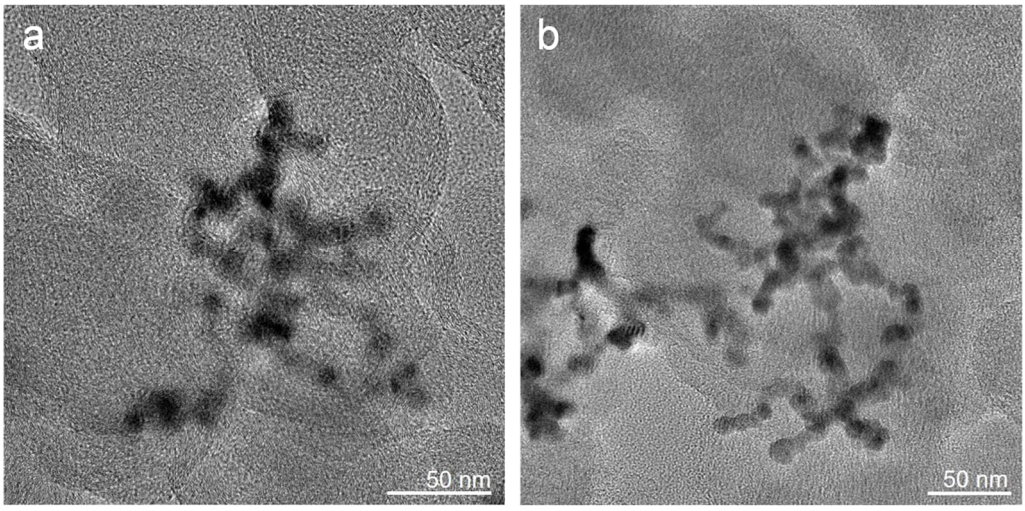

***Figure 8-9**. Defocused TEM images of **(a)** L-Au NAs/C and **(b)** H-Au NAs/C after durability tests, showing their elevated stability. The defocus was intentionally introduced to show better the carbon support.*

However, NAs with a similar morphology experience a different degradation behavior. In particular, Au NAs synthesized at higher flow rates (H-Au NAs) show an enhanced durability compared to those synthesized at lower flow rates (M-Au NAs and L-Au NAs). This can be explained by the preservation of structural defects such as GBs, dislocations and atomic step

ridges. Notably, L-Au NAs manifest a substantial decrease in both GBs and other defects (**Figure 8-7c**) while most of these defects, including GBs, dislocations and steps are conserved in H-Au NAs (**Figure 8-7d, Figure A8-20**). This could be attributed to differences in the chemical composition at the GBs of these Au NAs. Indeed, segregation of heteroatoms was shown to decrease the free energy of GBs in NAs[253,254], and more generally in metallic and ceramic materials[253,254,295,296]. X-ray photoelectron spectroscopy analysis reveals a shift toward lower binding energy in the Au 4f spectra of Au NAs with increasing flow rates (**Figure A8-21**), indicating a fine-tuning of their electronic structure. Furthermore, trace amounts of boron (B) have been detected within Au NAs (**Figure A8-21**); however, the precision of XPS in quantifying B and its special resolution are limited, posing challenges to achieving precise quantitative analyses. These B species stem from the boric acid used in the NP synthesis process (see Experimental section for more details).

To overcome this limitation and accurately ascertain the spatial distribution of B, atom probe tomography is employed (**Figure A8-22**). The near-atomic-scale APT analysis of Au NPs reveals that B is located on their surfaces (~10 at.%.) and no B is detected inside the particles (**Figure A8-23**). In the atom probe tomograms for the different NAs (**Figure 8-7e-j**, **Figure A8-24, Figure A8-25-Figure A8-27**), individual NP building blocks can be readily discerned, and the concave regions were used to identify GB joining two particles. No B is detected on the surface of the NAs. B atoms appear all distributed in the vicinity of GBs (**Figure 8-7f,i**, **Figure A8-26**). 1D composition profiles along the arrow indicate an atomic concentration of approximately 2%, 5%, and 8% for B at GBs within L-Au NAs, M-Au NAs, and H-Au NAs, respectively (**Figure 8-7g,j**). The flow rate-dependent B concentration within GBs in Au NAs suggests a correlation between the collision rate among NPs and the detachment rate of surface-bound B species prior to NP attachment, strongly suggesting that B species are kinetically trapped within the GBs. After the durability testing, the concentration of B at the GBs of H-Au NAs remains nearly constant (**Figure A8-28**, **Figure A8-29**), whereas in L-Au NAs, B is nearly gone (**Figure A8-30**). This observation further underlines that the concentration of B species at GBs is a primary contributor to the superior stability exhibited by H-Au NAs. Such a high concentration of B species in H-Au NAs strongly limits GB sliding[297], thereby ensuring the preservation of the microstructure and defects, which combine to provide the enhanced durability. While in this instance, we have limited our application to the two-electron ORR, it is noteworthy that the electronic effects resulting from the formation of GBs have the potential

for optimizing the catalytic performance in the context of various other electrochemical reactions.

8.3 Conclusions

To summarize, we have synthetized Au nanoassemblies (NAs) with tunable grain boundary density. The kinetic driving force for NP collisions is provided by the sustained bubbling of H_2 gas, with the ability to control collision frequency and adjust the GB density of NAs by varying the gas flow rate. During the collision process and posterior re-orientation, defects (i.e., dislocations, stacking faults and atomic step ridges) and local strain in the vicinity of the GBs are induced. As the flow rate increases, so does the density of GBs, steps, dislocations, stacking faults as well as lattice expansion within the NAs. The combination of higher GB surface density, lower coordination number, other structural defects and lattice expansion enhances the catalytic performance of these Au NAs in more than two orders of magnitude (in specific and mass activity) with respect to GB-poor Au NPs for the two-electron ORR, surpassing the performance of other state-of-the-art catalysts in acidic media reported in the literature. The experimental assessments of the d-band center, coupled with theoretical computations, consistently validate that lattice expansion is an additional factor contributing to the enhancement of the two-electron ORR performance by fine-tuning the adsorption strength of the reaction intermediate *OOH on the surface of Au. The durability of the NAs is also improved with respect to the NPs, with negligible activity decay observed over 100 hours of operation. Notably, there exists a positive correlation between the structural stability of Au NAs, their corresponding two-electron ORR durability and the presence of segregated boron (B) species at their GBs. Segregation of B species at the GBs was observed, with B concentration increasing as the flow rates of gas bubbling increase, indicating the kinetic trapping of B at GBs. The improved durability of Au NAs can be attributed to the high concentration of B species segregated at the GBs, which inhibits decohesion or sliding of GBs, thereby stabilizing the defect-rich structure.

Our study not only introduces a novel method for regulating GB density but also entails the development of a novel two-electron ORR catalyst in acidic media characterized by outstanding activity, selectivity, and stability. Of greater significance, our discoveries open a new pathway for the extended application of GB engineering as a means to govern the properties of heterogeneous catalysts.

8.4 Experimental section

Synthesis of OAm/OA-capped Au NPs

Initially, 1-octadecene (Sigma Aldrich) was subjected to heating at 130 °C for 30 min under N_2. Subsequently, a mixture comprising 2 mmol of oleic acid (OA, Sigma Aldrich), 2 mmol of oleylamine (Sigma Aldrich), 0.5 mmol of gold acetate (Sigma Aldrich), and 4 mmol of 1,2-hexadecanediol (Sigma Aldrich) was introduced. The reaction mixture was heated to 200°C and stirred for 2 h under N_2. Following this, the temperature was raised to 280°C and maintained for1 h. Subsequently, the reaction was terminated by cooling the mixture to room temperature. The Au NPs were precipitated using ethanol and subsequently subjected to washing with hexane. The precipitation and washing steps were iteratively performed multiple times.

Preparation of citrate-capped Au NPs

A two-step methodology was employed to replace the capping agents on the surface of Au NPs from oleylamine/oleic acid (OA) to citrate. The initial step involved the substitution of OAm/OA capping agents with diethanolamine (Sigma Aldrich). Specifically, 5 mL of OAm/OA-capped Au NPs were mixed with 5 mL of DEA and stirred for 24 h, followed by centrifugation for precipitation. Subsequently, 10 mL of DEA was added, and continuous stirring was maintained for 24 h, followed by another centrifugation step and dispersion in 5 mL of DI H_2O. Fourier-transform infrared spectroscopy (FTIR) analysis (**Figure A8-1**) conclusively confirmed the complete replacement of OAm/OA capping agents with DEA. The second step involved the replacement of DEA capping agents with citrate. Specifically, 5 mL of DEA-capped Au NPs were mixed with 1 mL of 10 mg/mL sodium citrate (Sigma Aldrich) and 1 mL of 10 mg/mL boric acid (Sigma Aldrich), followed by 24 h of stirring. Subsequent centrifugation and dispersion in 5 mL of DI H_2O were performed. FTIR results (**Figure A8-1**) provided unequivocal evidence for the full replacement of DEA with citrate capping agents.

Preparation of Au NAs

Initially, we employed a dialysis method to eliminate impurity ions from the citrate-capped Au NP solution. Specifically, the Au NP solution was placed inside dialysis tubing, which was immersed in a 1 L beaker containing DI water. Simultaneously, magnetic stirring was applied to expedite the diffusion of impurity ions away from the NP solution. The dialysis process was carried out continuously for three days, with DI water refreshed twice daily.

Subsequently, we introduced high-purity H_2 gas into a 10 mL solution of citrate-capped Au NPs, with a concentration of ~1.6 μM, and maintained this bubbling process for 10 h. To investigate the influence of H_2 gas flow rate on the assembly of Au NPs, we employed three distinct flow rates, denoted as low (30 sccm), medium (100 sccm), and high (300 sccm), resulting in the formation of Au NAs named L-Au NAs, M-Au NAs, and H-Au NAs, respectively. The completion of Au NAs assembly was indicated by a change in the color of the Au NP solution from dark brownish-red to transparent. After discontinuing the H_2 gas bubbling, the solution was allowed to stand for 10 h, during which the Au NAs sedimented at the bottom of the beaker. Subsequently, careful removal of the supernatant was performed using a pipette, followed by thorough rinsing of the Au NAs with DI water.

Transmission electron microscopy characterization

HAADF-STEM and HR-TEM were employed for characterization purposes. HAADF-STEM imaging was carried out using a Thermo Fisher Titan microscope with probe C_s correction at an accelerating voltage of 300 kV, while HR-TEM was performed utilizing an C_s image aberration-corrected Thermo Fischer Titan Themis 60-300 microscope, also operated at 300 kV. The HAADF-STEM and HR-TEM images were analyzed and post-processed utilizing the Gatan Microscopy Suite 3.0 (GMS 3.0) software package. To discern the crystallographic planes and zone axis, measurements of the interplanar spacing (d-spacing) and their respective angles were conducted through FFT applied to the HAADF-STEM and HR-TEM images. In accordance with the coincidence site lattice theory, the types of GBs existing between neighboring grains were identified. For better visualization, Hann-windowed FFT are provided in the text.

To map the strain of individual atoms, we employed STATSTEM[96], a MATLAB-based program that allows for the fitting of two-dimensional Gaussians on the intensity maxima of HAADF-STEM images (i.e., the atomic columns) and posterior interatomic distance evaluation. After having calculated the interatomic distances, the strain of individual grains was analyzed by selecting the center of the corresponding grain as reference (unstrained) lattice. Afterwards, these strain maps of individual grains were combined for generating the complete strain map of the sample.

4D-STEM was used for performing grain orientation mapping and strain analysis of the nanoassemblies. The data was collected in the same C_s-probe corrected Thermo Fisher Titan microscope at 300 kV using the pixelated detector EMPAD. For the acquisition, a camera

length of 940 mm and a probe convergence semiangle of 0.65 mrad were used. The detector pixel size was calibrated using a sample with (unstrained) Au NPs under the same conditions. The open source python library py4DSTEM was used for the preprocessing, visualization and orientation and strain mapping. For the strain mapping, the relative strain is plotted. This is achieved by assuming that the average lattice parameter of the Au NAs is the same as that of an unstrained gold lattice. Using build in functions, the orientation maps were exported to ".ang" format, compatible with EDAX OIM Analysis software, where the grain misorientation angles were extracted for GB identification using coincidence site lattice theory. For that step, only the points with an image quality factor over 5.0 were considered to ensure a correct GB identification. Virtual dark field images were generated from the 4D-STEM datasets using a virtual annular detector centered around the bright field disk.

X-ray characterization

We investigated the crystal structures of Au NPs and Au NAs utilizing a Bruker Powder X-ray diffractometer, which was equipped with a Cu Kα radiation source. Subsequently, we employed an Al Kα X-ray Photoelectron Spectrometer (Thermo Scientific) to analyze the elemental composition and chemical states of Au NPs and Au NAs. To ensure precision in our XPS spectra, we calibrated them with reference to the C1s peak at 284.8 eV. For the analysis and fitting of the XPS data, we utilized the Avantage software and employed a composite function (comprising 30% Lorentzian and 70% Gaussian components). To calculate the center of gravity (ε_d) for the valence band spectra for both Au NPs and Au NAs within the energy range of -10 eV to -1 eV, we utilized the following integral equation $\varepsilon_d = \frac{\int N(\varepsilon)\varepsilon d\varepsilon}{\int N(\varepsilon) d\varepsilon}$, where *N(ε)* represents the density of states and *ε* the energy level.

XAS, encompassing X-ray Absorption Near-Edge Spectroscopy (XANES) and EXAFS measurements, were conducted at the BL14W1 beamline of the Shanghai Synchrotron Radiation Facility. The synchrotron storage ring operated at an energy of 3.5 GeV, while the linear electron accelerator operated at 150 MeV. Monochromatization of X-rays occurred through the utilization of a Si (311) double crystal monochromator, operating within an energy range spanning 9,000–35,000 eV. The specimens were homogeneously mounted onto Kapton Tape for subsequent XAS assessments. XAFS spectra at the Au L3 edge were collected via transmission mode at a controlled temperature of 25°C. Rigorous data reliability measures were adopted, with all XAFS spectra being acquired within a defined beamtime and subjected to triplicate testing. Data preprocessing was facilitated through the employment of the Athena

software, encompassing baseline subtraction prior to post-edge baseline normalization to yield the spectroscopic data. Furthermore, the EXAFS analysis involved Fourier transformation of k3-weighted EXAFS oscillations to assess the contribution of each shell to the peaks in the Fourier transform, followed by fitting using the Artemis software.

Atom probe tomography characterization

Initially, the incorporation of Au NPs and Au NAs into Ni matrix was achieved through the application of a co-electrodeposition technique. Specifically, a copper foil (0.2 cm^2) was employed as working electrodes (pre-etched by 0.5 M H_2SO_4), while a Pt mesh (2 cm^2) served as the counter electrode. An electrolyte solution consisting of 1.5 g $NiSO4 \cdot 6H_2O$ and 0.225 g citric acid dissolved in 5 mL of DI water was prepared. Subsequently, a mixture of 10 mg of Au NPs and Au NAs was sonicated with the electrolyte for 1 h, and the resulting solution was poured into an electrodeposition cell. An established constant current of -19 mA was applied to the working electrode for 500 s, resulting in the deposition of an Au/Ni thin film, with Au NPs and Au NAs encapsulated within the Ni matrix. Following this, needle-shaped APT samples were prepared using a Ga focused ion beam (FEI 600 DualBeam) in accordance with standard APT sample fabrication procedures. The embedding of Au NPs or Au NAs within the Ni matrix led to surface protrusions on the Ni film, which were meticulously sectioned and transferred onto silicon coupons as lamellas. The lamella containing Au NPs or Au NAs encapsulated within the Ni matrix was verified through cross-sectional analysis of the protrusion, followed by precise sharpening to achieve a needle-shaped APT specimen. Finally, the needle-shaped APT sample was loaded into the LEAP 5076 XS instrument (Cameca) for APT experiments. All APT experiments were conducted in pulse laser mode, with experimental parameters set at a temperature of 50 K, a detection rate of 1%, a laser energy of 60 pJ, and a laser pulse frequency of 125 kHz. Data obtained were analyzed and reconstructed using standard voltage reconstruction protocols with the assistance of the commercially available IVAS 3.8.4 software. For APT, the broadening of segregation profiles at GBs is a frequently observed phenomenon attributed to the distinct field evaporation behavior at these interfaces. In order to discern the segregation behavior independently of the broadening effects, we employ the Gibbsian interfacial excess (Γ) as an integrated metric. The computation of Γ_B is based on the following equation:

$$\Gamma_B = t \times \Delta\rho_B = t \times \left(\frac{N_B^{\mathrm{GB}}}{V_{\mathrm{GB}}} - \frac{N_B^{\mathrm{NP}}}{V_{\mathrm{NP}}}\right) \qquad \textit{Eq. 8-1}$$

wherein *t* represents the width of the GB region, $\Delta\rho_B$ signifies the difference in atomic density of the B element between the NP building blocks and the GB region, N_B^{NP} and N_B^{GB} denote the number of atoms of the B element in the respective unit cells of the NP building block and the GB region, while V_{NP} and V_{GB} represent the unit cell volumes of the NP building block and the GB region.

Other characterizations

The zeta potential of the Au NP solution loaded into quartz cuvettes was determined using a Zetasizer Nano-ZS instrument (Malvern Instruments, UK) in high-resolution mode. Fourier-transform infrared spectroscopy (FTIR) spectra were acquired using a Bruker Tensor 27 FTIR spectrophotometer. The Au concentration in the ink was quantified via ICP-AES using a 710-ES instrument from Varian.

Grain boundary surface density determination

The GB surface density, defined as the length of the GB in the surface of the NAs (l_{GB}) divided by the surface area of the NAs (A_{NAs}) is assessed following a previously reported method:[243]

$$GB_{surface\ density} = \frac{l_{GB}}{A_{NAs}} \qquad \textit{Eq. 8-2}$$

Assuming that the GBs assume a disk-like morphology, 'l_{GB}' is equivalent to '$2A_{GB}/r$', being A_{GB} the average area of a GB and '*r*' the average GB projected length, estimated from the STEM images (~100 GBs measured).

$$GB_{surface\ density} = \frac{l_{GB}}{A_{NAs}} = \frac{2A_{GB}}{r \times A_{NAs}} \qquad \textit{Eq. 8-3}$$

8. Tuning GB density of Au nanoparticle assemblies

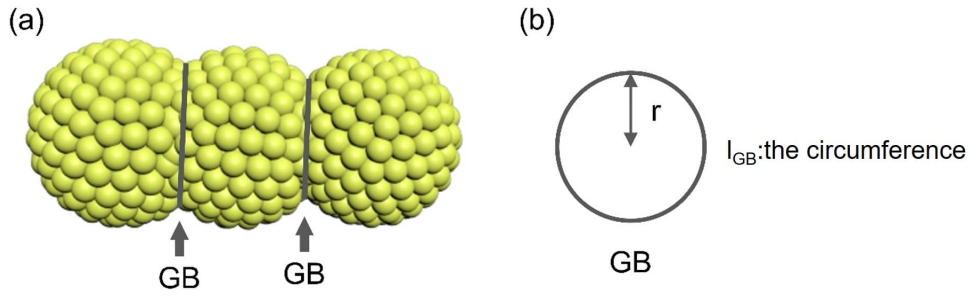

The GB surface length (l_{GB}) can be defined as the circumference of a circular region with a radius denoted as 'r,' which is mathematically expressed as $2\pi r$. Meanwhile, the GB surface area (A_{GB}) corresponds to the area enclosed by this circular boundary and can be quantified as πr^2.

Our investigations reveal that the crystallite size remains notably invariant both in pre- and post-NP assembly (**Figure A8-2**). Consequently, the observed reduction in surface area within NAs in relation to their NP precursors is primarily attributed to the attachment of NPs. With that assumption, *'$2A_{GB}$'* can be expressed as the overall loss in surface area ($A_{NP}-A_{NAs}$), which can be experimentally determined via cyclic voltammetry to measure the electrochemically active surface area.

$$GB_{surface\ density} = \frac{l_{GB}}{A_{NAs}} = \frac{2A_{GB}}{r \times A_{NAs}} = \frac{(A_{NP} - A_{NAs})}{r \times A_{NAs}} \qquad Eq.\ 8\text{-}4$$

Similarly, the surface area of the NAs (A_{NAs}) can also be experimentally measured via cyclic voltammetry.

Electrochemical measurements

The electrochemical measurements were carried out using a CHI760E potentiostat (CHI Instrument) using 0.1 M $HClO_4$ aqueous solution as the electrolyte. The RRDE measurements were run at 25°C in a typical three-electrode cell. A Pt foil (99.99%, Sigma Aldrich) and an Ag/AgCl electrode (3.0 M KCl, CH Instrument) were used as the counter and reference electrode, respectively. All the potentials were converted to RHE. The RHE calibration of Ag/AgCl reference electrode in 3.0 M KCl was performed in a high purity of H_2 saturated 0.1 M $HClO_4$ solution where polished Pt wires were used as the working and counter electrodes.

The linear scanning voltammetry was run at a scan rate of 1 mV/s, and the potential of zero current was taken as the reaction potential of the hydrogen electrode. The potential measured with the Ag/AgCl electrode in 3.0 M KCl were calculated as following: $E_{RHE} = E_{Ag/AgCl} +$ 0.279V. A RRDE assembly (PINE Instrument) consisting of a glassy carbon rotating disk

electrode (Φ=5.6 mm, geometric area=0.247cm^2) and a Pt ring (Φ=15.0 mm) was used, with a theoretical collection efficiency of 40%. Experimentally, the apparent collection efficiency (*N*) was determined to be 36% in the ferrocyanide/ferricyanide half reaction system at a rotation rate between 400 and 1600 rpm.

To prepare the ink, 0.3 mg of as-synthesized Au catalysts were dispersed in 495 μL DI water by sonicating for 1 h, followed by adding commercial Vulcan carbon (XC-72) with a mass four times than Au samples and sonicating for another 1 h to make Au catalysts/C. Then, the Au catalysts/C were dispersed in the mixture of 495 μL isopropanol and 10 μL 5% Nafion solution to from a homogeneous ink by sonicating for 1 h. The concentration of Au was controlled to be 0.3 mg_{Au}/mL measured by ICP-AES. The uniform catalyst layer was prepared by pipetted 5 μL of the ink onto the disc electrode without obvious pin holes or uncovered edge followed by vacuum drying at ambient conditions. The loading amount of Au was controlled at 6.1 μg/cm^2.

Before the activity test, both glassy carbon rotating disk electrode with Au catalysts and ring electrode were cleaned by CV for 500 cycles in N_2-saturated 0.1 M $HClO_4$ electrolyte solution until a stable CV curve was obtained. The ECSA was calculated by integrating the charge for the reduction of gold oxide on CV curves in the range of 0.03─1.6 V at 100 mV/s by assuming a value of 390 μC/cm^2. The H_2O_2 activity and selectivity were measured from polarization curves in O_2-saturated 0.1 M $HClO_4$ electrolyte solution between 0.8 and 1.4 V with a scan rate of 10 mV/s with rotating rate of 1600 rpm, while holding the potential of the Pt ring electrode at 1.2 V. The ORR current was corrected by subtracting the current obtained in an N_2-saturated electrolyte from that measured in O_2-saturated conditions. All the measured ring currents were also corrected using the collection efficiency, N, of RRDE set-up to obtain the overall current density as all the H_2O_2 generated was detected. The H_2O_2 selectivity was calculated using the equation:

$$H_2O_2(\%) = 200 \times \frac{\mathrm{I_{ring}/N}}{\mathrm{I_{disk}} + \mathrm{I_{ring}/N}} \qquad \textit{Eq. 8-5}$$

where I_{ring} is the ring current, I_{disk} is the disk current, and *N* is the collection efficiency.

The long-term stability tests for Au catalysts were conducted in the RRDE set-up (chronoamperometry at 0.35 V vs. RHE, rotation speed of 1,600 rpm).

Theoretical calculations

8. Tuning GB density of Au nanoparticle assemblies

We conducted DFT calculations employing the Vienna Ab initio Simulation Package (VASP) in conjunction with the Atomic Simulation Environment (ASE)[298–302]. To account for spin polarization effects, appropriate adjustments were applied. The exchange correlation energy was assessed utilizing the generalized gradient approximation (GGA) method[303], specifically employing the revised Perdew-Burke-Ernzerhof (RPBE) functional[261]. To accurately describe the behavior of core electrons, we employed the projector-augmented wave (PAW) method[259,260]. To ensure precision, lattice constants within our calculations were systematically optimized according to their respective crystal systems. The modeling of the (111) surface of various metals and alloys (Au, Hg, Pt, Pd, Ir, Rh, PdAu, PdHg) were executed using six-layer slabs, with the bottom three layers constrained while permitting relaxation of the upper three layers and adsorbates. For sampling the Brillouin zones, we utilized a 4×4×1 Monkhorst-Pack k-points grid16. To mitigate interlayer interactions, a minimum separation of at least 16 Å of vacuum was enforced between successive slabs in all computational simulations. Furthermore, an energy cutoff of 500 eV was imposed, and all structures were subjected to relaxation in all spatial dimensions until residual forces reached a level below 0.05 eV/Å, ensuring the attainment of thermodynamically stable configurations.

The computation of adsorption energies was carried out with reference to H_2O(l) and H_2(g):

$$\Delta E_{*OOH} = E_{*OOH} - E_{*} - E_{H_2O} + \frac{3}{2}E_{H_2} \qquad \textit{Eq. 8-6}$$

Zero-point energies and entropy terms have been encompassed within the framework of our energetic computations:

$$\Delta G^{\circ} = \Delta E_{DET} + \Delta E_{ZPE} - T\Delta S \qquad \textit{Eq. 8-7}$$

Under an arbitrary potential, relative to RHE, the electron's chemical potential undergoes a perturbation of -eU. Consequently, the reaction's free energy is expressed as:

$$\Delta G = \Delta G0 + eU \qquad \textit{Eq. 8-8}$$

The determination of the limiting potential (U_L) is formulated as follows:[224]

$$U_L = \min(-\Delta G_{*OOH} + 4.92\ x\ \Delta G_{*OOH} - 3.52\ ) \qquad \textit{Eq. 8-9}$$

The two constituent terms within the aforementioned equation correspond to the limiting potentials associated with the individual elementary steps comprising the two-electron oxygen

reduction pathway. It is worth noting that the lower of these limiting potentials, characterizing the complete catalytic reaction, establishes the overarching limiting potential governing the overall reaction kinetics.

9 Summary and Outlook

9.1 Summary

This thesis has investigated the impact of the nano- and atomic structure on the performance of a range of electrocatalysts needed for implementing a hydrogen-based economy. By employing state-of-the-art (scanning) transmission electron microscopy techniques, it was possible to study the local (atomic) structure in a representative manner and to explore how it evolves during catalysis. This yielded valuable insights into the degradation mechanisms affecting electrocatalysts and fundamental knowledge on the role of defects such as grain boundaries on the catalytic performance. Moreover, in instances where the current techniques were unable to be applied, method development was pursued in order to enable this type of research.

For instance, using IL-STEM it has been possible to study the changes during catalysis in the local structure of Rh@Pt/C NPs, which are potential anode catalysts for fuel cells. It was found that, despite their overall high stability, these particles could detach from the carbon support during catalysis. Thanks to these insights, it was proposed that efforts to enhance the stability of this material system should focus on novel support materials, or on increasing the interactions with the support, for example by having NP assemblies with several anchoring points.

Having seen the potential of IL-STEM for elucidating the degradation mechanisms of electrocatalysts, it was studied how to expand the potential of this technique for gas-evolving reactions which cause difficulties due to bubble formation. The results indicated that using tweezers from an inert material as a contact method for the TEM grid was a viable, easy-to-implement approach for performing IL-STEM experiments on gas-evolving reactions.

This newly developed method was used to study catalysts for the oxygen evolution reaction. In particular, $LaNiO_3$ perovskite oxide materials rich with Ruddlesden-Popper faults were investigated. It was observed that Fe traces on the electrolyte could diffuse into the RP faults, causing them to expand. Such expansion reduces the distance at neighboring $LaNiO_3$ layers. This displacement in the lattice can increase the OER activity of the $LaNiO_3$ particles.

The potential of structural defects for increasing the catalytic activity was further explored on grain boundary-rich Pt nanoparticle assemblies. These samples were found to have an elevated mass and specific activity toward the oxygen reduction reaction. The high specific activity was

attributed to their high density of concave grain boundary sites, with an optimized (higher) coordination number and binding energy. Moreover, boron doping of the grain boundaries emerged as a successful strategy for stabilizing the high-energy defects during catalysis.

In the last part of the thesis, it was evaluated how the density of grain boundaries can be controlled in electrocatalytic materials. For these experiments, nanoparticle assemblies of gold were chosen as a model system. Moreover, having assemblies with a controlled grain boundary density allowed us to study the relationship between grain boundaries, coordination number, and catalytic activity. A linear relationship between grain boundary density and two-electron oxygen reduction reaction activity was found, which was attributed to a tuning of the binding energy between the Au surface and the critical *OOH reaction intermediate, mediated by an increased lattice parameter and decreased coordination number.

This thesis has exemplified how material science can enhance the stability and activity of catalysts by means of structural investigations and the exploitation of the potential offered by defects.

9.2 Outlook

Despite this work's numerous insights, numerous questions arise for future studies. Firstly, having managed to perform identical location experiments on gas-evolving reactions in a simple and reproducible way, many more material systems and reactions (i.e., CO_2 reduction reaction, NH_3 oxidation, N_2 cracking…) can now be easily explored. This will allow to explore how the local structure of many catalysts evolves during these reactions, potentially finding ways to enhance their stability and activity.

Secondly, it was observed in the $LaNiO_3$ system that Fe traces in the electrolyte have a positive effect on the OER activity and that Fe segregation into the Ruddlesden-Popper faults caused compression of the neighboring $LaNiO_3$ layers. However, it is unclear how much the Fe segregation into the Ruddlesden-Popper faults actually contributes to the changes in OER activity. Experiments in thin films with a controlled density of RP faults could help to clarify this point.

Thirdly, it was found that the two-electron ORR catalytic activity of gold nanoparticle assemblies possesses a linear relationship with grain boundary density. However, how the different grain boundary types, e.g., ∑3, ∑9…, affect the catalytic activity remains unanswered. It would be interesting to perform a systematic study on the catalytic activity of samples with

a varying grain boundary type. Such a study, if paired with high-resolution STEM images of the corresponding grain boundaries and theoretical calculations, would provide valuable insights into the role of grain boundaries as active centers for electrocatalysis.

An additional interesting direction for a future study stems from the different behavior of the coordination number during the assembly process of Pt and Au nanoparticles. It was measured that Pt nanoparticles had a lower coordination number than the corresponding Pt nanoassembly, while in the case of Au, the behavior was the opposite (the coordination number of Au nanoparticles was higher than Au nanoassemblies). It is unclear how much of this difference is explained by the difference in particle size between the Pt and Au nanoparticles, or if other factors such as the stacking fault formation energy, and facet energy also play a role. Therefore, studying systematically how the coordination number changes during the assembly process for varying nanoparticle sizes and/or different materials would also provide insights into how to rationally control the binding energy and catalytic activity for different reactions.

Many other points can also be explored; for example, boron was found to stabilize the high energy defects on the nanoassemblies. Is B segregated with a similar Gibbs excess in all grain boundaries or does it depend on the grain boundary type? Can other heteroatoms have a similar, or even better stabilization effect? Can heteroatoms be used for stabilizing also other defects and high-energy facets of nanoparticles?...

Lastly, 4D-STEM is a rapidly developing technique that has the enormous potential to characterize the local atomic structure of electrocatalysts in a representative manner. The information can then be directly combined with the atomic column-resolved structural data of defects and used to perform a length-bridging, statistical analysis of the effects of defects in catalysis, as shown in this thesis with the example of grain boundaries. Future studies could adopt a comparable approach to the one demonstrated in this work, capitalizing on the potential of integrating material science into catalysis to investigate the role of other structural features and defects in catalysis.

10 Bibliography

(1) Richardson, J. T. *Principles of Catalyst Development*; Springer, 2013.

(2) Taseska, T.; Yu, W.; Wilsey, M. K.; Cox, C. P.; Meng, Z.; Ngarnim, S. S.; Müller, A. M. Analysis of the Scale of Global Human Needs and Opportunities for Sustainable Catalytic Technologies. *Top. Catal.* **2023**, *66* (5), 338–374. https://doi.org/10.1007/s11244-023-01799-3.

(3) IEA. *Electrification*. https://www.iea.org/energy-system/electricity/electrification.

(4) O'Mullane, A. P.; Escudero-Escribano, M.; Stephens, I. E. L.; Krischer, K. The Role of Electrocatalysis in a Sustainable Future: From Renewable Energy Conversion and Storage to Emerging Reactions. *ChemPhysChem* **2019**, *20* (22), 2900–2903. https://doi.org/https://doi.org/10.1002/cphc.201901058.

(5) Seh, Z. W.; Kibsgaard, J.; Dickens, C. F.; Chorkendorff, I.; Nørskov, J. K.; Jaramillo, T. F. Combining Theory and Experiment in Electrocatalysis: Insights into Materials Design. *Science (80-.).* **2017**, *355* (6321), eaad4998. https://doi.org/10.1126/science.aad4998.

(6) Moritz, M.; Schönfisch, M.; Schulte, S. Estimating Global Production and Supply Costs for Green Hydrogen and Hydrogen-Based Green Energy Commodities. *Int. J. Hydrogen Energy* **2023**, *48* (25), 9139–9154. https://doi.org/https://doi.org/10.1016/j.ijhydene.2022.12.046.

(7) Winter, C.-J. Into the Hydrogen Energy Economy—Milestones. *Int. J. Hydrogen Energy* **2005**, *30* (7), 681–685. https://doi.org/https://doi.org/10.1016/j.ijhydene.2004.12.011.

(8) Perry, S. C.; Pangotra, D.; Vieira, L.; Csepei, L.-I.; Sieber, V.; Wang, L.; Ponce de León, C.; Walsh, F. C. Electrochemical Synthesis of Hydrogen Peroxide from Water and Oxygen. *Nat. Rev. Chem.* **2019**, *3* (7), 442–458. https://doi.org/10.1038/s41570-019-0110-6.

(9) Jovičević-Klug, M.; Souza Filho, I. R.; Springer, H.; Adam, C.; Raabe, D. Green Steel from Red Mud through Climate-Neutral Hydrogen Plasma Reduction. *Nature* **2024**, *625* (7996), 703–709. https://doi.org/10.1038/s41586-023-06901-z.

(10) Wang, S.; Lu, A.; Zhong, C.-J. Hydrogen Production from Water Electrolysis: Role of

Catalysts. *Nano Converg.* **2021**, *8* (1), 4. https://doi.org/10.1186/s40580-021-00254-x.

(11) Wei, D.; Shi, X.; Qu, R.; Junge, K.; Junge, H.; Beller, M. Toward a Hydrogen Economy: Development of Heterogeneous Catalysts for Chemical Hydrogen Storage and Release Reactions. *ACS Energy Lett.* **2022**, *7* (10), 3734–3752. https://doi.org/10.1021/acsenergylett.2c01850.

(12) Wang, Y.; Chen, K. S.; Mishler, J.; Cho, S. C.; Adroher, X. C. A Review of Polymer Electrolyte Membrane Fuel Cells: Technology, Applications, and Needs on Fundamental Research. *Applied Energy*. 2011. https://doi.org/10.1016/j.apenergy.2010.09.030.

(13) Chen, S.; Jelic, J.; Rein, D.; Najafishirtari, S.; Schmidt, F.-P.; Girgsdies, F.; Kang, L.; Wandzilak, A.; Rabe, A.; Doronkin, D. E.; Wang, J.; Friedel Ortega, K.; DeBeer, S.; Grunwaldt, J.-D.; Schlögl, R.; Lunkenbein, T.; Studt, F.; Behrens, M. Highly Loaded Bimetallic Iron-Cobalt Catalysts for Hydrogen Release from Ammonia. *Nat. Commun.* **2024**, *15* (1), 871. https://doi.org/10.1038/s41467-023-44661-6.

(14) Zhang, X.-L.; Yu, P.-C.; Su, X.-Z.; Hu, S.-J.; Shi, L.; Wang, Y.-H.; Yang, P.-P.; Gao, F.-Y.; Wu, Z.-Z.; Chi, L.-P.; Zheng, Y.-R.; Gao, M.-R. Efficient Acidic Hydrogen Evolution in Proton Exchange Membrane Electrolyzers over a Sulfur-Doped Marcasite-Type Electrocatalyst. *Sci. Adv.* **2024**, *9* (27), eadh2885. https://doi.org/10.1126/sciadv.adh2885.

(15) Abbott, D. F.; Lebedev, D.; Waltar, K.; Povia, M.; Nachtegaal, M.; Fabbri, E.; Copéret, C.; Schmidt, T. J. Iridium Oxide for the Oxygen Evolution Reaction: Correlation between Particle Size, Morphology, and the Surface Hydroxo Layer from Operando XAS. *Chem. Mater.* **2016**, *28* (18), 6591–6604. https://doi.org/10.1021/acs.chemmater.6b02625.

(16) Li, M.; Zhao, Z.; Cheng, T.; Fortunelli, A.; Chen, C.-Y.; Yu, R.; Zhang, Q.; Gu, L.; Merinov, B. V; Lin, Z.; Zhu, E.; Yu, T.; Jia, Q.; Guo, J.; Zhang, L.; Goddard, W. A.; Huang, Y.; Duan, X. Ultrafine Jagged Platinum Nanowires Enable Ultrahigh Mass Activity for the Oxygen Reduction Reaction. *Science (80-.).* **2016**, *354* (6318), 1414–1419. https://doi.org/10.1126/science.aaf9050.

(17) Chang, F.; Gao, W.; Guo, J.; Chen, P. Emerging Materials and Methods toward Ammonia-Based Energy Storage and Conversion. *Adv. Mater.* **2021**, *33* (50), 2005721.

https://doi.org/https://doi.org/10.1002/adma.202005721.

(18) Ciriminna, R.; Falletta, E.; Della Pina, C.; Teles, J. H.; Pagliaro, M. Industrial Applications of Gold Catalysis. *Angew. Chemie Int. Ed.* **2016**, *55* (46), 14210–14217. https://doi.org/https://doi.org/10.1002/anie.201604656.

(19) *Daily Metal Prices*. https://www.dailymetalprice.com/.

(20) Alayoglu, S.; Zavalij, P.; Eichhorn, B.; Wang, Q.; Frenkel, A. I.; Chupas, P. Structural and Architectural Evaluation of Bimetallic Nanoparticles: A Case Study of Pt−Ru Core−Shell and Alloy Nanoparticles. *ACS Nano* **2009**, *3* (10), 3127–3137. https://doi.org/10.1021/nn900242v.

(21) Alayoglu, S.; Eichhorn, B. Rh-Pt Bimetallic Catalysts: Synthesis, Characterization, and Catalysis of Core-Shell, Alloy, and Monometallic Nanoparticles. *J. Am. Chem. Soc.* **2008**, *130* (51), 17479–17486. https://doi.org/10.1021/ja8061425.

(22) Li, Z.; Fu, J.-Y.; Feng, Y.; Dong, C.-K.; Liu, H.; Du, X.-W. A Silver Catalyst Activated by Stacking Faults for the Hydrogen Evolution Reaction. *Nat. Catal.* **2019**, *2* (12), 1107–1114. https://doi.org/10.1038/s41929-019-0365-9.

(23) Bak, J.; Yun, T. G.; An, J. S.; Bae, H. Bin; Chung, S. Y. Comparison of Fe-Enhanced Oxygen Evolution Electrocatalysis in Amorphous and Crystalline Nickel Oxides to Evaluate the Structural Contribution. *Energy Environ. Sci.* **2022**, *15* (2), 610–620. https://doi.org/10.1039/d1ee01826d.

(24) Li, R.; Liang, J.; Li, T.; Yue, L.; Liu, Q.; Luo, Y.; Hamdy, M. S.; Sun, Y.; Sun, X. Recent Advances in MoS2-Based Materials for Electrocatalysis. *Chem. Commun.* **2022**, *58* (14), 2259–2278. https://doi.org/10.1039/D1CC04004A.

(25) Sun, Y.; Polani, S.; Luo, F.; Ott, S.; Strasser, P.; Dionigi, F. Advancements in Cathode Catalyst and Cathode Layer Design for Proton Exchange Membrane Fuel Cells. *Nat. Commun.* **2021**, *12* (1), 1–14. https://doi.org/10.1038/s41467-021-25911-x.

(26) Wang, Z.; Guo, X.; Montoya, J.; Nørskov, J. K. Predicting Aqueous Stability of Solid with Computed Pourbaix Diagram Using SCAN Functional. *npj Comput. Mater.* **2020**, *6* (1), 160. https://doi.org/10.1038/s41524-020-00430-3.

(27) Dong, C.; Li, Y.; Cheng, D.; Zhang, M.; Liu, J.; Wang, Y.-G.; Xiao, D.; Ma, D. Supported Metal Clusters: Fabrication and Application in Heterogeneous Catalysis. *ACS*

Catal. **2020**, *10* (19), 11011–11045. https://doi.org/10.1021/acscatal.0c02818.

(28) Wang, H.; Xu, S.; Tsai, C.; Li, Y.; Liu, C.; Zhao, J.; Liu, Y.; Yuan, H.; Abild-Pedersen, F.; Prinz, F. B.; Nørskov, J. K.; Cui, Y. Direct and Continuous Strain Control of Catalysts with Tunable Battery Electrode Materials. *Science (80-.).* **2016**, *354* (6315), 1031–1036. https://doi.org/10.1126/science.aaf7680.

(29) Feng, X.; Jiang, K.; Fan, S.; Kanan, M. W. Grain-Boundary-Dependent CO2 Electroreduction Activity. *J. Am. Chem. Soc.* **2015**, *137* (14), 4606–4609. https://doi.org/10.1021/ja5130513.

(30) Kim, J.; Yin, X.; Tsao, K.-C.; Fang, S.; Yang, H. Ca2Mn2O5 as Oxygen-Deficient Perovskite Electrocatalyst for Oxygen Evolution Reaction. *J. Am. Chem. Soc.* **2014**, *136* (42), 14646–14649. https://doi.org/10.1021/ja506254g.

(31) Da, Y.; Zeng, L.; Wang, C.; Gong, C.; Cui, L. A Simple Approach to Tailor OER Activity of SrxCo0.8Fe0.2O3 Perovskite Catalysts. *Electrochim. Acta* **2019**, *300*, 85–92. https://doi.org/https://doi.org/10.1016/j.electacta.2019.01.052.

(32) Sha, H.; Cui, J.; Yu, R. Deep Sub-Angstrom Resolution Imaging by Electron Ptychography with Misorientation Correction. *Sci. Adv.* **2024**, *8* (19), eabn2275. https://doi.org/10.1126/sciadv.abn2275.

(33) Longo, P.; Thomas, P. J.; Twesten, R. D. Atomic-Level EELS Mapping Using High-Energy Edges in Dualeels^{TM} Mode. *Micros. Today* **2012**, *20* (4), 30–36. https://doi.org/DOI: 10.1017/S1551929512000478.

(34) Ophus, C. Four-Dimensional Scanning Transmission Electron Microscopy (4D-STEM): From Scanning Nanodiffraction to Ptychography and Beyond. *Microsc. Microanal.* **2019**, *25* (3), 563–582. https://doi.org/DOI: 10.1017/S1431927619000497.

(35) Goris, B.; Bals, S.; Van den Broek, W.; Carbó-Argibay, E.; Gómez-Graña, S.; Liz-Marzán, L. M.; Van Tendeloo, G. Atomic-Scale Determination of Surface Facets in Gold Nanorods. *Nat. Mater.* **2012**, *11* (11), 930–935. https://doi.org/10.1038/nmat3462.

(36) Goris, B.; De Beenhouwer, J.; De Backer, A.; Zanaga, D.; Batenburg, K. J.; Sánchez-Iglesias, A.; Liz-Marzán, L. M.; Van Aert, S.; Bals, S.; Sijbers, J.; Van Tendeloo, G. Measuring Lattice Strain in Three Dimensions through Electron Microscopy. *Nano Lett.* **2015**, *15* (10), 6996–7001. https://doi.org/10.1021/acs.nanolett.5b03008.

(37) Hodnik, N.; Cherevko, S. Spot the Difference at the Nanoscale: Identical Location Electron Microscopy in Electrocatalysis. *Curr. Opin. Electrochem.* **2019**, *15*, 73–82. https://doi.org/https://doi.org/10.1016/j.coelec.2019.03.007.

(38) Fan, Z.; Zhang, L.; Baumann, D.; Mei, L.; Yao, Y.; Duan, X.; Shi, Y.; Huang, J.; Huang, Y.; Duan, X. In Situ Transmission Electron Microscopy for Energy Materials and Devices. *Adv. Mater.* **2019**, *31* (33), 1900608. https://doi.org/https://doi.org/10.1002/adma.201900608.

(39) Zhou, X.; Mathews, P.; Berkels, B.; Ahmad, S.; Alhassan, A. S. A.; Neugebauer, J.; Dehm, G.; Hickel, T.; Scheu, C.; Zhang, S. The Chemistry at Defects: Atomic-Scale Phase Transformations of Grain Boundaries. *arXiv Prepr. arXiv2303.09465* **2023**.

(40) Allen, F. I.; Pekin, T. C.; Persaud, A.; Rozeveld, S. J.; Meyers, G. F.; Ciston, J.; Ophus, C.; Minor, A. M. Fast Grain Mapping with Sub-Nanometer Resolution Using 4D-STEM with Grain Classification by Principal Component Analysis and Non-Negative Matrix Factorization. *Microsc. Microanal.* **2021**, *27* (4), 794–803. https://doi.org/10.1017/S1431927621011946.

(41) Harvey, D. *Electrochemical Methods*; DePauw University, 2021.

(42) Banoth, P.; Kandula, C.; Kollu, P. Introduction to Electrocatalysts. *ACS Symp. Ser.* **2022**, *1432*, 1–37. https://doi.org/10.1021/bk-2022-1432.ch001.

(43) *Electrochemistry*. https://chem.libretexts.org/@go/page/250 (accessed 2024-02-28).

(44) The Arrhenius Law - Activation Energies. https://chem.libretexts.org/@go/page/1444.

(45) Medford, A. J.; Vojvodic, A.; Hummelshøj, J. S.; Voss, J.; Abild-Pedersen, F.; Studt, F.; Bligaard, T.; Nilsson, A.; Nørskov, J. K. From the Sabatier Principle to a Predictive Theory of Transition-Metal Heterogeneous Catalysis. *J. Catal.* **2015**, *328*, 36–42. https://doi.org/https://doi.org/10.1016/j.jcat.2014.12.033.

(46) Aymerich-Armengol, R.; Vega-Paredes, M.; Mingers, A.; Camuti, L.; Kim, J.; Jeongwook, B.; Efthimiopoulos, I.; Sahu, R.; Podjaski, F.; Rabe, M.; Scheu, C.; Lim, J.; Zhang, S. Operando Insights on the Degradation Mechanisms of Rhenium Doped Molybdenum Disulfide Nanocatalysts for Electrolyzer Applications. **2024**. https://doi.org/10.48550/arXiv.2309.08977.

(47) Li, Z.; Wei, P.; Wang, G. Recent Advances on Perovskite Electrocatalysts for Water

Oxidation in Alkaline Medium. *Energy & Fuels* **2022**, *36* (19), 11724–11744. https://doi.org/10.1021/acs.energyfuels.2c02236.

(48) Cheraparambil, H.; Vega-Paredes, M.; Wang, Y.; Tüysüz, H.; Scheu, C.; Weidenthaler, C. Deciphering the Role of Fe Impurities in the Electrolyte Boosting the OER Activity of LaNiO3. *J. Mater. Chem. A* **2024**, *12* (9), 5194–5203. https://doi.org/10.1039/D3TA06733E.

(49) Aminudin, M. A.; Kamarudin, S. K.; Lim, B. H.; Majilan, E. H.; Masdar, M. S.; Shaari, N. An Overview: Current Progress on Hydrogen Fuel Cell Vehicles. *Int. J. Hydrogen Energy* **2023**, *48* (11), 4371–4388. https://doi.org/https://doi.org/10.1016/j.ijhydene.2022.10.156.

(50) Vega Paredes, M.; Garzón Manjón, A.; Hill, B.; Schwarz, T.; Rivas, N. A.; Jurzinsky, T.; Hengge, K.; Mack, F.; Scheu, C. Evaluation of Functional Layers Thinning of High Temperature Polymer Electrolyte Membrane Fuel Cells after Long Term Operation. *Nanoscale* **2022**, *14*, 11543–11551. https://doi.org/10.1039/D2NR02892A.

(51) Garzón Manjón, A.; Vega Paredes, M.; Berova, V.; Gänsler, T.; Schwarz, T.; Rivas, N. A.; Hengge, K.; Jurzinsky, T.; Scheu, C. Insights into the Performance and Degradation of Ru@Pt Core-Shell Catalysts for Fuel Cells by Advanced (Scanning) Transmission Electron Microscopy. *Nanoscale* **2022**, *14*, 18060–18069. https://doi.org/10.1039/d2nr04869h.

(52) Berova, V.; Manjón, A. G.; Vega Paredes, M.; Schwarz, T.; Rivas, N. A.; Hengge, K.; Jurzinsky, T.; Scheu, C. Influence of the Shell Thickness on the Degradation of Ru@Pt Core-Shell Catalysts in PEM Fuel Cells. *J. Power Sources* **2023**, *554*, 232327. https://doi.org/https://doi.org/10.1016/j.jpowsour.2022.232327.

(53) Schalenbach, M.; Kasian, O.; Ledendecker, M.; Speck, F. D.; Mingers, A. M.; Mayrhofer, K. J. J.; Cherevko, S. The Electrochemical Dissolution of Noble Metals in Alkaline Media. *Electrocatalysis* **2018**, *9* (2), 153–161. https://doi.org/10.1007/s12678-017-0438-y.

(54) Obermaier, M.; Jozwiak, K.; Rauber, M.; Bauer, A.; Scheu, C. Comparative Study of Pinhole Detection Methods for Automotive Fuel Cell Degradation Analysis. *J. Power Sources* **2021**, *488*, 229405. https://doi.org/https://doi.org/10.1016/j.jpowsour.2020.229405.

(55) Haynes, W. M. *CRC Handbook of Chemistry and Physics*; CRC Handbook of Chemistry and Physics; CRC Press, 2014.

(56) Yang, S.; Verdaguer-Casadevall, A.; Arnarson, L.; Silvioli, L.; Čolić, V.; Frydendal, R.; Rossmeisl, J.; Chorkendorff, I.; Stephens, I. E. L. Toward the Decentralized Electrochemical Production of H2O2: A Focus on the Catalysis. *ACS Catal.* **2018**, *8* (5), 4064–4081. https://doi.org/10.1021/acscatal.8b00217.

(57) Meier, J. C.; Galeano, C.; Katsounaros, I.; Witte, J.; Bongard, H. J.; Topalov, A. A.; Baldizzone, C.; Mezzavilla, S.; Schüth, F.; Mayrhofer, K. J. J. Design Criteria for Stable Pt/C Fuel Cell Catalysts. *Beilstein J. Nanotechnol.* **2014**, *5*, 44–67. https://doi.org/10.3762/bjnano.5.5.

(58) Hengge, K.; Gänsler, T.; Pizzutilo, E.; Heinzl, C.; Beetz, M.; Mayrhofer, K. J. J.; Scheu, C. Accelerated Fuel Cell Tests of Anodic Pt/Ru Catalyst via Identical Location TEM: New Aspects of Degradation Behavior. *Int. J. Hydrogen Energy* **2017**, *42* (40), 25359–25371. https://doi.org/10.1016/j.ijhydene.2017.08.108.

(59) Mariano, R. G.; McKelvey, K.; White, H. S.; Kanan, M. W. Selective Increase in CO2 Electroreduction Activity at Grain-Boundary Surface Terminations. *Science (80-.).* **2017**, *358* (6367), 1187–1192. https://doi.org/10.1126/science.aao3691.

(60) Mariano, R. G.; Kang, M.; Wahab, O. J.; McPherson, I. J.; Rabinowitz, J. A.; Unwin, P. R.; Kanan, M. W. Microstructural Origin of Locally Enhanced CO2 Electroreduction Activity on Gold. *Nat. Mater.* **2021**, *20* (7), 1000–1006. https://doi.org/10.1038/s41563-021-00958-9.

(61) Huang, W.; Johnston-Peck, A. C.; Wolter, T.; Yang, W.-C. D.; Xu, L.; Oh, J.; Reeves, B. A.; Zhou, C.; Holtz, M. E.; Herzing, A. A.; Lindenberg, A. M.; Mavrikakis, M.; Cargnello, M. Steam-Created Grain Boundaries for Methane C–H Activation in Palladium Catalysts. *Science (80-.).* **2021**, *373* (6562), 1518–1523. https://doi.org/10.1126/science.abj5291.

(62) Bueno Villoro, R.; Zavanelli, D.; Jung, C.; Mattlat, D. A.; Hatami Naderloo, R.; Pérez, N.; Nielsch, K.; Snyder, G. J.; Scheu, C.; He, R.; Zhang, S. Grain Boundary Phases in NbFeSb Half-Heusler Alloys: A New Avenue to Tune Transport Properties of Thermoelectric Materials. *Adv. Energy Mater.* **2023**, *13* (13), 2204321. https://doi.org/https://doi.org/10.1002/aenm.202204321.

(63) Nie, J.; Hu, C.; Yan, Q.; Luo, J. Discovery of Electrochemically Induced Grain Boundary Transitions. *Nat. Commun.* **2021**, *12* (1), 2374. https://doi.org/10.1038/s41467-021-22669-0.

(64) Vega-Paredes, M.; Aymerich-Armengol, R.; Arenas Esteban, D.; Martí-Sánchez, S.; Bals, S.; Scheu, C.; Garzón Manjón, A. Electrochemical Stability of Rhodium–Platinum Core–Shell Nanoparticles: An Identical Location Scanning Transmission Electron Microscopy Study. *ACS Nano* **2023**, *17* (17), 16943–16951. https://doi.org/10.1021/acsnano.3c04039.

(65) Zhao, X.; Sasaki, K. Advanced Pt-Based Core–Shell Electrocatalysts for Fuel Cell Cathodes. *Acc. Chem. Res.* **2022**, *55* (9), 1226–1236. https://doi.org/10.1021/acs.accounts.2c00057.

(66) Haase, F. T.; Bergmann, A.; Jones, T. E.; Timoshenko, J.; Herzog, A.; Jeon, H. S.; Rettenmaier, C.; Cuenya, B. R. Size Effects and Active State Formation of Cobalt Oxide Nanoparticles during the Oxygen Evolution Reaction. *Nat. Energy* **2022**, *7* (8), 765–773. https://doi.org/10.1038/s41560-022-01083-w.

(67) Nesselberger, M.; Ashton, S.; Meier, J. C.; Katsounaros, I.; Mayrhofer, K. J. J.; Arenz, M. The Particle Size Effect on the Oxygen Reduction Reaction Activity of Pt Catalysts: Influence of Electrolyte and Relation to Single Crystal Models. *J. Am. Chem. Soc.* **2011**, *133* (43), 17428–17433. https://doi.org/10.1021/ja207016u.

(68) Perez-Alonso, F. J.; McCarthy, D. N.; Nierhoff, A.; Hernandez-Fernandez, P.; Strebel, C.; Stephens, I. E. L.; Nielsen, J. H.; Chorkendorff, I. The Effect of Size on the Oxygen Electroreduction Activity of Mass-Selected Platinum Nanoparticles. *Angew. Chemie Int. Ed.* **2012**, *51* (19), 4641–4643. https://doi.org/https://doi.org/10.1002/anie.201200586.

(69) Nørskov, J. K.; Rossmeisl, J.; Logadottir, A.; Lindqvist, L.; Kitchin, J. R.; Bligaard, T.; Jónsson, H. Origin of the Overpotential for Oxygen Reduction at a Fuel-Cell Cathode. *J. Phys. Chem. B* **2004**, *108* (46), 17886–17892. https://doi.org/10.1021/jp047349j.

(70) Verdaguer-Casadevall, A.; Deiana, D.; Karamad, M.; Siahrostami, S.; Malacrida, P.; Hansen, T. W.; Rossmeisl, J.; Chorkendorff, I.; Stephens, I. E. L. Trends in the Electrochemical Synthesis of H2O2: Enhancing Activity and Selectivity by Electrocatalytic Site Engineering. *Nano Lett.* **2014**, *14* (3), 1603–1608. https://doi.org/10.1021/nl500037x.

(71) Surface Structures- Fcc Metals. Queen Mary, University of London. https://chem.libretexts.org/@go/page/25356.

(72) Kodama, K.; Nagai, T.; Kuwaki, A.; Jinnouchi, R.; Morimoto, Y. Challenges in Applying Highly Active Pt-Based Nanostructured Catalysts for Oxygen Reduction Reactions to Fuel Cell Vehicles. *Nat. Nanotechnol.* **2021**, *16* (2), 140–147. https://doi.org/10.1038/s41565-020-00824-w.

(73) Calle-Vallejo, F.; Tymoczko, J.; Colic, V.; Vu, Q. H.; Pohl, M. D.; Morgenstern, K.; Loffreda, D.; Sautet, P.; Schuhmann, W.; Bandarenka, A. S. Finding Optimal Surface Sites on Heterogeneous Catalysts by Counting Nearest Neighbors. *Science (80-.).* **2015**, *350* (6257), 185–189. https://doi.org/10.1126/science.aab3501.

(74) Calle-Vallejo, F. The ABC of Generalized Coordination Numbers and Their Use as a Descriptor in Electrocatalysis. *Adv. Sci.* **2023**, *10* (20), 2207644. https://doi.org/https://doi.org/10.1002/advs.202207644.

(75) Wu, T.; Han, M.-Y.; Xu, Z. J. Size Effects of Electrocatalysts: More Than a Variation of Surface Area. *ACS Nano* **2022**, *16* (6), 8531–8539. https://doi.org/10.1021/acsnano.2c04603.

(76) Xu, Z.; Zhang, H.; Zhong, H.; Lu, Q.; Wang, Y.; Su, D. Effect of Particle Size on the Activity and Durability of the Pt/C Electrocatalyst for Proton Exchange Membrane Fuel Cells. *Appl. Catal. B Environ.* **2012**, *111–112*, 264–270. https://doi.org/https://doi.org/10.1016/j.apcatb.2011.10.007.

(77) Luo, M.; Guo, S. Strain-Controlled Electrocatalysis on Multimetallic Nanomaterials. *Nat. Rev. Mater.* **2017**, *2* (11), 17059. https://doi.org/10.1038/natrevmats.2017.59.

(78) Mavrikakis, M.; Hammer, B.; Nørskov, J. K. Effect of Strain on the Reactivity of Metal Surfaces. *Phys. Rev. Lett.* **1998**, *81* (13), 2819–2822. https://doi.org/10.1103/PhysRevLett.81.2819.

(79) Hammer, B.; Nørskov, J. K. Electronic Factors Determining the Reactivity of Metal Surfaces. *Surf. Sci.* **1995**, *343* (3), 211–220. https://doi.org/https://doi.org/10.1016/0039-6028(96)80007-0.

(80) Stamenkovic, V.; Mun, B. S.; Mayrhofer, K. J. J.; Ross, P. N.; Markovic, N. M.; Rossmeisl, J.; Greeley, J.; Nørskov, J. K. Changing the Activity of Electrocatalysts for

Oxygen Reduction by Tuning the Surface Electronic Structure. *Angew. Chemie Int. Ed.* **2006**, *45* (18), 2897–2901. https://doi.org/https://doi.org/10.1002/anie.200504386.

(81) Stamenkovic, V. R.; Fowler, B.; Mun, B. S.; Wang, G.; Ross, P. N.; Lucas, C. A.; Marković, N. M.; Markovic, N. M. Improved Oxygen Reduction Activity on Pt3Ni(111) via Increased Surface Site Availability. *Science (80-.).* **2007**, *315* (5811), 493–497. https://doi.org/10.1126/science.1135941.

(82) Huang, X.; Zhao, Z.; Cao, L.; Chen, Y.; Zhu, E.; Lin, Z.; Li, M.; Yan, A.; Zettl, A.; Wang, Y. M.; Duan, X.; Mueller, T.; Huang, Y. High-Performance Transition Metal–Doped Pt3Ni Octahedra for Oxygen Reduction Reaction. *Science (80-.).* **2015**, *348* (6240), 1230–1234. https://doi.org/10.1126/science.aaa8765.

(83) Han, B.; Carlton, C. E.; Kongkanand, A.; Kukreja, R. S.; Theobald, B. R.; Gan, L.; O'Malley, R.; Strasser, P.; Wagner, F. T.; Shao-Horn, Y. Record Activity and Stability of Dealloyed Bimetallic Catalysts for Proton Exchange Membrane Fuel Cells. *Energy Environ. Sci.* **2015**, *8* (1), 258–266. https://doi.org/10.1039/C4EE02144D.

(84) Bu, L.; Zhang, N.; Guo, S.; Zhang, X.; Li, J.; Yao, J.; Wu, T.; Lu, G.; Ma, J.-Y.; Su, D.; Huang, X. Biaxially Strained PtPb/Pt Core/Shell Nanoplate Boosts Oxygen Reduction Catalysis. *Science (80-.).* **2016**, *354* (6318), 1410–1414. https://doi.org/10.1126/science.aah6133.

(85) Hengge, K.; Heinzl, C.; Perchthaler, M.; Varley, D.; Lochner, T.; Scheu, C. Unraveling Micro- and Nanoscale Degradation Processes during Operation of High-Temperature Polymer-Electrolyte-Membrane Fuel Cells. *J. Power Sources* **2017**, *364*, 437–448. https://doi.org/10.1016/j.jpowsour.2017.08.042.

(86) Porter, D. A.; Easterling, K. E. *Phase Transformations in Metals and Alloys (Revised Reprint)*; CRC Press, 2009.

(87) Sutton, A. P.; Balluffi, R. W. *Interfaces in Crystalline Materials*; Monographs on the physics and chemistry of materials; Clarendon Press, 1995.

(88) Föll, H. *The Coincidence Site Lattice*. Uni-kiel. https://www.tf.uni-kiel.de/matwis/amat/def_en/kap_7/backbone/r7_1_2.html.

(89) Rittner, J. D.; Seidman, D. N. 〈110〉 Symmetric Tilt Grain-Boundary Structures in Fcc Metals with Low Stacking-Fault Energies. *Phys. Rev. B* **1996**, *54* (10), 6999–7015.

https://doi.org/10.1103/PhysRevB.54.6999.

(90) Williams, D. B.; Carter, C. B. *Transmission Electron Microscopy: A Textbook for Materials Science*; 2009. https://doi.org/10.1007/978-0-387-76501-3.

(91) *Scanning Transmission Electron Microscopy*, 1st ed.; Pennycook, S. J., Nellist, P. D., Eds.; Springer New York, NY. https://doi.org/https://doi.org/10.1007/978-1-4419-7200-2.

(92) Goodhew, P. J.; Humphreys, J. Electron Microscopy and Analysis, Third Edition. *Electron Microsc. Anal.* **2014**.

(93) Rottenfusser, R.; Wilson, R. *Education in Microscopy and Digital Imaging*. Zeiss Microscopy. https://zeiss-campus.magnet.fsu.edu/articles/basics/resolution.html.

(94) Smith, D. J. Ultimate Resolution in the Electron Microscope? *Mater. Today* **2008**, *11*, 30–38. https://doi.org/https://doi.org/10.1016/S1369-7021(09)70005-7.

(95) Jia, C. L.; Lentzen, M.; Urban, K. High-Resolution Transmission Electron Microscopy Using Negative Spherical Aberration. *Microsc. Microanal.* **2004**, *10* (2), 174–184. https://doi.org/10.1017/S1431927604040425.

(96) De Backer, A.; van den Bos, K. H. W.; Van den Broek, W.; Sijbers, J.; Van Aert, S. StatSTEM: An Efficient Approach for Accurate and Precise Model-Based Quantification of Atomic Resolution Electron Microscopy Images. *Ultramicroscopy* **2016**, *171*, 104–116. https://doi.org/https://doi.org/10.1016/j.ultramic.2016.08.018.

(97) Geng, X.; Vega-Paredes, M.; Ophus, C.; Lu, P.; Ma, Y.; Zhang, S.; Scheu, C.; Liebscher, C. H.; Gault, B. *Grain Boundary Engineering for Efficient and Durable Electrocatalysis*; 2024. (Under reivew).

(98) *Electron Tomography*; Frank, J., Ed.; Springer New York, NY, 1992. https://doi.org/https://doi.org/10.1007/978-1-4757-2163-8.

(99) Gürsoy, D.; De Carlo, F.; Xiao, X.; Jacobsen, C. TomoPy: A Framework for the Analysis of Synchrotron Tomographic Data. *J. Synchrotron Radiat.* **2014**, *21* (Pt 5), 1188–1193. https://doi.org/10.1107/S1600577514013939.

(100) Sofroniew, N.; Lambert, T.; Evans, K.; Nunez-Iglesias, J.; Bokota, G.; Winston, P.; Peña-Castellanos, G.; Yamauchi, K.; Bussonnier, M.; Doncila Pop, D.; Can Solak, A.;

Liu, Z.; Wadhwa, P.; Burt, A.; Buckley, G.; Sweet, A.; Migas, L.; Hilsenstein, V.; Gaifas, L.; Bragantini, J.; Rodríguez-Guerra, J.; Muñoz, H.; Freeman, J.; Boone, P.; Lowe, A.; Gohlke, C.; Royer, L.; PIERRÉ, A.; Har-Gil, H.; McGovern, A. Napari: A Multi-Dimensional Image Viewer for Python. Zenodo November 2022. https://doi.org/10.5281/zenodo.7276432.

(101) van Aarle, W.; Palenstijn, W. J.; De Beenhouwer, J.; Altantzis, T.; Bals, S.; Batenburg, K. J.; Sijbers, J. The ASTRA Toolbox: A Platform for Advanced Algorithm Development in Electron Tomography. *Ultramicroscopy* **2015**, *157* (2015), 35–47. https://doi.org/10.1016/j.ultramic.2015.05.002.

(102) de la Peña, F.; Prestat, E.; Fauske, V. T.; Burdet, P.; Lähnemann, J.; Jokubauskas, P.; Furnival, T.; Nord, M.; Ostasevicius, T.; MacArthur, K. E.; Johnstone, D. N.; Sarahan, M.; Taillon, J.; Aarholt, T.; pquinn-dls; Migunov, V.; Eljarrat, A.; Caron, J.; Francis, C.; Nemoto, T.; Poon, T.; Mazzucco, S.; actions-user; Tappy, N.; Cautaerts, N.; Somnath, S.; Slater, T.; Walls, M.; Winkler, F.; Ånes, H. W. Hyperspy/Hyperspy: Release v1.7.3. Zenodo October 2022. https://doi.org/10.5281/zenodo.7263263.

(103) Xin, B. *Synthesis of Nanoporous Ca3Co4O9 Thin Films for Flexible Thermoelectrics*; 2020. https://doi.org/10.3384/lic.diva-170837.

(104) Elgrishi, N.; Rountree, K. J.; McCarthy, B. D.; Rountree, E. S.; Eisenhart, T. T.; Dempsey, J. L. A Practical Beginner's Guide to Cyclic Voltammetry. *J. Chem. Educ.* **2018**, *95* (2), 197–206. https://doi.org/10.1021/acs.jchemed.7b00361.

(105) Vega-Paredes, M.; Scheu, C.; Aymerich-Armengol, R. Expanding the Potential of Identical Location Scanning Transmission Electron Microscopy for Gas Evolving Reactions: Stability of Rhenium Molybdenum Disulfide Nanocatalysts for Hydrogen Evolution Reaction. *ACS Appl. Mater. Interfaces* **2023**, *15* (40), 46895–46901. https://doi.org/10.1021/acsami.3c09188.

(106) Geng, X.; Vega-Paredes, M.; Chakraborty, P.; Li, Y.; Scheu, C.; Wang, Z.; Gault, B. *Concave Grain Boundaries Stabilized by Boron Segregation for Efficient and Durable Oxygen Reduction*; 2024. (Under review).

(107) Du, C.; Sun, Y.; Shen, T.; Yin, G.; Zhang, J. 7 - Applications of RDE and RRDE Methods in Oxygen Reduction Reaction; Xing, W., Yin, G., Zhang, J. B. T.-R. E. M. and O. R. E., Eds.; Elsevier: Amsterdam, 2014; pp 231–277.

https://doi.org/https://doi.org/10.1016/B978-0-444-63278-4.00007-0.

(108) Hwang, S.; Chen, X.; Zhou, G.; Su, D. In Situ Transmission Electron Microscopy on Energy-Related Catalysis. *Adv. Energy Mater.* **2020**, *10* (11), 1–24. https://doi.org/10.1002/aenm.201902105.

(109) Soleymani, A. P.; Parent, L. R.; Jankovic, J. Challenges and Opportunities in Understanding Proton Exchange Membrane Fuel Cell Materials Degradation Using In-Situ Electrochemical Liquid Cell Transmission Electron Microscopy. *Adv. Funct. Mater.* **2022**, *32* (5). https://doi.org/10.1002/adfm.202105188.

(110) Mayrhofer, K. J. J.; Meier, J. C.; Ashton, S. J.; Wiberg, G. K. H.; Kraus, F.; Hanzlik, M.; Arenz, M. Fuel Cell Catalyst Degradation on the Nanoscale. *Electrochem. commun.* **2008**, *10* (8), 1144–1147. https://doi.org/10.1016/j.elecom.2008.05.032.

(111) Wang, Q.; Gao, Y.; Ma, Z.; Zhang, Y.; Ni, W.; Younus, H. A.; Zhang, C.; Chen, Z.; Zhang, S. Supported Ionic Liquid Phase-Boosted Highly Active and Durable Electrocatalysts towards Hydrogen Evolution Reaction in Acidic Electrolyte. *J. Energy Chem.* **2021**, *54*, 342–351. https://doi.org/https://doi.org/10.1016/j.jechem.2020.06.012.

(112) Nilekar, A. U.; Alayoglu, S.; Eichhorn, B.; Mavrikakis, M. Preferential CO Oxidation in Hydrogen: Reactivity of Core-Shell Nanoparticles. *J. Am. Chem. Soc.* **2010**, *132* (21), 7418–7428. https://doi.org/10.1021/ja101108w.

(113) Twigg, M. V. Catalytic Control of Emissions from Cars. *Catal. Today* **2011**, *163* (1), 33–41. https://doi.org/10.1016/j.cattod.2010.12.044.

(114) Zou, Y.; Goei, R.; Ong, S. A.; Ong, A. J.; Huang, J.; Tok, A. I. Y. Development of Core-Shell Rh@Pt and Rh@Ir Nanoparticle Thin Film Using Atomic Layer Deposition for HER Electrocatalysis Applications. *Processes* **2022**, *10* (5). https://doi.org/10.3390/pr10051008.

(115) Harak, E. W.; Koczkur, K. M.; Harak, D. W.; Patton, P.; Skrabalak, S. E. Designing Efficient Catalysts through Bimetallic Architecture: Rh@Pt Nanocubes as a Case Study. *ChemNanoMat* **2017**, *3* (11), 815–821. https://doi.org/10.1002/cnma.201700167.

(116) El Sawy, E. N.; Pickup, P. G. Carbon Monoxide and Formic Acid Oxidation at Rh@Pt Nanoparticles. *Electrochim. Acta* **2019**, *302*, 234–240. https://doi.org/10.1016/j.electacta.2019.02.047.

(117) Sheng, Y.; Liu, Y.; Yin, Y.; Zou, X.; Ren, J.; Wu, B.; Wang, X.; Lu, X. Rh Promotional Effects on Pt–Rh Alloy Catalysts for Chemoselective Hydrogenation of Nitrobenzene to p-Aminophenol. *Chem. Eng. J.* **2023**, *452*, 139448. https://doi.org/https://doi.org/10.1016/j.cej.2022.139448.

(118) Liao, Y. J.; Pan, H. Bin; Wai, C. M. Pt, Rh and Pt-Rh Nanoparticles on Modified Single-Walled Carbon Nanotubes for Hydrogenation of Benzene at Room Temperature. *J. Nanosci. Nanotechnol.* **2011**, *11* (10), 8580–8585. https://doi.org/10.1166/jnn.2011.4966.

(119) Sethuraman, V. A.; Weidner, J. W.; Haug, A. T.; Pemberton, M.; Protsailo, L. V. Importance of Catalyst Stability Vis-à-Vis Hydrogen Peroxide Formation Rates in PEM Fuel Cell Electrodes. *Electrochim. Acta* **2009**, *54* (23), 5571–5582. https://doi.org/10.1016/j.electacta.2009.04.062.

(120) El Sawy, E. N.; Brueckner, T. M.; Pickup, P. G. Electrochemical Oxidation of Methanol and Ethanol at Rh@Pt and Ru@Pt Catalysts. *J. Electrochem. Soc.* **2020**, *167* (10), 106507. https://doi.org/10.1149/1945-7111/ab98f1.

(121) Silva, C. D.; Corradini, P. G.; Del Colle, V.; Mascaro, L. H.; de Lima, F. H. B.; Pereira, E. C. Pt/Rh/Pt and Pt/Ru/Pt Multilayers for the Electrochemical Oxidation of Methanol and Ethanol. *Electrochim. Acta* **2020**, *354*, 136674. https://doi.org/10.1016/j.electacta.2020.136674.

(122) Lima, F. H. B.; Gonzalez, E. R. Electrocatalysis of Ethanol Oxidation on Pt Monolayers Deposited on Carbon-Supported Ru and Rh Nanoparticles. *Appl. Catal. B Environ.* **2008**, *79* (4), 341–346. https://doi.org/10.1016/j.apcatb.2007.10.028.

(123) Housmans, T. H. M.; Feliu, J. M.; Gómez, R.; Koper, M. T. M. CO Oxidation on Pt-Modified Rh(111) Electrodes. *ChemPhysChem* **2005**, *6* (8), 1522–1529. https://doi.org/https://doi.org/10.1002/cphc.200400658.

(124) Avgouropoulos, G.; Ioannides, T. CO Tolerance of Pt and Rh Catalysts: Effect of CO in the Gas-Phase Oxidation of H2 over Pt and Rh Supported Catalysts. *Appl. Catal. B Environ.* **2005**, *56* (1-2 SPEC. ISS.), 77–86. https://doi.org/10.1016/j.apcatb.2004.07.016.

(125) Ren, P.; Pei, P.; Li, Y.; Wu, Z.; Chen, D.; Huang, S. Degradation Mechanisms of Proton

Exchange Membrane Fuel Cell under Typical Automotive Operating Conditions. *Prog. Energy Combust. Sci.* **2020**, *80*, 100859. https://doi.org/10.1016/j.pecs.2020.100859.

(126) Rasouli, S.; Ortiz Godoy, R. A.; Yang, Z.; Gummalla, M.; Ball, S. C.; Myers, D.; Ferreira, P. J. Surface Area Loss Mechanisms of Pt3Co Nanocatalysts in Proton Exchange Membrane Fuel Cells. *J. Power Sources* **2017**, *343*, 571–579. https://doi.org/10.1016/j.jpowsour.2017.01.058.

(127) Beermann, V.; Holtz, M. E.; Padgett, E.; De Araujo, J. F.; Muller, D. A.; Strasser, P. Real-Time Imaging of Activation and Degradation of Carbon Supported Octahedral Pt-Ni Alloy Fuel Cell Catalysts at the Nanoscale Using: In Situ Electrochemical Liquid Cell STEM. *Energy Environ. Sci.* **2019**, *12* (8), 2476–2485. https://doi.org/10.1039/c9ee01185d.

(128) Dubau, L.; Maillard, F.; Chatenet, M.; Guetaz, L.; André, J.; Rossinot, E. Durability of Pt[Sub 3]Co/C Cathodes in a 16 Cell PEMFC Stack: Macro/Microstructural Changes and Degradation Mechanisms. *J. Electrochem. Soc.* **2010**, *157* (12), B1887. https://doi.org/10.1149/1.3485104.

(129) Molochas, C.; Tsiakaras, P. Carbon Monoxide Tolerant Pt-Based Electrocatalysts for H2-PEMFC Applications: Current Progress and Challenges. *Catalysts* **2021**, *11* (9). https://doi.org/10.3390/catal11091127.

(130) Wee, J. H.; Lee, K. Y. Overview of the Development of CO-Tolerant Anode Electrocatalysts for Proton-Exchange Membrane Fuel Cells. *J. Power Sources* **2006**, *157* (1), 128–135. https://doi.org/10.1016/j.jpowsour.2005.08.010.

(131) Xie, J.; Zhang, Q.; Gu, L.; Xu, S.; Wang, P.; Liu, J.; Ding, Y.; Yao, Y. F.; Nan, C.; Zhao, M.; You, Y.; Zou, Z. Ruthenium–Platinum Core–Shell Nanocatalysts with Substantially Enhanced Activity and Durability towards Methanol Oxidation. *Nano Energy* **2016**, *21*, 247–257. https://doi.org/https://doi.org/10.1016/j.nanoen.2016.01.013.

(132) Hsieh, Y. C.; Zhang, Y.; Su, D.; Volkov, V.; Si, R.; Wu, L.; Zhu, Y.; An, W.; Liu, P.; He, P.; Ye, S.; Adzic, R. R.; Wang, J. X. Ordered Bilayer Ruthenium-Platinum Core-Shell Nanoparticles as Carbon Monoxide-Tolerant Fuel Cell Catalysts. *Nat. Commun.* **2013**, *4*. https://doi.org/10.1038/ncomms3466.

(133) Arán-Ais, R. M.; Yu, Y.; Hovden, R.; Solla-Gullón, J.; Herrero, E.; Feliu, J. M.; Abruña,

H. D. Identical Location Transmission Electron Microscopy Imaging of Site-Selective Pt Nanocatalysts: Electrochemical Activation and Surface Disordering. *J. Am. Chem. Soc.* **2015**, *137* (47), 14992–14998. https://doi.org/10.1021/jacs.5b09553.

(134) Rossouw, D.; Chinchilla, L.; Kremliakova, N.; Botton, G. A. The 3D Nanoscale Evolution of Platinum–Niobium Oxide Fuel Cell Catalysts via Identical Location Electron Tomography. *Part. Part. Syst. Charact.* **2017**, *34* (7), 1700051. https://doi.org/https://doi.org/10.1002/ppsc.201700051.

(135) Hrnjic, A.; Kamšek, A. R.; Pavlišič, A.; Šala, M.; Bele, M.; Moriau, L.; Gatalo, M.; Ruiz-Zepeda, F.; Jovanovič, P.; Hodnik, N. Observing, Tracking and Analysing Electrochemically Induced Atomic-Scale Structural Changes of an Individual Pt-Co Nanoparticle as a Fuel Cell Electrocatalyst by Combining Modified Floating Electrode and Identical Location Electron Microscopy. *Electrochim. Acta* **2021**, *388*, 138513. https://doi.org/https://doi.org/10.1016/j.electacta.2021.138513.

(136) Yu, H.; Zachman, M. J.; Li, C.; Hu, L.; Kariuki, N. N.; Mukundan, R.; Xie, J.; Neyerlin, K. C.; Myers, D. J.; Cullen, D. A. Recreating Fuel Cell Catalyst Degradation in Aqueous Environments for Identical-Location Scanning Transmission Electron Microscopy Studies. *ACS Appl. Mater. Interfaces* **2022**, *14* (18), 20418–20429. https://doi.org/10.1021/acsami.1c23281.

(137) Souza, N. E.; Bott-Neto, J. L.; Rocha, T. A.; da Silva, G. C.; Teixeira-Neto, E.; Gonzalez, E. R.; Ticianelli, E. A. Support Modification in Pt/C Electrocatalysts for Durability Increase: A Degradation Study Assisted by Identical Location Transmission Electron Microscopy. *Electrochim. Acta* **2018**, *265*, 523–531. https://doi.org/https://doi.org/10.1016/j.electacta.2018.01.180.

(138) Wen, Y. N.; Zhang, J. M. Surface Energy Calculation of the Fcc Metals by Using the MAEAM. *Solid State Commun.* **2007**, *144* (3–4), 163–167. https://doi.org/10.1016/j.ssc.2007.07.012.

(139) Henning, S.; Shimizu, R.; Herranz, J.; Kühn, L.; Eychmüller, A.; Uchida, M.; Kakinuma, K.; Schmidt, T. J. Unsupported Pt 3 Ni Aerogels as Corrosion Resistant PEFC Anode Catalysts under Gross Fuel Starvation Conditions . *J. Electrochem. Soc.* **2018**, *165* (6), F3001–F3006. https://doi.org/10.1149/2.0531802jes.

(140) Oyarce, A.; Zakrisson, E.; Ivity, M.; Lagergren, C.; Ofstad, A. B.; Bodén, A.; Lindbergh,

G. Comparing Shut-down Strategies for Proton Exchange Membrane Fuel Cells. *J. Power Sources* **2014**, *254*, 232–240. https://doi.org/https://doi.org/10.1016/j.jpowsour.2013.12.058.

(141) Yu, Y.; Li, H.; Wang, H.; Yuan, X.-Z.; Wang, G.; Pan, M. A Review on Performance Degradation of Proton Exchange Membrane Fuel Cells during Startup and Shutdown Processes: Causes, Consequences, and Mitigation Strategies. *J. Power Sources* **2012**, *205*, 10–23. https://doi.org/https://doi.org/10.1016/j.jpowsour.2012.01.059.

(142) Han, S. H.; Liu, H. M.; Bai, J.; Tian, X. L.; Xia, B. Y.; Zeng, J. H.; Jiang, J. X.; Chen, Y. Platinum-Silver Alloy Nanoballoon Nanoassemblies with Super Catalytic Activity for the Formate Electrooxidation. *ACS Appl. Energy Mater.* **2018**, *1* (3), 1252–1258. https://doi.org/10.1021/acsaem.8b00004.

(143) Velásquez, J. D.; Tomczykowa, M.; Plonska-Brzezinska, M. E.; Chaur, M. N. Evaluation of the Covalent Functionalization of Carbon Nano-Onions with Pyrene Moieties for Supercapacitor Applications. *Materials (Basel).* **2020**, *13* (5), 16–19. https://doi.org/10.3390/ma13051141.

(144) Rasouli, S.; Myers, D.; Kariuki, N.; Higashida, K.; Nakashima, N.; Ferreira, P. Electrochemical Degradation of Pt–Ni Nanocatalysts: An Identical Location Aberration-Corrected Scanning Transmission Electron Microscopy Study. *Nano Lett.* **2019**, *19* (1), 46–53. https://doi.org/10.1021/acs.nanolett.8b03022.

(145) Schlögl, K.; Mayrhofer, K. J. J.; Hanzlik, M.; Arenz, M. Identical-Location TEM Investigations of Pt/C Electrocatalyst Degradation at Elevated Temperatures. *J. Electroanal. Chem.* **2011**, *662* (2), 355–360. https://doi.org/https://doi.org/10.1016/j.jelechem.2011.09.003.

(146) Ferreira, P. J.; la O', G. J.; Shao-Horn, Y.; Morgan, D.; Makharia, R.; Kocha, S.; Gasteiger, H. A. Instability of Pt/C Electrocatalysts in Proton Exchange Membrane Fuel Cells: A Mechanistic Investigation. *J. Electrochem. Soc.* **2005**, *152* (11), A2256. https://doi.org/10.1149/1.2050347.

(147) Shao-Horn, Y.; Sheng, W. C.; Chen, S.; Ferreira, P. J.; Holby, E. F.; Morgan, D. Instability of Supported Platinum Nanoparticles in Low-Temperature Fuel Cells. *Top. Catal.* **2007**, *46* (3), 285–305. https://doi.org/10.1007/s11244-007-9000-0.

(148) Dubau, L.; Castanheira, L.; Berthomé, G.; Maillard, F. An Identical-Location Transmission Electron Microscopy Study on the Degradation of Pt/C Nanoparticles under Oxidizing, Reducing and Neutral Atmosphere. *Electrochim. Acta* **2013**, *110*, 273–281. https://doi.org/https://doi.org/10.1016/j.electacta.2013.03.184.

(149) Feng, Z.; Lin, Y.; Tian, C.; Hu, H.; Su, D. Combined Study of the Ground and Excited States in the Transformation of Nanodiamonds into Carbon Onions by Electron Energy-Loss Spectroscopy. *Sci. Rep.* **2019**, *9* (1), 3784. https://doi.org/10.1038/s41598-019-40529-2.

(150) Ponsonnet, L.; Donnet, C.; Varlot, K.; Martin, J. M.; Grill, A.; Patel, V. EELS Analysis of Hydrogenated Diamond-like Carbon Films. *Thin Solid Films* **1998**, *319* (1), 97–100. https://doi.org/https://doi.org/10.1016/S0040-6090(97)01094-8.

(151) He, D.; Mu, S.; Pan, M. Perfluorosulfonic Acid-Functionalized Pt/Carbon Nanotube Catalysts with Enhanced Stability and Performance for Use in Proton Exchange Membrane Fuel Cells. *Carbon N. Y.* **2011**, *49* (1), 82–88. https://doi.org/https://doi.org/10.1016/j.carbon.2010.08.045.

(152) Heinzl, C.; Hengge, K. A.; Perchthaler, M.; Hacker, V.; Scheu, C. Insight into the Degradation of HT-PEMFCs Containing Tungsten Oxide Catalyst Support Material for the Anode. *J. Electrochem. Soc.* **2015**, *162* (3), F280–F290. https://doi.org/10.1149/2.0541503jes.

(153) Devrim, Y.; Arıca, E. D.; Albostan, A. Graphene Based Catalyst Supports for High Temperature PEM Fuel Cell Application. *Int. J. Hydrogen Energy* **2018**, *43* (26), 11820–11829. https://doi.org/https://doi.org/10.1016/j.ijhydene.2018.03.047.

(154) Erlebacher, J.; Margetis, D. Mechanism of Hollow Nanoparticle Formation Due to Shape Fluctuations. *Phys. Rev. Lett.* **2014**, *112* (15), 155505. https://doi.org/10.1103/PhysRevLett.112.155505.

(155) Martí-Sánchez, S.; Botifoll, M.; Oksenberg, E.; Koch, C.; Borja, C.; Spadaro, M. C.; Di Giulio, V.; Ramasse, Q.; García de Abajo, F. J.; Joselevich, E.; Arbiol, J. Sub-Nanometer Mapping of Strain-Induced Band Structure Variations in Planar Nanowire Core-Shell Heterostructures. *Nat. Commun.* **2022**, *13* (1), 1–10. https://doi.org/10.1038/s41467-022-31778-3.

(156) Bernal, S.; Botana, F. J.; Calvino, J. J.; López-Cartes, C.; Pérez-Omil, J. A.; Rodríguez-Izquierdo, J. M. The Interpretation of HREM Images of Supported Metal Catalysts Using Image Simulation: Profile View Images. *Ultramicroscopy* **1998**, *72* (3), 135–164. https://doi.org/https://doi.org/10.1016/S0304-3991(98)00009-6.

(157) Rahm, J.; Erhart, P. WulffPack: A Python Package for Wulff Constructions. *J. Open Source Softw.* **2020**, *5* (45), 1944. https://doi.org/10.21105/joss.01944.

(158) Cliff, G.; Lorimer, G. W. The Quantitative Analysis of Thin Specimens. *J. Microsc.* **1975**, *103* (2), 203–207. https://doi.org/https://doi.org/10.1111/j.1365-2818.1975.tb03895.x.

(159) Altantzis, T.; Lobato, I.; De Backer, A.; Béché, A.; Zhang, Y.; Basak, S.; Porcu, M.; Xu, Q.; Sánchez-Iglesias, A.; Liz-Marzán, L. M.; Van Tendeloo, G.; Van Aert, S.; Bals, S. Three-Dimensional Quantification of the Facet Evolution of Pt Nanoparticles in a Variable Gaseous Environment. *Nano Lett.* **2019**, *19* (1), 477–481. https://doi.org/10.1021/acs.nanolett.8b04303.

(160) van der Walt, S.; Schönberger, J. L.; Nunez-Iglesias, J.; Boulogne, F.; Warner, J. D.; Yager, N.; Gouillart, E.; Yu, T.; the scikit-image contributors. Scikit-Image: Image Processing in {P}ython. *PeerJ* **2014**, *2*, e453. https://doi.org/10.7717/peerj.453.

(161) Pelt, D. M.; Gürsoy, D.; Palenstijn, W. J.; Sijbers, J.; De Carlo, F.; Batenburg, K. J. Integration of TomoPy and the ASTRA Toolbox for Advanced Processing and Reconstruction of Tomographic Synchrotron Data. *J. Synchrotron Radiat.* **2016**, *23* (Pt 3), 842–849. https://doi.org/10.1107/S1600577516005658.

(162) Meier, J. C.; Katsounaros, I.; Galeano, C.; Bongard, H. J.; Topalov, A. A.; Kostka, A.; Karschin, A.; Schüth, F.; Mayrhofer, K. J. J. Stability Investigations of Electrocatalysts on the Nanoscale. *Energy Environ. Sci.* **2012**, *5* (11), 9319–9330. https://doi.org/10.1039/C2EE22550F.

(163) Arenz, M.; Zana, A. Nano Energy Fuel Cell Catalyst Degradation : Identical Location Electron Microscopy and Related Methods. **2016**, *29*, 299–313.

(164) Lopes, P. P.; Chung, D. Y.; Rui, X.; Zheng, H.; He, H.; Martins, P. F. B. D.; Strmcnik, D.; Stamenkovic, V. R.; Zapol, P.; Mitchell, J. F.; Klie, R. F.; Markovic, N. M. Dynamically Stable Active Sites from Surface Evolution of Perovskite Materials during

the Oxygen Evolution Reaction. *J. Am. Chem. Soc.* **2021**, *143* (7), 2741–2750. https://doi.org/10.1021/jacs.0c08959.

(165) Hodnik, N.; Dehm, G.; Mayrhofer, K. J. J. Importance and Challenges of Electrochemical in Situ Liquid Cell Electron Microscopy for Energy Conversion Research. *Acc. Chem. Res.* **2016**, *49* (9), 2015–2022. https://doi.org/10.1021/acs.accounts.6b00330.

(166) Mayrhofer, K. J. J.; Ashton, S. J.; Meier, J. C.; Wiberg, G. K. H.; Hanzlik, M.; Arenz, M. Non-Destructive Transmission Electron Microscopy Study of Catalyst Degradation under Electrochemical Treatment. *J. Power Sources* **2008**, *185* (2), 734–739. https://doi.org/https://doi.org/10.1016/j.jpowsour.2008.08.003.

(167) Nikkuni, F. R.; Ticianelli, E. A.; Dubau, L.; Chatenet, M. Identical-Location Transmission Electron Microscopy Study of Pt / C and Pt – Co / C Nanostructured Electrocatalyst Aging : Effects of Morphological and Compositional Changes on the Oxygen Reduction Reaction Activity. **2013**, 104–116. https://doi.org/10.1007/s12678-013-0126-5.

(168) Yu, Y.; Xin, H. L.; Hovden, R.; Wang, D.; Rus, E. D.; Mundy, J. A.; Muller, D. A.; Abruña, H. D. Three-Dimensional Tracking and Visualization of Hundreds of Pt−Co Fuel Cell Nanocatalysts During Electrochemical Aging. *Nano Lett.* **2012**, *12* (9), 4417–4423. https://doi.org/10.1021/nl203920s.

(169) Zana, A.; Speder, J.; Roefzaad, M.; Altmann, L.; Bäumer, M.; Arenz, M. Probing Degradation by IL-TEM: The Influence of Stress Test Conditions on the Degradation Mechanism. *J. Electrochem. Soc.* **2013**, *160* (6), F608. https://doi.org/10.1149/2.078306jes.

(170) Rasouli, S.; Ferreira, P. J. Understanding the Stability of Nanoscale Catalysts in PEM Fuel Cells by Identical Location TEM BT - Nanocarbons for Energy Conversion: Supramolecular Approaches; Nakashima, N., Ed.; Springer International Publishing: Cham, 2019; pp 119–134. https://doi.org/10.1007/978-3-319-92917-0_5.

(171) Yu, K.; Li, C.; Xie, J.; Ferreira, P. J. Understanding the Degradation Mechanisms of Pt Electrocatalysts in PEMFCs by Combining 2D and 3D Identical Location TEM. *Nano Lett.* **2023**, *23* (5), 1858–1864. https://doi.org/10.1021/acs.nanolett.2c04764.

(172) Liu, Z. Y.; Zhang, J. L.; Yu, P. T.; Zhang, J. X.; Makharia, R.; More, K. L.; Stach, E. A. Transmission Electron Microscopy Observation of Corrosion Behaviors of Platinized Carbon Blacks under Thermal and Electrochemical Conditions. *J. Electrochem. Soc.* **2010**, *157* (6), B906. https://doi.org/10.1149/1.3391737.

(173) Spinner, N.; Zhang, L.; Mustain, W. E. Investigation of Metal Oxide Anode Degradation in Lithium-Ion Batteries via Identical-Location TEM. *J. Mater. Chem. A* **2014**, *2* (6), 1627–1630. https://doi.org/10.1039/C3TA14377E.

(174) Palmieri, A.; Spinner, N.; Zhao, S.; Mustain, W. E. Explaining the Role and Mechanism of Carbon Matrices in Enhancing Reaction Reversibility of Metal Oxide Anodes for High Performance Li Ion Batteries. *Carbon N. Y.* **2018**, *130*, 515–524. https://doi.org/https://doi.org/10.1016/j.carbon.2018.01.059.

(175) Wang, X.; Tai, G.; Wu, Z.; Hu, T.; Wang, R. Ultrathin Molybdenum Boride Films for Highly Efficient Catalysis of the Hydrogen Evolution Reaction. *J. Mater. Chem. A* **2017**, *5* (45), 23471–23475. https://doi.org/10.1039/C7TA08597D.

(176) Tai, G.; Xu, M.; Hou, C.; Liu, R.; Liang, X.; Wu, Z. Borophene Nanosheets as High-Efficiency Catalysts for the Hydrogen Evolution Reaction. *ACS Appl. Mater. Interfaces* **2021**, *13* (51), 60987–60994. https://doi.org/10.1021/acsami.1c15953.

(177) Xu, M.; Wang, R.; Bian, K.; Hou, C.; Wu, Y.; Tai, G. Triclinic Boron Nanosheets High-Efficient Electrocatalysts for Water Splitting. *Nanotechnology* **2022**, *33* (7), 75601. https://doi.org/10.1088/1361-6528/ac368a.

(178) Hu, T.; Bian, K.; Tai, G.; Zeng, T.; Wang, X.; Huang, X.; Xiong, K.; Zhu, K. Oxidation-Sulfidation Approach for Vertically Growing MoS2 Nanofilms Catalysts on Molybdenum Foils as Efficient HER Catalysts. *J. Phys. Chem. C* **2016**, *120* (45), 25843–25850. https://doi.org/10.1021/acs.jpcc.6b08120.

(179) Hota, P.; Das, A.; Maiti, D. K. A Short Review on Generation of Green Fuel Hydrogen through Water Splitting. *Int. J. Hydrogen Energy* **2023**, *48* (2), 523–541. https://doi.org/https://doi.org/10.1016/j.ijhydene.2022.09.264.

(180) Jia, Y.; Zhang, L.; Du, A.; Gao, G.; Chen, J.; Yan, X.; Brown, C. L.; Yao, X. Defect Graphene as a Trifunctional Catalyst for Electrochemical Reactions. *Adv. Mater.* **2016**, *28* (43), 9532–9538. https://doi.org/https://doi.org/10.1002/adma.201602912.

(181) da Silva, G. C.; Perini, N.; Ticianelli, E. A. Effect of Temperature on the Activities and Stabilities of Hydrothermally Prepared IrOx Nanocatalyst Layers for the Oxygen Evolution Reaction. *Appl. Catal. B Environ.* **2017**, *218*, 287–297. https://doi.org/https://doi.org/10.1016/j.apcatb.2017.06.044.

(182) Jovanovič, P.; Hodnik, N.; Ruiz-Zepeda, F.; Arčon, I.; Jozinović, B.; Zorko, M.; Bele, M.; Šala, M.; Šelih, V. S.; Hočevar, S.; Gaberšček, M. Electrochemical Dissolution of Iridium and Iridium Oxide Particles in Acidic Media: Transmission Electron Microscopy, Electrochemical Flow Cell Coupled to Inductively Coupled Plasma Mass Spectrometry, and X-Ray Absorption Spectroscopy Study. *J. Am. Chem. Soc.* **2017**, *139* (36), 12837–12846. https://doi.org/10.1021/jacs.7b08071.

(183) Claudel, F.; Dubau, L.; Berthomé, G.; Sola-Hernandez, L.; Beauger, C.; Piccolo, L.; Maillard, F. Degradation Mechanisms of Oxygen Evolution Reaction Electrocatalysts: A Combined Identical-Location Transmission Electron Microscopy and X-Ray Photoelectron Spectroscopy Study. *ACS Catal.* **2019**, *9* (5), 4688–4698. https://doi.org/10.1021/acscatal.9b00280.

(184) Roy, C.; Sebok, B.; Scott, S. B.; Fiordaliso, E. M.; Sørensen, J. E.; Bodin, A.; Trimarco, D. B.; Damsgaard, C. D.; Vesborg, P. C. K.; Hansen, O.; Stephens, I. E. L.; Kibsgaard, J.; Chorkendorff, I. Impact of Nanoparticle Size and Lattice Oxygen on Water Oxidation on NiFeOxHy. *Nat. Catal.* **2018**, *1* (11), 820–829. https://doi.org/10.1038/s41929-018-0162-x.

(185) Paciok, P.; Schalenbach, M.; Carmo, M.; Stolten, D. On the Mobility of Carbon-Supported Platinum Nanoparticles towards Unveiling Cathode Degradation in Water Electrolysis. *J. Power Sources* **2017**, *365*, 53–60. https://doi.org/https://doi.org/10.1016/j.jpowsour.2017.07.033.

(186) Jovanovič, P.; Stojanovski, K.; Bele, M.; Dražić, G.; Koderman Podboršek, G.; Suhadolnik, L.; Gaberšček, M.; Hodnik, N. Methodology for Investigating Electrochemical Gas Evolution Reactions: Floating Electrode as a Means for Effective Gas Bubble Removal. *Anal. Chem.* **2019**, *91* (16), 10353–10356. https://doi.org/10.1021/acs.analchem.9b01317.

(187) Koderman Podboršek, G.; Kamšek, A. R.; Lončar, A.; Bele, M.; Suhadolnik, L.; Jovanovič, P.; Hodnik, N. Atomically-Resolved Structural Changes of Ceramic

Supported Nanoparticulate Oxygen Evolution Reaction Ir Catalyst. *Electrochim. Acta* **2022**, *426*, 140800. https://doi.org/https://doi.org/10.1016/j.electacta.2022.140800.

(188) Kwak, I. H.; Debela, T. T.; Kwon, I. S.; Seo, J.; Yoo, S. J.; Kim, J.-G.; Ahn, J.-P.; Park, J.; Kang, H. S. Anisotropic Alloying of Re1−xMoxS2 Nanosheets to Boost the Electrochemical Hydrogen Evolution Reaction. *J. Mater. Chem. A* **2020**, *8* (47), 25131–25141. https://doi.org/10.1039/D0TA09299A.

(189) Yang, S.-Z.; Gong, Y.; Manchanda, P.; Zhang, Y.-Y.; Ye, G.; Chen, S.; Song, L.; Pantelides, S. T.; Ajayan, P. M.; Chisholm, M. F.; Zhou, W. Rhenium-Doped and Stabilized MoS2 Atomic Layers with Basal-Plane Catalytic Activity. *Adv. Mater.* **2018**, *30* (51), 1803477. https://doi.org/https://doi.org/10.1002/adma.201803477.

(190) Xie, J.; Zhang, J.; Li, S.; Grote, F.; Zhang, X.; Zhang, H.; Wang, R.; Lei, Y.; Pan, B.; Xie, Y. Controllable Disorder Engineering in Oxygen-Incorporated MoS2 Ultrathin Nanosheets for Efficient Hydrogen Evolution. *J. Am. Chem. Soc.* **2013**, *135* (47), 17881–17888. https://doi.org/10.1021/ja408329q.

(191) Sun, T.; Li, Z.; Liu, X.; Ma, L.; Wang, J.; Yang, S. Oxygen-Incorporated MoS2 Microspheres with Tunable Interiors as Novel Electrode Materials for Supercapacitors. *J. Power Sources* **2017**, *352*, 135–142. https://doi.org/https://doi.org/10.1016/j.jpowsour.2017.03.123.

(192) Kim, S.-H.; Lim, J.; Sahu, R.; Kasian, O.; Stephenson, L. T.; Scheu, C.; Gault, B. Direct Imaging of Dopant and Impurity Distributions in 2D MoS2. *Adv. Mater.* **2020**, *32* (8), 1907235. https://doi.org/https://doi.org/10.1002/adma.201907235.

(193) Wang, X.; Zhong, H.; Xi, S.; Lee, W. S. V.; Xue, J. Understanding of Oxygen Redox in the Oxygen Evolution Reaction. *Adv. Mater.* **2022**, *34* (50), 2107956. https://doi.org/https://doi.org/10.1002/adma.202107956.

(194) Zhu, K.; Shi, F.; Zhu, X.; Yang, W. The Roles of Oxygen Vacancies in Electrocatalytic Oxygen Evolution Reaction. *Nano Energy* **2020**, *73*, 104761. https://doi.org/https://doi.org/10.1016/j.nanoen.2020.104761.

(195) Seitz, L. C.; Dickens, C. F.; Nishio, K.; Hikita, Y.; Montoya, J.; Doyle, A.; Kirk, C.; Vojvodic, A.; Hwang, H. Y.; Norskov, J. K.; Jaramillo, T. F. A Highly Active and Stable IrOx/SrIrO3 Catalyst for the Oxygen Evolution Reaction. *Science (80-.).* **2016**, *353*

(6303), 1011–1014. https://doi.org/10.1126/science.aaf5050.

(196) Lin, Y.; Tian, Z.; Zhang, L.; Ma, J.; Jiang, Z.; Deibert, B. J.; Ge, R.; Chen, L. Chromium-Ruthenium Oxide Solid Solution Electrocatalyst for Highly Efficient Oxygen Evolution Reaction in Acidic Media. *Nat. Commun.* **2019**, *10* (1), 162. https://doi.org/10.1038/s41467-018-08144-3.

(197) Yan, D.; Xia, C.; Zhang, W.; Hu, Q.; He, C.; Xia, B. Y.; Wang, S. Cation Defect Engineering of Transition Metal Electrocatalysts for Oxygen Evolution Reaction. *Adv. Energy Mater.* **2022**, *12* (45), 2202317. https://doi.org/https://doi.org/10.1002/aenm.202202317.

(198) Shao, M.; Chang, Q.; Dodelet, J. P.; Chenitz, R. Recent Advances in Electrocatalysts for Oxygen Reduction Reaction. *Chemical Reviews*. American Chemical Society March 23, 2016, pp 3594–3657. https://doi.org/10.1021/acs.chemrev.5b00462.

(199) Zhu, Y.; Zhang, L.; Zhao, B.; Chen, H.; Liu, X.; Zhao, R.; Wang, X.; Liu, J.; Chen, Y.; Liu, M. Improving the Activity for Oxygen Evolution Reaction by Tailoring Oxygen Defects in Double Perovskite Oxides. *Adv. Funct. Mater.* **2019**, *29* (34), 1901783. https://doi.org/https://doi.org/10.1002/adfm.201901783.

(200) Liu, D.; Zhou, P.; Bai, H.; Ai, H.; Du, X.; Chen, M.; Liu, D.; Ip, W. F.; Lo, K. H.; Kwok, C. T.; Chen, S.; Wang, S.; Xing, G.; Wang, X.; Pan, H. Development of Perovskite Oxide-Based Electrocatalysts for Oxygen Evolution Reaction. *Small* **2021**, *17* (43), 2101605. https://doi.org/https://doi.org/10.1002/smll.202101605.

(201) Zhao, J.; Wang, X. Screening Perovskites from ABO3 Combinations Generated by Constraint Satisfaction Techniques Using Machine Learning. *ACS Omega* **2022**, *7* (12), 10483–10491. https://doi.org/10.1021/acsomega.2c00002.

(202) Rahman, S.; Hussain, A.; Noreen, S.; Bibi, N.; Arshad, S.; Rehman, J. U.; Tahir, M. B. Structural, Electronic, Optical and Mechanical Properties of Oxide-Based Perovskite ABO3 (A = Cu, Nd and B = Sn, Sc): A DFT Study. *J. Solid State Chem.* **2023**, *317*, 123650. https://doi.org/https://doi.org/10.1016/j.jssc.2022.123650.

(203) Pham, T. H. M.; Shen, T.-H.; Ko, Y.; Zhong, L.; Lombardo, L.; Luo, W.; Horike, S.; Tileli, V.; Züttel, A. Elucidating the Mechanism of Fe Incorporation in In Situ Synthesized Co–Fe Oxygen-Evolving Nanocatalysts. *J. Am. Chem. Soc.* **2023**, *145* (43),

23691–23701. https://doi.org/10.1021/jacs.3c08099.

(204) Trotochaud, L.; Young, S. L.; Ranney, J. K.; Boettcher, S. W. Nickel–Iron Oxyhydroxide Oxygen-Evolution Electrocatalysts: The Role of Intentional and Incidental Iron Incorporation. *J. Am. Chem. Soc.* **2014**, *136* (18), 6744–6753. https://doi.org/10.1021/ja502379c.

(205) Stevens, M. B.; Trang, C. D. M.; Enman, L. J.; Deng, J.; Boettcher, S. W. Reactive Fe-Sites in Ni/Fe (Oxy)Hydroxide Are Responsible for Exceptional Oxygen Electrocatalysis Activity. *J. Am. Chem. Soc.* **2017**, *139* (33), 11361–11364. https://doi.org/10.1021/jacs.7b07117.

(206) Cheraparambil, H.; Vega-Paredes, M.; Scheu, C.; Weidenthaler, C. Unraveling the Evolution of Dynamic Active Sites of LaNixFe1–XO3 Catalysts During OER. *ACS Appl. Mater. Interfaces* **2024**, *16* (17), 21997–22006. https://doi.org/10.1021/acsami.4c02502.

(207) Porokhin, S. V; Nikitina, V. A.; Abakumov, A. M. Enhancement of Catalytic Activity and Stability of La0.6Ca0.4Fe0.7Ni0.3O2.9 Perovskite with Ppm Concentration of Fe in the Electrolyte for the Oxygen Evolution Reaction. *Materials*. 2021. https://doi.org/10.3390/ma14216403.

(208) Petrie, J. R.; Cooper, V. R.; Freeland, J. W.; Meyer, T. L.; Zhang, Z.; Lutterman, D. A.; Lee, H. N. Enhanced Bifunctional Oxygen Catalysis in Strained LaNiO3 Perovskites. *J. Am. Chem. Soc.* **2016**, *138* (8), 2488–2491. https://doi.org/10.1021/jacs.5b11713.

(209) Bak, J.; Bin Bae, H.; Chung, S.-Y. Atomic-Scale Perturbation of Oxygen Octahedra via Surface Ion Exchange in Perovskite Nickelates Boosts Water Oxidation. *Nat. Commun.* **2019**, *10* (1), 2713. https://doi.org/10.1038/s41467-019-10838-1.

(210) Bak, J.; Bae, H. Bin; Kim, J.; Oh, J.; Chung, S.-Y. Formation of Two-Dimensional Homologous Faults and Oxygen Electrocatalytic Activities in a Perovskite Nickelate. *Nano Lett.* **2017**, *17* (5), 3126–3132. https://doi.org/10.1021/acs.nanolett.7b00561.

(211) Bak, J.; Bae, H. Bin; Oh, C.; Son, J.; Chung, S.-Y. Y. Effect of Lattice Strain on the Formation of Ruddlesden–Popper Faults in Heteroepitaxial LaNiO3 for Oxygen Evolution Electrocatalysis. *J. Phys. Chem. Lett.* **2020**, *11* (17), 7253–7260. https://doi.org/10.1021/acs.jpclett.0c01426.

(212) Hong, Y.; Byeon, P.; Bak, J.; Heo, Y.; Kim, H.-S.; Bae, H. Bin; Chung, S.-Y. Local-Electrostatics-Induced Oxygen Octahedral Distortion in Perovskite Oxides and Insight into the Structure of Ruddlesden–Popper Phases. *Nat. Commun.* **2021**, *12* (1), 5527. https://doi.org/10.1038/s41467-021-25889-6.

(213) Burke, M. S.; Kast, M. G.; Trotochaud, L.; Smith, A. M.; Boettcher, S. W. Cobalt–Iron (Oxy)Hydroxide Oxygen Evolution Electrocatalysts: The Role of Structure and Composition on Activity, Stability, and Mechanism. *J. Am. Chem. Soc.* **2015**, *137* (10), 3638–3648. https://doi.org/10.1021/jacs.5b00281.

(214) Burke, M. S.; Enman, L. J.; Batchellor, A. S.; Zou, S.; Boettcher, S. W. Oxygen Evolution Reaction Electrocatalysis on Transition Metal Oxides and (Oxy)Hydroxides: Activity Trends and Design Principles. *Chem. Mater.* **2015**, *27* (22), 7549–7558. https://doi.org/10.1021/acs.chemmater.5b03148.

(215) Bera, P. Solution Combustion Synthesis as a Novel Route to Preparation of Catalysts. *Int. J. Self-Propagating High-Temperature Synth.* **2019**, *28* (2), 77–109. https://doi.org/10.3103/S106138621902002X.

(216) Ruddlesden, S. N.; Popper, P. The Compound Sr 3 Ti 2 O 7 and Its Structure . *Acta Crystallogr.* **1958**, *11* (1), 54–55. https://doi.org/10.1107/s0365110x58000128.

(217) Ruddlesden, S. N.; Popper, P. New Compounds of the K 2 NIF 4 Type . *Acta Crystallogr.* **1957**, *10* (8), 538–539. https://doi.org/10.1107/s0365110x57001929.

(218) Park, J. C.; Kim, D. K.; Byeon, S. H.; Kim, D. XANES Study on Ruddlesden-Popper Phase, Lan+1NinO3n+1 (n = 1, 2 and ∞). *J. Synchrotron Radiat.* **2001**, *8* (2), 704–706. https://doi.org/10.1107/S0909049500015983.

(219) Twight, L.; Tonsberg, A.; Samira, S.; Velinkar, K.; Dumpert, K.; Ou, Y.; Wang, L.; Nikolla, E.; Boettcher, S. W. Trace Fe Activates Perovskite Nickelate OER Catalysts in Alkaline Media via Redox-Active Surface Ni Species Formed during Electrocatalysis. *J. Catal.* **2024**, *432*, 115443. https://doi.org/https://doi.org/10.1016/j.jcat.2024.115443.

(220) Nord, M.; Vullum, P. E.; MacLaren, I.; Tybell, T.; Holmestad, R. Atomap: A New Software Tool for the Automated Analysis of Atomic Resolution Images Using Two-Dimensional Gaussian Fitting. *Adv. Struct. Chem. Imaging* **2017**, *3* (1), 9. https://doi.org/10.1186/s40679-017-0042-5.

(221) Zhang, S.; Scheu, C. Evaluation of EELS Spectrum Imaging Data by Spectral Components and Factors from Multivariate Analysis. *Microscopy* **2018**, *67* (suppl_1), i133–i141. https://doi.org/10.1093/jmicro/dfx091.

(222) McCrory, C. C. L.; Jung, S.; Peters, J. C.; Jaramillo, T. F. Benchmarking Heterogeneous Electrocatalysts for the Oxygen Evolution Reaction. *J. Am. Chem. Soc.* **2013**, *135* (45), 16977–16987. https://doi.org/10.1021/ja407115p.

(223) Debe, M. K. Electrocatalyst Approaches and Challenges for Automotive Fuel Cells. *Nature* **2012**, *486* (7401), 43–51. https://doi.org/10.1038/nature11115.

(224) Kulkarni, A.; Siahrostami, S.; Patel, A.; Nørskov, J. K. Understanding Catalytic Activity Trends in the Oxygen Reduction Reaction. *Chem. Rev.* **2018**, *118* (5), 2302–2312. https://doi.org/10.1021/acs.chemrev.7b00488.

(225) Tian, X.; Zhao, X.; Su, Y.-Q.; Wang, L.; Wang, H.; Dang, D.; Chi, B.; Liu, H.; Hensen, E. J. M.; Lou, X. W. (David); Xia, B. Y. Engineering Bunched Pt-Ni Alloy Nanocages for Efficient Oxygen Reduction in Practical Fuel Cells. *Science (80-.).* **2019**, *366* (6467), 850–856. https://doi.org/10.1126/science.aaw7493.

(226) Gasteiger, H. A.; Kocha, S. S.; Sompalli, B.; Wagner, F. T. Activity Benchmarks and Requirements for Pt, Pt-Alloy, and Non-Pt Oxygen Reduction Catalysts for PEMFCs. *Appl. Catal. B Environ.* **2005**, *56* (1), 9–35. https://doi.org/https://doi.org/10.1016/j.apcatb.2004.06.021.

(227) de Bruijn, F. A.; Dam, V. A. T.; Janssen, G. J. M. Review: Durability and Degradation Issues of PEM Fuel Cell Components. *Fuel Cells* **2008**, *8* (1), 3–22. https://doi.org/https://doi.org/10.1002/fuce.200700053.

(228) Gasteiger, H. A.; Marković, N. M. Just a Dream—or Future Reality? *Science (80-.).* **2009**, *324* (5923), 48–49. https://doi.org/10.1126/science.1172083.

(229) Tang, L.; Han, B.; Persson, K.; Friesen, C.; He, T.; Sieradzki, K.; Ceder, G. Electrochemical Stability of Nanometer-Scale Pt Particles in Acidic Environments. *J. Am. Chem. Soc.* **2010**, *132* (2), 596–600. https://doi.org/10.1021/ja9071496.

(230) Tang, L.; Li, X.; Cammarata, R. C.; Friesen, C.; Sieradzki, K. Electrochemical Stability of Elemental Metal Nanoparticles. *J. Am. Chem. Soc.* **2010**, *132* (33), 11722–11726. https://doi.org/10.1021/ja104421t.

(231) Greeley, J.; Stephens, I. E. L.; Bondarenko, A. S.; Johansson, T. P.; Hansen, H. A.; Jaramillo, T. F.; Rossmeisl, J.; Chorkendorff, I.; Nørskov, J. K. Alloys of Platinum and Early Transition Metals as Oxygen Reduction Electrocatalysts. *Nat. Chem.* **2009**, *1* (7), 552–556. https://doi.org/10.1038/nchem.367.

(232) Bligaard, T.; Nørskov, J. K. Ligand Effects in Heterogeneous Catalysis and Electrochemistry. *Electrochim. Acta* **2007**, *52* (18), 5512–5516. https://doi.org/https://doi.org/10.1016/j.electacta.2007.02.041.

(233) Greeley, J.; Nørskov, J. K.; Mavrikakis, M. Electronic Structure and Catalysis on Metal Surfaces. *Annu. Rev. Phys. Chem.* **2002**, *53*, 319–348. https://doi.org/10.1146/annurev.physchem.53.100301.131630.

(234) Cui, C.; Gan, L.; Heggen, M.; Rudi, S.; Strasser, P. Compositional Segregation in Shaped Pt Alloy Nanoparticles and Their Structural Behaviour during Electrocatalysis. *Nat. Mater.* **2013**, *12* (8), 765–771. https://doi.org/10.1038/nmat3668.

(235) Huang, X.; Zhu, E.; Chen, Y.; Li, Y.; Chiu, C.-Y.; Xu, Y.; Lin, Z.; Duan, X.; Huang, Y. A Facile Strategy to Pt3Ni Nanocrystals with Highly Porous Features as an Enhanced Oxygen Reduction Reaction Catalyst. *Adv. Mater.* **2013**, *25* (21), 2974–2979. https://doi.org/https://doi.org/10.1002/adma.201205315.

(236) Lin, F.; Lv, F.; Zhang, Q.; Luo, H.; Wang, K.; Zhou, J.; Zhang, W.; Zhang, W.; Wang, D.; Gu, L.; Guo, S. Local Coordination Regulation through Tuning Atomic-Scale Cavities of Pd Metallene toward Efficient Oxygen Reduction Electrocatalysis. *Adv. Mater.* **2022**, *34* (27), 2202084. https://doi.org/https://doi.org/10.1002/adma.202202084.

(237) Meng, T.; Sun, P.; Yang, F.; Zhu, J.; Mao, B.; Zheng, L.; Cao, M. Double-Atom Dealloying-Derived Frank Partial Dislocations in Cobalt Nanocatalysts Boost Metal–Air Batteries and Fuel Cells. *Proc. Natl. Acad. Sci.* **2022**, *119* (45), e2214089119. https://doi.org/10.1073/pnas.2214089119.

(238) Calle-Vallejo, F.; Pohl, M. D.; Reinisch, D.; Loffreda, D.; Sautet, P.; Bandarenka, A. S. Why Conclusions from Platinum Model Surfaces Do Not Necessarily Lead to Enhanced Nanoparticle Catalysts for the Oxygen Reduction Reaction. *Chem. Sci.* **2017**, *8* (3), 2283–2289. https://doi.org/10.1039/C6SC04788B.

(239) Chattot, R.; Le Bacq, O.; Beermann, V.; Kühl, S.; Herranz, J.; Henning, S.; Kühn, L.; Asset, T.; Guétaz, L.; Renou, G.; Drnec, J.; Bordet, P.; Pasturel, A.; Eychmüller, A.; Schmidt, T. J.; Strasser, P.; Dubau, L.; Maillard, F. Surface Distortion as a Unifying Concept and Descriptor in Oxygen Reduction Reaction Electrocatalysis. *Nat. Mater.* **2018**, *17* (9), 827–833. https://doi.org/10.1038/s41563-018-0133-2.

(240) Strasser, P.; Koh, S.; Anniyev, T.; Greeley, J.; More, K.; Yu, C.; Liu, Z.; Kaya, S.; Nordlund, D.; Ogasawara, H.; Toney, M. F.; Nilsson, A. Lattice-Strain Control of the Activity in Dealloyed Core–Shell Fuel Cell Catalysts. *Nat. Chem.* **2010**, *2* (6), 454–460. https://doi.org/10.1038/nchem.623.

(241) Du, M.; Cui, L.; Cao, Y.; Bard, A. J. Mechanoelectrochemical Catalysis of the Effect of Elastic Strain on a Platinum Nanofilm for the ORR Exerted by a Shape Memory Alloy Substrate. *J. Am. Chem. Soc.* **2015**, *137* (23), 7397–7403. https://doi.org/10.1021/jacs.5b03034.

(242) Asano, M.; Kawamura, R.; Sasakawa, R.; Todoroki, N.; Wadayama, T. Oxygen Reduction Reaction Activity for Strain-Controlled Pt-Based Model Alloy Catalysts: Surface Strains and Direct Electronic Effects Induced by Alloying Elements. *ACS Catal.* **2016**, *6* (8), 5285–5289. https://doi.org/10.1021/acscatal.6b01466.

(243) Geng, X.; Li, S.; Heo, J.; Peng, Y.; Hu, W.; Liu, Y.; Huang, J.; Ren, Y.; Li, D.; Zhang, L.; Luo, L. Grain-Boundary-Rich Noble Metal Nanoparticle Assemblies: Synthesis, Characterization, and Reactivity. *Adv. Funct. Mater.* **2022**, *32* (34), 2204169. https://doi.org/https://doi.org/10.1002/adfm.202204169.

(244) Grimmer, H.; Bollmann, W.; Warrington, D. H. Coincidence-Ste Lattices and Complete Patter-Shift Lattices in Cubic Crystals. *Acta Crystallogr A* **1974**, *30* (2), 197–207.

(245) Li, X. Y.; Jin, Z. H.; Zhou, X.; Lu, K. Constrained Minimal-Interface Structures in Polycrystalline Copper with Extremely Fine Grains. *Science (80-.).* **2020**, *370* (6518), 831–836. https://doi.org/10.1126/science.abe1267.

(246) Haasen, P. *Physical Metallurgy*; Physical Metallurgy; Cambridge University Press, 1996.

(247) Lu, K. Stabilizing Nanostructures in Metals Using Grain and Twin Boundary Architectures. *Nat. Rev. Mater.* **2016**, *1* (5), 16019.

https://doi.org/10.1038/natrevmats.2016.19.

(248) Li, X.; Wei, Y.; Yang, W.; Gao, H. Competing Grain-Boundary- and Dislocation-Mediated Mechanisms in Plastic Strain Recovery in Nanocrystalline Aluminum. *Proc. Natl. Acad. Sci.* **2009**, *106* (38), 16108–16113. https://doi.org/10.1073/pnas.0901765106.

(249) Guo, Y.; Britton, T. B.; Wilkinson, A. J. Slip Band–Grain Boundary Interactions in Commercial-Purity Titanium. *Acta Mater.* **2014**, *76*, 1–12. https://doi.org/https://doi.org/10.1016/j.actamat.2014.05.015.

(250) Song, M.; Zhou, G.; Lu, N.; Lee, J.; Nakouzi, E.; Wang, H.; Li, D. Oriented Attachment Induces Fivefold Twins by Forming and Decomposing High-Energy Grain Boundaries. *Science (80-.).* **2020**, *367* (6473), 40–45. https://doi.org/10.1126/science.aax6511.

(251) Wang, L.; Zhang, Y.; Zeng, Z.; Zhou, H.; He, J.; Liu, P.; Chen, M.; Han, J.; Srolovitz, D. J.; Teng, J.; Guo, Y.; Yang, G.; Kong, D.; Ma, E.; Hu, Y.; Yin, B.; Huang, X.; Zhang, Z.; Zhu, T.; Han, X. Tracking the Sliding of Grain Boundaries at the Atomic Scale. *Science (80-.).* **2022**, *375* (6586), 1261–1265. https://doi.org/10.1126/science.abm2612.

(252) White, C. L.; Keiser, J. R.; Braski, D. N. Boron Segregation to Grain Boundaries and Improved Ductility in Pt + 30 Wt Pct Rh + 8WtPctW. *Metall. Trans. A* **1981**, *12* (8), 1485–1490. https://doi.org/10.1007/BF02643694.

(253) Kim, S.-H.; Yoo, S.-H.; Chakraborty, P.; Jeong, J.; Lim, J.; El-Zoka, A. A.; Zhou, X.; Stephenson, L. T.; Hickel, T.; Neugebauer, J.; Scheu, C.; Todorova, M.; Gault, B. Understanding Alkali Contamination in Colloidal Nanomaterials to Unlock Grain Boundary Impurity Engineering. *J. Am. Chem. Soc.* **2022**, *144* (2), 987–994. https://doi.org/10.1021/jacs.1c11680.

(254) Kim, S.-H.; Yoo, S.-H.; Shin, S.; El-Zoka, A. A.; Kasian, O.; Lim, J.; Jeong, J.; Scheu, C.; Neugebauer, J.; Lee, H.; Todorova, M.; Gault, B. Controlled Doping of Electrocatalysts through Engineering Impurities. *Adv. Mater.* **2022**, *34* (28), 2203030. https://doi.org/https://doi.org/10.1002/adma.202203030.

(255) Lee, I.; Kim, W.-J.; Lee, D. C. Design of Metallic Cocatalysts in Heterostructured Nanoparticles for Photocatalytic CO2-to-Hydrocarbon Conversion. *J. Phys. D. Appl. Phys.* **2020**, *53* (12), 123001. https://doi.org/10.1088/1361-6463/ab5cb7.

(256) Dong, C.; Lian, C.; Hu, S.; Deng, Z.; Gong, J.; Li, M.; Liu, H.; Xing, M.; Zhang, J. Size-Dependent Activity and Selectivity of Carbon Dioxide Photocatalytic Reduction over Platinum Nanoparticles. *Nat. Commun.* **2018**, *9* (1), 1252. https://doi.org/10.1038/s41467-018-03666-2.

(257) Rossmeisl, J.; Karlberg, G. S.; Jaramillo, T.; Nørskov, J. K. Steady State Oxygen Reduction and Cyclic Voltammetry. *Faraday Discuss.* **2009**, *140* (0), 337–346. https://doi.org/10.1039/B802129E.

(258) Kim, S.-H.; Kang, P. W.; Park, O. O.; Seol, J.-B.; Ahn, J.-P.; Lee, J. Y.; Choi, P.-P. A New Method for Mapping the Three-Dimensional Atomic Distribution within Nanoparticles by Atom Probe Tomography (APT). *Ultramicroscopy* **2018**, *190*, 30–38. https://doi.org/https://doi.org/10.1016/j.ultramic.2018.04.005.

(259) Kresse, G.; Hafner, J. Ab Initio Molecular Dynamics for Liquid Metals. *Phys. Rev. B* **1993**, *47* (1), 558–561. https://doi.org/10.1103/PhysRevB.47.558.

(260) Blöchl, P. E. Projector Augmented-Wave Method. *Phys. Rev. B* **1994**, *50* (24), 17953–17979. https://doi.org/10.1103/PhysRevB.50.17953.

(261) Hammer, B.; Hansen, L. B.; Nørskov, J. K. Improved Adsorption Energetics within Density-Functional Theory Using Revised Perdew-Burke-Ernzerhof Functionals. *Phys. Rev. B - Condens. Matter Mater. Phys.* **1999**, *59* (11), 7413–7421. https://doi.org/10.1103/PhysRevB.59.7413.

(262) Pack, J. D.; Monkhorst, H. J. "special Points for Brillouin-Zone Integrations"-a Reply. *Phys. Rev. B* **1977**, *16* (4), 1748–1749. https://doi.org/10.1103/PhysRevB.16.1748.

(263) Calle-Vallejo, F.; Martínez, J. I.; García-Lastra, J. M.; Sautet, P.; Loffreda, D. Fast Prediction of Adsorption Properties for Platinum Nanocatalysts with Generalized Coordination Numbers. *Angew. Chemie Int. Ed.* **2014**, *53* (32), 8316–8319. https://doi.org/https://doi.org/10.1002/anie.201402958.

(264) Kibsgaard, J.; Chorkendorff, I. Considerations for the Scaling-up of Water Splitting Catalysts. *Nat. Energy* **2019**, *4* (6), 430–433. https://doi.org/10.1038/s41560-019-0407-1.

(265) He, T.; Wang, W.; Shi, F.; Yang, X.; Li, X.; Wu, J.; Yin, Y.; Jin, M. Mastering the Surface Strain of Platinum Catalysts for Efficient Electrocatalysis. *Nature* **2021**, *598*

(7879), 76–81. https://doi.org/10.1038/s41586-021-03870-z.

(266) Li, C. W.; Ciston, J.; Kanan, M. W. Electroreduction of Carbon Monoxide to Liquid Fuel on Oxide-Derived Nanocrystalline Copper. *Nature* **2014**, *508* (7497), 504–507. https://doi.org/10.1038/nature13249.

(267) Wang, L.; Zeng, Z.; Gao, W.; Maxson, T.; Raciti, D.; Giroux, M.; Pan, X.; Wang, C.; Greeley, J. Tunable Intrinsic Strain in Two-Dimensional Transition Metal Electrocatalysts. *Science (80-.).* **2019**, *363* (6429), 870–874. https://doi.org/10.1126/science.aat8051.

(268) Yoo, S.-H.; Aota, L. S.; Shin, S.; El-Zoka, A. A.; Kang, P. W.; Lee, Y.; Lee, H.; Kim, S.-H.; Gault, B. Dopant Evolution in Electrocatalysts after Hydrogen Oxidation Reaction in an Alkaline Environment. *ACS Energy Lett.* **2023**, *8* (8), 3381–3386. https://doi.org/10.1021/acsenergylett.3c00842.

(269) Podjaski, F.; Weber, D.; Zhang, S.; Diehl, L.; Eger, R.; Duppel, V.; Alarcón-Lladó, E.; Richter, G.; Haase, F.; Fontcuberta i Morral, A.; Scheu, C.; Lotsch, B. V. Rational Strain Engineering in Delafossite Oxides for Highly Efficient Hydrogen Evolution Catalysis in Acidic Media. *Nat. Catal.* **2020**, *3* (1), 55–63. https://doi.org/10.1038/s41929-019-0400-x.

(270) Gsell, M.; Jakob, P.; Menzel, D. Effect of Substrate Strain on Adsorption. *Science (80-.).* **1998**, *280* (5364), 717–720. https://doi.org/10.1126/science.280.5364.717.

(271) Zhu, E.; Xue, W.; Wang, S.; Yan, X.; Zhou, J.; Liu, Y.; Cai, J.; Liu, E.; Jia, Q.; Duan, X.; Li, Y.; Heinz, H.; Huang, Y. Enhancement of Oxygen Reduction Reaction Activity by Grain Boundaries in Platinum Nanostructures. *Nano Res.* **2020**, *13* (12), 3310–3314. https://doi.org/10.1007/s12274-020-3007-2.

(272) Kabiraz, M. K.; Ruqia, B.; Kim, J.; Kim, H.; Kim, H. J.; Hong, Y.; Kim, M. J.; Kim, Y. K.; Kim, C.; Lee, W.-J.; Lee, W.; Hwang, G. H.; Ri, H. C.; Baik, H.; Oh, H.-S.; Lee, Y. W.; Gao, L.; Huang, H.; Paek, S. M.; Jo, Y.-J.; Choi, C. H.; Han, S. W.; Choi, S.-I. Understanding the Grain Boundary Behavior of Bimetallic Platinum–Cobalt Alloy Nanowires toward Oxygen Electro-Reduction. *ACS Catal.* **2022**, *12* (6), 3516–3523. https://doi.org/10.1021/acscatal.1c05766.

(273) Dubau, L.; Nelayah, J.; Asset, T.; Chattot, R.; Maillard, F. Implementing Structural

Disorder as a Promising Direction for Improving the Stability of PtNi/C Nanoparticles. *ACS Catal.* **2017**, *7* (4), 3072–3081. https://doi.org/10.1021/acscatal.7b00410.

(274) Dubau, L.; Nelayah, J.; Moldovan, S.; Ersen, O.; Bordet, P.; Drnec, J.; Asset, T.; Chattot, R.; Maillard, F. Defects Do Catalysis: CO Monolayer Oxidation and Oxygen Reduction Reaction on Hollow PtNi/C Nanoparticles. *ACS Catal.* **2016**, *6* (7), 4673–4684. https://doi.org/10.1021/acscatal.6b01106.

(275) Xia, C.; Xia, Y.; Zhu, P.; Fan, L.; Wang, H. Direct Electrosynthesis of Pure Aqueous H2O2 Solutions up to 20% by Weight Using a Solid Electrolyte. *Science (80-.).* **2019**, *366* (6462), 226–231. https://doi.org/10.1126/science.aay1844.

(276) Zhang, Z.; Luo, Z.; Chen, B.; Wei, C.; Zhao, J.; Chen, J.; Zhang, X.; Lai, Z.; Fan, Z.; Tan, C.; Zhao, M.; Lu, Q.; Li, B.; Zong, Y.; Yan, C.; Wang, G.; Xu, Z. J.; Zhang, H. One-Pot Synthesis of Highly Anisotropic Five-Fold-Twinned PtCu Nanoframes Used as a Bifunctional Electrocatalyst for Oxygen Reduction and Methanol Oxidation. *Adv. Mater.* **2016**, *28* (39), 8712–8717. https://doi.org/https://doi.org/10.1002/adma.201603075.

(277) Da Rosa, G.; Maugis, P.; Portavoce, A.; Drillet, J.; Valle, N.; Lentzen, E.; Hoummada, K. Grain-Boundary Segregation of Boron in High-Strength Steel Studied by Nano-SIMS and Atom Probe Tomography. *Acta Mater.* **2020**, *182*, 226–234. https://doi.org/https://doi.org/10.1016/j.actamat.2019.10.029.

(278) Tytko, D.; Choi, P.-P.; Klöwer, J.; Kostka, A.; Inden, G.; Raabe, D. Microstructural Evolution of a Ni-Based Superalloy (617B) at 700°C Studied by Electron Microscopy and Atom Probe Tomography. *Acta Mater.* **2012**, *60* (4), 1731–1740. https://doi.org/https://doi.org/10.1016/j.actamat.2011.11.020.

(279) Feng, B.; Yokoi, T.; Kumamoto, A.; Yoshiya, M.; Ikuhara, Y.; Shibata, N. Atomically Ordered Solute Segregation Behaviour in an Oxide Grain Boundary. *Nat. Commun.* **2016**, *7* (1), 11079. https://doi.org/10.1038/ncomms11079.

(280) Yang, C.; Wang, Y.; Sigle, W.; van Aken, P. A. Determination of Grain-Boundary Structure and Electrostatic Characteristics in a SrTiO3 Bicrystal by Four-Dimensional Electron Microscopy. *Nano Lett.* **2021**, *21* (21), 9138–9145. https://doi.org/10.1021/acs.nanolett.1c02960.

(281) Moglianetti, M.; Solla-Gullón, J.; Donati, P.; Pedone, D.; Debellis, D.; Sibillano, T.; Brescia, R.; Giannini, C.; Montiel, V.; Feliu, J. M.; Pompa, P. P. Citrate-Coated, Size-Tunable Octahedral Platinum Nanocrystals: A Novel Route for Advanced Electrocatalysts. *ACS Appl. Mater. Interfaces* **2018**, *10* (48), 41608–41617. https://doi.org/10.1021/acsami.8b11774.

(282) Matter, F.; Luna, A. L.; Niederberger, M. From Colloidal Dispersions to Aerogels: How to Master Nanoparticle Gelation. *Nano Today* **2020**, *30*, 100827. https://doi.org/https://doi.org/10.1016/j.nantod.2019.100827.

(283) Zhang, H.; Banfield, J. F. Energy Calculations Predict Nanoparticle Attachment Orientations and Asymmetric Crystal Formation. *J. Phys. Chem. Lett.* **2012**, *3* (19), 2882–2886. https://doi.org/10.1021/jz301161j.

(284) Zhu, C.; Peng, H.-C.; Zeng, J.; Liu, J.; Gu, Z.; Xia, Y. Facile Synthesis of Gold Wavy Nanowires and Investigation of Their Growth Mechanism. *J. Am. Chem. Soc.* **2012**, *134* (50), 20234–20237. https://doi.org/10.1021/ja3091214.

(285) Ophus, C.; Zeltmann, S. E.; Bruefach, A.; Rakowski, A.; Savitzky, B. H.; Minor, A. M.; Scott, M. C. Automated Crystal Orientation Mapping in Py4DSTEM Using Sparse Correlation Matching. *Microsc. Microanal.* **2022**, *28* (2), 390–403. https://doi.org/DOI: 10.1017/S1431927622000101.

(286) Barth, J. V.; Brune, H.; Ertl, G.; Behm, R. J. Scanning Tunneling Microscopy Observations on the Reconstructed Au(111) Surface. *Phys. Rev. B* **1990**, *42* (15), 9307.

(287) Durand, W. J.; Peterson, A. A.; Studt, F.; Abild-Pedersen, F.; Nørskov, J. K. Structure Effects on the Energetics of the Electrochemical Reduction of CO2 by Copper Surfaces. *Surf. Sci.* **2011**, *605* (15), 1354–1359. https://doi.org/https://doi.org/10.1016/j.susc.2011.04.028.

(288) Hansen, H. A.; Varley, J. B.; Peterson, A. A.; Nørskov, J. K. Understanding Trends in the Electrocatalytic Activity of Metals and Enzymes for CO2 Reduction to CO. *J. Phys. Chem. Lett.* **2013**, *4* (3), 388–392. https://doi.org/10.1021/jz3021155.

(289) Gao, J.; Yang, H. bin; Huang, X.; Hung, S.-F.; Cai, W.; Jia, C.; Miao, S.; Chen, H. M.; Yang, X.; Huang, Y.; Zhang, T.; Liu, B. Enabling Direct H2O2 Production in Acidic Media through Rational Design of Transition Metal Single Atom Catalyst. *Chem* **2020**,

6 (3), 658–674. https://doi.org/https://doi.org/10.1016/j.chempr.2019.12.008.

(290) Huang, L.; Zaman, S.; Tian, X.; Wang, Z.; Fang, W.; Xia, B. Y. Advanced Platinum-Based Oxygen Reduction Electrocatalysts for Fuel Cells. *Acc. Chem. Res.* **2021**, *54* (2), 311–322. https://doi.org/10.1021/acs.accounts.0c00488.

(291) Yamamoto, K.; Imaoka, T.; Chun, W.-J.; Enoki, O.; Katoh, H.; Takenaga, M.; Sonoi, A. Size-Specific Catalytic Activity of Platinum Clusters Enhances Oxygen Reduction Reactions. *Nat. Chem.* **2009**, *1* (5), 397–402. https://doi.org/10.1038/nchem.288.

(292) Kang, W.-J.; Feng, Y.; Li, Z.; Chen, Z.-N.; Dong, C.-K.; Yang, J.; Yin, P.-F.; Liu, H.; Du, X.-W. Engineering Dense Stacking Faults in Silver Nanoparticles for Boosting the Oxygen Reduction Reaction. *ACS Energy Lett.* **2023**, *8* (8), 3512–3519. https://doi.org/10.1021/acsenergylett.3c01173.

(293) Kudo, D.; Kaneko, S.; Myochi, R.; Chida, Y.; Todoroki, N.; Tanabe, T.; Wadayama, T. Ligand-Effect-Induced Oxygen Reduction Reaction Activity Enhancement for Pt/Zr/Pt(111) Surfaces with Tensile Strain Relieved by Stacking Faults. *ACS Appl. Energy Mater.* **2019**, *2* (7), 4597–4601. https://doi.org/10.1021/acsaem.9b00873.

(294) Jin, C.; Wang, Q.; Liu, J. Pb Induced Dislocation Defects of PtCo Systems: Strain-Triggered Oxygen Reduction Reaction for PEMFC. *Nano Res.* **2024**, *17* (4), 2462–2472. https://doi.org/10.1007/s12274-023-6151-7.

(295) Buban, J. P.; Matsunaga, K.; Chen, J.; Shibata, N.; Ching, W. Y.; Yamamoto, T.; Ikuhara, Y. Grain Boundary Strengthening in Alumina by Rare Earth Impurities. *Science (80-.).* **2006**, *311* (5758), 212–215. https://doi.org/10.1126/science.1119839.

(296) Kontis, P.; Yusof, H. A. M.; Pedrazzini, S.; Danaie, M.; Moore, K. L.; Bagot, P. A. J.; Moody, M. P.; Grovenor, C. R. M.; Reed, R. C. On the Effect of Boron on Grain Boundary Character in a New Polycrystalline Superalloy. *Acta Mater.* **2016**, *103*, 688–699. https://doi.org/https://doi.org/10.1016/j.actamat.2015.10.006.

(297) Scheiber, D. Segregation and Embrittlement of Gold Grain Boundaries. *Comput. Mater. Sci.* **2021**, *187*, 110110. https://doi.org/https://doi.org/10.1016/j.commatsci.2020.110110.

(298) Grabow, L. C.; Gokhale, A. A.; Evans, S. T.; Dumesic, J. A.; Mavrikakis, M. Mechanism of the Water Gas Shift Reaction on Pt: First Principles, Experiments, and

Microkinetic Modeling. *J. Phys. Chem. C* **2008**, *112* (12), 4608–4617. https://doi.org/10.1021/jp7099702.

(299) Hohenberg, P.; Kohn, W. Inhomogeneous Electron Gas. *Phys. Rev.* **1964**, *136* (3B), B864–B871. https://doi.org/10.1103/PhysRev.136.B864.

(300) Kresse, G.; Furthmüller, J. Efficiency of Ab-Initio Total Energy Calculations for Metals and Semiconductors Using a Plane-Wave Basis Set. *Comput. Mater. Sci.* **1996**, *6* (1), 15–50. https://doi.org/https://doi.org/10.1016/0927-0256(96)00008-0.

(301) Hjorth Larsen, A.; Jørgen Mortensen, J.; Blomqvist, J.; Castelli, I. E.; Christensen, R.; Dułak, M.; Friis, J.; Groves, M. N.; Hammer, B.; Hargus, C.; Hermes, E. D.; Jennings, P. C.; Bjerre Jensen, P.; Kermode, J.; Kitchin, J. R.; Leonhard Kolsbjerg, E.; Kubal, J.; Kaasbjerg, K.; Lysgaard, S.; Bergmann Maronsson, J.; Maxson, T.; Olsen, T.; Pastewka, L.; Peterson, A.; Rostgaard, C.; Schiøtz, J.; Schütt, O.; Strange, M.; Thygesen, K. S.; Vegge, T.; Vilhelmsen, L.; Walter, M.; Zeng, Z.; Jacobsen, K. W. The Atomic Simulation Environment—a Python Library for Working with Atoms. *J. Phys. Condens. Matter* **2017**, *29* (27), 273002. https://doi.org/10.1088/1361-648X/aa680e.

(302) Phatak, A. A.; Delgass, W. N.; Ribeiro, F. H.; Schneider, W. F. Density Functional Theory Comparison of Water Dissociation Steps on Cu, Au, Ni, Pd, and Pt. *J. Phys. Chem. C* **2009**, *113* (17), 7269–7276. https://doi.org/10.1021/jp810216b.

(303) Perdew, J. P.; Burke, K.; Ernzerhof, M. Generalized Gradient Approximation Made Simple. *Phys. Rev. Lett.* **1996**, *77* (18), 3865–3868. https://doi.org/10.1103/PhysRevLett.77.3865.

11 Appendix

In the Appendix, additional data is provided which complements the information in the main text.

11.1 Supplementary information from Chapter 7

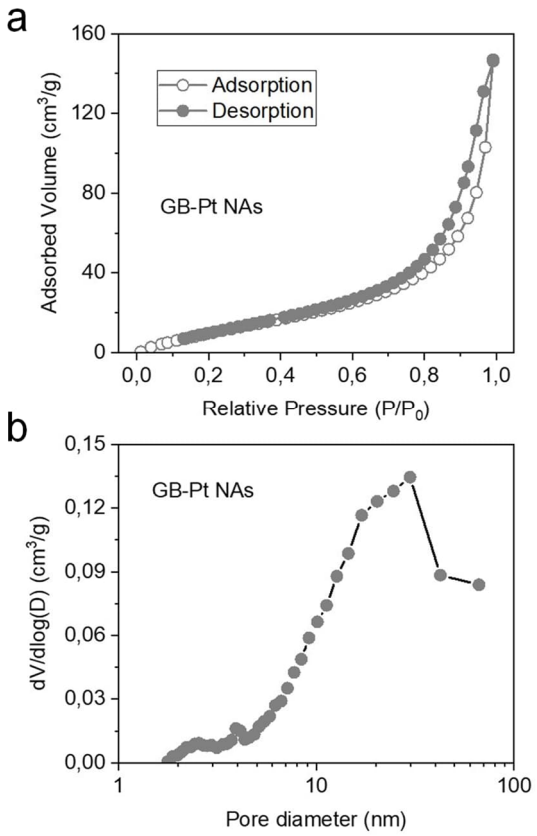

***Figure A7-1**. (a) Nitrogen adsorption-desorption isotherms, (b) Barrett–Joyner–Halenda pore size distribution plots of GB-Pt NAs.*

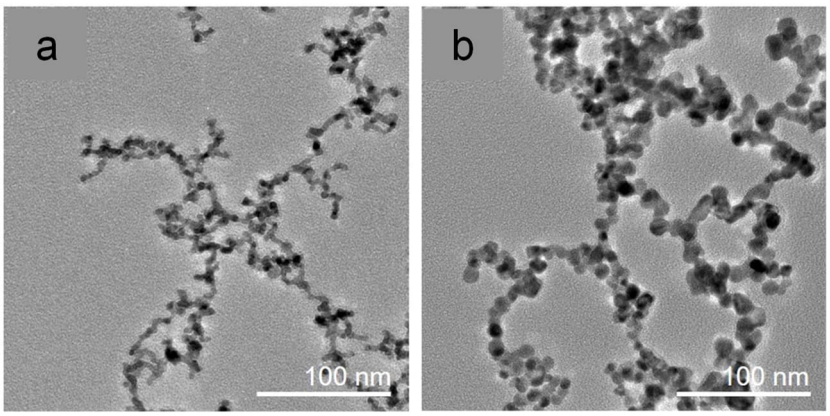

***Figure A7-2**. HR-TEM images of Pt NAs with diameters of 4 nm (a) and 10 nm (b) by attaching and coalescing NPs of corresponding sizes.*

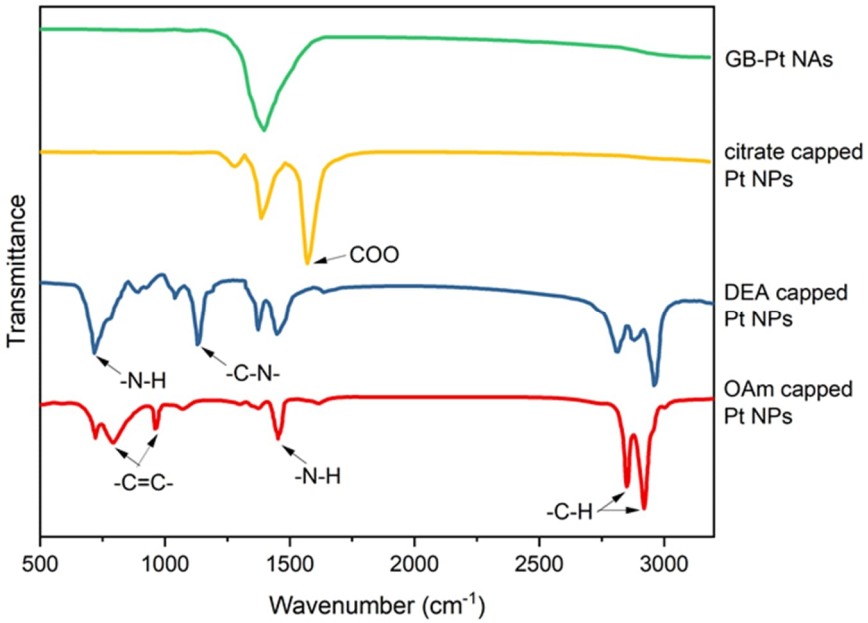

Figure A7-3. *FTIR spectra of OAm, DEA, citrate-capped Pt NPs, and GB-Pt NAs.*

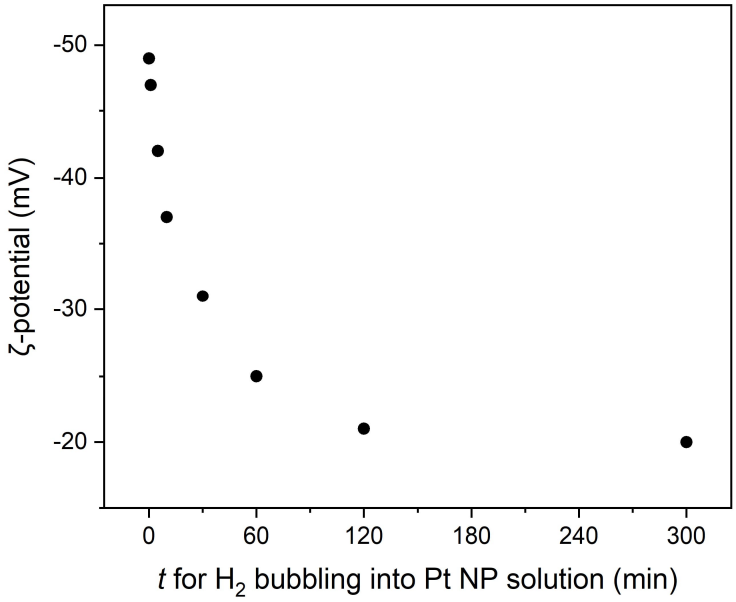

Figure A7-4. *Time dependence of the ζ-potential measured for citrate-capped Pt NP solution during H_2 gas bubbling.*

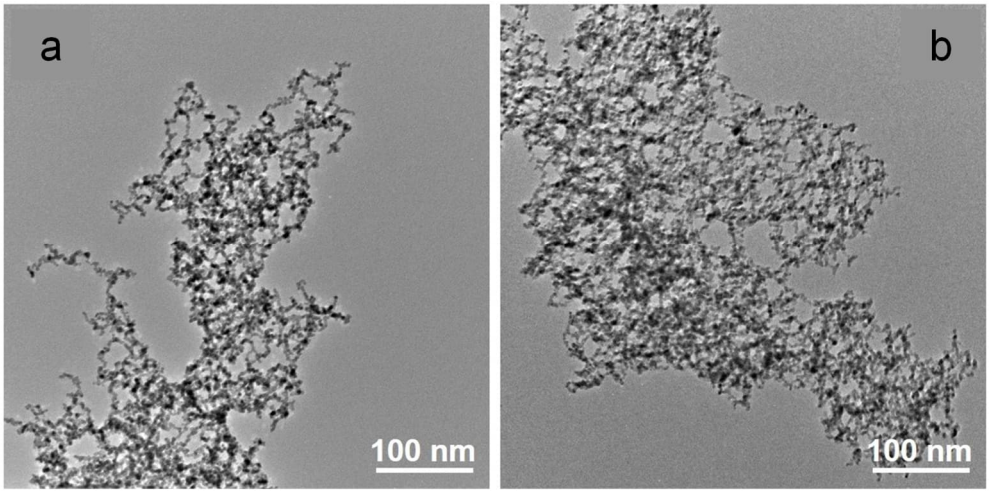

Figure A7-5. *TEM images of the Pt NAs synthesized from Pt NP solutions with concentrations of ~11 μM (a) and ~36 μM (b), respectively.*

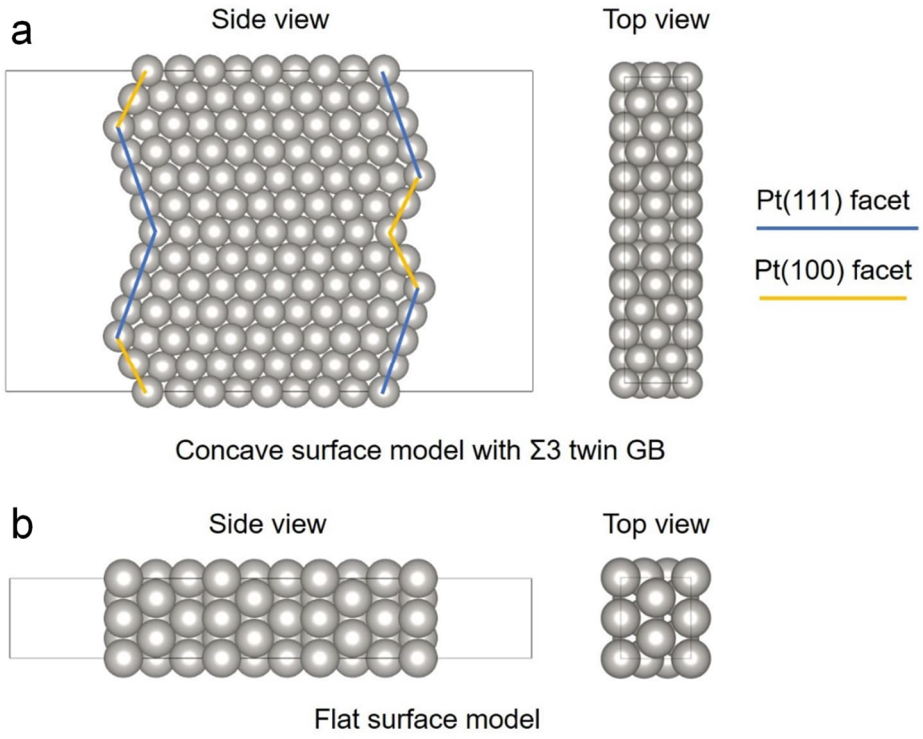

Figure A7-6. *Top and side views of the models used for surface energy calculations: (a) concave surface model with Σ3 twin GB and (b) flat surface model. The surface energies of the concave surface model with Σ3 GB and the flat (111) surface model are calculated to be 53 meV/Å² and 73 meV/Å², respectively.*

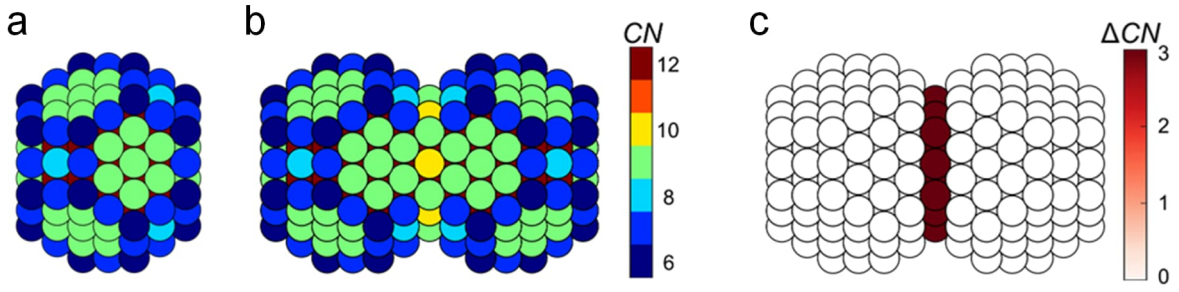

***Figure A7-7**. Coordination numbers (CNs) for (a) the Pt_{201} NP and (b) the Pt_{383} Σ3 (111) twin GB model, with subscripts indicating the total number of Pt atoms in each model. (c) The difference in coordination numbers (ΔCN) between the NP building block in the Pt_{383} Σ3 (111) twin GB model and the Pt_{201} NP.*

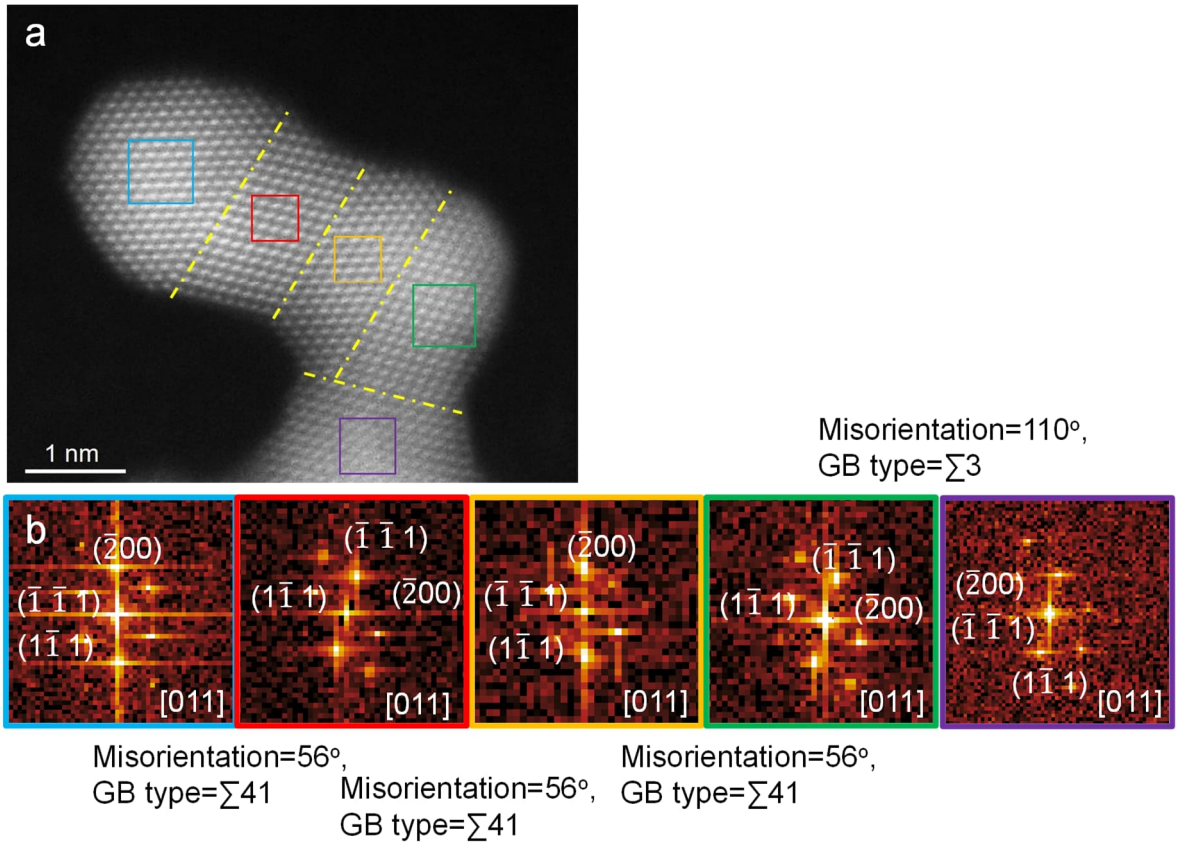

***Figure A7-8**. Identification of GB types based on the coincidence site lattice theory. From the HAADF-STEM image (a), FFT diffractograms (b) were obtained for individual NP building blocks to confirm that these NP were aligned along the same zone axis [011]. Subsequently, the misorientation between adjacent NP building blocks on the same crystal plane was measured, allowing for the identification of the GB types in GB-Pt NAs.*

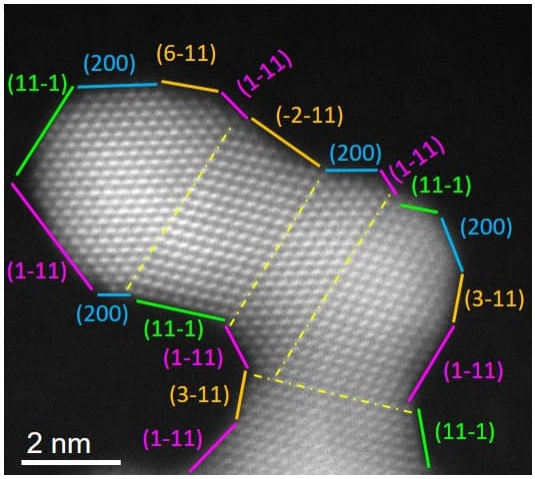

Figure A7-9. *HAADF-STEM image of GB-Pt NAs, where the GBs are delineated by yellow dashed lines while surface facets are highlighted by lines of varying colors.*

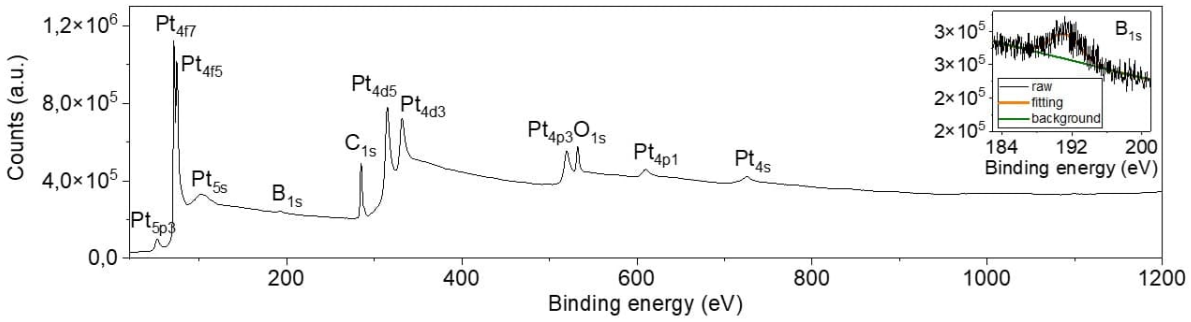

Figure A7-10. *XPS data of GB-Pt NAs. The inset shows the XPS spectrum of B 1s.*

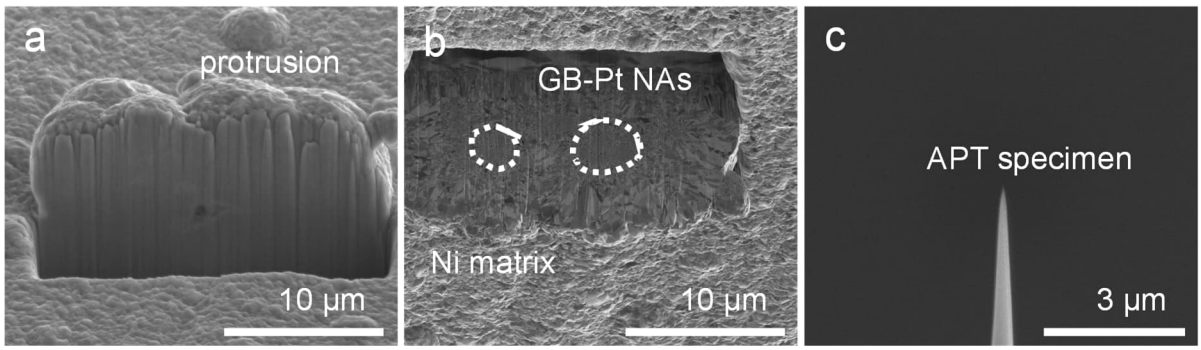

Figure A7-11. *(a) Cross-sectional SEM image of a FIB section of a protrusion. (b) Cross-sectional SEM image of one protrusion, which indicates that GB-Pt NAs (circled by white short dash lines) were embedded in the Ni matrix. (c) A sharpened needle-shaped specimen from GB-Pt NAs embedded in Ni matrix for APT measurement.*

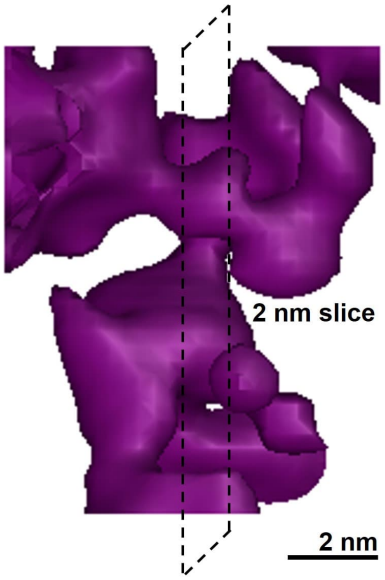

Figure A7-12*. 3D atom map of GB-Pt NAs (Pt>90 at.% iso-surface). Tomogram of the 3D atom map is shown in* ***Figure 7-5e*** *in Chapter 7.*

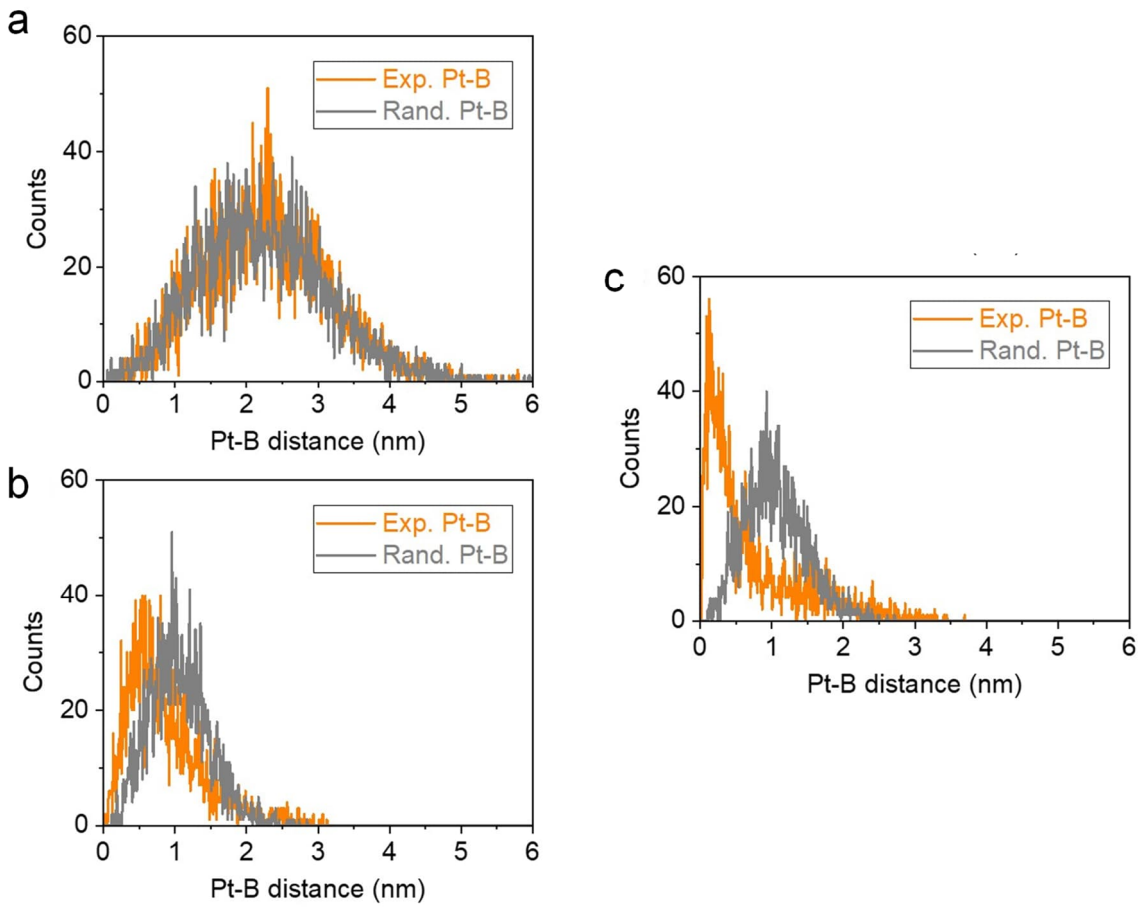

Figure A7-13*.Comparison Pt-B nearest neighbor experimental (orange) and simulated (grey) distance distribution of (a) OAm/OA-capped Pt NPs with B species on the surface, (b) citrate-capped Pt NPs with B species adsorbed on the surface, and (c) GB-Pt NAs with B species trapped in the GBs using APT.*

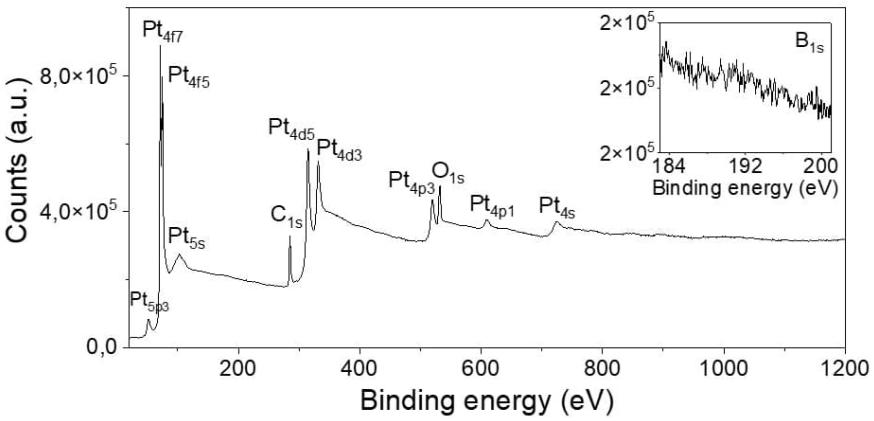

Figure A7-14*.XPS data of boron free-Pt NAs. The inset shows the high-resolution XPS spectrum of B 1s.*

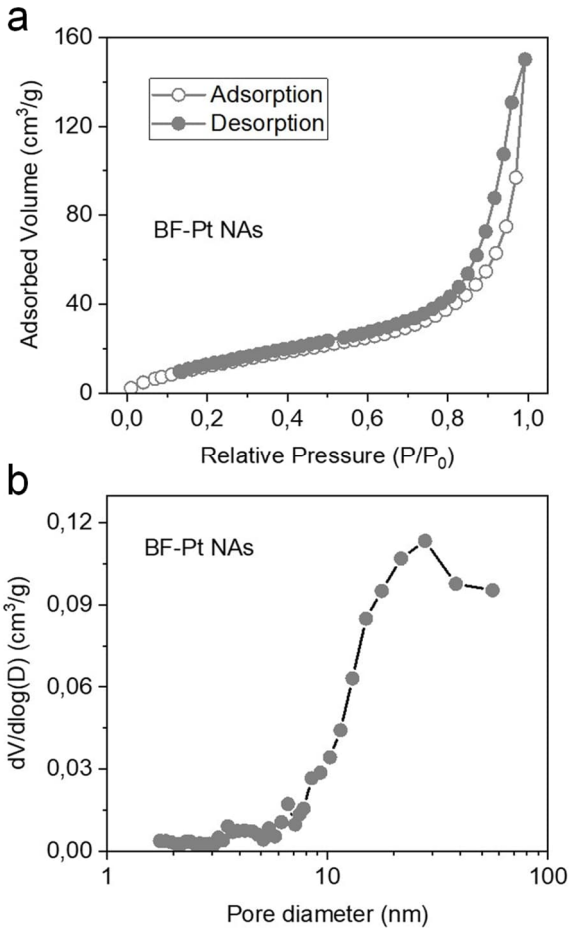

Figure A7-15*. Nitrogen adsorption-desorption isotherms, (b) Barrett–Joyner–Halenda pore size distribution plots of BF-Pt NAs.*

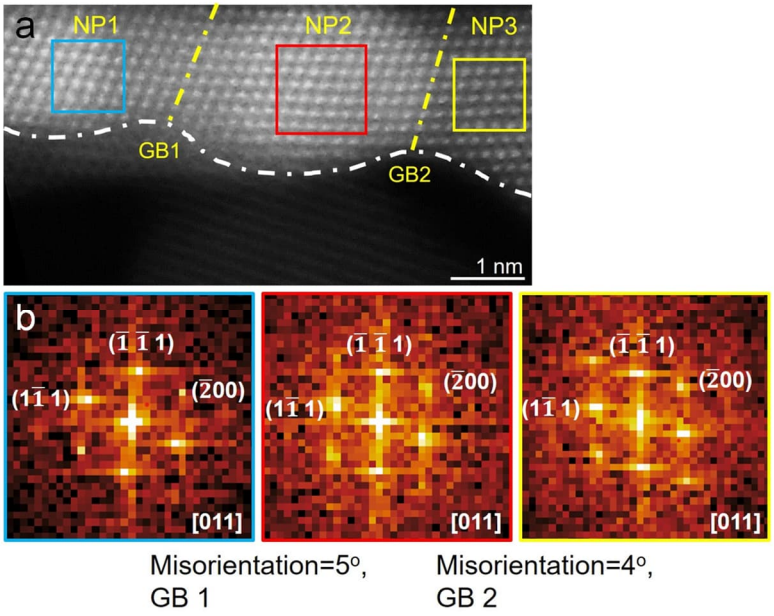

***Figure A7-16**. HAADF-STEM image (a) and FFT diffractograms (b) of GBs in BF-Pt NAs.*

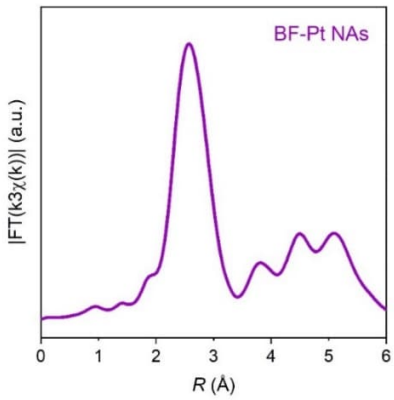

***Figure A7- 17**. Fourier-transformed EXAFS spectra for Pt L3-edge for BF-Pt NAs.*

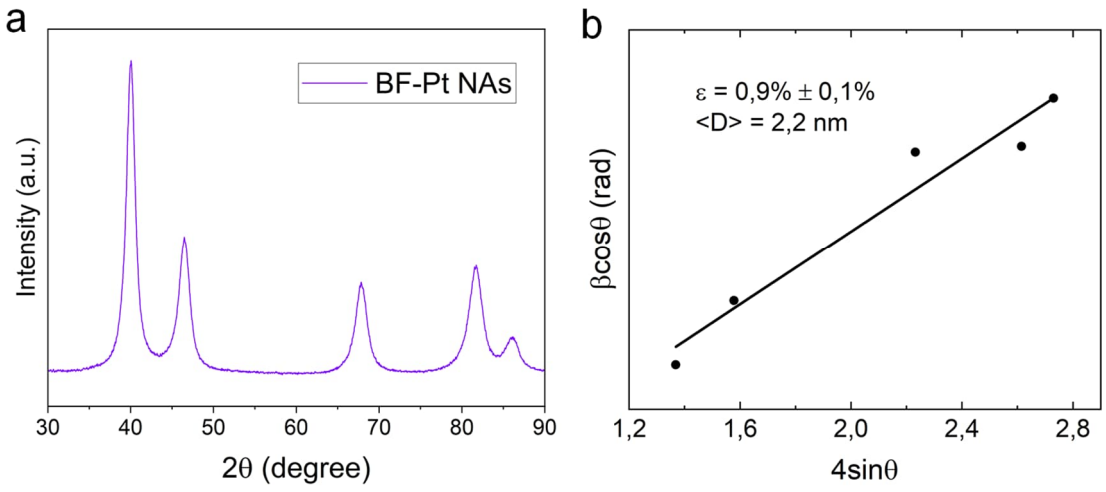

***Figure A7- 18**. (a) High-resolution XRD patterns of BF-Pt NAs showing (111), (200), (220), (311), and (222) diffraction peaks. (b) Williamson–Hall plot derived from the XRD pattern.*

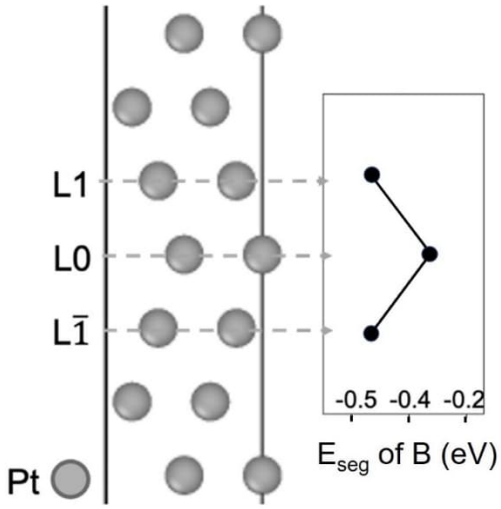

Figure A7-19. *Σ3(111) twin-boundary structure and E_{seg} at twin region calculated by DFT at GB marked by layer L0 and two adjacent layers L1 and $L\bar{1}$.*

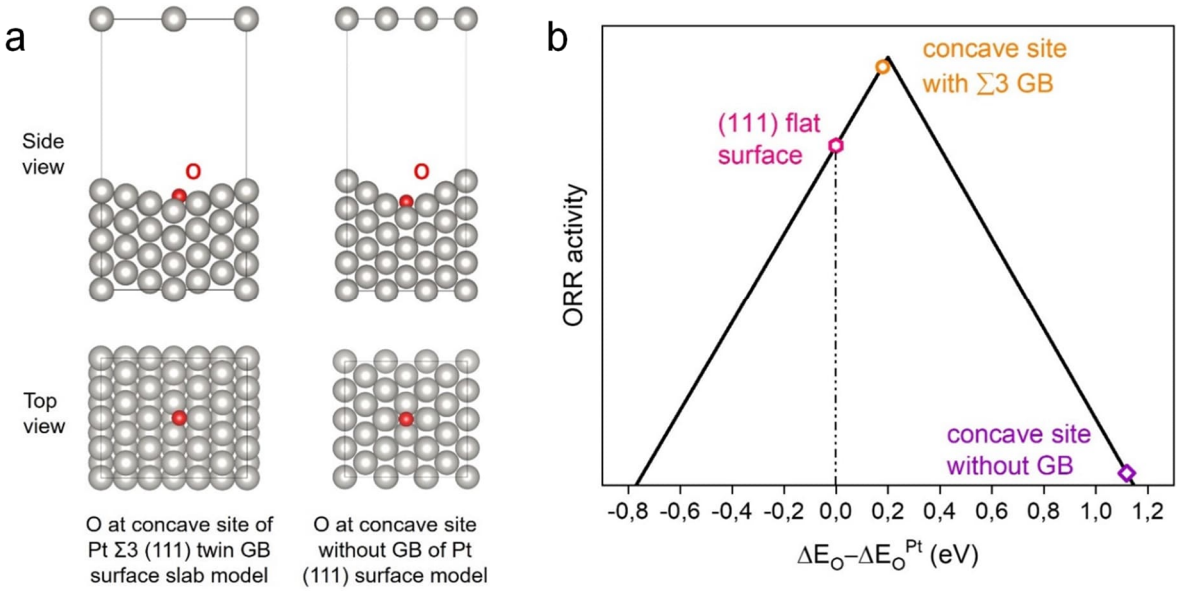

Figure A7-20. *(a) Side and top views of slab models showing an oxygen atom at concave sites of Σ3 GB and concave sites without GB. (b) Volcano plot of ORR activity as a function of the calculated oxygen adsorption energy relative to that on the flat Pt (111) surface.13 The pink hexagon represents the flat (111) surface, the orange circle denotes the concave site at the Σ3 GB, and the violet diamond represents the concave site without a GB. It is evident that the oxygen binding energy at the concave site with the Σ3 GB is close to the optimal value, indicating potentially optimal ORR activity. In contrast, the oxygen binding energy at the concave site without a GB is significantly further from the volcano peak, even less favorable than that of the flat (111) surface.*

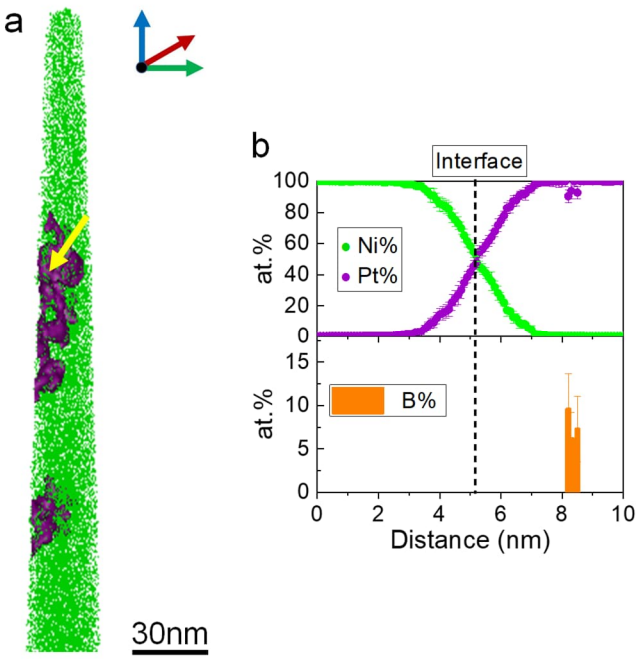

Figure A7-21. *(a) 3D atom map of GB-Pt NAs after 60000 durability test fully embedded in Ni matrix as indicated by the Pt iso-surfaces (iso-composition surface >50 at.% Pt) with a cylindrical region of interest (diameter=3 x 10 nm³, with a bin size of 0.1 nm) located perpendicular to the Ni matrix/GB-Pt NAs interface. (b) 1D compositional profiles of the elements Ni, Pt, and B contained in GB-Pt NAs after 60000 durability test shown along the direction indicated by the yellow arrow in the 3D atom map on left side.*

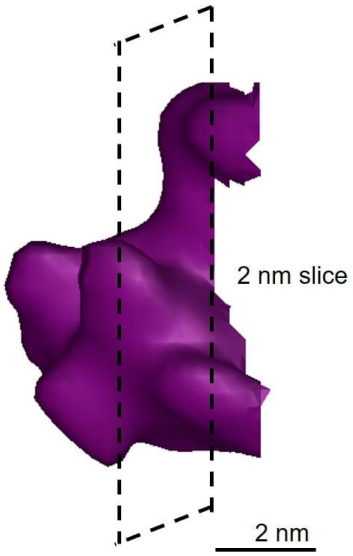

Figure A7-22. *3D atom map of GB-Pt NAs after 60000 durability test (Pt>90 at.% iso-surface). Tomogram of the 3D atom map is shown in* ***Figure 7-9***.

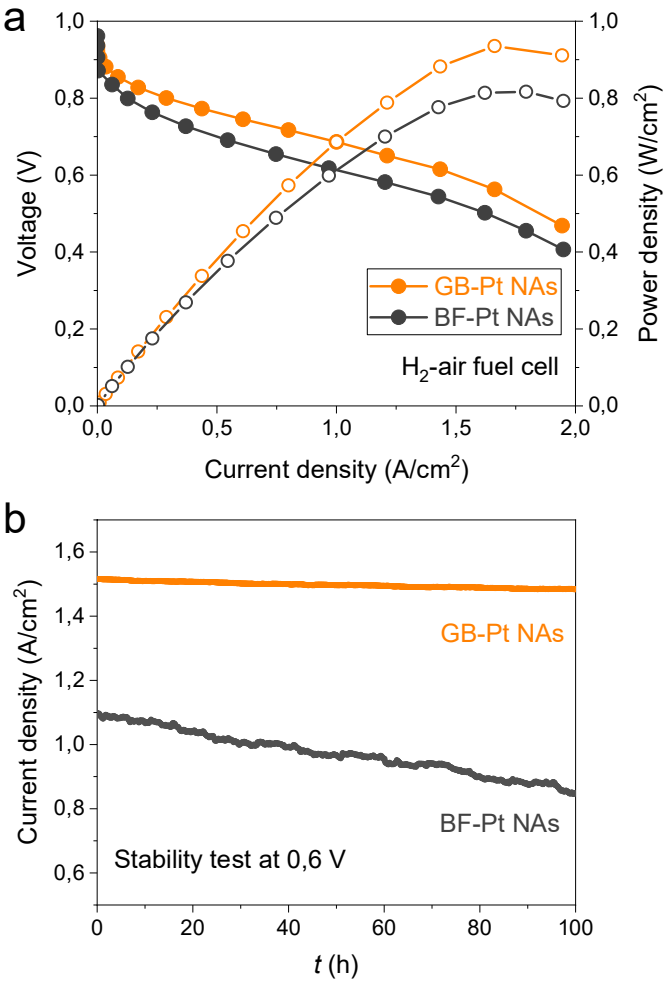

Figure A7-23. *(a) H2-air fuel cell polarization plots with GB-Pt NAs/C and BF-Pt NAs/C as the cathode catalysts. (b) Stability test of H_2-air fuel cell at 0.6 V.*

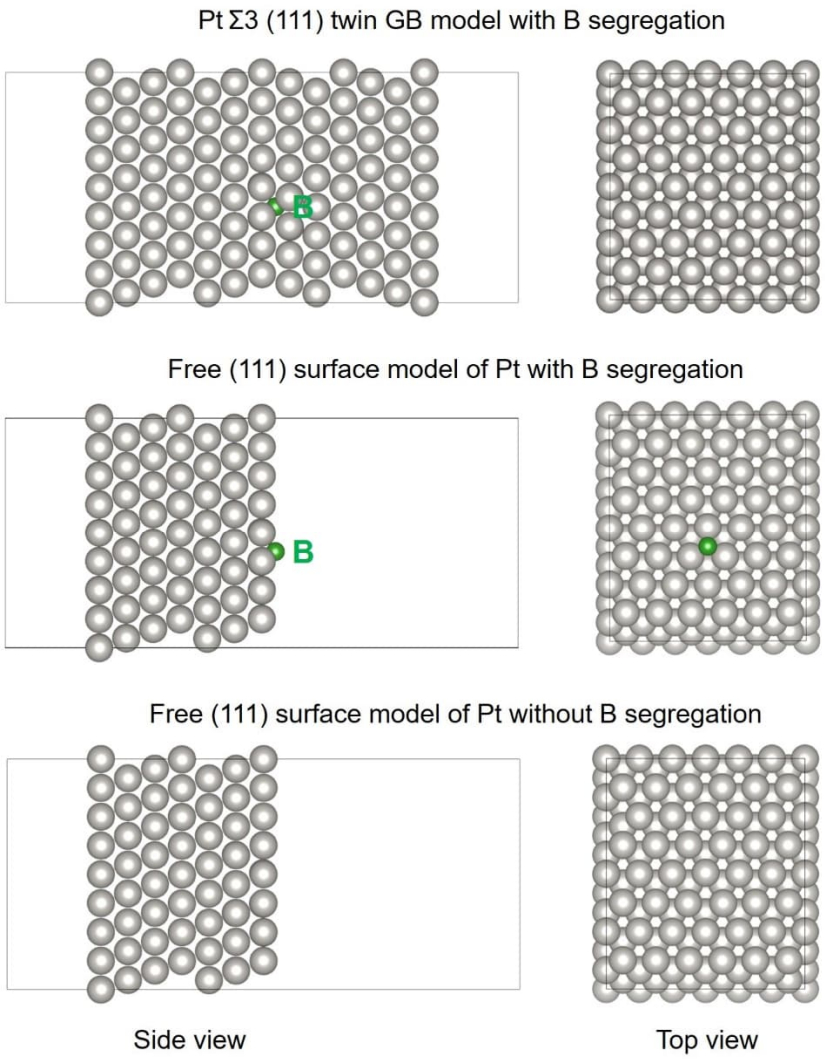

Figure A7-24*. Top and side views of the models for the calculation of the strengthening energy (Estr) of the GB. A negative Estr indicates that the GB is strengthened, whereas a positive Estr signifies that the GB is weakened. We found that Estr is -0.23 eV, indicating that B segregation can strengthen the GB.*

***Table A7-1**. BET results of GB-Pt NAs and BF-Pt NAs.*

Sample	BET surface area (m^2/g)	Pore diameter (nm)	Pore volume (cm^3/g)
GB-Pt NAs	88.2	12.5	0.12
BF-Pt NAs	80.6	13.5	0.10

Table A7-2*. EXAFS fitting results of Pt L3 edge for Pt NPs, GB-Pt NAs, BF-Pt NAs, and Pt foil.*

Sample	*CN*	*R (Å)*	σ^2 (10^{-3} Å^2)	ΔE_0 (eV)	*R* factor
Pt NPs	8.2±0.2	2.76±0.03	5.5±1.8	6.4±1.8	0.0061
GB-Pt NAs	9.3±0.3	2.70±0.02	6.4±2.1	9.3±2.5	0.0079
BF-Pt NAs	8.8±0.3	2.72±0.03	5.8±1.9	7.1±2.2	0.0068
Pt foil	11.8±0.2	2.76±0.02	4.2±1.4	5.5±1.7	0.0057

CN: coordination number; *R:* bond length; σ*:* Debye-Waller factor; ΔE_0: inner potential shift; *R factor* describing goodness of the fit.

***Table A7-3**. ORR performance of GB-Pt NAs and state-of-art Pt-based nanocatalysts.*

Catalyst	ECSA (m^2/g_{Pt})	Specific activity (mA/cm^2) at 0.90V	Mass activity (A/mg_{Pt}) at 0.90V	References
20 wt.% Pt/C	57.1	---	0.095	Science 2009, 324, 1302
Pt Nanocage	38.2	1.98	0.75	Science 2015, 349, 412
Mo-Pt_3Ni	67.5	10.3	6.98	Science 2015, 348, 1230
PtPb/Pt plate	55.1	7.8	4.3	Science 2016, 354, 1410
Jagged Pt NW	118	11.5	13.6	Science 2016, 354, 1414
Bunched Pt-Ni alloy	68.2	5.16	3.52	Science 2019, 366, 850
PtNi thin film	9	2.4	0.216	Nat. Mater. 2012, 11, 1051
Intermetallic Pt_3Co NP			0.52	Nat. Mater. 2013, 12, 81
PtNiCo NW	82.2	5.11	4.2	Sci. Adv. 2017, 3 1601705
Pt_3Co NW	52.1	7.12	3.71	Nat. Commun. 2016, 7, 11850
PtNi-NiB NP	59	9.05	5.3	Nat. Commun. 2016, 7, 12362
L10-CoPt/Pt	27.3	8.26	2.26	Joule 2018, 3, 1
$Pt_4FeCoCuNi$ NP	---	---	3.79	Adv. Mater. 2023, 2302067
Pt_3Fe NW	34.0	4.34	2.11	Adv. Mater. 2018, 30, 1705515
PtNiPd NW	55.4	3.48	1.93	Adv. Mater. 2017, 29, 1603774
PtCu OFAs	54.5	5.98	3.26	Adv. Mater. 2016, 29, 1601687
Rh-Pt NW	86.4	1.63	1.41	J. Am. Chem. Soc. 2017, 139, 8152
PtPb/PtNi IM	37.2	5.16	1.92	J. Am. Chem. Soc. 2017, 139, 9576
Pd@Pt NP	96.4	1.66	1.6	J. Am. Chem. Soc. 2015, 137, 15036
Pt Nantube	34.2	1.48	0.50	J. Am. Chem. Soc. 2016, 138, 6332
Pt Nanocages	45.2	2.48	1.12	J. Am. Chem. Soc. 2016, 138, 1494
Pd@$Pt_{1.8}Ni$ NP	---	0.45	0.79	J. Am. Chem. Soc. 2015, 137, 2804
Sub-Pt_3Co-MC	49.7	1.74	0.92	PNAS 2021, 118, e2104026118
PtCu nanoframe	53.3	4.69	2.47	Nano Lett. 2020, 20, 7413
Ga-doped PtNi	49	2.53	1.24	Nano Lett. 2018, 18, 2450
PtNi frame	73.4	2.05	1.51	Nano Lett. 2018, 18, 2930
Pt Nanocage	36.6	3.50	1.28	Nano Lett. 2016, 16, 1467
Rh-PtNi	---	---	1.14	Nano Lett. 2016, 16, 1719
PtNi frame	54.8	0.44	0.24	ACS Nano 2018, 12, 8697
Pt cube	24.5	1.77	0.43	Mater. Today 2018, 08, 5
GB-Pt NAs	**69.7**	**9.18**	**6.40**	**This work**

11.2 Supplementary information from Chapter 8

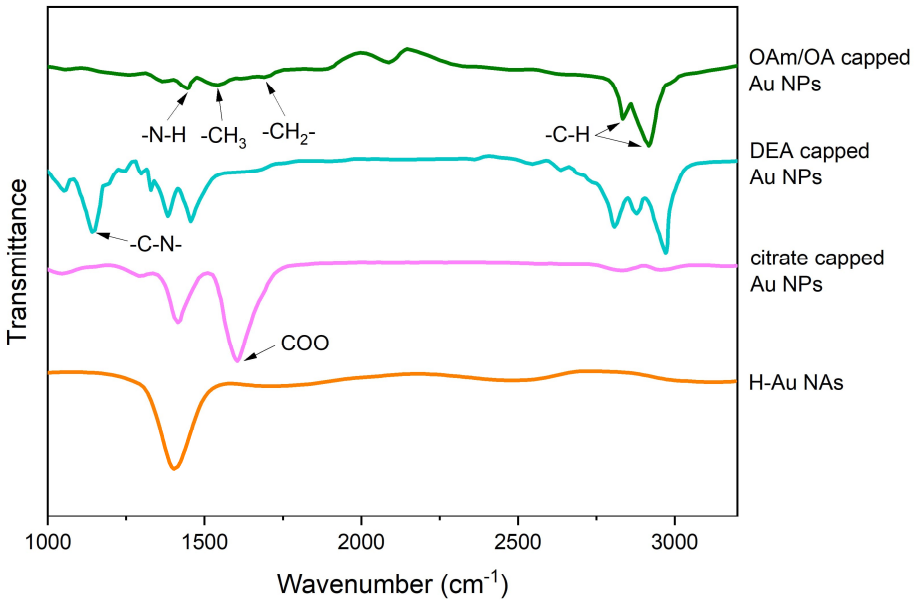

***Figure A8-1**. FTIR spectra of OAm, DEA, citrate-capped Au NPs, and Au NAs.*

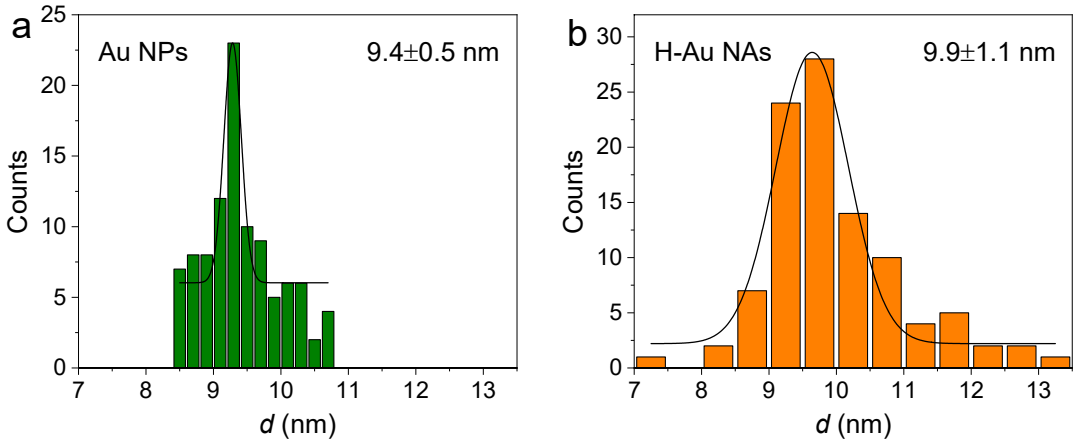

***Figure A8-2**. The size distribution was obtained by analyzing 100 NPs or crystallites in (a) Au NPs and (b) H-Au NAs derived from STEM images.*

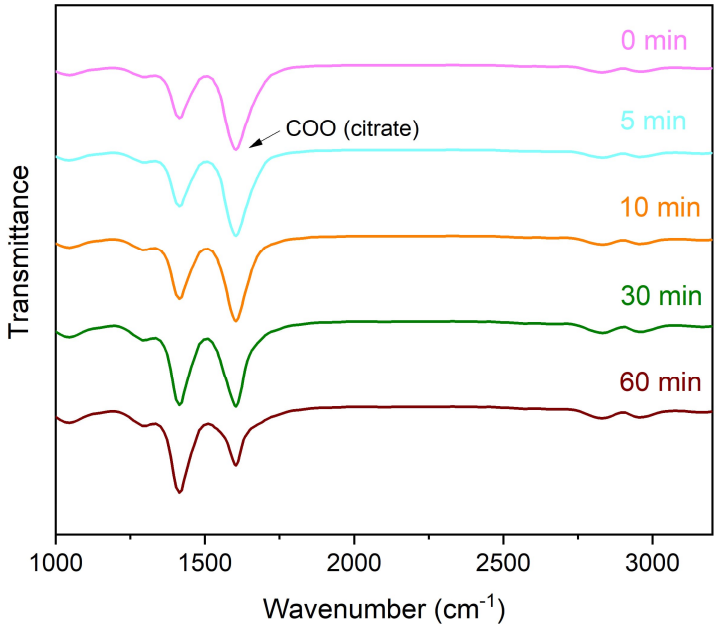

Figure A8-3. *Variation of FTIR spectra for citrate-capped Au NP solution after adding ammonia solution (pH=10), which show that the amount of citrate capping agents on the surface Au NPs reduces progressively.*

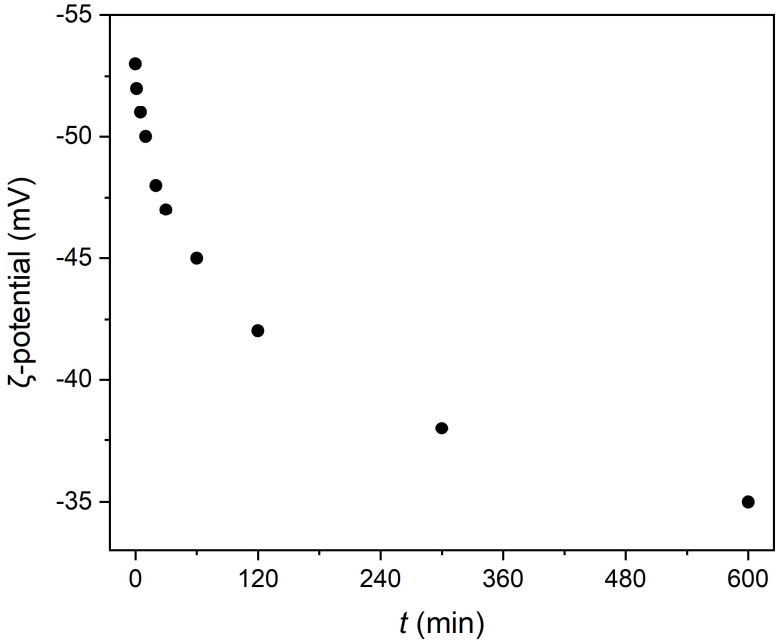

Figure A8-4. *Variation of the ζ-potential measured for citrate-capped Au NP solution versus the time after adding ammonia solution (pH=10).*

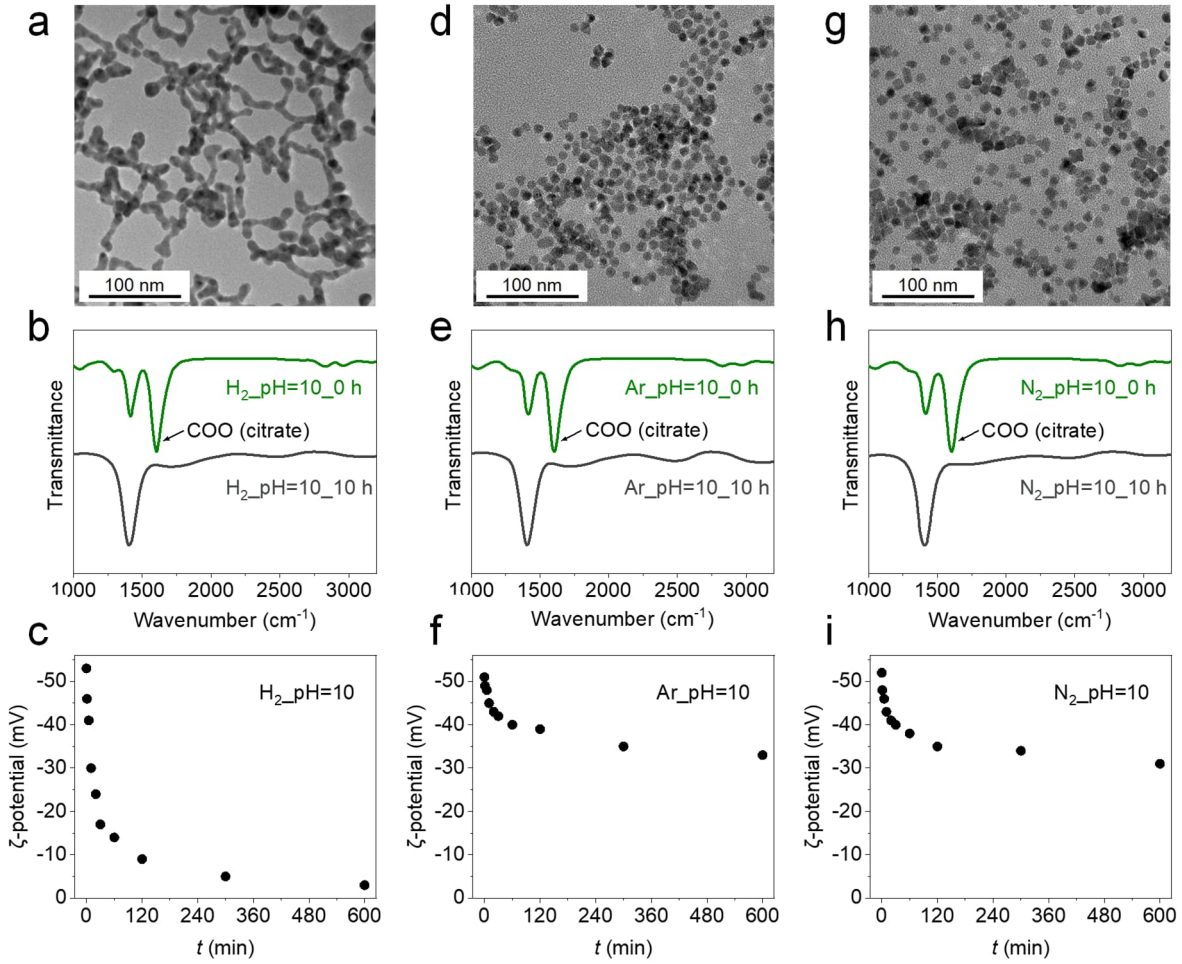

Figure A8-5. *(a) TEM image of the NPs obtained by purging Ar gas into a citrate-capped Au NP solution at pH 10 for 10 h. (b) FTIR spectrum of the Au NP solution at pH 10 subjected to Ar gas purging for 0 h and 10 h, respectively. (c) Time-dependent variation of the ζ-potential for citrate-capped Au NP solution at pH 10 during Ar gas purging. TEM image (d), FTIR spectrum (e) and time-dependent variation of ζ-potential (f) for citrate-capped Au NP solution at pH 10 during N_2 gas purging. TEM image (g), FTIR spectrum (h) and time-dependent variation of ζ-potential (i) for citrate-capped Au NP solution at pH 10 during H_2 gas purging.*

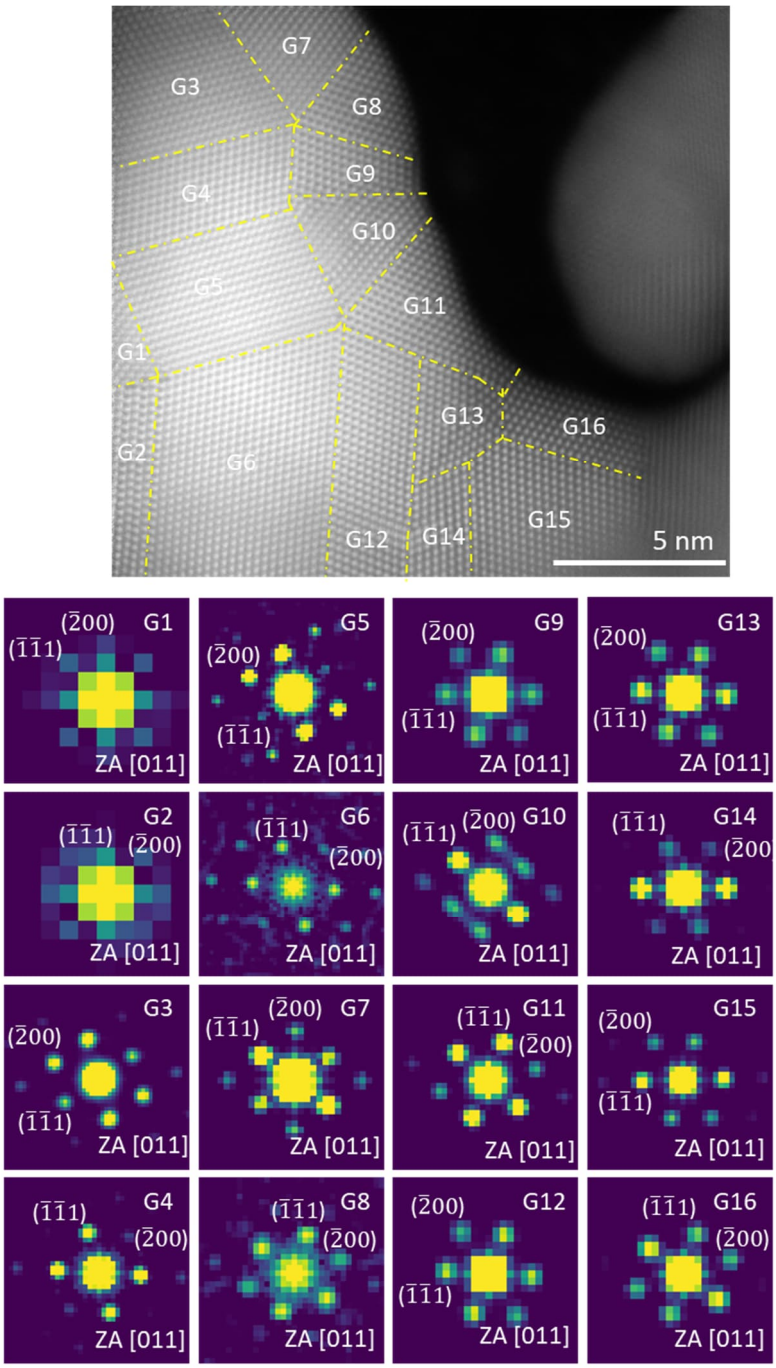

***Figure A8-6**. FFT analysis of the NA displayed in **Figure 8-1d** from Chapter 8. From the FFT diffractograms (bottom rows) of individual NP building blocks in the HAADF-STEM image (top rows), the zone axis ([011] for all NP building blocks) and misorientation can be determined. This allows for the identification of the GB types in H-Au NAs using coincidence site lattice theory.*

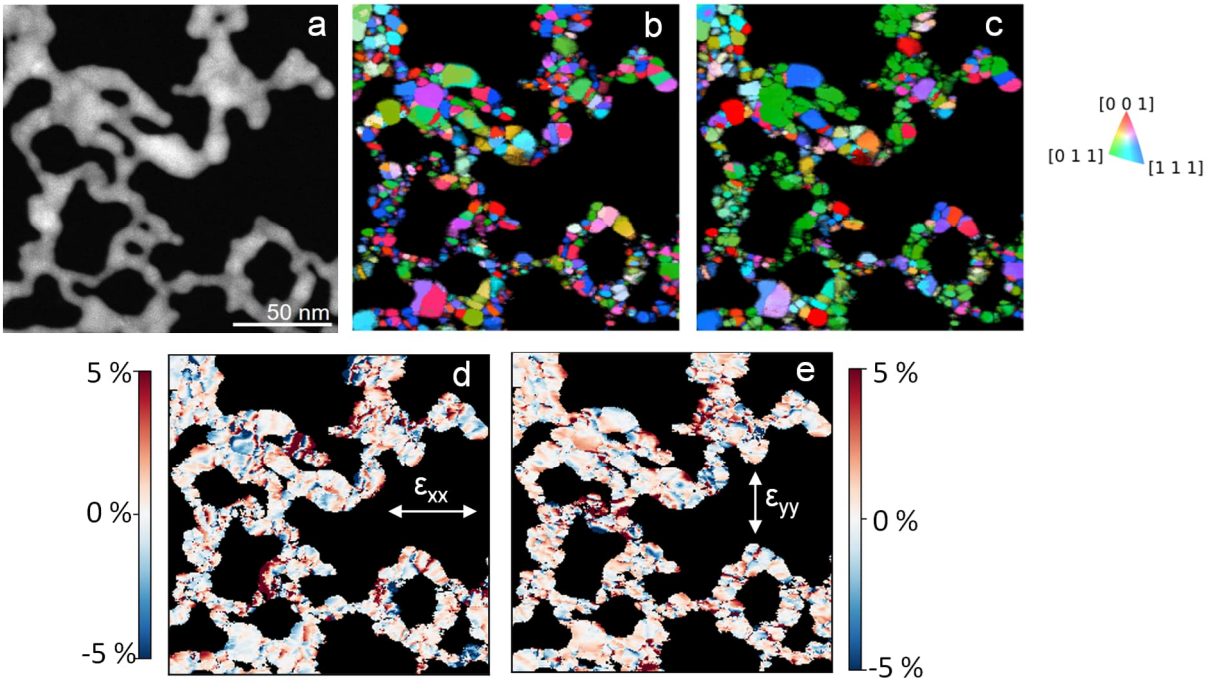

***Figure A8-7**. HAADF-STEM image (a), grain orientation maps (b-c) and corresponding relative strain maps along the x (ε_{xx}) and y (ε_{yy}) direction obtained from corresponding 4D-STEM datasets for H-Au NAs.*

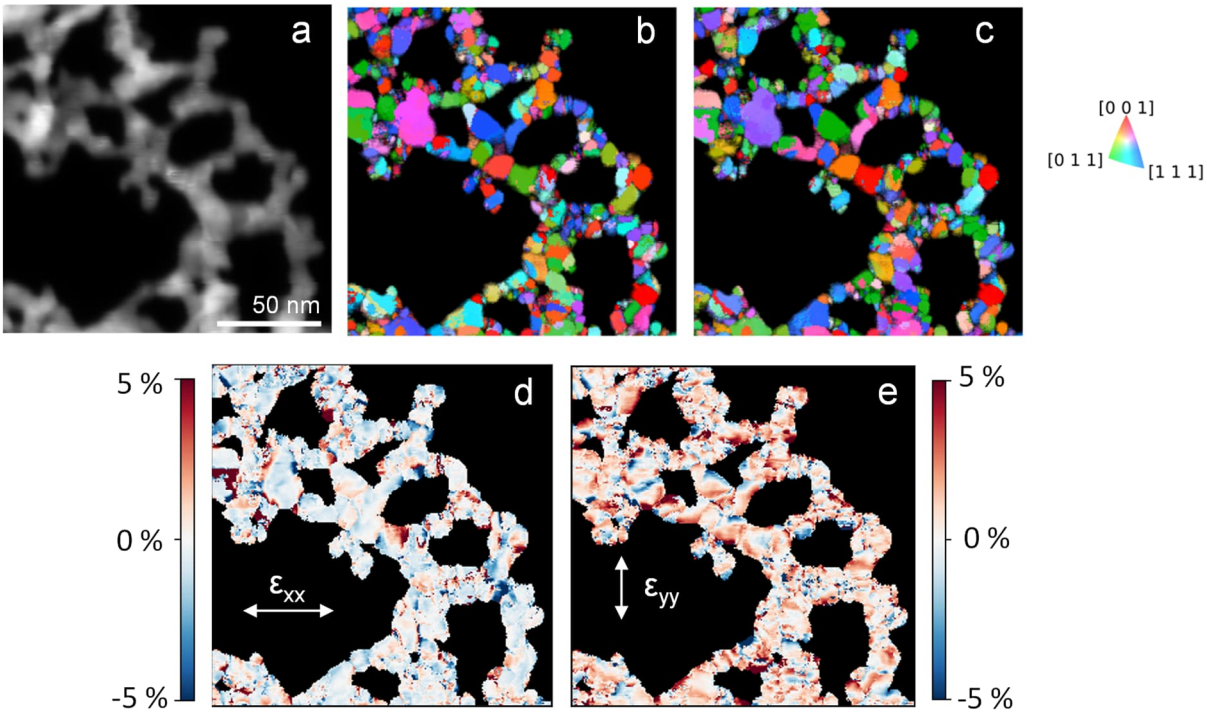

***Figure A8-8**. 4D-STEM data from a different region of H-Au NAs, comprising the virtual HAADF image (a), grain orientation maps (b-c) and relative strain maps.*

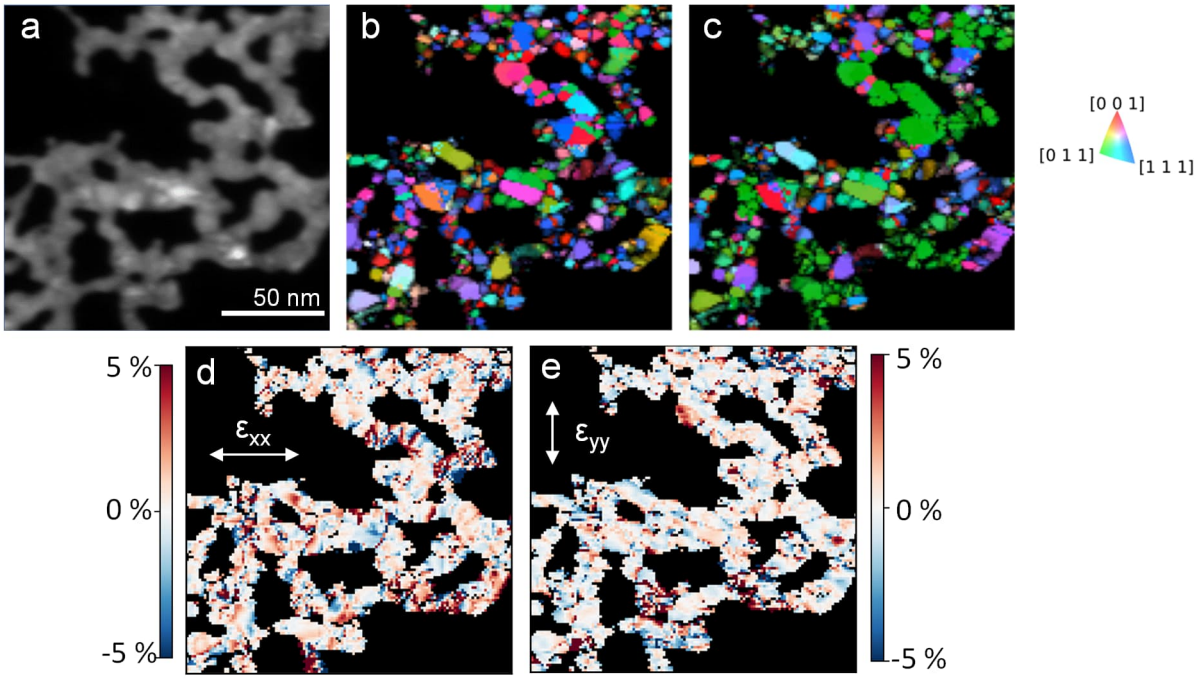

Figure A8-9. *Virtual dark field images (a), grain orientation maps (b-c) and relative strain maps for an additional region of H-Au NAs.*

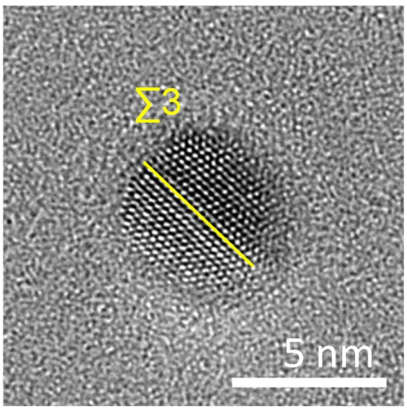

Figure A8-10. *High resolution TEM image of an individual Au NP, showing that a small number of Au NPs possess low energy ∑3 GBs before assembling.*

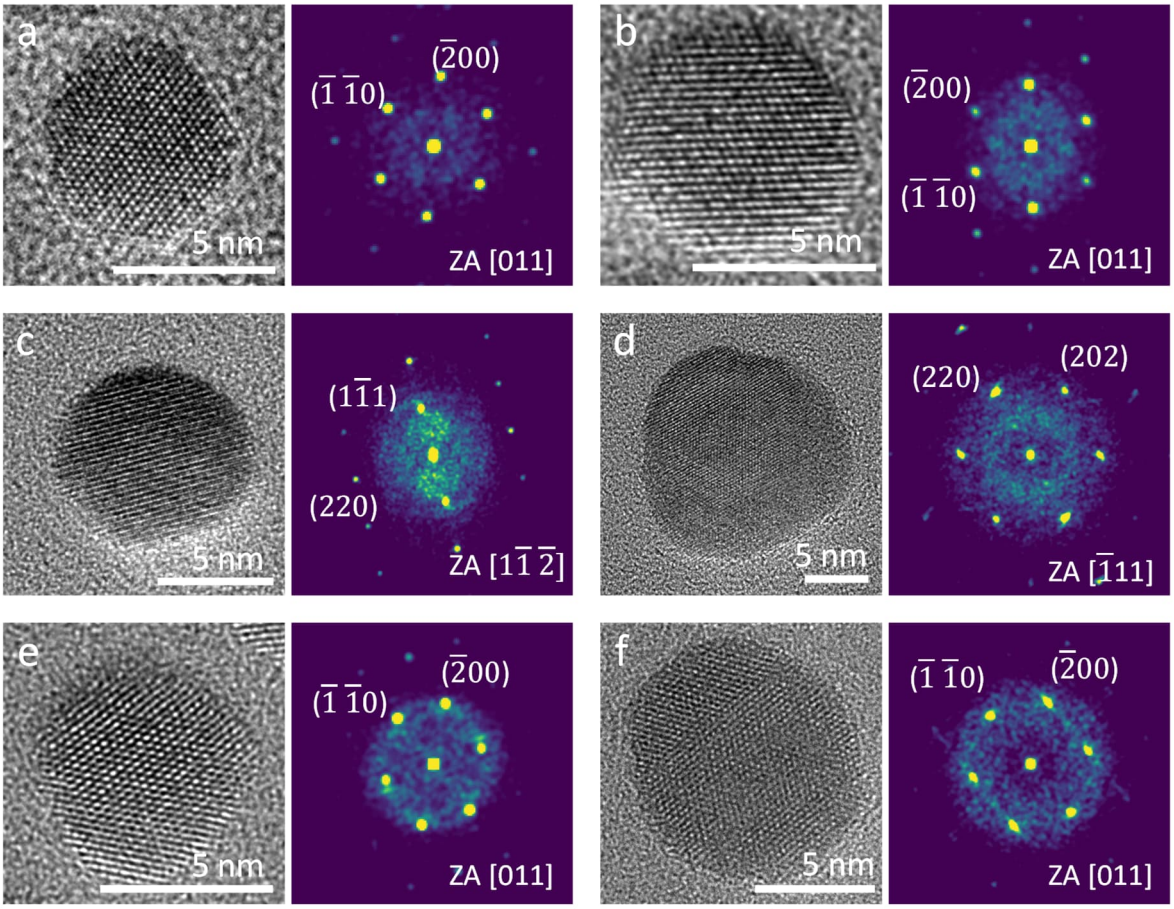

***Figure A8-11**. High resolution TEM images of Au NPs before assembling with corresponding indexed FFT. Notice how before the assembly process, most of the Au NPs are defect-free.*

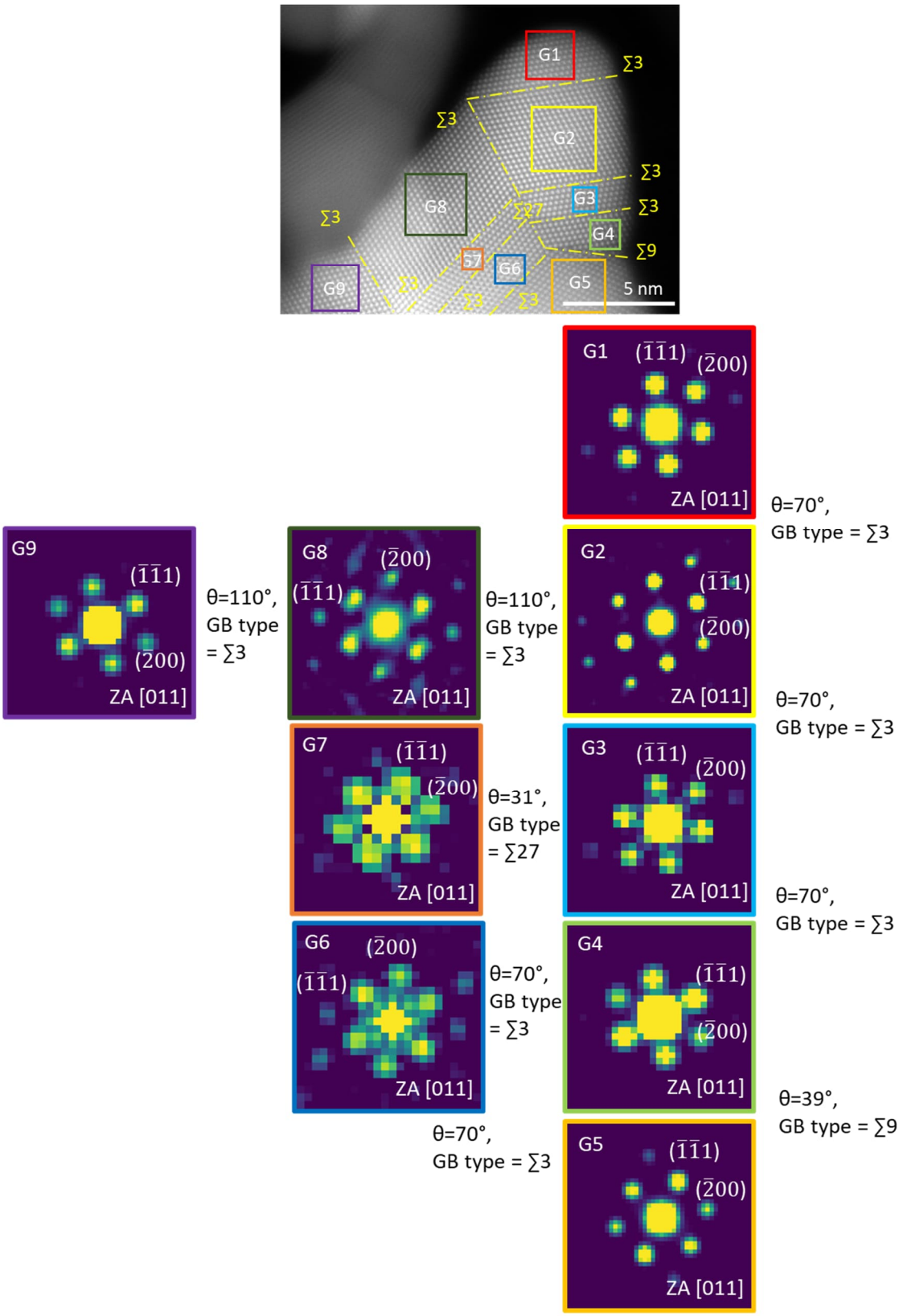

Figure A8-12*. Determination of GB types based on the coincidence site lattice theory of NA in* ***Figure 8-3a*** *(Chapter 8). Initially, FFT diffractograms were obtained for individual NP building blocks in HAADF-STEM image to determine the zone axis. Subsequently, the misorientation between adjacent NP building blocks on the same crystal plane was measured, allowing for the identification of the GB types in H-Au NAs.*

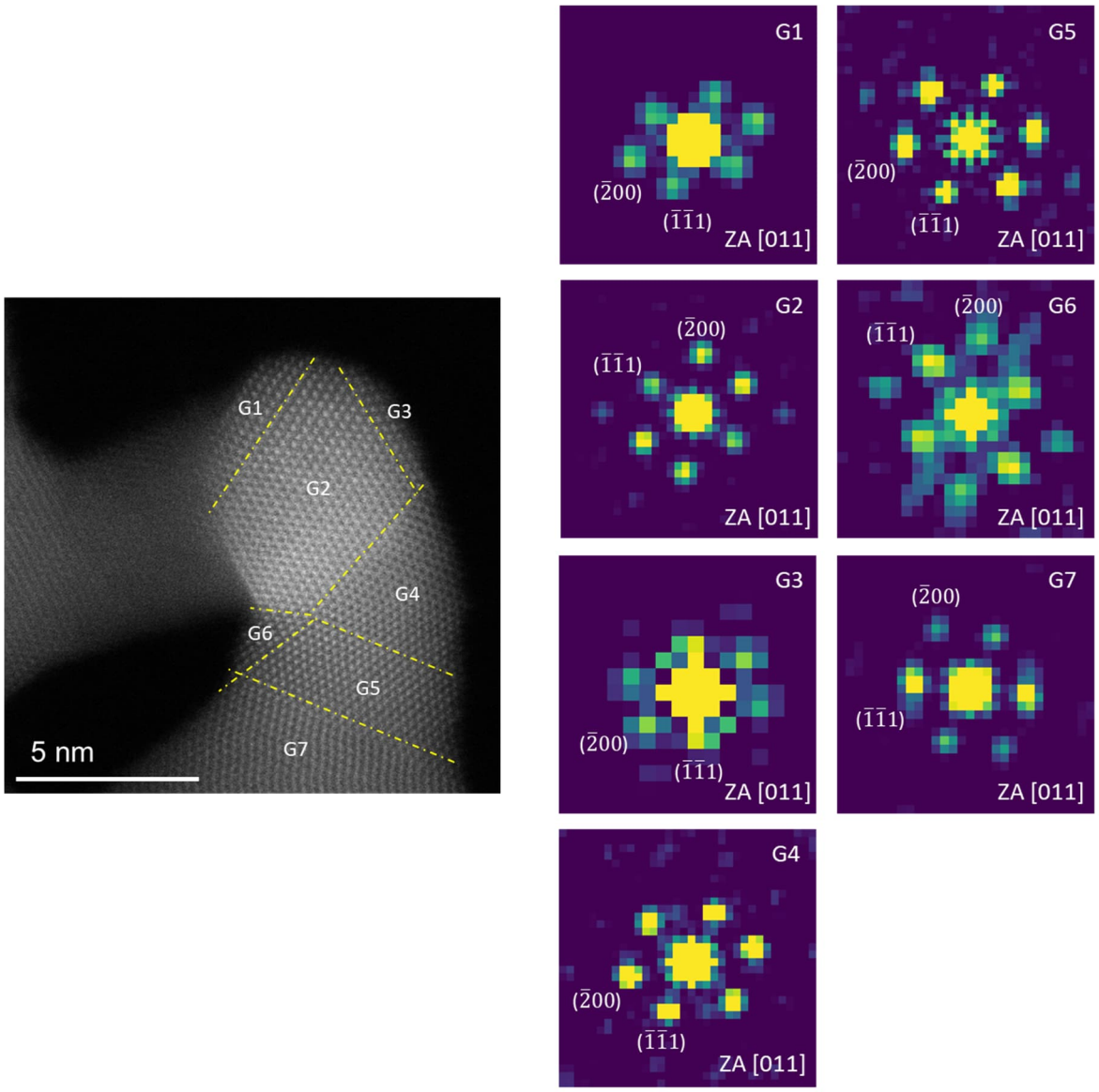

Figure A8-13*.HAADF STEM image and corresponding FFT analysis for the identification of GB types in L-Au NAs of* ***Figure 8-5d*** *(Chapter 8) based on the coincidence site lattice theory.*

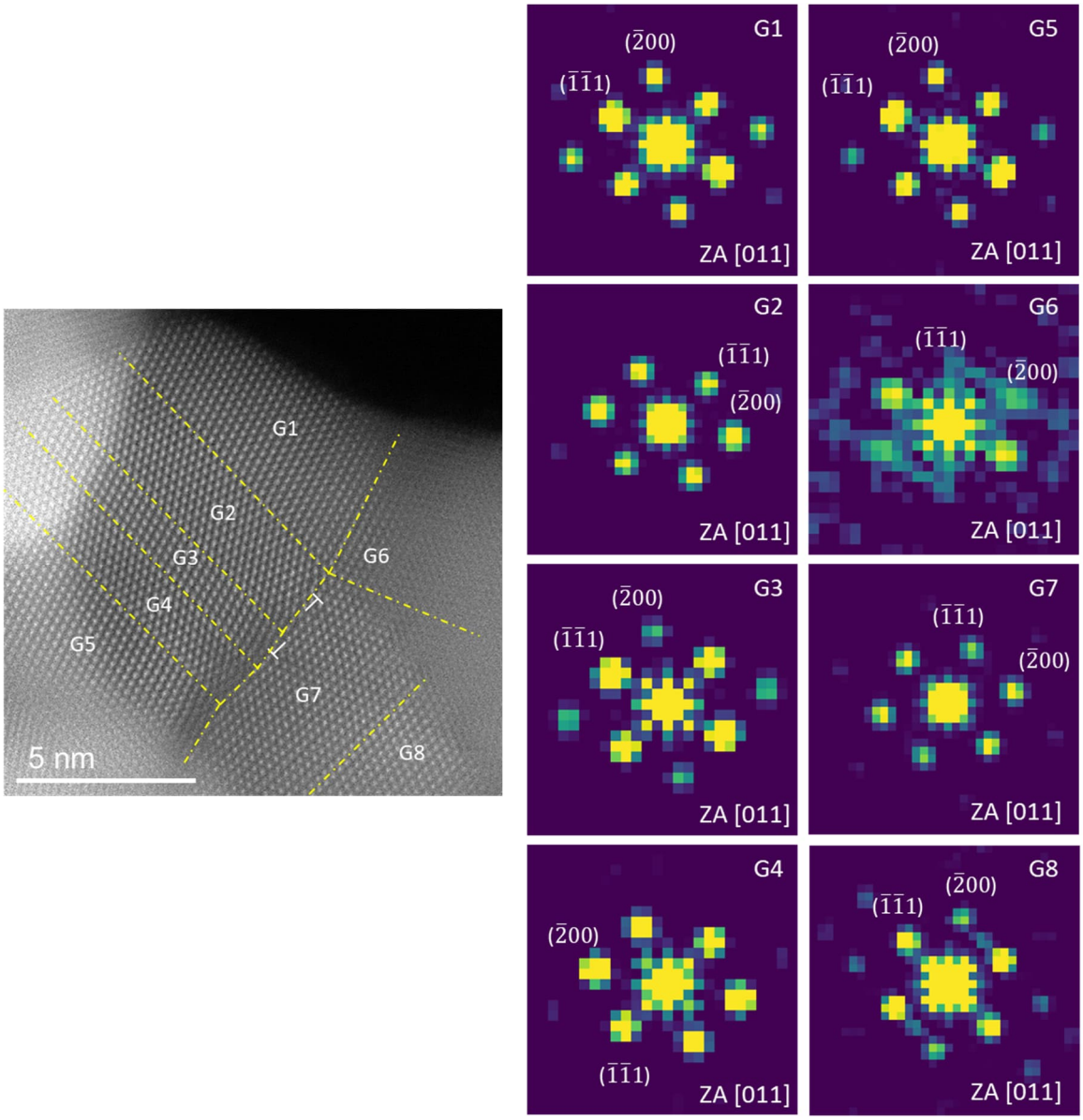

***Figure A8-14**. HAADF-STEM image and corresponding FFT analysis of M-Au NAs (**Figure 8-5e**, Chapter 8) for GB identification.*

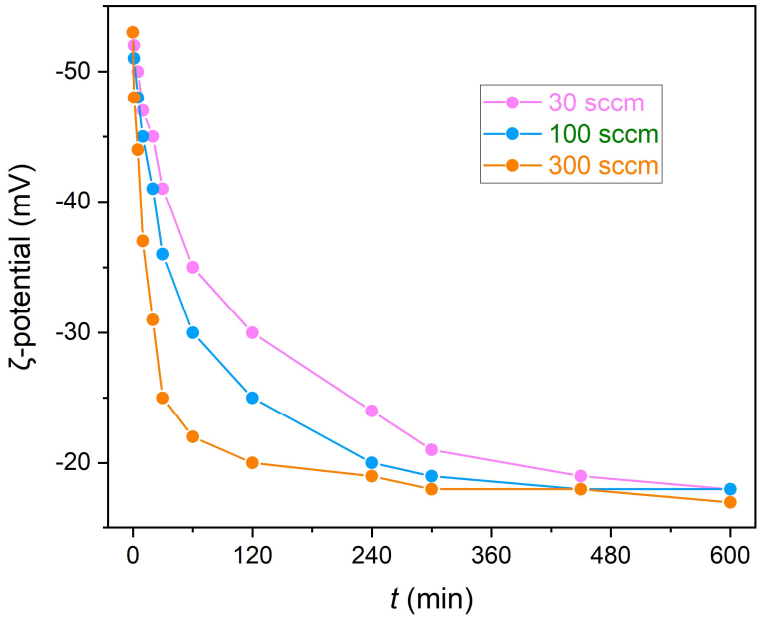

***Figure A8-15**. Change over time of the ζ-potential measured for citrate-capped Au NP solution with respect to the duration (t) of different flow rates of H_2 gas bubbling.*

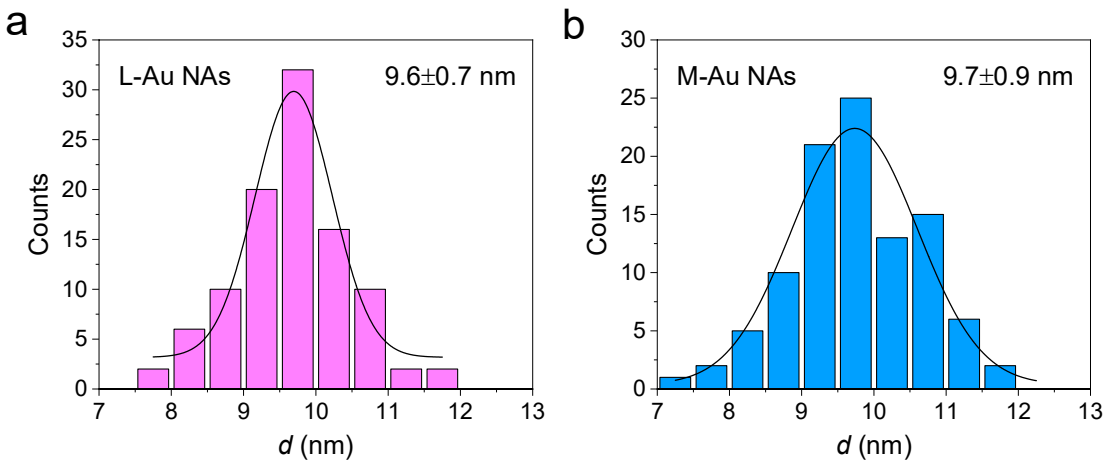

***Figure A8-16**. The size distribution was obtained by analyzing 100 NPs or crystallites in **(a)** L-Au NAs and **(b)** M-Au NAs derived from STEM images.*

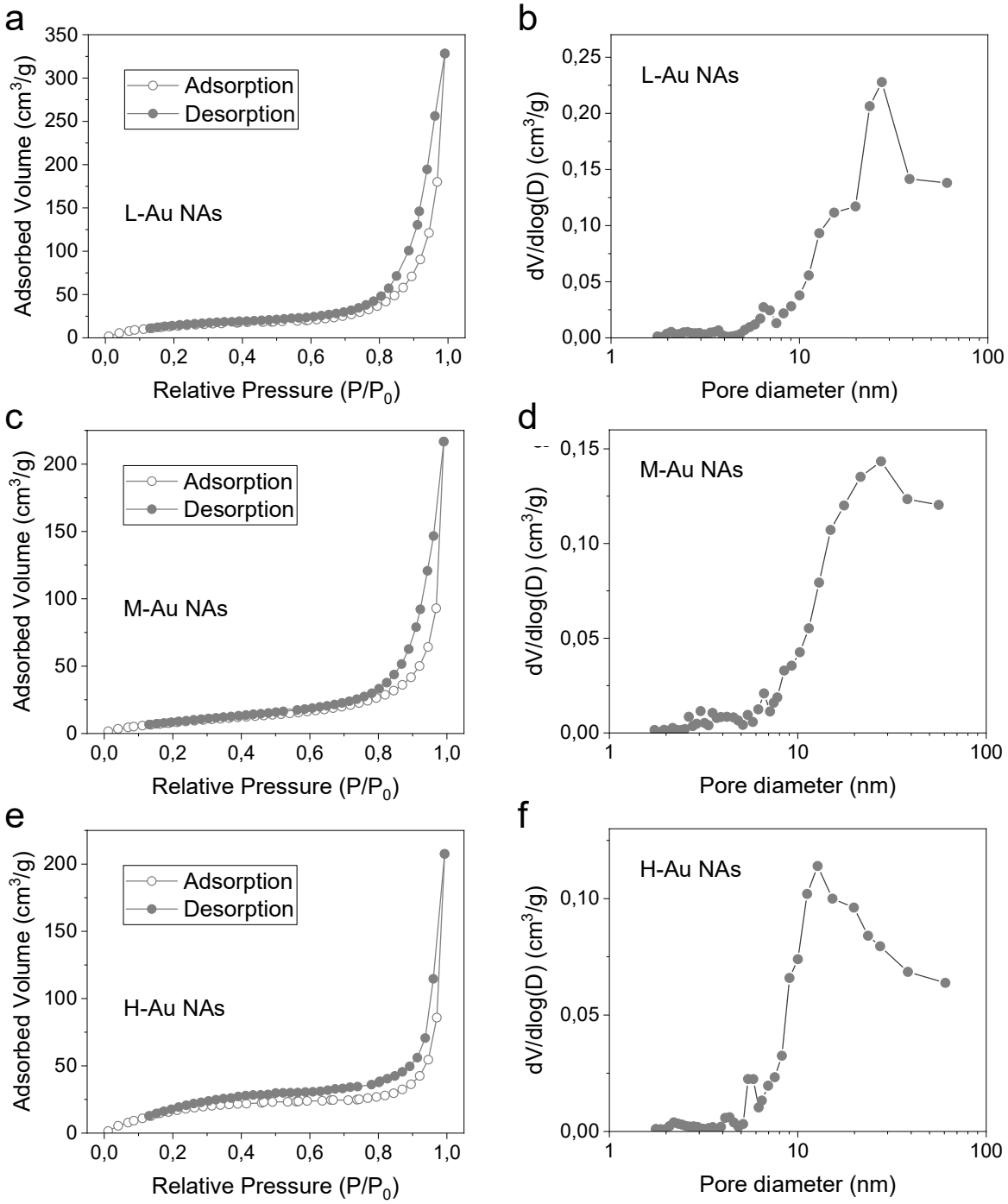

Figure A8-17*. Nitrogen adsorption-desorption isotherms of L-Au NAs (a), M-Au NAs (c) and H-Au NAs (e). Barrett–Joyner–Halenda pore size distribution plots of L-Au NAs (b), M-Au NAs (d) and H-Au NAs (f).*

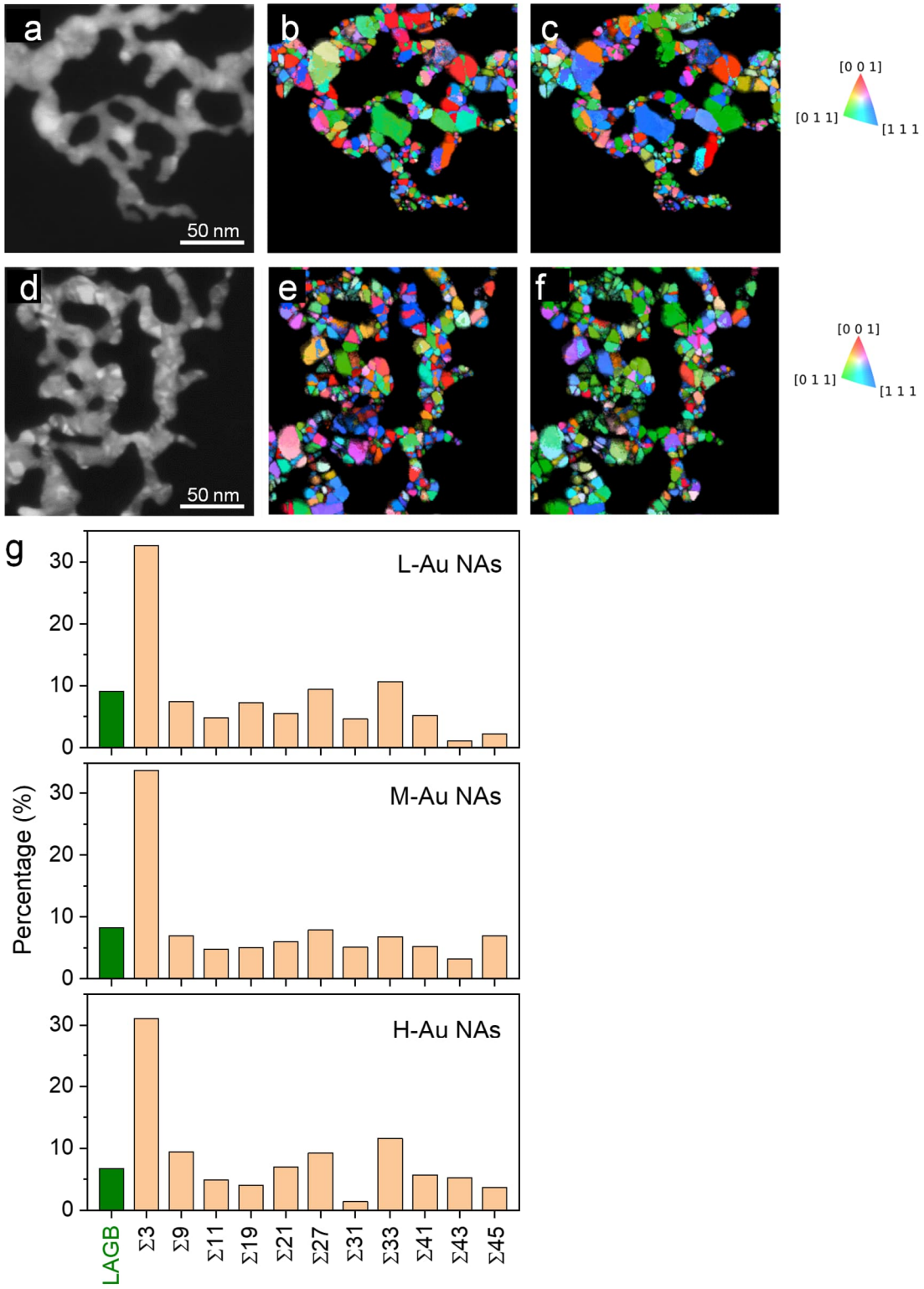

Figure A8-18*.(a) HAADF-STEM image, (b) in-plane and (c) out-of-plane orientation maps from the corresponding 4D-STEM dataset for L-Au NAs. (d) HAADF-STEM image and grain orientation maps (e: in-plane, f: out-of-plane) from the corresponding 4D-STEM dataset for M-Au NAs. (g) Histogram plots of the GB types derived from over 100 GBs in the 4D-STEM data.*

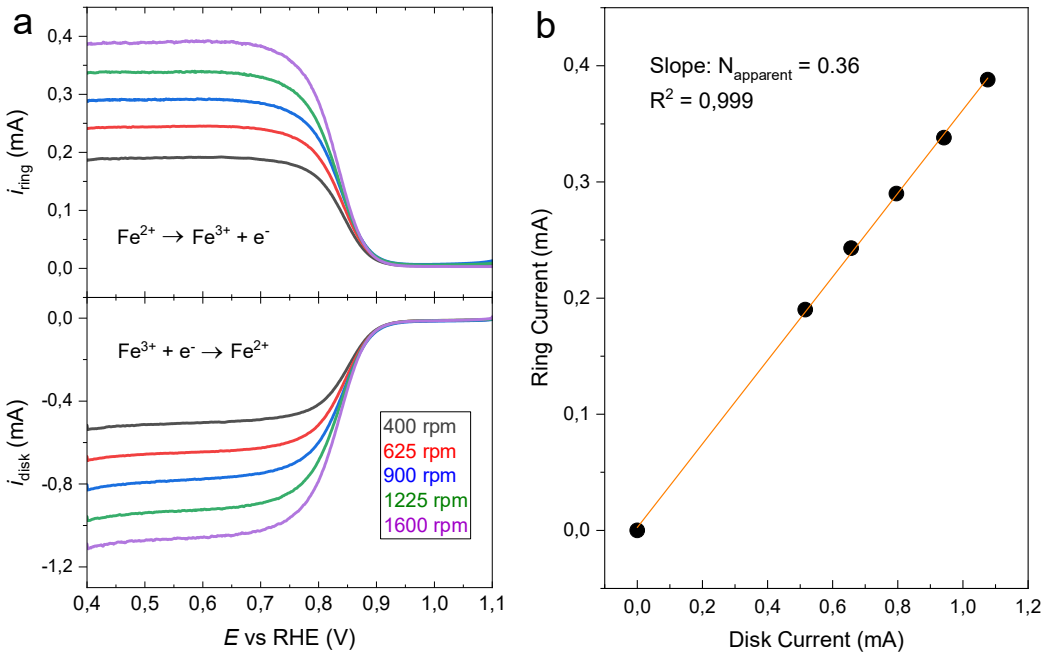

Figure A8-19. *RRDE collection efficiency calibration. (a) Linear sweep voltammetry curves recorded on a bare glassy carbon rotation disk electrode (diameter = 5.6 mm) with a Pt ring (diameter = 15.0 mm) in 0.1 M $HClO_4$ supporting electrolyte with 10 mM $K_3Fe(CN)_6$. Sweep rates: 10 mV s^{-1}, E_{ring} = 1.2 V vs. RHE. (b) Linear fitting of the diffusion-limited current densities recorded on ring and disk electrodes at different rotation speeds. The experimentally determined apparent collection efficiency (N) is 36%, close to the theoretical value of 40%.*

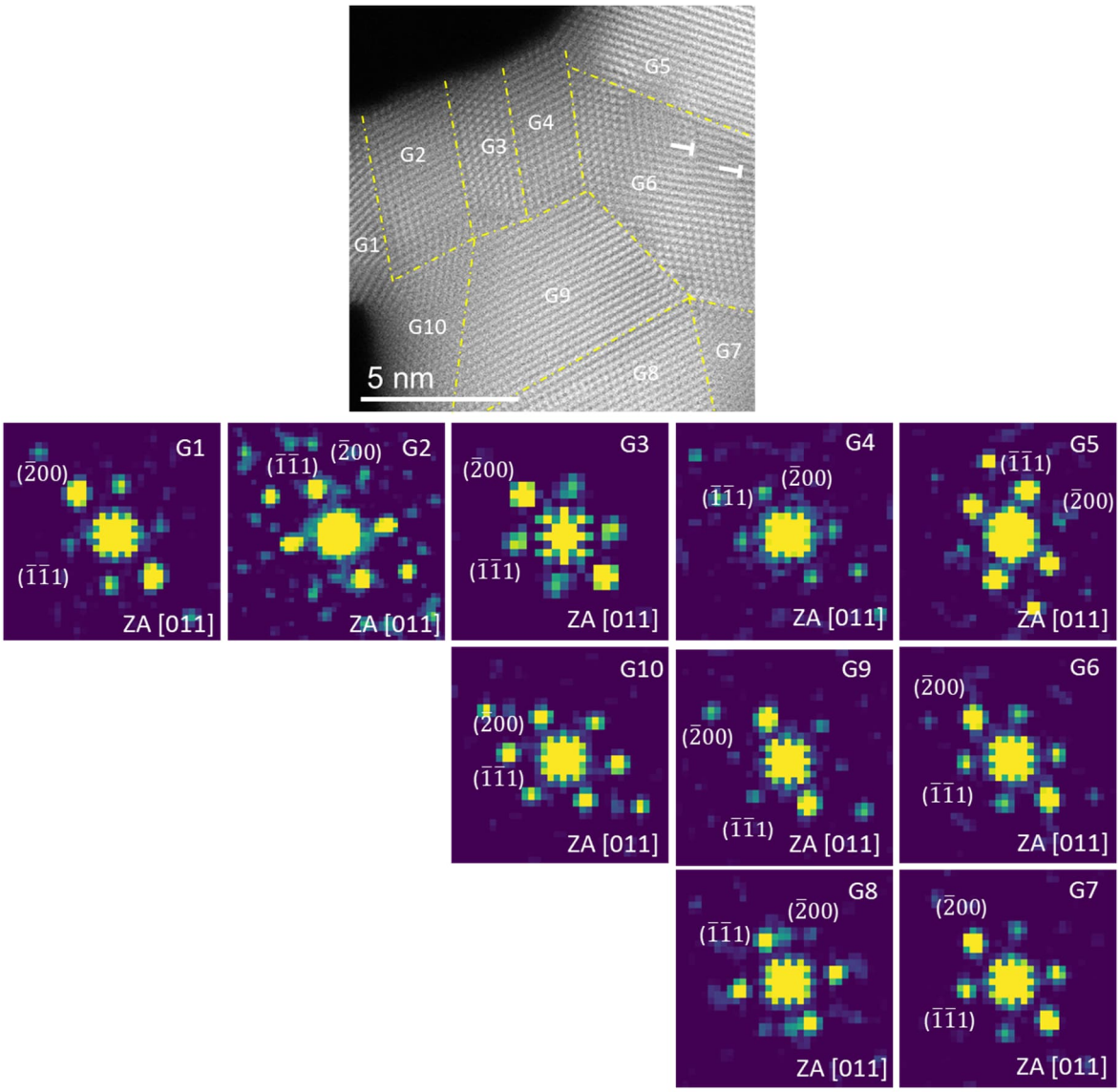

Figure A8-20. *HAADF image and FFT analysis for the identification of GB types based on the coincidence site lattice theory for H-Au NA after the durability test (**Figure 8-6d** in Chapter 8).*

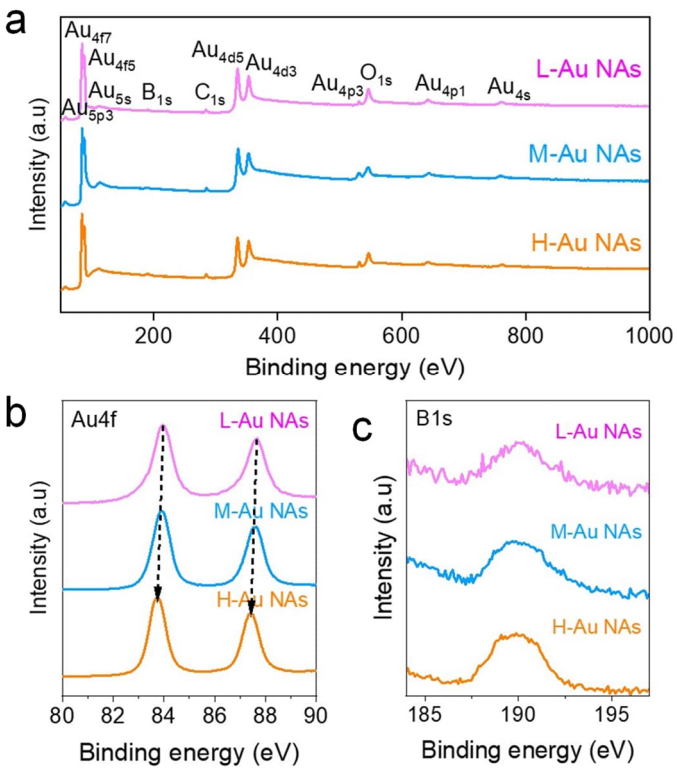

Figure A8-21. *(a) XPS overview survey, (b) Au 4f spectra and (c) B 1s spectra of L-Au NAs, M-Au NAs and H-Au NAs.*

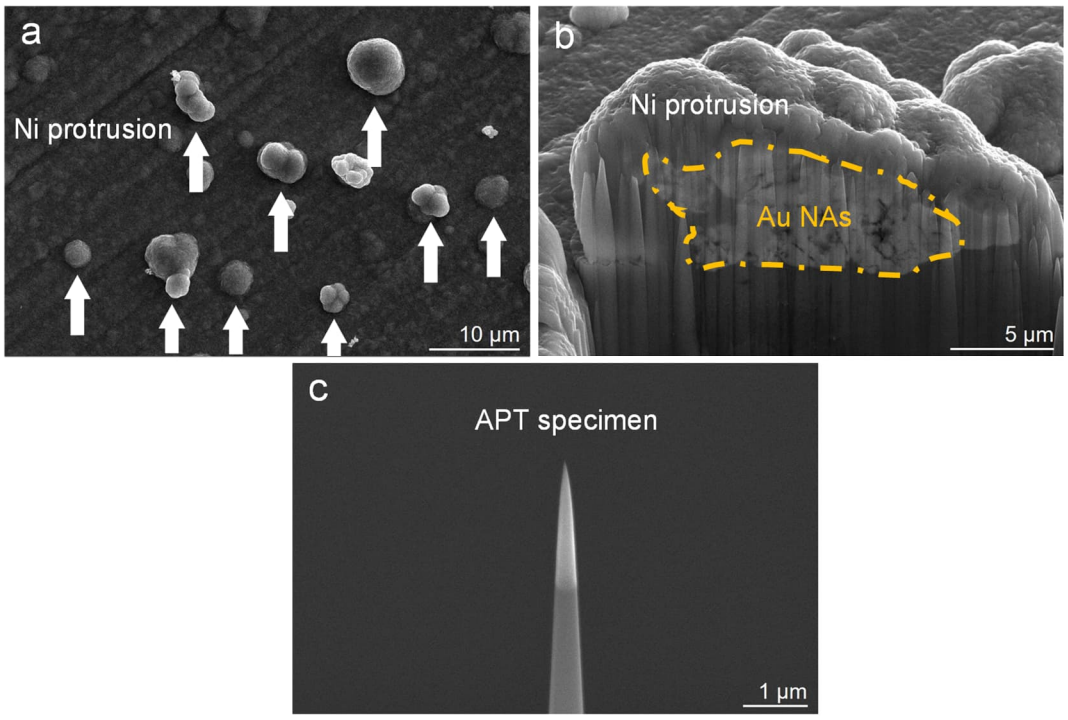

Figure A8-22. *(a) SEM image of the protrusions (indicated by white arrows) with Au NAs embedded in Ni matrix. (b) The cross-sectional SEM image of one protrusion cut by the ion beam, which indicates that Au NAs (circled by orange short dash line) are embedded in the Ni matrix. (c) A sharpened specimen from Au NAs embedded in Ni matrix for APT measurement.*

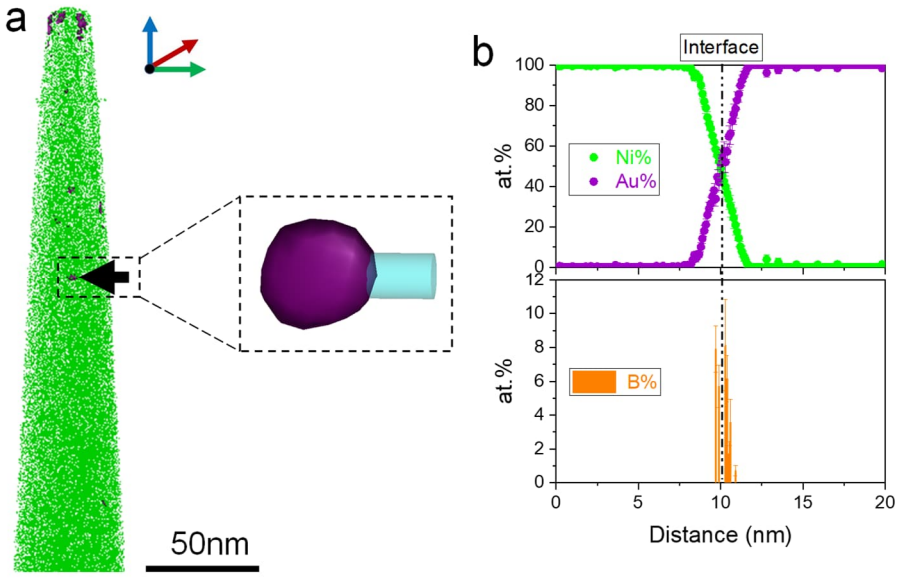

Figure A8-23. *APT analysis of Au NPs embedded in a Ni matrix. (a) 3D atom map (iso-composition surface >50 at.% Au). The inset shows the NP with the cylindrical region of interest located perpendicular to the Ni matrix/Au NP interface. (b) 1D compositional profiles of the elements Ni, Au, and B contained in Au NPs.*

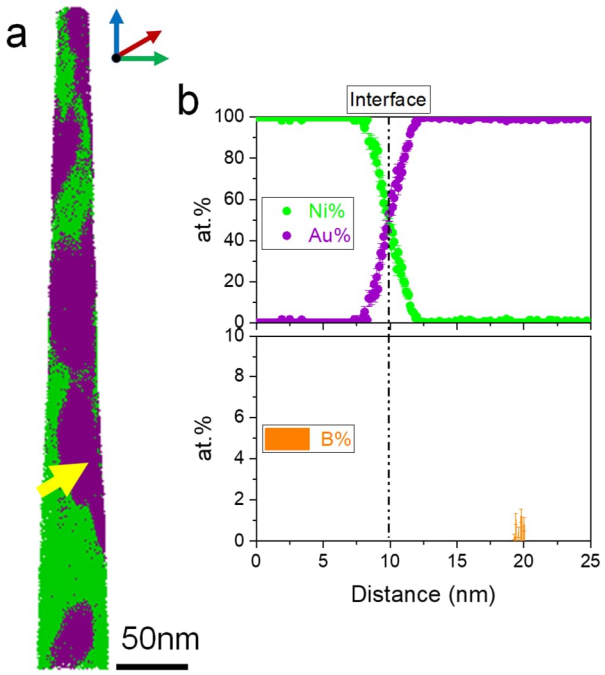

Figure A8-24. *(a) 3D atom maps of L-Au NAs fully embedded in a Ni matrix as indicated by the Au iso-surfaces (iso-composition surface >50 at.% Au. (b) 1D compositional profiles of the elements Ni, Au, and B contained in L-Au NAs shown along the direction indicated by the yellow arrow. The Gibbsian interfacial excess of B is determined to be 1.1 B atoms/nm^2. It implies that a minimal quantity of B segregates at GBs within L-Au NAs.*

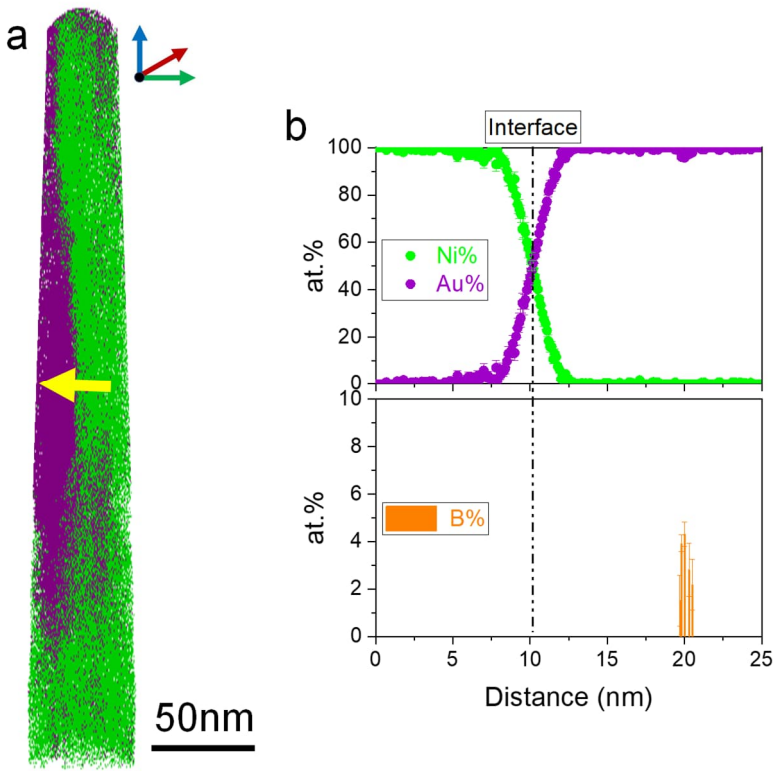

Figure A8-25. *APT analysis of M-Au NAs , showing the (a) 3D atom maps of the M-Au NAs fully embedded in a Ni matrix (Au iso-composition surface >50 at.% Au). (b) 1D compositional profiles of the elements Ni, Au, and B contained in M-Au NAs shown along the direction indicated by the yellow arrow in the 3D atom map on left panel. The determination of the Gibbsian interfacial excess of B, yields a value of 2.6 B atoms/nm^2. This observation indicates a greater segregation of B atoms at GBs in M-Au NAs when compared to L-Au NAs.*

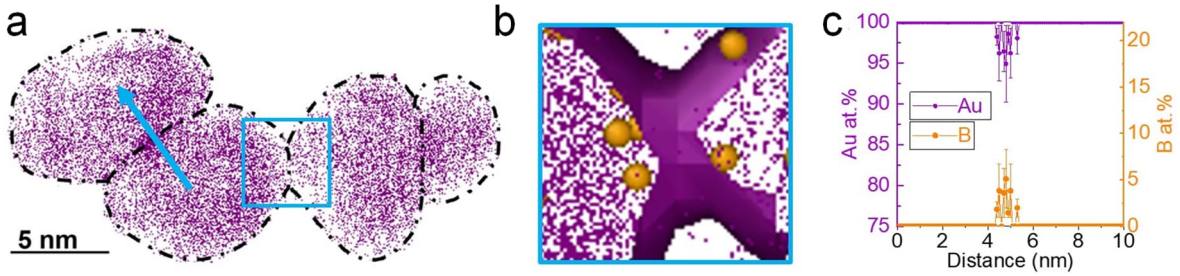

Figure A8-26. *(a) 2 nm thin-sliced tomogram from a 3D atom map (**Figure A8-25**) of M-Au NAs (iso-composition surface >90 at.% Au). (b) Extracted GB tomogram of M-Au NAs of the region delineated by the blue box, in which the orange spheres signify B atoms. (c) 1D compositional profiles of identified Au and B elements of M-Au NAs along the direction indicated by the blue arrow.*

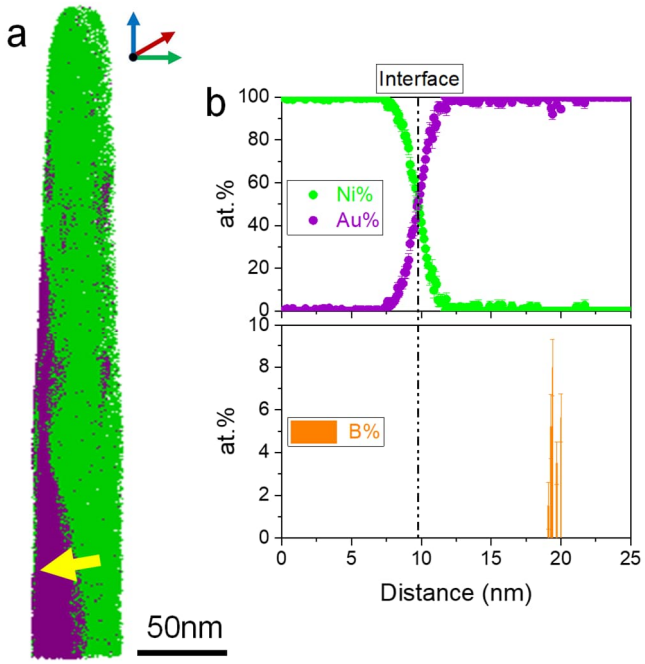

***Figure A8-27**. (a) 3D atom maps of H-Au NAs embedded in a Ni matrix. (iso-composition surface >50 at.% Au) (b) 1D compositional profiles along the direction indicated by the yellow arrow in (a) of the elements Ni, Au, and B. The computation of the Gibbsian interfacial excess of B, denoted as Γ_B, reveals a value of 4.2 B atoms/nm^2. The observed trend in the concentration of B segregated at GBs follows the order of H-Au NAs > M-Au NAs > L-Au NAs.*

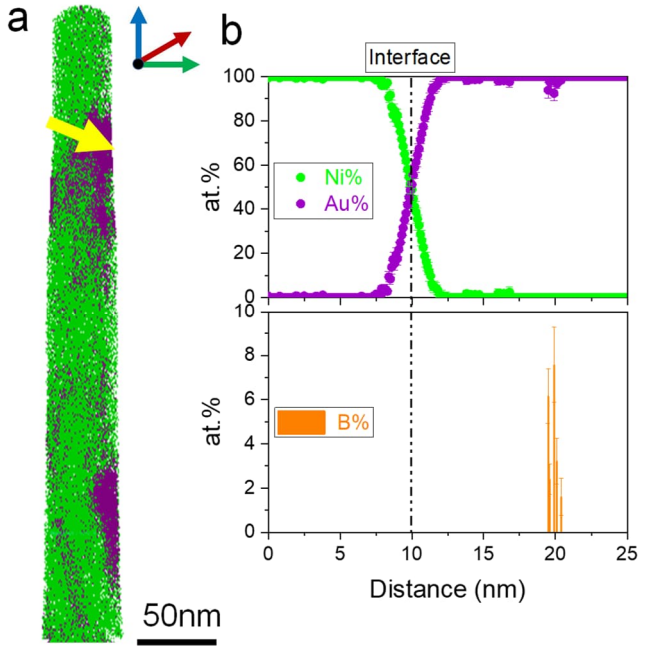

***Figure A8-28**. APT of H-Au NAs after durability test. (a) 3D atom maps (iso-composition surface >50 at.% Au) (b) 1D compositional profiles. Gibbsian interfacial excess of B, = 4.0 B atoms/nm^2. This finding indicates that no leaching of B has occurred during durability testing, affirming the robustness of the trapping of B at GBs.*

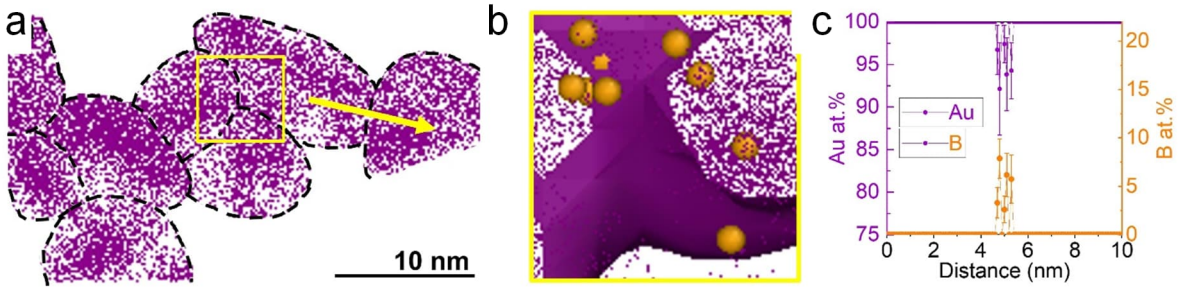

Figure A8-29. *(a) 2 nm thin-sliced tomogram from a 3D atom map of H-Au NAs after durability tests. (b) Extracted GB tomogram of H-Au NAs of the region delineated by the yellow box, in which the orange spheres signify B atoms. (c) 1D compositional profiles of identified Au and B elements of H-Au NAs along the direction indicated by the yellow arrow.*

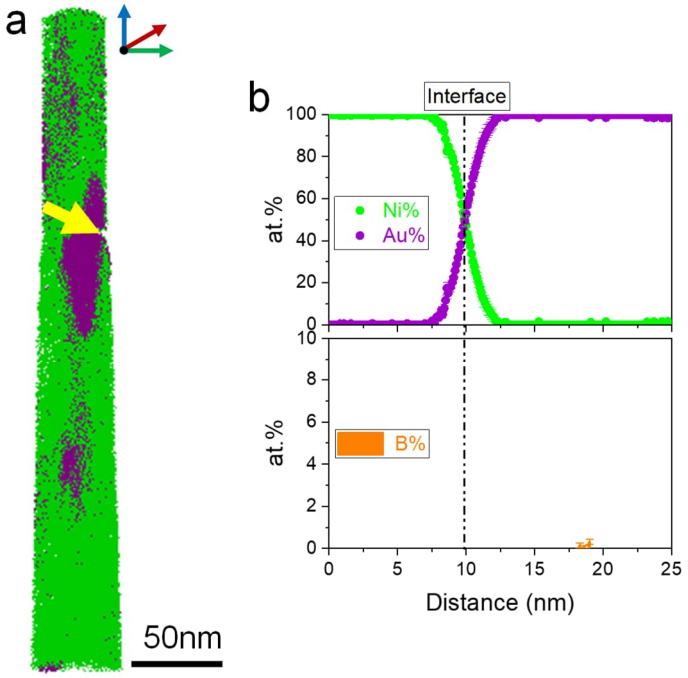

Figure A8-30. *(a) 3D atom maps of L-Au NAs after durability test fully embedded in a Ni matrix (b) 1D compositional profiles of the elements Ni, Au, and B contained in L-Au NAs after the durability test shown along the direction indicated by the yellow arrow in the 3D atom map. Calculated Gibbsian interfacial excess of B = 0.2 B atoms/nm^2, indicative of substantial leaching of B atoms subsequent to the stability test. This observation suggests a notable reduction in the retention of B within the GB following the stability assessment.*

Table A8-1. *EXAFS fitting results of Au L3 edge for Au NPs, L-Au NAs, M-Au NAs, and H-Au NAs.*

Sample	CN	R (Å)	σ^2 (10^{-3} Å^2)	ΔE_0 (eV)	R factor
Au NPs	11.8±0.2	2.62±0.02	2.9±1.4	4.4±1.2	0.013
L-Au NAs	10.9±0.3	2.67±0.01	2.1±1.1	2.3±1.5	0.008
M-Au NAs	9.9±0.2	2.73±0.02	3.6±1.5	4.1±2.0	0.017
H-Au NAs	8.7±0.2	2.78±0.02	2.8±1.2	3.5±1.7	0.012

CN: coordination number; R: bond length; σ: Debye-Waller factor; ΔE_0: inner potential shift; R factor depicting quality of the fit.

Table A8-2. *Two-electron ORR performance between state-of-the-art two-electron ORR nanocatalysts reported in recent publications and the catalysts Chapter 8. S=Selectivity*

Catalyst	E_{onset} vs. RHE	S at 0.6 V	S at 0.5 V	S at 0.4 V	S at 0.3 V	S at 0.2 V	Ref.
Pt–Hg NPs	0.54 V	77%	93%	95%	91%	83%	Nat. Mater. 12, 1137–1143 (2013)
PtP_2 NCs	0.66 V	73%	80%	87%	99%	97%	Nat. Commun. 11, 3928 (2020)
partially oxidized Pd with defect carbon	0.60 V	–	–	92%	91%	88%	Nat. Commun. 11, 2178 (2020)
Pt/HSC	0.51 V	93%	94%	95%	94%	94%	Nat. Commun. 7, 10922 (2016)
h-Pt_1-CuSx NPs	0.61 V	95%	95%	96%	95%	93%	Chem 5, 2099–2110 (2019)
N-doped single-wall carbon nanohorns	0.4 V	–	–	–	97%	97%	Chem 4, 106–123 (2018)
0.35% Pt/TiN	0.63 V	38%	45%	52%	55%	57%	Angew. Chem. Int. Ed. 55, 2058 (2016)
Hierarchically porous carbon	0.2 V	–	–	–	–	96%	Angew. Chem. Int. Ed. 54, 6837–6841 (2015)
Pd-Hg NPs	0.62 V	91%	99%	97%	92%	85%	Nano Lett. 14, 1603 (2014)
$Au_{0.92}Pd_{0.08}$ NPs	0.55 V	–	90%	92%	92%	87%	J. Am. Chem. Soc. 133, 19432 (2011)
Au–Pd_2Hg_5 aerogel	0.49 V	–	–	96%	92%	92%	Adv. Mater. 35, 2211512 (2023)
Pd_4Se NPs	0.39 V	–	90%	92%	92%	90%	Nano Energy 89, 106480 (2021)
Au NPs	**0.5 V**	**–**	**77.90%**	**69.90%**	**68.90%**	**68.80%**	**This work**
L-Au NAs	**0.57 V**	**–**	**80.00%**	**79.70%**	**78.90%**	**79.60%**	**This work**
M-Au NAs	**0.61 V**	**90.70%**	**90.80%**	**90.50%**	**90.10%**	**91.50%**	**This work**
H-Au NAs	**0.66 V**	**99.50%**	**99.00%**	**98.90%**	**98.70%**	**98.00%**	**This work**

Miquel Vega Paredes

EDUCATION

09.2021 - Present	**PhD in Material Science** *Max-Planck-Institute for Sustainable Materials, Düsseldorf (Germany)* PhD defense date (tentative): October 2024
10.2020 - 09.2021	**Master's degree in Industrial Chemistry and Introduction to Chemical Research** *Universitat Autonòma de Barcelona, Bellaterra (Spain)* Average mark: 9.45/10.00
09.2016 - 07.2020	**Bachelor's degree in Nanoscience and Nanotechnology** *Universitat Autonòma de Barcelona, Bellaterra (Spain)* Average mark: 8.99/10.00

RELEVANT EXPERIENCE

09.2021 - Present	**PhD Thesis** *Max-Planck-Institute for Sustainable Materials, Düsseldorf (Germany)* Thesis: Improving Electrocatalysts through Advanced Nanostructure Characterization Supervisors: Prof. Christina Scheu (MPIE), Prof. Dr. Jochen Schneider (RWTH)
10.2023 - Present	**Co-Responsable of Chemical Laboratory of Independent Research Group Nanoanalytics and Interfaces** *Max-Planck-Institut für Eisenforschung, Düsseldorf (Germany)*
01.2023 - Present	**Responsable of Electrochemical Laboratory of Independent Research Group Nanoanalytics and Interfaces** *Max-Planck-Institut für Eisenforschung, Düsseldorf (Germany)*
02.2021 - 07.2021	**Master Thesis** *Max-Planck-Institut für Eisenforschung, Düsseldorf (Germany)* Thesis: Electron Microscopy Degradation Studies of Ruthenium-Platinum Core-Shell Nanoparticles for Polymer Electrolyte Membrane Fuel Cells Supervisors: Prof. Christina Scheu (MPIE), Dr. Alba Garzón Manjón (ICN2, Spain)
07.2020 - 09.2020	**Summer Internship** *Max-Planck-Institut für Eisenforschung, Düsseldorf (Germany)* Topic: Degradation Mechanisms During Operation of High Temperature Polymer Electrolyte Membrane Fuel Cells Supervisors: Prof. Christina Scheu (MPIE), Dr. Alba Garzón Manjón (ICN2, Spain)

HONORS AND AWARDS

04.2024	German Academic Exchange Service (**DAAD**) **scholarship** – support for **research stay** at **National Center for Electron Microscopy** (Lawrence Berkeley National Laboratory, USA)
04.2024	Selected as **MPIE young scientist** to give a talk on "Tuning Catalysts for a Sustainable Future" - MPIE Renaming Ceremony (Düsseldorf, Germany) https://plan.events.mpg.de/event/159/program
03.2024	Selected as **Young Scientist Participant** - 73rd **Lindau Nobel Laurate Meeting** Physics (Lindau, Germany)
09.2023	Selected for the **IFSM Young Scientist Assembly** - 20th International Microscopy Congress (Busan, Korea)
04.2023	**DGE Conference Travel Sponsorship** – support for 20th International Microscopy Congress (Busan, Korea)
04.2023	Appointed **Hiring Manager** of the Young Deutsche Gesellschaft für Elektronen-mikroskopie (DGE) https://ydge.de/members/
02.2023	**Invited Speaker** at DGE Young Microscopists Symposium - Microscopy Conference 2023 (Darmstadt, Germany)
08.2022	Approval of **ESTEEM3 Transnational Access Proposal** on "HAADF-STEM tomography of Ru@Pt core shell NPs for fuel cell applications" to perform experiments in the center of Electron Microscopy for Material Science (Antwerp, Belgium).
01.2021	**Special End of Studies Award** ("Premio Extraordinario") - Bachelor's degree in Nanoscience and Nanotechnology (Universitat Autonòma de Barcelona, Spain)

CONFERENCES, SEMINARS and SCHOOLS

09.2023 Electrolyte Fe impurities effects on Ruddlesden-Popper planar defects in $LaNiO_3$ perovskites during oxygen evolution reaction by identical location STEM
Vega-Paredes, M., Cheraparambil, H., Shoji Aota, L., Jung, C., Weidenthaler, C., & Scheu, C.
20th International Microscopy Congress
Busan, South Korea
Oral Presentation

09.2023 Determining the degradation mechanisms and active species of electrocatalysts by identical location electron microscopy
Vega-Paredes, M., Aymerich-Armengol, R., & Scheu, C.
NRF-DFG workshop at the Korea Institute for Energy Research on "Electrodes for direct sea-water splitting and microstructure-based stability analyses"
Daejeon, South Korea
Invited Presentation

03.2023 Spring School Hydrogen Technology 2023
Lauenburg/Elbe, Germany 27th-31st March
Participation in Spring School

03.2023 Insights into the degradation of metallic core-shell nanoparticles under fuel cell conditions by 3D identical location STEM
Vega Paredes, M., Aymerich Armengol, R., Rivas Rivas, N., Garzón Manjón, A., & Scheu, C.
Microscopy Conference MC 2023
Darmstadt, Germany
Poster Presentation

11.2022 How can electron tomography be used for studying the catalyst degradation of fuel cells
Vega Paredes, M., Arenas Esteban, D., Garzón Manjón, A., & C. Scheu
Advanced Electron Nanoscopy Group - Institut Catala de Nanociència i Nanotecnologia
Bellaterra, Spain
Invited Presentation

10.2022 EELS & EFTEM Analysis
Gatan, Fall 2022 (Online)
Participation in Online School

05.2022 Quantitative Electron Microscopy 2022
Port Barcares, France 8th-20th May
Participation in Summer School

01.2022 Ruthenium-Platinum Core-Shell Nanoparticles as durable, CO tolerant catalyst for Polymer Electrolyte Membrane Fuel Cells
Vega Paredes, M., Garzón Manjón, A., Rivas Rivas, N., Berova, V., Hengge, K., Gänsler, T., Jurzinsky, T., & Scheu, C.
International Symposium on Nanoparticles, Nanomaterials and Applications 2022
Caparica, Portugal
Shotgun Presentation

11.3 Appendix: Curriculum Vitae

PUBLICATION LIST

In total **15 publications** in peer-reviewed journals and **6 as first/equally contributing author**.

- Geng, X.*, **Vega-Paredes, M.***, Wang, Z., Ophus, C., Lu, P., Ma, Y., Zhang, S., Scheu, C., Liebscher, C., & Gault, B. (2024) Grain Boundary Engineering for Efficient and Durable Electrocatalysis. *Nature Communications*, 15, 8534. https://doi.org/10.1038/s41467-024-52919-w.

- Geng, X.*, **Vega-Paredes, M.***, Lu, X., Chakraborty, P., Li, Y., Scheu, C., Wang, Z., & Gault, B. (2024). Concave Grain Boundaries Stabilized by Boron Segregation for Efficient and Durable Oxygen Reduction. *Advanced Materials*, 36, 2404839. https://doi.org/10.1002/adma.202404839.

- Aymerich-Armengol, R., **Vega-Paredes, M.**, Mingers, A., Camuti, L., Kim J., Bae, J., Efthimiopoulos, I., Sahu, R., Podjaski, F., Rabe, M., Scheu, C., Lim, J., & Zhang, S. (2024) Operando Insights on the Degradation Mechanisms of Rhenium doped Molybdenum Disulfide Nanocatalysts for Electrolyzer Applications. *Advanced Functional Materials*, 2413720. https://doi.org/10.1002/adfm.202413720

- Cheraparambil, H., **Vega-Paredes, M.**, Scheu, C., & Weidenthaler, C. (2024) Unraveling the Evolution of Dynamic Active Sites of $LaNi_xFe_{1-x}O_3$ Catalysts During OER. *ACS Applied Materials and Interfaces*, *16*, 21997–22006. https://doi.org/10.1021/acsami.4c02502.

- Jang, K., Son, J., Jang, J., Kim, B., **Vega-Paredes, M.**, Jang, H., Allahyari, M., Kim, S., Ryou, K., Chae, D., Park, H., Jung, S., Oh, M., Jung, C., Scheu, C., & Choi, P. (2024) Impact of hierarchical dopant-induced microstructure on the thermoelectric properties of p-type Si-Ge alloys revealed by comprehensive multi-scale characterization. *Advanced Functional Materials*, 2403785. https://doi.org/10.1002/adfm.202403785.

- Cheraparambil, H., **Vega-Paredes, M.**, Wang, Y., Tüysüz, H., Scheu, C., & Weidenthaler, C. (2024). Deciphering the role of Fe impurities in the electrolyte boosting the OER activity of LaNiO3. *Journal of Materials Chemistry A,* 12, 5194-5203. https://doi.org/10.1039/D3TA06733E.

- **Vega-Paredes, M.***, Scheu, C., & Aymerich-Armengol, R.* (2023). Expanding the Potential of Identical Location Scanning Transmission Electron Microscopy for Gas Evolving Reactions: Stability of Rhenium Molybdenum Disulfide Nanocatalysts for Hydrogen Evolution Reaction. *ACS Applied Materials and Interfaces, 15* (40), 46895-46901. https://doi.org/10.1021/acsami.3c09188.

- **Vega-Paredes, M.**, Aymerich-Armengol, R., Arenas Esteban, D., Martí-Sánchez, S., Bals, S., Scheu, C., & Garzón Manjón, A. (2023). Electrochemical Stability of Rhodium–Platinum Core–Shell Nanoparticles: An Identical Location Scanning Transmission Electron Microscopy Study. *ACS Nano*, *17* (17)*,* 16943-16951. https://doi.org/10.1021/acsnano.3c04039.

- Rivas Rivas, N., Garzón Manjón, A., **Vega-Paredes, M.**, Kim, S., Gault, B., Jun, H., Jung, C., Berova, V., Hengge, K., Jurzinsky, T., & Scheu, C. (2023). Chemistry and microstructure of C-supported Ru catalyst nanoparticles: A correlative study. *Ultramicroscopy, 254*, 113831. https://doi.org/10.1016/j.ultramic.2023.113831.

- López Freixes, M., Zhou, X., Aymerich-Armengol, R., **Vega-Paredes, M.**, Peguet, L., Warner, T., & Gault, B. (2023). Crack arrest markings in stress corrosion cracking of 7xxx aluminium alloys: Insights into active hydrogen embrittlement mechanisms. *Scripta Materialia*, *237*, 115690. https://doi.org/10.1016/j.scriptamat.2023.115690.

- Liang, Y., Mrovec, M., Lysogorskiy, Y., **Vega-Paredes, M.**, Scheu, C., & Drautz, R. (2023) Atomic cluster expansion for Pt–Rh catalysts: From ab initio to the simulation of nanoclusters in few steps. *Journal of Materials Research*, *38,* 5125-5135. https://doi.org/10.1557/s43578-023-01123-5.

- Berova, V., Manjón Garzón, A., **Vega Paredes, M.**, Schwarz, T., Rivas, N. A., Hengge, K., Jurzinsky, T., & Scheu, C. (2023). Influence of the shell thickness on the degradation of Ru@Pt core-shell catalysts in PEM fuel cells. *Journal of Power Sources*, *554,* 232327. https://doi.org/10.1016/j.jpowsour.2022.232327.

- Zubair, M., Felten, M., Hallstedt, B., **Vega Paredes, M.**, Abdellaoui, L., Bueno Villoro, R., Lipinska-Chwalek, M., Ayeb, N., Springer, H., Mayer, J., Berkels, B., Zander, D., Korte-Kerzel, S., Scheu, C., & Zhang, S. (2023). Laves phases in Mg-Al-Ca alloys and their effect on mechanical properties. *Materials & Design*, *225*, 111470. https://doi.org/10.1016/j.matdes.2022.111470.

- Garzón Manjón, A.*, **Vega Paredes, M.***, Berova, V., Gänsler, T., Schwarz, T., Rivas, N. A., Hengge, K., Jurzinsky, T., & Scheu, C. (2022). Insights into the performance and degradation of Ru@Pt core-shell catalysts for fuel cells by advanced (scanning) transmission electron microscopy. *Nanoscale*, *14*, 18060–18069. https://doi.org/10.1039/d2nr04869h.

- **Vega Paredes, M.***, Garzón Manjón, A.*, Hill, B., Schwarz, T., Rivas, N. A., Jurzinsky, T., Hengge, K., Mack, F., & Scheu, C. (2022). Evaluation of functional layers thinning of high temperature polymer electrolyte membrane fuel cells after long term operation. *Nanoscale*, *14*, 11543–11551. https://doi.org/10.1039/D2NR02892A.

  *=equally contributing

Düsseldorf, 04.11.2024 Miquel Vega Paredes